Understanding the ^{7}Li(d, n)^{8}Be Reaction at Very Low Energies

by

Amanda Sabourov

Department of Physics
Duke University

Date

Approved:

Henry R. Weller, Supervisor

Shailesh Chandrasekharan

Haiyan Gao

Calvin Howell

Ashutosh Kotwal

Dissertation submitted in partial fulfillment of
the requirements for the degree of
Doctor of Philosophy in the Department of
Physics in the Graduate School
of Duke University

2006

Abstract

(Physics – TUNL)

Understanding the ^{7}Li(d, n)^{8}Be Reaction at Very Low Energies

by

Amanda Sabourov

Department of Physics
Duke University

_____

Date

Approved:

_____

Henry R. Weller, Supervisor

_____

Shailesh Chandrasekharan

_____

Haiyan Gao

_____

Calvin Howell

_____

Ashutosh Kotwal

An abstract of a dissertation submitted in partial
fulfillment of the requirements for the degree
of Doctor of Philosophy in the Department
of Physics in the Graduate School
of Duke University

2006

Abstract

Understanding the ^{7}Li(d, n)^{8}Be Reaction at Very Low Energies

The ^{7}Li(d, n)^{8}Be reaction was studied at energies between E_d= 45 keV and 160 keV at Triangle Universities Nuclear Laboratory (TUNL) using the polarized ion source and stopping the beam in the target. The differential cross section, vector analyzing power $iT_{11}(\theta)$, and tensor analyzing powers $T_{20}(\theta)$, $T_{21}(\theta)$, and $T_{22}(\theta)$ were measured for the ^{7}Li($\vec{d}$, n_0)^{8}Be and ^{7}Li($\vec{d}$, n_1)^{8}Be reactions at beam energies of E_d= 80 keV, 130 keV, and 160 keV. The polarization observables were compared with Distorted Wave Born Approximation (DWBA) and coupled reaction channels calculations. In addition, the Transition Matrix Elements (TMEs) were extracted from the data and compared with the coupled reaction channels predictions. The absolute cross section and astrophysical S factor were also measured for the ^{7}Li(d, n_0)^{8}Be and ^{7}Li(d, n_1)^{8}Be reactions at beam energies of E_d= 45 keV, 60 keV, and 80 keV. The results of these measurements were compared with previous measurements and the predictions of the DWBA and coupled channels models.

The TME analysis of the polarization data revealed unique solutions for both neutron states, both solutions being dominated by p-waves in the entrance chan-

nel. Although DWBA calculations failed to reproduce the data, the coupled reaction channels model using the code FRESCO was able to qualitatively reproduce the data once a large target spin-orbit potential and coupling to the first excited state of the target were included in the calculation. However, the TME solution produced by the FRESCO calculations consisted of predominantly d-waves in the entrance channel for the n_0 state and p-waves for the n_1 state.

The absolute cross section and S factor measurements confirmed that for the ^{7}Li(d, n_0+n_1)^{8}Be reaction, the astrophysical S factor in the low energy region relevant to Big Bang Nucleosynthesis models has zero slope, as assumed by Boyd, *et al.*, with a value of 4×10^3 ($\pm$ 1×10^3) keV b. The average DWBA value of 340 keV b for the n_0 state is in good agreement with the measured value of 430 ± 120 keV b. The FRESCO code predicted an S factor with a positive slope and possibly some higher-order energy dependence in this energy region for the ^{7}Li(d, n_0)^{8}Be and ^{7}Li(d, n_1)^{8}Be reactions, which does not agree with the experimental results. The S factor results and the TME solution from FRESCO indicate that a more sophisticated theory is necessary to fully explain the data.

Acknowledgements

Completion of this work was made possible by the help and support of many people. I'd like to begin by thanking first and foremost Dr. Henry Weller, my thesis advisor and long-time mentor. I can honestly say that I would not have finished (several times) without his encouragement and patience. A big, big thanks is extended to Dr. Richard Prior, my "second" advisor, friend, and mentor. Thanks to the past and present members of the Radiative Capture group at TUNL who have sacrificed weekends, holidays, and sleep for runs and taught me what I needed to know: Steve-O, Kaveri, Brendan, especially Kon, Matthew, and Brent, our postdocs, Anton and Mohammed, and our visiting profs Mark and Nasser. Big thanks to Kara, who has been a wonderful mentor and friend. A very, very special thank you for the guys who make the runs possible in the first place: John Dunham, Richard O'Quinn, Paul Carter, and Chris Westerfeldt. I'd like to thank the members of NTOF for mucho, mucho support on this project. Specifically, Alex for all the computer help and guidance and for all the assistance with the detectors, daq, etc .... I'd like to thank Bruno for working on our theory even when he'd moved on to better things. Thanks to the guys in my graduate class, Joe, John, Brad, Josh, and DJ. They made the first few years tolerable and even fun. A great big thanks to Donna Ruger, my "Duke mom" who was there to make sure I was okay.

And finally, I want to thank my family: Mom, Dad, Bonny, Emily, Ally, Tyler, Nina, and Vitali for all the encouragement and support. Kostya, I don't know if I could have persevered without you. Thanks for encouraging me every step of the way, even if it meant dealing with take-out for dinner and a messy house. Ya tebya lyublyu.

Anna, thank you so much for coming into my life and sharing the latter portion of this experience with me. You've made it more bearable and more interesting. After all, now I am intimately familiar with the detailed rules of a tweetle beetle puddle paddle battle and how exactly one would eat green eggs and ham. You keep me laughing and smiling even when things seem hopeless. Oh, and the color you've added to my life, text books, calculations, walls, floors, and cupboards is priceless.

And now, let's have a little talk about tweetle beetles ...

Contents

List of Figures

List of Tables

Chapter 1

Introduction and Motivation

The experimental study of the ^{7}Li(d, n)^{8}Be reaction presented here succeeded in providing the most complete picture to date of the ^{7}Li(d, n_0)^{8}Be and ^{7}Li(d, n_1)^{8}Be reactions in the region between $E_{c.m.}$= 33 keV and 124 keV. The present work consists of both cross section measurements and polarization observable measurements. The experimental polarization observables were compared with both Distorted Wave Born Approximation (DWBA) and coupled reaction channels (CRC) calculations. Because the CRC calculation gave a reasonable description of the polarization observables, the model's prediction for the behavior of the contributing Transition Matrix Elements (TMEs) was compared with those that were obtained from a detailed TME analysis of the experimental data in an energy region between $E_{c.m.}$= 62 keV to 124 keV. The absolute cross section measurements allowed for determination of the astrophysical S factor for both the ^{7}Li(d, n_0)^{8}Be and ^{7}Li(d, n_1)^{8}Be reactions at $E_{c.m.,eff}$ = 33 keV, 43 keV, and 57 keV. These results were compared with previous measurements and the predictions of the DWBA and CRC calculations.

1.1 Reaction Mechanisms for the $^{7}\mathrm{Li}(\mathrm{d},\mathrm{n})^{8}\mathrm{Be}$ Reaction

In general, the $^{7}\mathrm{Li}(\mathrm{d},\mathrm{n})^{8}\mathrm{Be}$ reaction is not well understood at very low energies. Very little experimental data are available below several hundred keV, especially data investigating the vector and tensor analyzing powers which result from polarized deuteron beams on the ^{7}Li target. These analyzing powers provide information about the reaction dynamics which enable theorists to test interaction models. As described in the next section, understanding this reaction at energies below 200 keV is also important for cosmological calculations.

The polarization observables can be compared directly to the observables predicted by theoretical calculations. However, this comparison only reveals major differences between theory and experiment; greater insight can be obtained by investigating the origins of these differences. One powerful way to do this is to expand the observables in terms of the complex Transition Matrix Elements (TMEs). The TMEs can then be fitted to the measured data to obtain the amplitudes and phases of the TMEs that best represent the data. This provides a deeper insight into the reaction mechanisms themselves, and, by comparing these TMEs with those calculated from theory, critical information about why the theory and experiment may differ can be gleaned. In addition, by finding a theory which reproduces the TME results, a reliable extrapolation of the astrophysical $S(E)$ factor to lower energies can be performed.

1.2 Astrophysical Importance of the $^{7}\mathrm{Li}(\mathrm{d},\mathrm{n})^{8}\mathrm{Be}$ Reaction

Once the temperature of the early universe had dropped to just below 10^9 K, deuterium was able to remain intact, and Big Bang Nucleosynthesis (BBN) began. The bulk of the deuterium produced by the interaction of the protons and neutrons was rapidly burned in the creation of ^{4}He, but some small amount may have been left unburned if the density of the universe was too low for the deuterium-burning reactions to go to completion [Boy01, Rol88].

Within a few minutes, the expansion of the universe reduced its temperature and density and increased its entropy to a point where further thermonuclear reactions were impossible. As a result, carbon and heavier elements were unable to form in any appreciable amounts. These elements could be produced later in stars and other such objects by burning the lighter elements created in the big bang [Rol88, Arn96].

1.2.1 Big Bang Nucleosynthesis Models

The standard model of BBN assumes that the baryon distribution was uniform and isotropic during the period when light elements were being formed. The abundances of the light nuclei as predicted by the standard model depend only on the present average universal baryon density ρ_b, which is directly related to the baryon density at the time of nucleosynthesis, and the temperature of the microwave background radiation [Rol88]. Figure 1.1 shows the mass fraction of the light elements synthesized in the standard model as a function of the present density ρ_b. These predicted abundances are in reasonable agreement with observational data [Dol02].

However, an observed diffuse x-ray glow, which also determines baryon density, suggests a value for the baryon density significantly higher than the upper limit set by the standard model [Boy01].

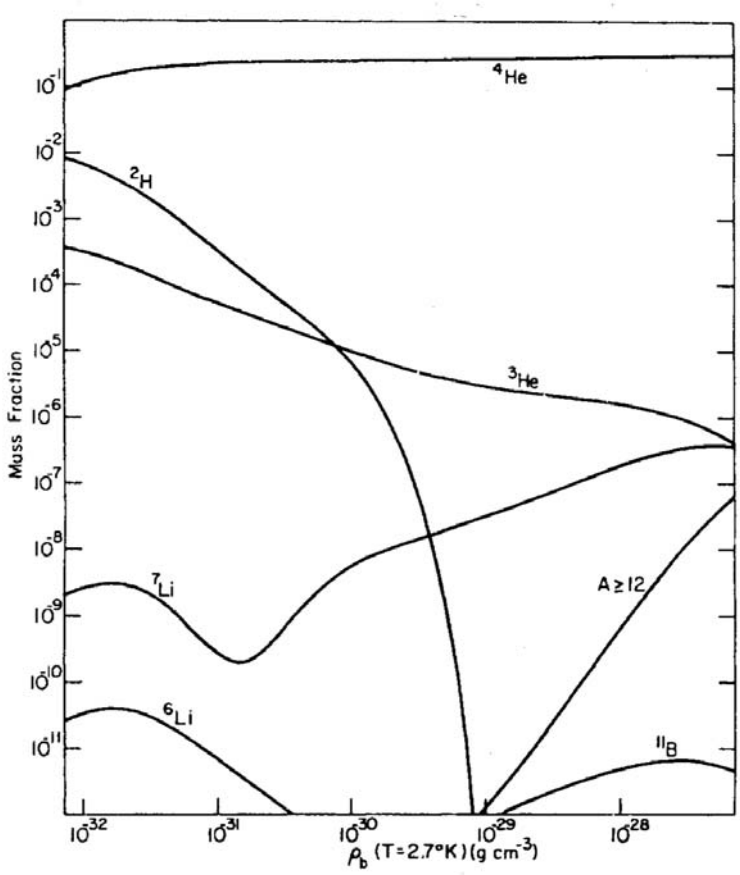

Figure 1.1: Mass fraction of the light elements synthesized by standard big-bang models as a function of the present baryon density of the universe ρ_b. From [Wag72].

Inhomogeneous models assume that the baryon distribution of the universe was "lumpy" at the time of BBN. In these models, the universe would have developed into a high-density region and a low-density region. Although very similar to the standard model, new reaction possibilities exist that can increase the abundance of ^{7}Li and heavier nuclides [Boy01]. The inhomogeneous models have several more parameters than the standard model but do allow for a higher baryon density value.

Because the abundance of ^{7}Li is also very sensitive to baryon inhomogeneity (see Figure 1.1), it can be used to differentiate between the standard and inhomogeneous models of BBN. This abundance is determined by reactions that produce and those that destroy ^{7}Li. Of particular interest are the destruction reactions ^{7}Li+d since both ^{7}Li and deuterium coexist in the low density regions of the inhomogeneous models, and the deuterium abundance can be large. These abundances, however, depend heavily on reaction rates which require nuclear reaction cross sections (see Chapter 6). The largest uncertainty in the BBN models is introduced by the values of these cross-sections. For ^{7}Li, this theoretical accuracy is about 20-30% [Dol02]. An accurate knowledge of this reaction and its mechanisms is necessary for cosmological model calculations to be reliable.

1.2.2 Reaction Rates

An understanding of the nucleosynthesis of the elements hinges directly on the magnitude of the reaction rate per particle pair:

$$\langle \sigma v \rangle = \sqrt{\frac{8}{\pi \mu}} \frac{1}{(kT)^{3/2}} \int_0^\infty \sigma(E) E \exp\left(\frac{-E}{kT}\right) dE, \tag{1.1}$$

where v is the relative velocity between the projectile and target nucleus, k is Boltzmann's constant, μ is the entrance-channel reduced mass, T is the temperature, E is the center-of-mass energy, and $\sigma(E)$ is the energy-dependent nuclear reaction cross section.

The cross section can be written as

$$\sigma(E) = \frac{S(E)}{E} \exp(-2\pi\eta), \tag{1.2}$$

where η is the Sommerfeld parameter defined as

$$\eta = \frac{\mathrm{Z}_1\mathrm{Z}_2 e^2}{\hbar v}, \tag{1.3}$$

which can also be written

$$2\pi\eta = 31.29\ Z_1 Z_2 \sqrt{\frac{\mu}{E}}. \tag{1.4}$$

The projectile and target charges are Z_1 and Z_2, respectively, e is the charge of the electron, v is the relative velocity, and μ is the reduced mass in amu. Written in this form, the cross section can be separated into three components:

$$\sigma(E) \propto \exp(-2\pi\eta) \tag{1.5}$$

refers to the rapid decrease in the cross section due to the Coulomb barrier,

$$\sigma(E) \propto \pi\lambda\!\!\!^{-2} \propto \frac{1}{E} \tag{1.6}$$

refers to the cross-sectional dependence on the de Broglie wavelength, and $S(E)$ contains all the strictly nuclear effects [Rol88]. For nonresonant reactions, it varies smoothly with energy and less rapidly than the cross section, making it more useful in extrapolating the measured cross sections to astrophysical energies.

Using Equation 1.2 for the cross section in Equation 1.1 gives the following for the reaction rate per particle:

$$\langle \sigma v \rangle = \left(\frac{8}{\mu\pi}\right)^{1/2} \frac{1}{(kT)^{3/2}} \int_0^\infty S(E) \exp\left(-\frac{E}{kT} - \frac{b}{E^{1/2}}\right) dE, \tag{1.7}$$

where b^2 is the Gamow energy $E_G = 2\mu(\pi e^2 Z_1 Z_2)^2/\hbar^2$.

The exponential term in Equation 1.7 primarily governs the energy dependence of the integrand. The portion of this term representing penetration through the Coulomb barrier $\exp(-b/E^{1/2}) = \exp(-(E_G/E)^{1/2})$ becomes very small at low energies, whereas the $\exp(-E/kT)$ term representing the number of particles available in

the high-energy tail of the Maxwell-Boltzmann distribution vanishes at high energies [Rol88]. As shown in Figure 1.2, the product of the two results in the integrand peaking near an energy E_0. The Gamow factor shifts the effective energy of the peak from the maximum energy of the Maxwell-Boltzmann distribution at $E = kT$ to the effective mean energy [Rol88]

$$E_0 = \left(\frac{bkT}{2}\right)^{2/3} = \left(\frac{\mu}{2}\left(\frac{\pi e^2 Z_1 Z_2 kT}{\hbar}\right)^2\right)^{1/3} \tag{1.8}$$

and gives the peak a width at $1/e$ of

$$\Delta = \frac{4}{3^{1/2}}\left(E_0 kT\right)^{1/2}. \tag{1.9}$$

For a given temperature T, the nuclear reactions are most likely to occur in the energy window around E_0, and frequently, $S(E)$ is nearly constant over this window. Based on this assumption, $S(E) = S(E_0)$ and the definitions in Equations 1.8 and 1.9, the reaction rate becomes [Rol88]

$$\langle \sigma v \rangle = \left(\frac{2}{\mu}\right)^{1/2} \frac{\Delta}{(kT)^{3/2}} S(E_0) \exp\left(-\frac{3E_0}{kT}\right). \tag{1.10}$$

For BBN temperature $T = 0.12 \times 10^9$ K, the Gamow window is centered at $E_0 = 72$ keV and has a width $\Delta = 63$ keV, therefore spaning the region from 9 to 135 keV. For the high temperature region, $T = 10^{10}$ K, $E_0 = 1.3$ MeV and $\Delta = 2.5$ MeV, encompassing a region from 113 keV to 2.6 MeV.

The reaction rate can be either resonant or nonresonant. For ^{7}Li+d in the BBN energy and temperature region ($E_{c.m.}$= 10 to 900 keV and $T = 0.12 \times 10^9$ to 10^{10} K), there is a nonresonant contribution as well as two resonances: a narrow resonance at 280 keV and a broad resonance at 600 keV [Ser04, Boy93].

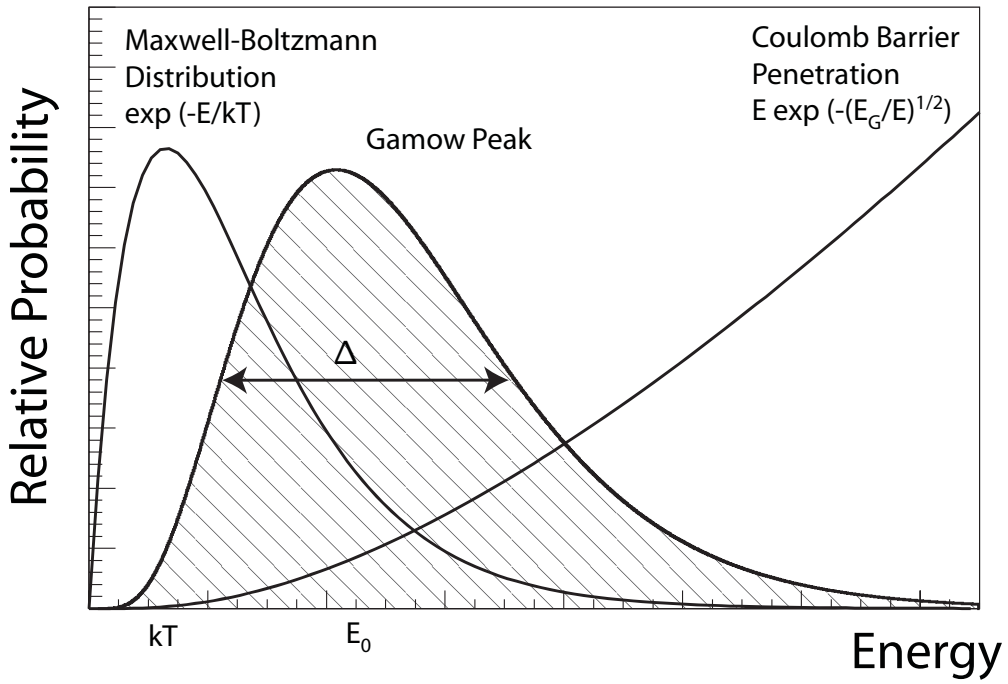

Figure 1.2: The dominant energy-dependent contributions to the nuclear reaction rate. The shaded region represents the area of the Gamow peak, which is the product of the Maxwell-Boltzmann distribution function and the Coulomb barrier penetrability function. The peak is centered near an energy E_0 and has a width at $1/e$ of Δ.

The 280-keV Resonance Contribution

Because the 280-keV resonance is narrow with a total width $\Gamma \ll E_R$ the resonant energy, the cross section is expressed using the Breit-Wigner formula for a single-level resonance [Rol88]:

$$\sigma(E) = \pi \lambda\!\!\!^{-2} \frac{2J_R + 1}{(2J_1 + 1)(2J_2 + 1)} (1 + \delta_{12}) \frac{\Gamma_d(\Gamma_n + \Gamma_p + \Gamma_\alpha)}{(E - E_R)^2 + (\Gamma/2)^2}, \tag{1.11}$$

where J_R, J_1, and J_2 are the spins of the resonance and entrance channel particles and Γ_d, Γ_n, Γ_p, and Γ_α are the partial widths for deuteron, neutron, proton, and alpha decay, respectively. Using this expression for the cross section in Equation 1.1, the reaction rate becomes [Boy93]

$$\langle \sigma v \rangle = \left(\frac{2\pi}{\mu k T} \right)^{3/2} \hbar^2 \frac{2J_R + 1}{(2J_1 + 1)(2J_2 + 1)} \frac{\Gamma_d(\Gamma_n + \Gamma_p + \Gamma_\alpha)}{\Gamma} \exp\left(\frac{-E_R}{kT} \right). \quad (1.12)$$

This contribution to the reaction rate ($N_A\langle \sigma v \rangle$, where N_A is Avogadro's number) is shown as the dashed line in Figure 1.3.

The 600-keV Resonance Contribution

The 600-keV resonance is broad ($\Gamma/E_R \geq 10\%$), and therefore the cross section is [Rol88]:

$$\sigma(E) = \sigma_R \frac{E_R}{E} \frac{\Gamma_d(E)}{\Gamma_d(E_R)} \left(\frac{\Gamma_n(E)}{\Gamma_n(E_R)} + \frac{\Gamma_p(E)}{\Gamma_p(E_R)} + \frac{\Gamma_\alpha(E)}{\Gamma_\alpha(E_R)} \right) \frac{(\Gamma_R/2)^2}{(E - E_R)^2 + [\Gamma(E)/2]^2}, \quad (1.13)$$

where σ_R is the cross section at E_R and Γ_R is the width the resonance would have if $E = E_R$.

The resulting contribution to the reaction rate $N_A\langle \sigma v \rangle$ is the dotted line in Figure 1.3.

The Nonresonant Contribution

Previously, the value of $S(E_0)$ was determined by examining ^{7}Li(d, n) and ^{7}Li(d, p) data above the 600-keV resonance. The $S(E)$ value for both channels was found to be constant in the region between 1.6 and 2.0 MeV, with that for the (d,n) channel being 1.1×10^4 keV b [Sla57] and that of the (d,p) channel being 0.6×10^4 keV b

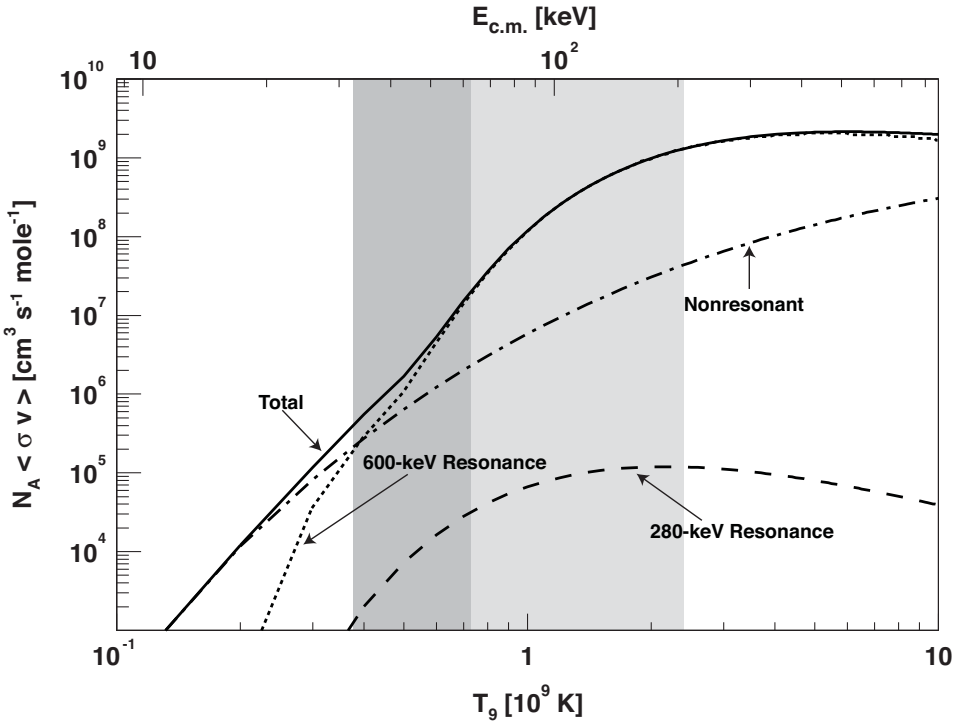

Figure 1.3: Thermonuclear reaction rate for ^{7}Li+d. The solid curve is the total reaction rate, which is the sum of the nonresonant contribution (dot-dashed line), 600-keV resonance contribution (dotted line), and 280-keV resonance contribution (dashed line). The shaded areas represent the energy and temperature region covered by the present work: the S factor (dark) and the polarization observable measurements (light).

[Sch76, McC75]. The sum of the two, 1.7×10^4 keV b was used for the value of $S(E_0)$ [Boy93]. When this value is inserted in Equation 1.10, the thermonuclear reaction rate $N_A\langle\sigma v\rangle$ for the nonresonant contribution is that shown as the dot-dashed line in Figure 1.3.

The reaction rates shown in Figure 1.3 were calculated for the BBN temperature region $T = 0.12 \times 10^9$ to 10^{10} K, corresponding to an energy region of $E_{c.m.}$= 10 to 900 keV, using measured resonance parameters for the resonant terms. However,

the S factor for the nonresonant term for energies below the 280-keV resonance was assumed to have zero slope on the basis of experimental (d,n) and (d,p) data taken between 1.6 to 2.0 MeV [Ser04, Boy93, Sla57]. The S factor from these data was assumed to be nonresonant and constant, and this constant value was used for the energy region below the 280-keV resonance. An evaluation of $S(E)$ in the energy region between 20 keV and 200 keV is important in validating the assumptions that data at higher energies are valid for the low energy region and that $S(E)$ is constant over the low energy regions of BBN.

1.3 Previous Work

The lowest energy measurement of the polarization observables for the $^7\mathrm{Li}(\vec{\mathrm{d}}, \mathrm{n}_0)^8\mathrm{Be}$ reaction was performed by von Möllendorff, *et al.* at an energy greater than 640 keV [vM73]. They measured the angular distribution of the analyzing powers between 0° and 160° for the n_0 state and performed a TME analysis, determining that the reaction proceeds primarily by s-wave and p-wave in the entrance channel at these energies. Unfortunately, the measurement is at an energy too high to compare with the present work and to be of much interest to cosmological models.

Absolute cross sections and astrophysical S factors are necessary for reliable reaction rate calculations used in cosmological models. Recent primordial nucleosynthesis codes have incorporated resonant terms at 280 keV and 600 keV in addition to the direct term [Boy93]. These reaction rates were calculated for the BBN temperature region $T = 0.12 \times 10^9$ to 10^{10} K, corresponding to an energy region of $\mathrm{E_{c.m.}}$= 10 to 900 keV, using measured astrophysical S factors. However, the direct term for energies below the 280-keV resonance was assumed to have zero slope on the basis of (d,n)

and (d,p) data taken between 1.6 to 2.0 MeV [Ser04, Boy93, Sla57]. An evaluation of the S factor in the energy region between 20 keV and 200 keV is important in validating the assumptions that data at higher energies are valid for the low energy region and that the S factor is constant over the low energy regions of BBN. To date, only one set of data exists for the ^{7}Li(d, n) reaction below $E_{c.m.}$= 100 keV, that of Hofstee, *et al.* ([Hof01]), which is for the energy region between $E_{c.m.}$= 50 and 100 keV. It is almost an order of magnitude higher than the assumption of Boyd, *et al.* and has a negative slope (see Figure 6.5). Below $E_{c.m.}$= 200 keV, only one other set besides the Hofstee, *et al.* data exists, that of Bagget, *et al.*, extending down to an energy of $E_{c.m.}$= 100 keV ([Bag52]), which indicates a value for the S factor that is 2 to 3 times higher than the Boyd, *et al.* value.

1.4 Present Work

The Atomic Beam Polarized Ion Source (ABPIS) at the Triangle Universities Nuclear Laboratory (TUNL) provides a unique opportunity to study the polarization observables by delivering beams with a relatively high beam current and high polarization. Chapter 2 describes the production and transport of these polarized beams as well as the evaporated ^{7}Li target design. The characteristics and details of the neutron detectors and signal processing electronics used allowed for reliable separation of the gamma background from the neutron signal. Chapter 3 covers the data analysis techniques for sorting events, utilizing pulse-shape discrimination to eliminate the gamma background, fitting the spectra, and determining errors.

A description and definition of the analyzing powers, their extraction from the experimental data, and their results are given in Chapter 4. Angular distributions of

the differential cross section, vector analyzing power, and all three tensor analyzing powers were obtained at $E_{c.m.}$= 62 keV to 124 keV for a complete set of polarization observables at three energies for transitions to the ground and first excited states of ^{8}Be (n_0 and n_1, respectively). The expansion of the polarization observables for each neutron state into the transition matrix elements is explained and the results are presented in Chapter 5. For the $^7\mathrm{Li}(\vec{d}, n_0)^8\mathrm{Be}$ reaction, s-, p-, and d-waves were considered in the entrance channel, while for the $^7\mathrm{Li}(\vec{d}, n_1)^8\mathrm{Be}$ reaction only s- and p-waves were necessary to explain the data. The analysis led to a unique solution for both transitions. The solution for the n_0 transition corresponded to an average of 82% p-waves in the entrance channel, 10% s-waves, and 8% d-waves, with the $^2p_2$ element carrying over 50% of the total strength. The n_1 solution was dominated by an average of 73% p-waves and 27% s-waves with the $^6p_4$ and $^6p_6$ elements carrying over 40% of the total amplitude.

The S-factor and absolute cross section results are detailed in Chapter 6. The measurement of the cross section, and thus the S factor, was done at $E_{c.m.}$= 33 keV to 62 keV. This corresponds to a temperature $T = 0.4 \times 10^9$ to 0.7×10^9 K, which covers the low energy end of BBN. Our work was able to determine $S(E)$ for the n_0 and n_1 transitions. Because we were unable to extract the transition to the second excited state of ^{8}Be (n_2) and get the full cross section, our measurement acts to only set a lower limit on the complete result. As such, our results indicate that $S(E)$ is indeed constant for n_0+n_1 giving a value of $S(E) = 5400(\pm1500) - 37(\pm21)E$ keV b in this region, where the slope can be attributed to electron screening effects. This lower limit is a factor of 3 smaller than that used by Boyd, *et al.*, a difference perhaps attributed to contributions from the n_2 state.

The DWBA formalism represents a direct view of the reaction; an assumption

is made when using this theory that the reaction is "nonresonant." In Chapter 7, the experimental data are compared to the results of a DWBA calculation and a CRC calculation. The DWBA calculation is unable to reproduce the polarization observables but predicts a nearly constant S factor of 3400 keV b for the n_0+n_1, which lies within the error bars of the experimental, bare nucleus value of 4000 ± 1000 keV b. This agreement suggests that the direct (nonresonant) mechanism is dominant at energies below $E_{c.m.}$= 70 keV. The CRC calculation using the code FRESCO provides a better description of the experimental results than the DWBA calculation once a large target spin-orbit potential and coupling to the first excited state of the target is included in the calculation. However, although the FRESCO result is in qualitative agreement with the experimental data, serious discrepancies remain. As detailed in Chapter 7, a more demanding comparison of the experimentally determined TMEs with the theoretical ones indicates that the theory fails to reproduce the significant features of the data. The FRESCO calculations produce a TME solution for the n_0 state consisting of primarily d-waves (46%) in the entrance channel with 35% p-waves and 18% s-waves; the n_1 solution is more similar to the experimental result with p-waves dominant (83%) in the entrance channel with 12% d-waves and 5% s-waves. Absolute cross section results of the CRC model do not agree with the experimental results for the n_0 state but are within the errors of the n_1 experimental data. In addition, predictions for the S factor do not agree with the experimental results and suggest that the S factor has a positive slope and possibly higher-order energy dependence. These discrepancies in the TME analysis, cross section result, and S factor result indicate that the reaction dynamics are not entirely understood and a more sophisticated model in needed.

The final chapter, Chapter 8, summarizes the important points and ties the pieces

together. In addition, there are four appendices to support these sections.

Chapter 2

Experimental Setup and Methods

The polarization observables, the absolute cross section, and the S factor of $^{7}\mathrm{Li}(\vec{\mathrm{d}},\mathrm{n})^{8}\mathrm{Be}$ were measured at Triangle Universities Nuclear Laboratory (TUNL) using the Atomic Beam Polarized Ion Source (ABPIS). The deuterium beam was transported to a $^{7}\mathrm{Li}_2\mathrm{O}$ target, generated by evaporating $^{7}\mathrm{Li}$ directly onto the back wall of the chamber. Nine liquid scintillators detected the resulting neutrons and gammas at six to eight angles between 0° and 150°. These detectors permitted the use of pulse-shape discrimination which allowed the separation of neutrons from gammas, effectively eliminating most background.

In addition to the primary measurements, response functions for the monoenergetic neutrons of interest were measured for the detectors using the TUNL FN-Tandem Van de Graaff, working in the Shielded Source Area (SSA). These response functions were then used to fit the raw spectra and extract the yields for the neutron groups of interest.

2.1 Polarized Beams

Early nuclear physics experiments relied primarily on studying decay processes or on bombarding targets with beams of charged particles in order to gain an understanding of nuclear structure. But with these unpolarized beams, only total cross sections or angular distributions of cross sections could be measured, yielding only a handful of observables that could be accurately compared with theory.

However, with the advent of polarized beams, additional information about a reaction can be gleaned. Analyzing powers are the difference in yields produced for two different states of polarization in the beam divided by their sum and arise as a result of the reaction cross section's dependence on the projectile's spin. Both the spin state population and the spin quantization axis direction must be controlled to produce beams with polarizations known well enough to accurately measure the polarization observables. In order to do this, the theory of beam polarization as well as polarized beam production and polarization measurements need to be understood.

2.1.1 Beam Polarization

For a spin-one particle such as a deuteron, either spherical (t_{kq}) or Cartesian (p_i and p_{ij}) tensor moments are used to describe the beam polarization. The signs and coordinate axes are chosen according to the Madison Convention [Bar71]. The tensor moments are related to the average values of the spin operator $\boldsymbol{S}$ as follows:

$$
\begin{aligned}
\mathrm{t}_{00} &= 1 \\
\mathrm{t}_{10} &= \sqrt{\frac{3}{2}}\langle \mathrm{S}_z \rangle \\
\mathrm{t}_{1\pm1} &= \mp\frac{\sqrt{3}}{2}\langle \mathrm{S}_x \ \pm i\mathrm{S}_y \rangle \\
\mathrm{t}_{20} &= \frac{1}{\sqrt{2}}\langle 3\mathrm{S}_z^2 - 2 \rangle \\
\mathrm{t}_{2\pm1} &= \mp\frac{\sqrt{3}}{2}\langle (\mathrm{S}_x \pm i\mathrm{S}_y)\,\mathrm{S}_z \ + \mathrm{S}_z\,(\mathrm{S}_x \pm i\mathrm{S}_y) \rangle \\
\mathrm{t}_{2\pm2} &= \frac{\sqrt{3}}{2}\langle (\mathrm{S}_x \pm i\mathrm{S}_y)^2 \rangle \\
\mathrm{p}_i &= \langle \mathrm{S}_i \rangle \quad i = x, y, z \\
\mathrm{p}_{ij} &= \langle \mathrm{S}_{ij} \rangle = \frac{3}{2}\langle \mathrm{S}_i\mathrm{S}_j + \mathrm{S}_j\mathrm{S}_i \rangle - 2\delta_{ij}
\end{aligned}
\tag{2.1}
$$

where the brackets represent the expectation value averaged over all the particles in the beam and where the spin-one operator is

$$
\mathrm{S}_x = \frac{1}{\sqrt{2}}\begin{pmatrix} 0 & 1 & 0 \\ 1 & 0 & 1 \\ 0 & 1 & 0 \end{pmatrix} \quad \mathrm{S}_y = \frac{1}{\sqrt{2}}\begin{pmatrix} 0 & -i & 0 \\ i & 0 & -i \\ 0 & i & 0 \end{pmatrix} \quad \mathrm{S}_z = \begin{pmatrix} 1 & 0 & 0 \\ 0 & 0 & 0 \\ 0 & 0 & -1 \end{pmatrix} \tag{2.2}
$$

From Equation 2.1, the Cartesian and spherical representations can be related as

$$
\begin{aligned}
\mathrm{t}_{10} &= \sqrt{\tfrac{3}{2}}\mathrm{p}_z & \mathrm{t}_{1\pm1} &= \mp\tfrac{\sqrt{3}}{2}\,(\mathrm{p}_x \pm i\mathrm{p}_y) \\
\mathrm{t}_{20} &= \tfrac{\mathrm{p}_{zz}}{\sqrt{2}} & \mathrm{t}_{2\pm1} &= \mp\tfrac{1}{\sqrt{3}}\,(\mathrm{p}_{xz} \pm i\mathrm{p}_{yz}) \\
\mathrm{t}_{2\pm2} &= \tfrac{1}{2\sqrt{3}}\,(\mathrm{p}_{xx} - \mathrm{p}_{yy} \pm 2i\mathrm{p}_{xy})
\end{aligned}
\tag{2.3}
$$

For polarized beams produced by a polarized ion source, the quantization axis for the nuclear spin, designated as $\hat{\zeta}$ in Figure 2.1, is defined by the direction of the magnetic field and is generally along the axis of the beam momentum. Because

the nuclear spin precesses around the magnetic field direction, only projections on the symmetry axis have non-vanishing, time-averaged values. In the case of the deuteron, these projections correspond to particles with spin along $+\zeta$ and magnetic substate $m_I = +1$, with spin along $-\zeta$ and m_I= -1, and with spin distributed in the plane perpendicular to ζ and $m_I = 0$. If the number of particles in each of these states is defined as N_+, N_-, and N_0, respectively, then the non-zero beam moments can be written as

$$p_\zeta = N_+ - N_- \tag{2.4}$$

and

$$p_{\zeta\zeta} = 1 - 3N_0 \tag{2.5}$$

where $N_+ + N_- + N_0 = 1$.

The right-handed coordinate system used to describe the analyzing powers uses the Madison Convention [Bar71] and is shown in Figure 2.1. The direction of the z-axis is parallel to the momentum of the incoming particles $\vec{k}_{in}$; the y-axis is along $\vec{k}_{in} \times \vec{k}_{out}$ where $\vec{k}_{out}$ is the direction of the outgoing particle; and the x-axis forms a right-handed system with $\hat{y}$ and $\hat{z}$. The angle θ between $\vec{k}_{in}$ and $\vec{k}_{out}$ defines the position of the detector. The angle β between $\hat{z}$ and $\hat{\zeta}$ is the quantization axis, and ϕ is the angle between $\hat{y}$ and the projection of $\hat{\zeta}$ on the $\hat{x}$-$\hat{y}$ plane.

The analyzing powers are a manifestation of the reaction cross section's dependence on the projectile spin. Therefore, by choosing specific polarization states, i.e. p_ζ and $p_{\zeta\zeta}$, and quantization axis directions, i.e. angles β and ϕ, any of the vector or tensor analyzing powers described in Chapter 4 can be measured.

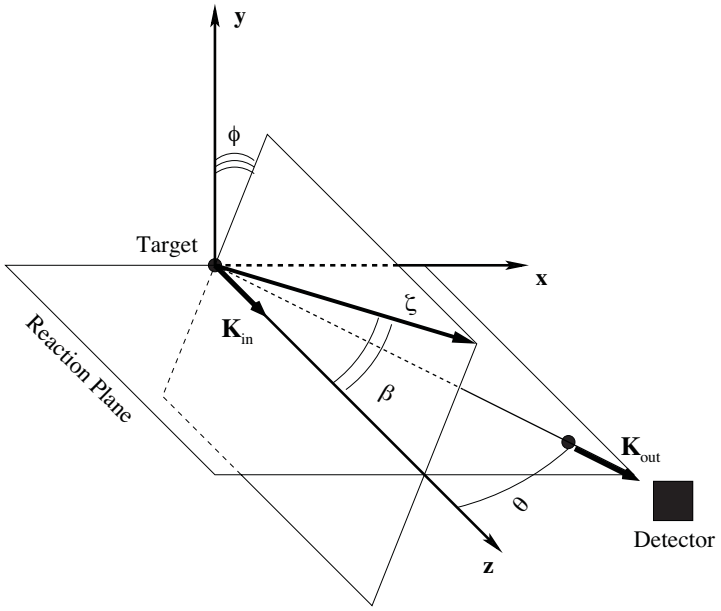

Figure 2.1: Coordinate system used to define analyzing powers according to the Madison Convention [Bar71].

2.1.2 Polarized Ion Source

The TUNL Atomic Beam Polarized Ion Source (ABPIS) [Cle90] uses four separate units to produce polarized proton and deuteron beams with specific spin symmetry axes and sub-state populations (see Figure 2.2). These four units work in conjunction to produce an atomic beam, to polarize the nuclear spins, to ionize the atomic beam, and finally to rotate the polarization to the direction required for the experiment.

To create the atomic beam, molecular hydrogen or deuterium gas is dissociated in the dissociator using a gas discharge with the radio-frequency energy supplied by

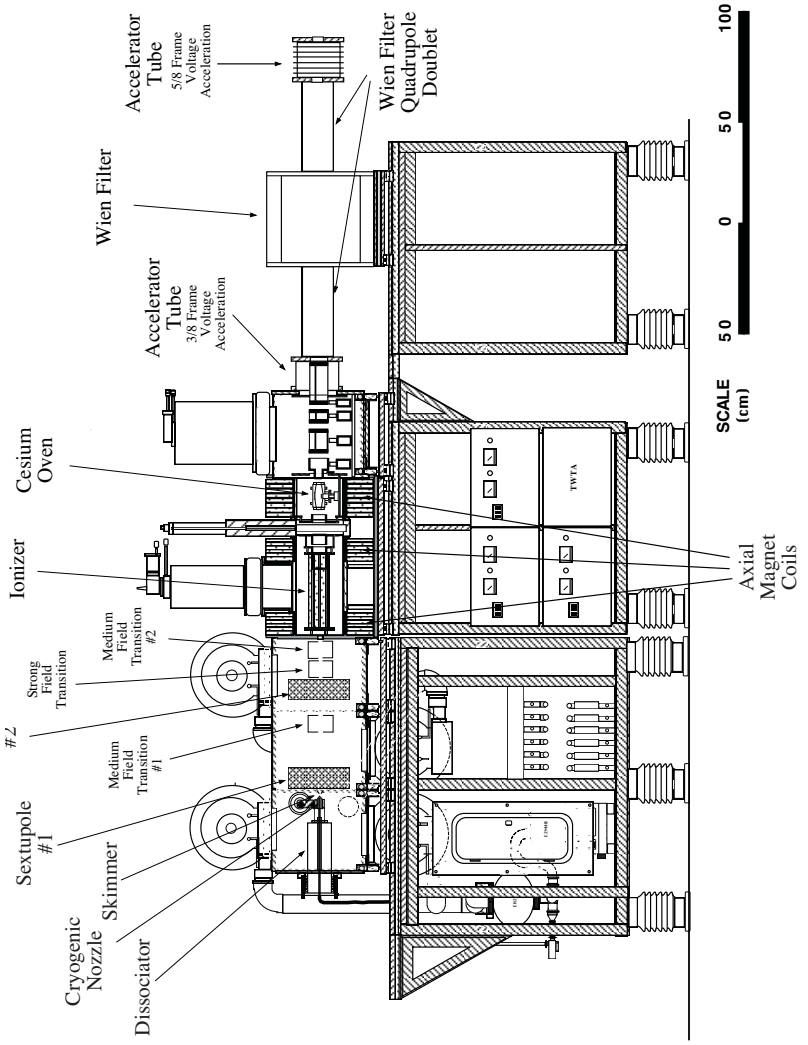

Figure 2.2: Schematic drawing of the Triangle Universities Nuclear Laboratory's Atomic Beam Polarized Ion Source. Hydrogen or deuterium gas is supplied to the dissociator on the left side of the figure. The gas atoms pass through a series of magnetic fields and rf-transition regions, are ionized in the ECR cavity, and exit the source through the Wein filter.

the Traveling Wave Tube Amplifier (TWTA). Because the polarization stages of the source prefer well-collimated, slowly moving particles, this neutral atomic gas then diffuses through a copper nozzle cooled to 30-35 K and is diluted with high purity nitrogen to discourage recombination.

The beam then proceeds to the nuclear spin polarization region of the source. This region consists of two Stern-Gerlach sextupole magnets and three radio-frequency transition units. In the absence of external fields, the angular momentum of the nucleus $\boldsymbol{I}$ is coupled to the electron angular momentum $\boldsymbol{J}$ forming the total angular momentum vector $\boldsymbol{F}$ such that $\boldsymbol{F} = \boldsymbol{I} + \boldsymbol{J}$. For the $1s$ state of the deuterium atom, the two zero-field levels correspond to $F = 3/2$ and $F = 1/2$. In Figure 2.3, the six hyperfine levels of the $1s$ deuterium atom are labeled by the circled numbers. When a magnetic field is applied to the atoms, energy splitting occurs between states of differing m_j (Zeeman effect) and among the m_I states within the m_j states (hyperfine splitting). In the figure the energy axis is measured in units of zero-field hyperfine splitting ΔW, which is 1.354×10^{-6} eV or 327.4 MHz; the magnetic field axis is given in units of the critical field $\mathrm{B}_c = \frac{\Delta \mathrm{W}}{(\mathrm{g}_I - \mathrm{g}_J)\mu_B}$ where μ_B is the Bohr magneton, $\mathrm{g}_I = -3.04 \times 10^{-3}$, and $\mathrm{g}_J = 2.002$. For deuterium, this gives a value for $\mathrm{B}_c = 11.7$ mT.

In the weak field region where the magnetic field B is less than B_c, the applied magnetic field is less than the magnetic field at the electron generated by the proton, and the good quantum numbers are F and $\mathrm{m}_F = \mathrm{m}_j + \mathrm{m}_I$. The weak field breaks the degeneracy of the m_F sub-states, and a transition in this region inverts the populations of their substates, resulting in $\mathrm{m}_F \leftrightarrow -\mathrm{m}_F$. In the strong field region when the magnetic field is larger than B_c, m_j and m_I are the good quantum numbers.

The electron and deuteron spins will still be coupled in a weak magnetic field, and

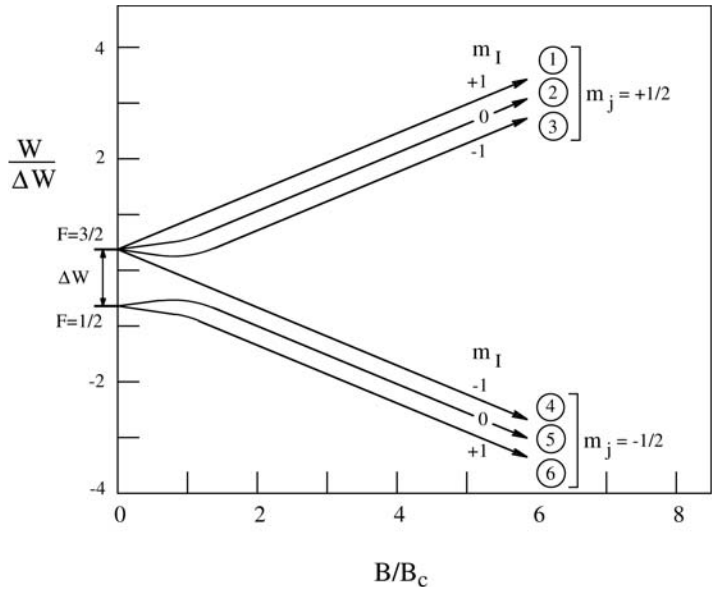

Figure 2.3: The Breit-Rabi diagram for deuterons. The sextupole magnets filter out atoms with states 4, 5, and 6 ($m_j = -1/2$), and the RF transition units produce population differences between states 1, 2, and 3, creating nuclear polarization in the deuteron beam.

the atomic levels are split by m_j and m_I values according to the Breit-Rabi formula [Bre31]. The sextupoles' magnetic field focuses atoms with electron spin projection $m_j = 1/2$ along the beam axis and sweeps atoms with m_j = -1/2 from the beam, resulting in a beam of almost pure $m_j = 1/2$ exiting from the sextupoles. This means only states 1, 2, and 3 in Figure 2.3 pass through the sextupole magnets. The nuclear spin states m_I must be selectively populated, however, in order to have a nuclear polarized beam. To achieve this, the adiabatic-fast passage method [Phi87], which uses population inversion between pairs of hyperfine states when the conditions for the static and radio-frequency magnetic fields are met, is utilized. In the example

above, a $3 \leftrightarrow 6$ transition can be induced by providing a RF magnetic field with the right parameters. This then leads to a depopulation of state 3 ($m_I = -1$) and a population of state 6 ($m_I = +1$). Therefore, a non-zero p_ζ is created which gives a vector-polarized beam. This is number 1 in Table 2.1, which also contains all of the states used in this experiment. The observables and the states used to measure each can be found in Chapter 4.

#	MF1	States	MF2	States	SF	Final	P_ζ	$P_{\zeta\zeta}$	I
1	off	1,2,3	off	1,2,3	$3 \leftrightarrow 6$	1,2,6	2/3	0	1
2	off	1,2,3	$1 \leftrightarrow 4$	2,3,4	off	2,3,4	-2/3	0	1
3	off	1,2,3,	off	1,2,3	$3 \leftrightarrow 5$	1,2,5	1/3	-1	1
4	off	1,2,3	$2 \leftrightarrow 4$	1,3,4	off	1,3,4	-1/3	1	1
5	$1 \leftrightarrow 4$	2,3	$1 \leftrightarrow 3$	1,3	off	1,3	0	1	2/3
6	$1 \leftrightarrow 4$	2,3	off	2,3	$3 \leftrightarrow 5$	2,5	0	-2	2/3

Table 2.1: The polarization states used in the ABPIS for the $^7\mathrm{Li}(\vec{\mathrm{d}}, \mathrm{n})^8\mathrm{Be}$ experiment. The symbol # corresponds to the number referred to in the text signifying which transition was used for a given observable. I is the beam intensity.

For analyzing power measurements, the ability to rapidly switch between one or more polarization states is preferred. To produce a beam of alternating polarization while keeping all other beam parameters constant, the RF units are rapidly turned on and off at a rate of 10 Hz. The sequence of transition states is $+-++-+--$, canceling out systematic asymmetries. Each time the unit is switched, the state of polarization is uncertain, and so a spin-veto bit is raised to disable spin-sorting for 7 ms to allow the polarization to stabilize. A clock module drives the spin flip, while the spin state bit for the hit register is set using the feedback signals from the polarized ion source. A scalar module checks the spin state asymmetry by counting every spin state and spin-veto bit.

The polarized atoms emerging from the transition regions are neutral and, there-

fore, cannot be accelerated. In order to be ionized, the atoms next pass through an Electron Cyclotron Resonance (ECR) ionizer that removes an electron from the atoms by collisions with fast electrons in a hot nitrogen plasma. An electrostatic lens extracts the now positive beam from this region. The lens' applied voltage is adjusted for maximum beam transmission.

The positive, polarized beam then passes through the cesium oven region. Collisions of the positive ions with the Cs atoms themselves results in approximately 30% of the ions being converted to neutral atoms in the $2s$ meta-stable state. Under the right conditions, the hyperfine population of these atoms can reflect the polarization of the beam. The Spin-Filter Polarimeter (SFP) RF cavity, located downstream from the Cs oven, measures these meta-stable atoms, and its operation is explained in detail in Section 2.1.3. However, the SFP is not used under normal operating conditions, and the cavity is used instead as an electrostatic lens.

Once through the SFP, the ions are accelerated to 3/8 of the frame voltage and then enter the Wien-filter spin precessor. The filter has crossed electric and magnetic fields that are perpendicular to the beam momentum. Because the magnetic field that produces the nuclear polarizations is axial, the particles' spins are precessing along their momenta axes. The plane of the crossed fields is rotated, and the field values are then adjusted to allow the beam to enter the inflection magnet and emerge in the experimental area with the polarization axis in the desired direction.

2.1.3 Polarimetry

To determine analyzing powers, the beam polarization must be accurately known. Two different methods have been utilized at TUNL. The first is by conducting po-

larimeter measurements using a reaction with well-known analyzing powers several times during the run. However, the second and more preferable approach is to use the Spin Filter Polarimeter (SFP) referred to in Section 2.1.2. The SFP also allows for tuning the ABPIS to maximum polarization.

As mentioned in Section 2.1.2, when the positive, polarized ions emerge from the ECR region, they enter the Cs oven. There, collisions with the Cs atoms result in the production of neutral atoms in the $2s$ meta-stable state. The SFP filters out the different nuclear spin states m_I using an RF cavity and a variable magnetic field. The RF electric field is tuned to excite a resonance in the atom; the axial magnetic field is then set to select a particular value of m_I. By removing the electric field, the atoms that pass are allowed to decay to their ground state, and the resulting photons are detected in a photo-multiplier tube (PMT). The magnetic field value is slowly varied to permit deuterons with $m_I = +1, -1$, and 0 to pass into the area of zero electric field and de-excite. The PMT current is proportional to the number of nuclei with a given m_I. From the magnetic field value scan, three peaks are obtained corresponding to the number of deuterium nuclei with different m_I: N_+, N_0, and N_-. The peak area asymmetries represent the differences in spin-state populations, or the beam polarization. The vector polarization p_ζ is given as

$$p_\zeta = \frac{N_+ - N_-}{N_+ + N_-}, \tag{2.6}$$

and the tensor polarization $p_{\zeta\zeta}$ as

$$p_{\zeta\zeta} = \frac{1 - 3N_0}{N_+ + N_0 + N_-}. \tag{2.7}$$

The polarization measurement requires neutral beam. Since positive beams were

used in our experiments, the Cs vapor had to be increased to produce a reasonable amount of neutral atoms to enter the SFP unit. When negative beams are used, the opposite must occur, and the Cs vapor is decreased. Heating and then cooling the oven each takes 15-20 minutes. In addition, the same amount of time is needed to actually do the measurement. The entire procedure lasts about an hour. In all of our experiments, SFP measurements were done 2-3 times each run and were relied on to tune the transition units to maximize the polarization of the beam.

Based on SFP calibrations with respect to high energy polarimeters in the lab, the SFP values are known to differ by 5-10% from those measured values [Wul99]. In addition, comparison with a nuclear polarimeter located on the LECAP line downstream from the slits indicates a similar discrepancy [Sab03]. Thus, the SFP values were given an error of 5% based on those measurements.

2.2 Beam Transport

Upon leaving the ABPIS, the polarized deuterons are deflected by 60° using an inflection magnet and directed down the Low-Energy Capture (LECAP) beam line. An overview of the experimental setup is shown in Figure 2.4. The target and beam current integration will be discussed in more detail in Section 2.2.1 and Section 2.2.2.

2.2.1 Evaporated Lithium Target

An evaporated lithium target has been previously used by other LECAP members, specifically Spraker *et al.* [Spr00] and Prior *et al.* [Pri04]. However, the target chamber they used was redesigned for the $^{7}\mathrm{Li}(\vec{\mathrm{d}},\mathrm{n})^{8}\mathrm{Be}$ experiments so that it would be easier to use. The new target chamber and its relation to the rest of the beamline

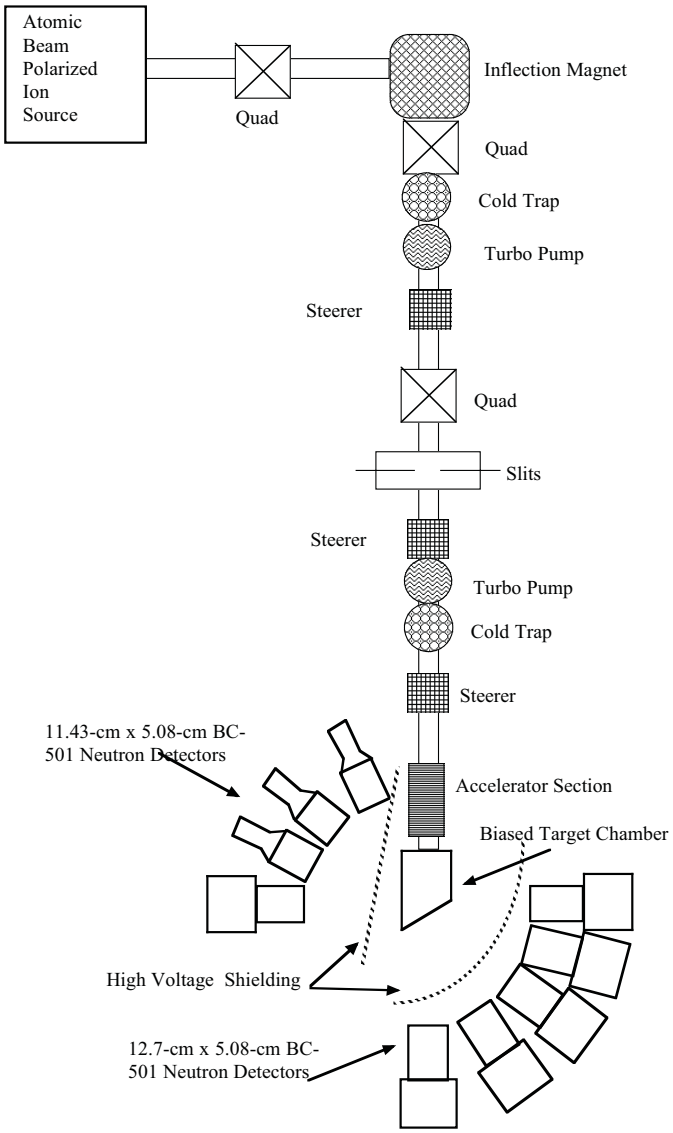

Figure 2.4: Experimental setup. Tensor-polarized deuterons are accelerated down the LECAP beam line onto the evaporated lithium target. The target chamber can be biased up to 80 kV and is isolated from the detectors with plastic. Six of the neutron detectors are 12.7 cm in diameter; the other three are 11.43 cm in diameter. The angular distribution shown for the detectors is that used for the cross section, S factor, T_{20}, and T_{22} measurements.

is shown in Figure 2.5 and Figure 2.6.

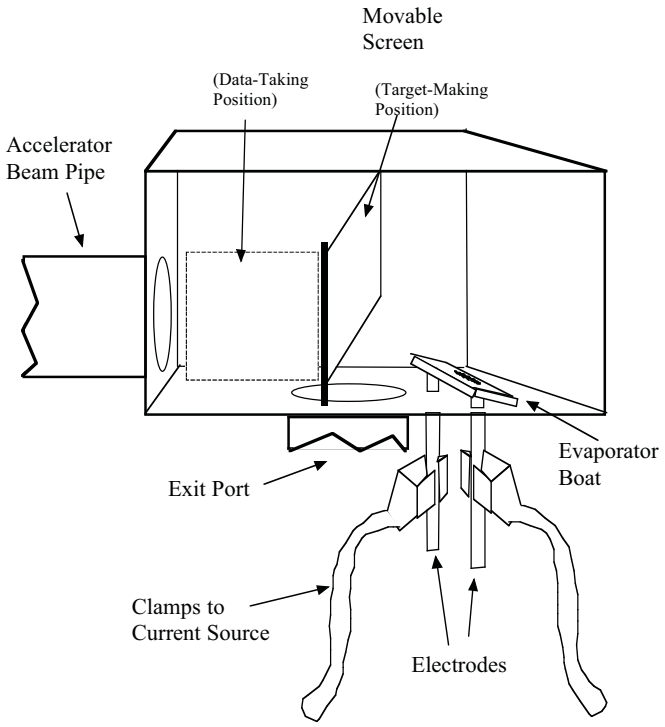

Figure 2.5: A three-quarter view of the target chamber. The movable screen can be rotated into the beam path when a target is being made. During data collection, however, the screen is moved off to the side with a magnet.

The chamber body is constructed of seamless 0.3175-cm thick aluminum and has grooves for an O-ring on both the top and bottom. The top plate is 1.27-cm thick lucite, and the bottom plate is 0.9525-cm thick stainless steel. A 5.08-cm Dependex flange on the rear side of the chamber attaches to the beam pipe.

A stainless steel nipple is attached through a hole in the bottom plate. A valve is connected to this nipple and then to a 60.96-cm long and 5.08-cm diameter piece of plastic tubing which then attaches to a turbomolecular pump used to maintain a high vacuum in the target chamber. Since the chamber will be biased to a maximum

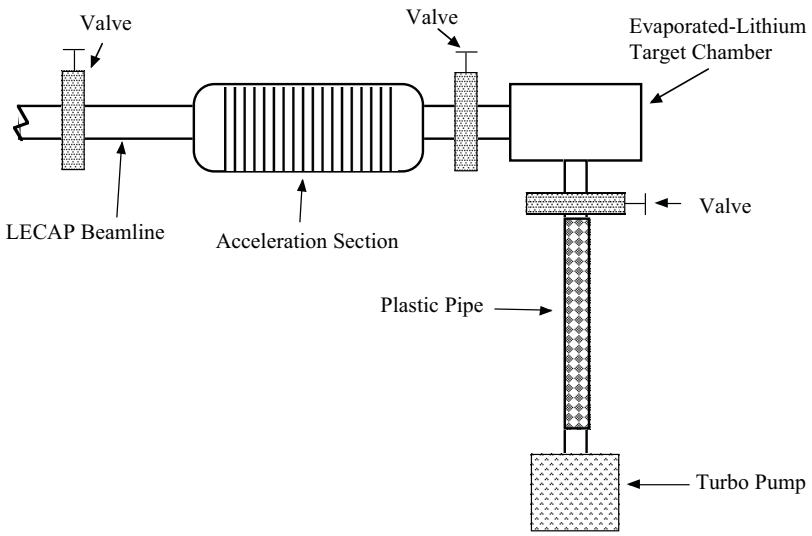

Figure 2.6: A side-view of the target chamber in relation to the rest of the immediate beamline. The acceleration section can be biased up to 80 kV and is isolated from the upstream beamline (not shown). The valves before and under the chamber are used to close the chamber off while evaporating a target, thus limiting the spread of lithium. The non-conductive plastic tubes allowed the turbo pump to be placed at ground potential and also helped prevent sparks from traveling to and damaging it.

voltage of 80 kV, the plastic tube is essential to electrically isolate the turbo pump. The valve is necessary to close off access to the pump when lithium is being evaporated in the target chamber. Otherwise, lithium would collect in the tubing, and when the chamber is biased, would cause sparking that could potentially damage the pump. Two electrical feedthroughs are also located in the bottom plate. Inside the chamber, a tungsten evaporator boat rests on the feedthrough posts.

New targets were made about every 8 hours during a one week run. Once the chunk of 99.9% ^{7}Li is in the evaporator boat, the chamber is pumped down to at least

10^{-6} Torr. Except under extreme circumstances, this vacuum is never again broken during the week-long run. To make a target, two leads from a variac are connected to the power feedthroughs on the bottom of the chamber. Valves between the chamber and beam line and between the chamber and turbo pump are closed to prevent lithium from traveling outside the chamber. A small screen, made of aluminum foil, is swung into place behind the evaporator boat by a magnet and prevents lithium from coating the rear part of the chamber. About 140 A are placed on the boat by the variac for about 60 seconds or until a film of lithium begins to cloud the lucite upper plate. The variac is then turned off and disconnected, and the valves are opened. Once the chamber has regained the necessary vacuum, the run is resumed. The entire process takes 5-10 minutes to perform. The lucite cover on the top of the chamber allows a visual inspection to be performed whenever it is deemed necessary.

The target has been determined to be $^{7}Li_2O$ due to oxidation of the evaporated lithium metal as a result of residual oxygen in the vacuum system [Pri04]. This is supported by a number of observations. First, in the work done by Spraker *et al.* [Spr00] on $^{7}\mathrm{Li}(\mathrm{p},\gamma)^{8}\mathrm{Be}$, the $^{7}\mathrm{Li}(\mathrm{p},\alpha)^{8}\mathrm{Be}$ reaction was also observed. This reaction's much higher cross section allowed for observation of yield variation over a relatively short time span. The counting rate decreased rapidly in the first several minutes after a new target was evaporated, leveled off to 40-50% of the initial rate, and then remained constant at that rate for many hours. Yield integral calculations show that the ratio of yields for a thick $^{7}Li_2O$ target to a thick pure ^{7}Li target is between 0.4 and 0.5. This indicates that the target is completely oxidized within a few minutes after being evaporated and exposed to the beam. Second, it has been noticed that the nearly opaque, reflective layer of lithium deposited on the lucite cover of the chamber changes to a nearly transparent film after the evaporation. This transformation occurs

in the same time span as the observed change in the ^{7}Li(p, α)^{8}Be yield after making a target [Pri05].

The evaporation is performed using an amount of Li metal and an evaporation time that assures that the resulting target is thick, specifically on the order of several mg/cm^2, and thus stops the low-energy deuteron beam. In fact, yield integral calculations show that a 160-keVdeuteron beam deposits 94% of its energy in the first 100 μg of the target.

2.2.2 Beam Current Integration

Accurate determination of the number of deuterons incident on the target is necessary for absolute cross section measurements. To do this, the charge incident on the target was integrated using a Beam Current Integrator (BCI) which has an accuracy of 1%. The BCI produces a logic pulse when a current is fed into it. These pulses are counted; the total number is proportional to the integrated current.

Secondary electrons leaving the target produce an effective positive current, contributing to an erroneously high BCI. To prevent this, the target is connected to a 90-V battery that attracts any free electrons and pulls them away from the target. The positive terminal of the battery is attached to the target and the negative terminal to the BCI.

2.3 Neutron Detectors

2.3.1 Physics of Fast Neutron Detection

The neutrons studied from the $^{7}\mathrm{Li}(\vec{\mathrm{d}},\mathrm{n})^{8}\mathrm{Be}$ reaction are relatively high energy (Q = 15.03 MeV), often called fast neutrons. One of the most common ways to detect fast neutrons is by using scintillators. These scintillators contain hydrogen and quite frequently are organic, i.e. they also contain carbon. For example, the detectors used in this experiment were all aromatic hydrocarbons with benzene-ring structures. Because of its neutral charge, the neutron is limited in how it can interact with the scintillation material; in particular, it can only interact with the hydrogen through the strong force, effectively striking the proton and then ideally scattering out of the scintillation material. The proton will recoil from the impact and, because it has charge, will interact with the material, exciting the other molecules and atoms therein. These molecules and atoms will emit light in the visible spectrum as they de-excite. Because the detector is encased in a light-tight case and lined on the inside with a reflective material, all of the light resulting from the de-excitation will travel toward a light guide and enter the photomultiplier tube (PMT). This process is illustrated in Figure 2.7.

The PMT is optically coupled to the scintillator and converts the emitted light into a useable signal. Upon entering the PMT, the light strikes a metal cathode, and electrons are ejected via the photoelectric effect. The ejected electrons are then attracted to a positively biased emission electrode or dynode. Secondary electrons are subsequently emitted and accelerated to the next dynode. Typical PMTs have 10 to 14 dynodes at increasingly positive potentials. Through this electron-multiplier network, a conventional PMT can achieve an overall total gain of up to 10^{7} [Leo94].

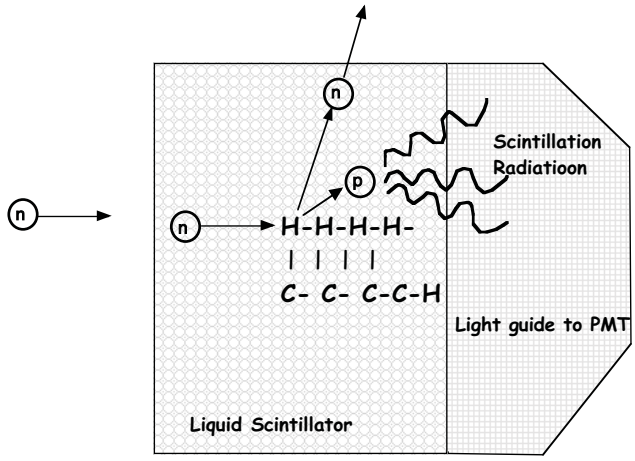

Figure 2.7: A simplified illustration of how a scintillator works. The neutron effectively "strikes" the hydrogen atom in the hydrocarbon and is scattered. The proton recoils and interacts with the material, resulting in scintillation radiation. This radiation is collected in the light guide and enters the photomultiplier tube (PMT).

The charge from the electron cascade is finally collected by an anode which produces a current that is analyzed using commercially available fast electronics.

2.3.2 Detector Response Function

When a fast neutron is incident on a hydrogen-containing scintillator, the resulting recoil protons should have an energy distribution dN/dE(E) that is approximately rectangular, ranging from zero to the full neutron energy. Usually the range of the recoil protons is small compared with the scintillator dimensions, so their full energy will be deposited in the material, resulting in the expected pulse height distribution to also be approximately rectangular [Kno00]. This is illustrated in Figure 2.8a. How-

ever, a variety of factors can distort this simple distribution and significantly effect the response function. Four of the more significant effects are detailed below.

Nonlinear Light Output

For most organic scintillators, the light output does not increase linearly with the deposited energy. According to [Kno00], the light output H of many organic scintillators can be related to the energy E by

$$H \cong kE^{3/2} \tag{2.8}$$

where k is a proportionality constant. The pulse height distribution, then, is

$$\frac{dN}{dH} = \frac{dN/dE}{dH/dE} = \frac{\text{constant}}{\frac{3}{2}kE^{1/2}} = k'H^{-1/3} \tag{2.9}$$

where k' is also a proportionality constant. This effects the shape of the spectrum as shown in Figure 2.8b.

Multiple Scattering

In a large detector, an incident neutron can scatter from more than one hydrogen nucleus before leaving the scintillator. These events normally occur within a small time window compared with the pulse-shape time; therefore, the light resulting from all recoil protons caused by that neutron are summed, creating a pulse whose amplitude is proportional to the total light output. The overall effect on the spectrum will be that the average pulse height will increase, and the response function will change so that the events of the larger pulses are added at the expense of those with lower amplitudes. [Kno00].

Carbon Scattering

Organic detectors, such as the ones used in this experiment, contain carbon in addition to hydrogen. Carbon recoils caused by elastic neutron scattering will not contribute much to the output because the scintillator's efficiency decreases for high dE/dx particles. However, the neutrons may still undergo hydrogen scattering before leaving the detector. The neutron can lose up to 28% of its original energy due to its initial encounter with the carbon nuclei before it scatters off the hydrogen. This will effectively lower the maximum energy of the recoil proton to as much as 72% of the original energy [Kno00]. This effect is shown in Figure 2.8c.

Finite Detector Resolution

The response function is further influenced by the detector's own limitations. Spread introduced by nonuniform light collection, photoelectron statistics, and other sources of noise will smooth out some of the expected distinct structure, as shown in Figure 2.8d.

2.3.3 Response Function Measurements

As described above, the detectors used in this experiment were composed of liquid aromatic hydrocarbons. In particular, the scintillating fluid used was BC-501, which has a density of 0.901 g/cm^3, a hydrogen-to-carbon ratio of 1.287, and a maximum wavelength emission of 425 nm [Cro01]. Six detectors with a 12.7-cm diameter and four detectors with a 11.43-cm diameter were used.

An accurate representation of the response function is needed in order to adequately fit the spectrum as described in Chapter 3. Therefore, the response functions

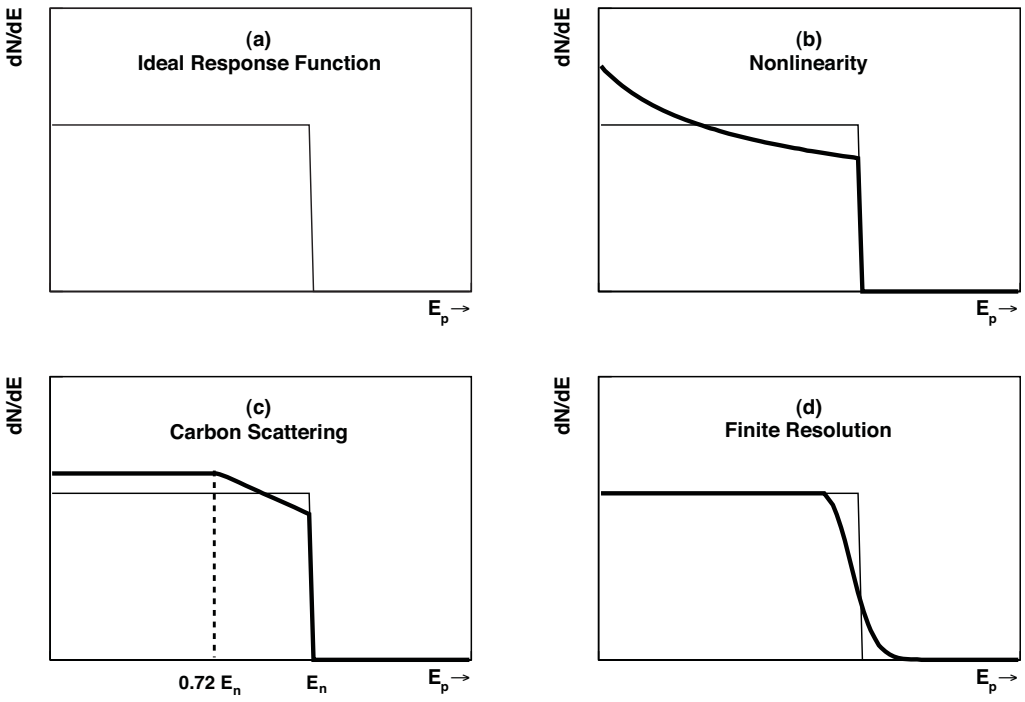

Figure 2.8: The ideal neutron response function spectrum (a), where E_p is the energy of the recoil proton. As illustrated in the text, the response function can be distorted by the scintillator's nonlinear light output (b), neutron scattering off carbon nuclei (c) where E_n is the energy of the incident neutron, and finite detector resolution (d).

for both 14-MeV and 11-MeV neutrons, corresponding to the n_0 and n_1 groups respectively, were measured in the Shielded-Source Area (SSA) at TUNL for both diameters of detectors.

An unpolarized, negatively charged deuteron beam was accelerated from the ion source and through the FN Tandem Van de Graaff, or "Tandem," at TUNL. The Tandem first accelerates the negative beam toward a very high positive potential. The deuterons then pass through a thin carbon foil which strips away two electrons, leaving a positively charged beam. This positive beam is then finally accelerated away from the positive potential. The positive terminal can be biased up to 10 MV; however, for this measurement, the terminal was biased to 5.770 MV for the 14-MeV neutrons and 4.211 MV for the 11-MeV neutrons.

After emerging from the Tandem, the deuterons are steered toward the SSA. A monoenergetic neutron beam is produced via the ^{2}H(d, n)^{3}He reaction by bombarding a deuterium gas cell. For the response function measurements, the gas cell pressure was kept at 45.8 PSI and is filled with research grade deuterium gas with a purity of 99.99% [Cro01]. The ^{2}H(d, n)^{3}He reaction is most commonly used to produce neutrons with energies between 7 and 20 MeV. The most energetic neutrons are emitted at 0°, making it ideal for use as a collimated neutron source. The reaction's 3.3-MeV Q-value also gives it more than a 5-MeV separation between the monoenergetic group at 0° and the neutron continuum from deuteron breakup reactions in the cell's gold beam stop or from the three- and four-body breakup reactions ^{2}H(d, n)dp and ^{2}H(d, n)ppn in the deuterium gas. Time-of-flight (TOF) techniques were used to separate the ^{2}H(d, n)^{3}He monoenergetic neutrons from the lower energy continuum neutrons generated by breakup reactions. A typical TOF spectrum is shown in Figure 2.9 for E_n = 14 MeV.

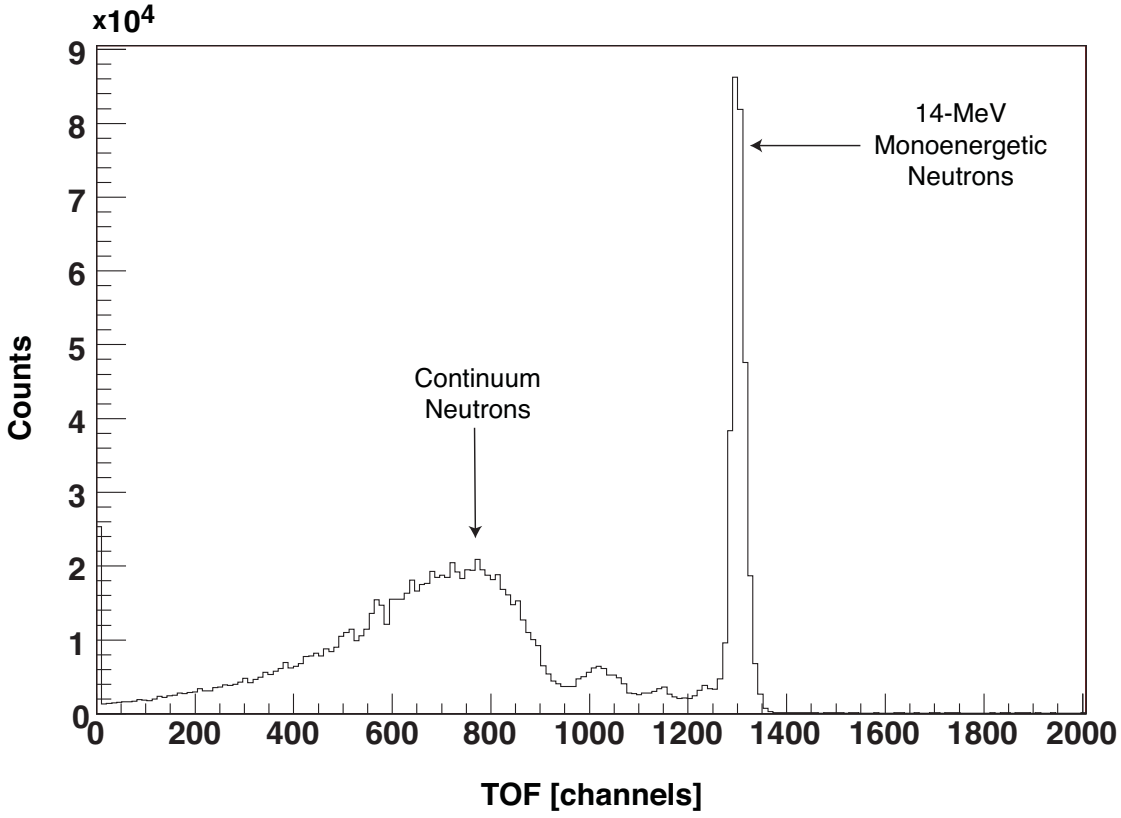

Figure 2.9: Typical time-of-flight spectrum for the ^{2}H(d, n)^{3}He source reaction near 0° for the response function measurements. Time increases from right to left. The monoenergetic neutron group of interest is followed by the continuum of neutrons from the breakup reactions ^{2}H(d, n)dp and ^{2}H(d, n)ppn in the deuterium gas.

Two 12.7-cm diameter detectors and two 11.43-cm diameter detectors were each placed separately in the neutron beam for fifteen minutes. This procedure was repeated for both the 14-MeV and 11- MeV neutron energies.

The n_0 neutron group at E_{lab} = 14 MeV has a width of 6.8 keV, so the nearly monoenergetic function measured above is a good representation of the state and is shown in Figure 2.10a. The n_1 group at E_{lab} = 11 MeV, however, has a width of 1.5 MeV. The raw monoenergetic function at 11 MeV is shown in Figure 2.10b. Because of the width of this state, the raw spectrum was convoluted with a Breit-Wigner function with a width of 1.5 MeV. This new spectrum, shown in Figure 2.10c, was taken as the representation for the detector response function for the n_1 state.

When analyzing the data for the absolute cross section and S-factor measurements, the n_2 neutron group at E_{lab} = 3.4 MeV was also considered in addition to the n_0 and n_1 groups. To obtain the response function for the n_2 group, a blank titanium target was implanted with deuterium and the E_{lab} = 2.8 MeV neutrons from the $^2H(d,n)^3He$ reaction were measured using a beam energy of E_d = 80 keV on the LECAP line. This signal was then convoluted with a Briet-Wigner function of width 3.5 MeV to represent the actual response function for the n_2 group. The raw spectrum and the convoluted spectrum are shown in Figure 2.11.

During the absolute cross section and *S*-factor measurements, a neutron group from the $^2H(d,n)^3He$ reaction was also evident in the spectrum in nearly the same location as the n_2 peak. This state at E_{lab} = 2.8 MeV was fitted with the response function mentioned in the previous paragraph and subtracted from the $^7Li(d,n)^8Be$ spectrum. This background peak was identified by studying the rise its yield in conjunction with the integrated beam current, especially with respect to the time at which a new ^7Li target layer was evaporated.

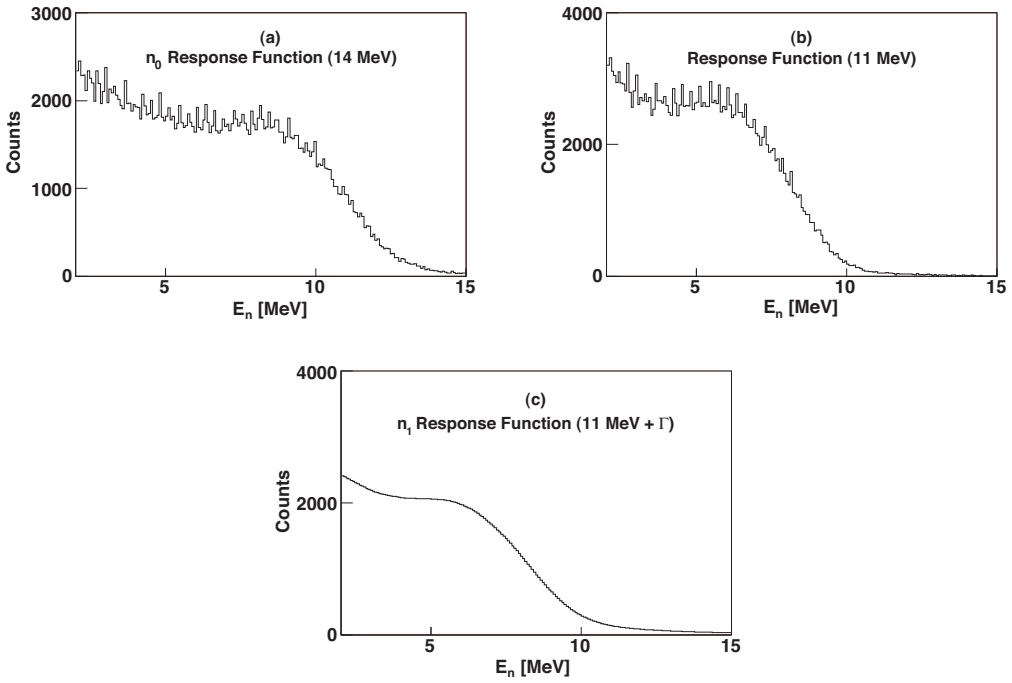

Figure 2.10: Experimental response functions measured for one of the neutron detectors used in these experiments. (a) The response function measured for 14-MeV monoenergetic neutrons corresponding to the n_0 neutron group in ^{7}Li(d, n)^{8}Be. (b) The response function measured for 11-MeV monoenergetic neutrons. (c) The response function for 11-MeV neutrons in (b) convoluted with a Breit-Wigner distribution with width Γ equal to 1.5 MeV corresponding to the n_1 neutron group from ^{7}Li(d, n)^{8}Be. The energy calibration used for the x-axis is uncertain to $\pm$ 0.5 MeV and was determined by pinpointing the channel corresponding to the 14 MeV endpoint energy of the n_0 state, dividing that channel number by the energy to obtain a calibration factor, and applying that calibration factor to all channels in the spectrum.

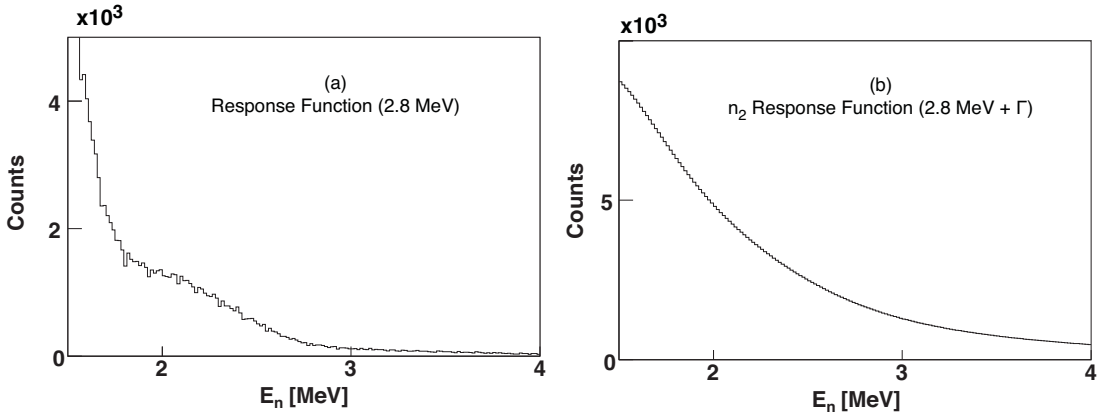

Figure 2.11: Experimental response functions measured for one of the neutron detectors used in these experiments. (a) The response function measured for 2.8-MeV neutrons from the ^{2}H(d, n)^{3}He reaction. (b) The response function for 2.8-MeV neutrons in (a) convoluted with a Breit-Wigner distribution with width Γ equal to 3.5 MeV corresponding to the width of the 3.4-MeV n_2 neutron group from ^{7}Li(d, n)^{8}Be. The energy calibration used for the x-axis is uncertain to $\pm$ 0.5 MeV and was determined by pinpointing the channel corresponding to the 14 MeV endpoint energy of the n_0 state, dividing that channel number by the energy to obtain a calibration factor, and applying that calibration factor to all channels in the spectrum.

2.3.4 Pulse-Shape Discrimination

Like many organic scintillators, the decay time constants of the detectors used in these experiments provide information about event type through pulse-shape analysis. Most of the observed scintillation light is prompt fluorescence. However, a longer-lived component corresponding to the delayed fluorescence can also be observed in some cases. The composite yield curve is then the sum of these two exponential decays, called the fast and slow components. The fast component has a decay time of a few nanoseconds, whereas the slow component typically takes several hundred nanoseconds. Although most of the light yield occurs in the fast component, this long-lived tail is extremely useful since the fraction of light that appears there usually depends on the nature of the exciting particle [Kno00]. This process of pulse-shape discrimination can then be used to separate neutron-induced events from γ-ray-induced events with the same pulse height. Figure 2.12 shows a simplified sketch of electrical pulses in a scintillator for neutron and γ-ray events with the same pulse height. The actual identification from these signals is described in Section 2.4.1 and Section 3.2.

The slow component of the scintillation pulse originates from the excitation of long-lived triplet states along the track of the ionizing particle. Interactions between two such excited molecules can lead to one molecule being in the lowest singlet state and the other being in the ground state. The singlet state molecule will then de-excite as usual, producing a delayed fluorescence. The yield variation of the slow component can then be explained by the differences expected in the density of triplet states along the particle's path. The slow component fraction will then depend primarily on the rate of energy loss dE/dx of the exciting particle and will be greatest for particles with a large dE/dx, such as the recoil proton [Kno00]. In the case of γ-rays, which are detected through Compton scattering, photoelectric effect, and pair production,

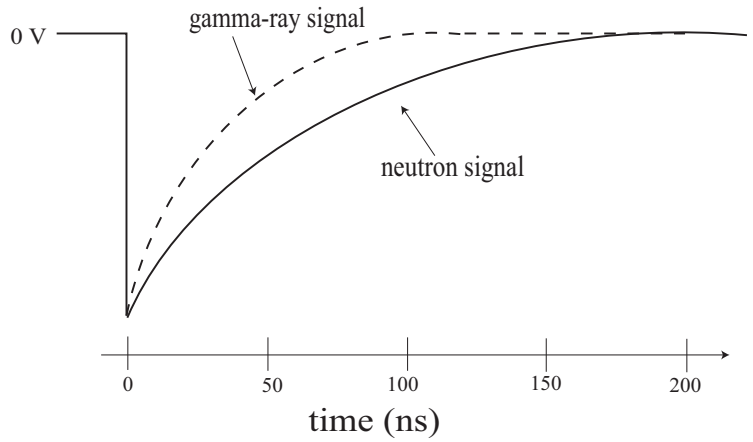

Figure 2.12: Electrical pulses for a neutron and γ-ray event with the same pulse height in a liquid organic scintillator that has good pulse-shape discrimination properties. Identification is possible due to the differences in decay times.

the electrons emitted in these processes have a small dE/dx, and therefore the slow component of the γ-ray-induced signal will be small.

2.4 Electronics

The analog signals from each detector are processed by a setup that shapes and discriminates the signals before they can be sent to the data acquisition system. These analog signals are particularly important for discriminating between γ-rays and neutrons, setting a hardware lower-level detector threshold, and providing a timing signal for the trigger circuit.

2.4.1 Detector Electronics

A simplified circuit diagram of the electronics for one neutron detector is shown in Figure 2.13.

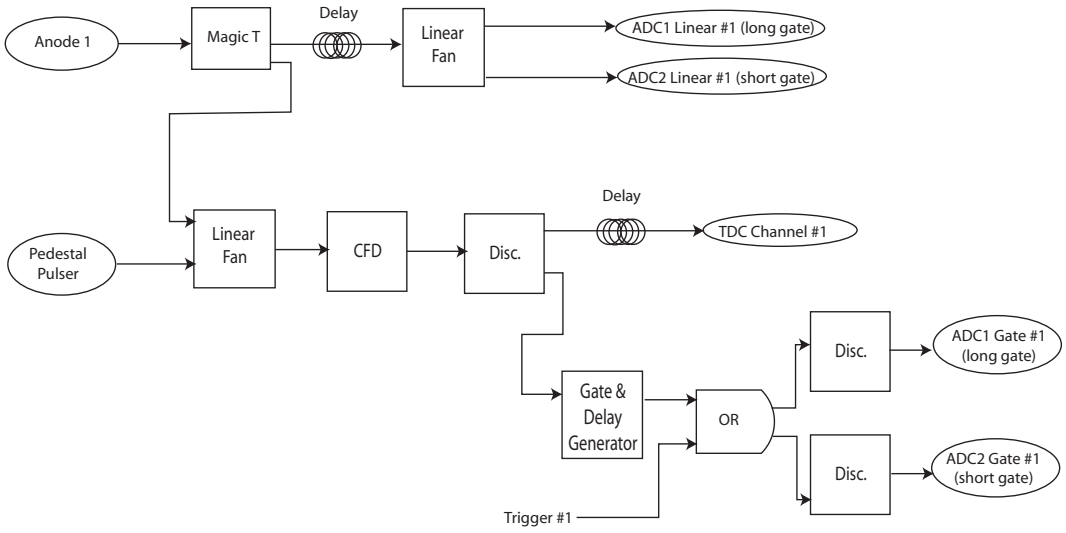

Figure 2.13: Circuit diagram of the electronics for one neutron detector.

The anode signals from the detectors were sent from the experimental area to the control room via low-loss cables. The signal was then fed into a splitter box known as the "Magic T." This passive apparatus is a voltage divider that matches the impedence to 50 Ω in both branches. One linear output was delayed approximately 600 ns by passing it through boxes of RG-58 coaxial cable before being duplicated by a linear fan module. The second output from the Magic T was routed into a linear

fan module where it was actively summed with a pulser signal, described in more detail below. The linear fan output was then input into a CFD where the lower-level detector thresholds were set and the timing signals produced. A discriminator then regenerated and increased the width of the CFD output signal. A discriminator output was used to generate the long and short gates for the ADCs.

PSD Electronics

Long and short gates, with integration starting at the leading edge of the pulse and continuing for the duration of the gate width, were used in the PSD technique described in Section 2.3.4 to measure the total charge and the charge in the tail of the pulse from the detector. One channel was given a short gate with an approximately 50-ns duration starting just before the arrival of the detector signal. The second channel's gate (the long gate) had a width of 400 ns starting from the same point as the short gate and integrating over the entire pulse. Figure 2.14 shows the timing of the analog signal and the gate signals. Subtracting the charge in the short gate from the charge in the long gate resulted in the charge in the pulse tail. The charge in this tail was plotted versus the total charge in the pulse, creating a two-dimensional histogram; this plot showed two distinct islands, one of γ-rays and the other of neutrons. Software cuts, as described in Section 3.2, were placed around the γ-ray island to eliminate those events.

Lower-Level Detector Thresholds

As noted above, each anode signal was used to set a lower level threshold for the hardware. The threshold on the CFD, through which all detector logic signals start as a pulse, sets a minimum amplitude for the input anode signal that will trigger

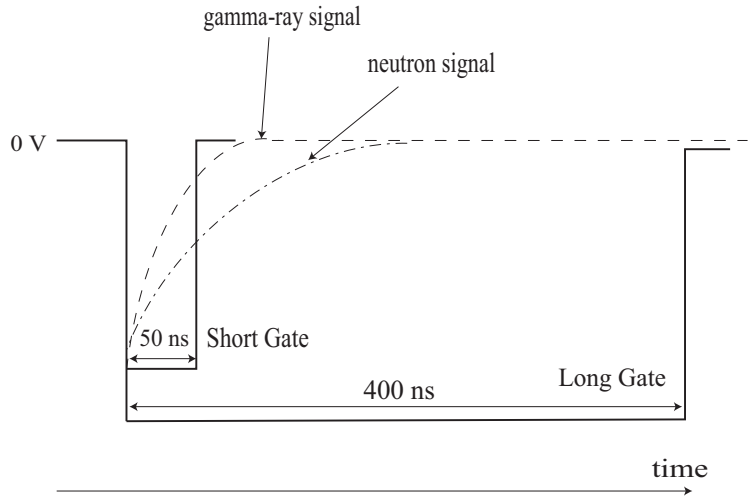

Figure 2.14: Graphical representation of the timing of the gate signals to the linear signals. It can be seen that by subtracting the charge encompassed in the Long Gate from the charge in the Short Gate, a differentiation can be made between a γ-ray and a neutron linear signal.

an ouput from the module; it also eliminates the low-level electronic noise and low pulse-height background events. Thresholds were set using the Compton edge of ^{137}Cs. For the analyzing power measurements, the threshold level was not critical and was set between three-quarters below and at the Cs edge (defined to be the point at which the yield falls to one-half its peak value). However, the detector efficiency is vital to the determination of the total cross section and S factor; this efficiency is well modeled for given fractions of the ^{137}Cs edge using the Physikalisch-Technische Bundesanstalt (PTB) group's Monte Carlo programs NRESP7 and NEFF7 [Die82] and has been experimentally measured previously at TUNL [GT97, SM98]. As shown in Figure 2.15, the efficiency is "flat" down to $E_n = 5$ MeV, which is sufficiently low in energy for measuring the 11- and 14-MeV neutrons of this experiment. Therefore, the thresholds were carefully set at 1.0 times the ^{137}Cs edge for these measurements.

Pedestals and Pulsers

When charge-integrating ADCs are used for measuring detector pulse heights, any DC level on the linear signal results in a pulse-height offset, or pedestal. The pedestals were continuously sampled during the data collection by gating the ADCs with signals from a pulser. The pulser was a gate generator whose NIM output was connected to the start input; the NIM output signal generated pulses at a rate of about 1 Hz. The pulser was then fanned into the detector circuit to satisfy first-level coincidence requirements. Because the ADC signals generated from the pulser were uncorrelated in time with real detector pulses, the DC background level could effectively be sampled on the ADC linear signals. However, the ADCs require negative inputs which limited the measurement to negative DC levels. To circumvent this, the front panel offsets of the last linear fans before the ADCs were adjusted to give the linear signals a slight negative level.

2.4.2 Trigger and Veto Circuits

The veto circuit ensured that all digitizers had adequate time for full conversion before new start signals arrived. A fast clear signal was sent to reset the hit and data registers of the TDCs and ADCs about 5 μs before the inhibit was released. A Silena ADC generated a DAQ busy signal by giving it a gate signal at the same time the digitizers were started. The busy signal remained active while the digitizers were read. Finally, the Silena's LAM (Look-at-Me) was cleared, thus stopping the DAQ busy signal. The fall of the DAQ busy signal approximately 500 μs after the arrival of the Silena gate generated the fast clear circuit. The veto was then maintained for about 5 μs longer to allow the ADC ample time for complete reset. An additional

inhibit signal was fanned into the veto circuit to hold off data acquisition when the beam current strayed out of a preset window.

2.5 Data Acquisition

The digitization and counting were done using CAMAC, and the data were stored event by event for off-line analysis. Event type and long and short pulse heights were recorded for each event from each of the neutron detectors. The event type was recorded in the data word of a BiRa Model 2351 12-bit input hit register. The long and short pulse heights were digitized by two Phillips Model 7167 12-bit, 16-channel charge-integrating ADCs.

A single-board computer (SBC) in a VME crate controlled the event readout and data flow through a VME-CAMAC interface module. A CES-8210 branch driver in the VME crate interfaced to the CAMAC A-2 crate controller through a standard branch highway cable. A trigger signal from the experimental electronics strobed the CES-8210, causing the data from the CAMAC crate digitizer modules to be read out. The data were then buffered in the MVME-162 memory and transferred to the DAQ workstation running the data acquisition and analysis software CODA@TUNL via Ethernet using standard TCP/IP protocol. The average event and data rates were approximately 420 Hz and 30 kilobytes/s, respectively, with a system dead time of typically 10% that is known to an uncertainty less than 1%. Due to the large quantities of data that accumulated during a given run, the data were periodically compressed and backed up on CD or DVD-ROM.

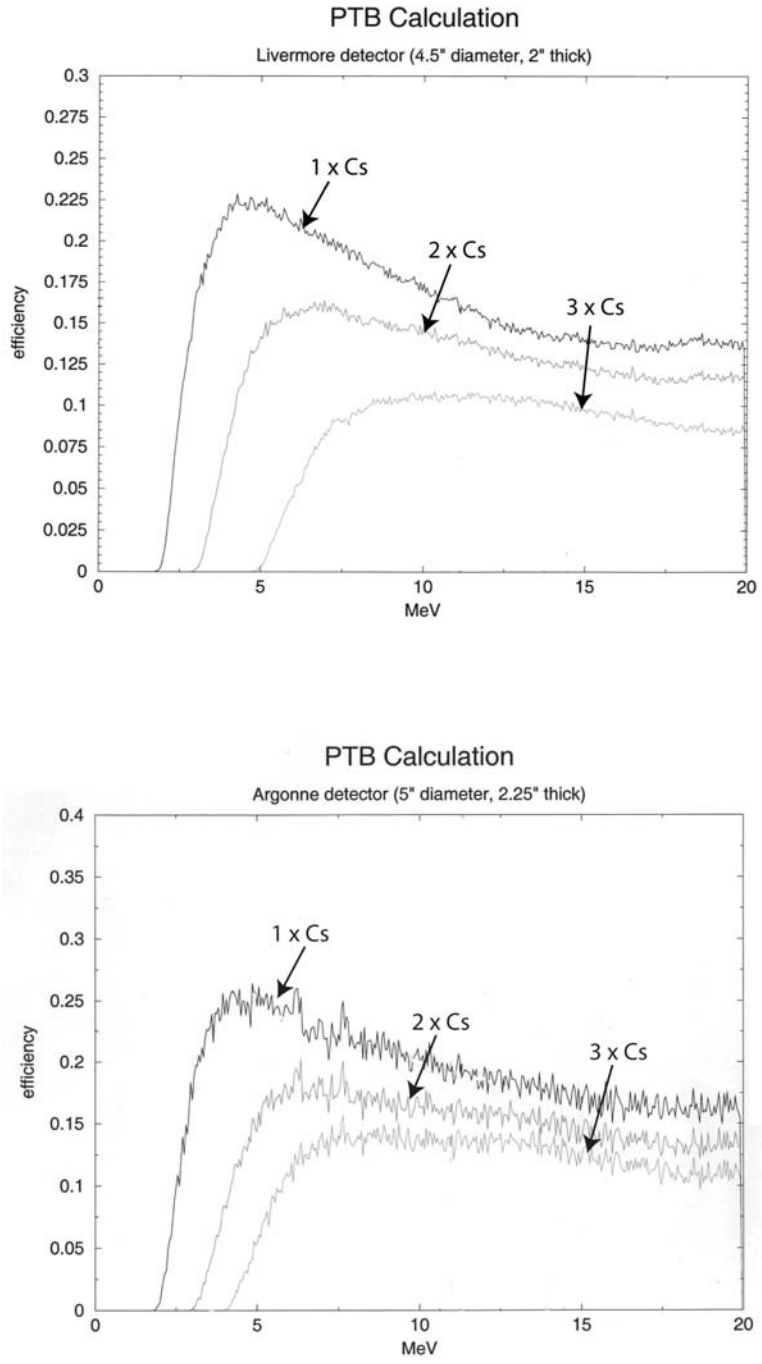

Figure 2.15: Efficiency curves for the two types of detectors used in these experiments as given by the PTB group's Monte Carlo program for detector threshold levels of $1\times$ ^{137}Cs edge, $2\times$ ^{137}Cs edge, and $3\times$ ^{137}Cs edge.

Chapter 3

Data Analysis

The incoming raw data is sorted according to spin state and written into histograms using the CODA@TUNL software. Cuts can be applied in this process using the two-dimensional pulse shape discrimination (PSD) spectra in order to obtain neutron-only spectra. These spectra are then fit with a composite of response functions, and the raw yields are extracted for use in determining polarization observables or cross sections as described in Chapter 4 and Chapter 6.

3.1 Sorting

After the raw data structures have been unpacked, they are sorted according to the value of the hit register. For the analyzing power measurements, events for each spin state were sorted into individual spectra and into a spectrum containing both states, using an off-line, user-manipulated C++ and FORTRAN code based on the original on-line data-taking software. In addition, neutron-only spectra were

created after the events had been sorted according to the pulse-shape discrimination stipulations.

The sorted HBOOK spectra were then converted to ROOT spectra and analyzed using the Object-Oriented Toolkit ROOT from CERN (http://root.cern.ch). ROOT has a built-in class based on the MINUIT minimization package, allowing the data to be fitted with pre-compiled or user-defined functions. ROOT also permits the user to have control over and receive feedback on the minimization procedure.

3.2 Pulse Shape Discrimination Revisited

Before neutron data analysis could begin, the γ-ray events were separated from the neutron events using pulse shape discrimination (PSD). The technique of using charge integration to distinguish between the two types of events and the necessary electronics setup was previously described in detail in Section 2.3.4 and Section 2.4.1. The result is a two-dimensional histogram like the one shown in Figure 3.1. This graph has been rotated so that the two arms are nearly vertical and has been shifted an arbitrary value along the x-axis for convenience. The software cut used to eliminate the γ-ray events is shown between the two arms. The version of the CTP software used for these experiments was not able to utilize two-dimensional gates, so points between the two arms were chosen in ROOT and fitted to a vertical line or occasionally to a higher-order polynomial function, depending on which provided the cleanest division. This line or function was evaluated on an event-by-event basis and compared to the horizontal value for each event. Those events whose horizontal value was greater than the function value were discarded. Figure 3.2 shows the effect of the PSD cut on a typical neutron spectrum.

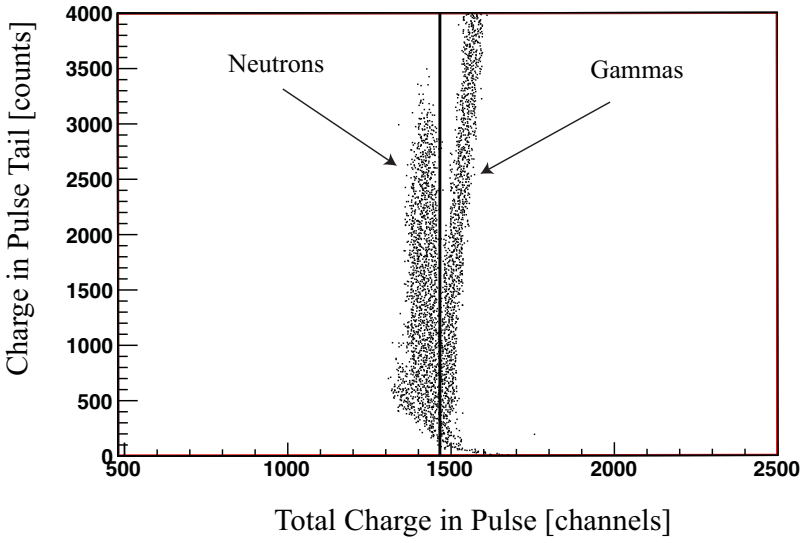

Figure 3.1: Two-dimensional PSD spectrum showing the separation of neutrons from γ-rays at a pulse-height threshold of 1×Cs. The entire spectrum has been rotated so that the two different event branches are nearly vertical and shifted an arbitrary number of channels for presentation. The solid line between the neutrons and gammas represents the software cut used to eliminate the γ-ray events.

3.3 Spectra Fitting

In addition to the neutron groups from the ^{7}Li(d, n)^{8}Be reaction, a neutron group from the ^{2}H(d, n)^{3}He reaction was also evident in the spectrum in nearly the same location as the n_2 peak. This state at E_{lab} = 2.8 MeV was fitted with the response function mentioned in the previous paragraph and subtracted from the ^{7}Li(d, n)^{8}Be spectrum. This background peak was identified by studying the rise in its yield in

conjunction with the integrated beam current, especially with respect to the time at which a new ^{7}Li target layer was evaporated. Other neutron-inducing background reactions which may be of concern, particularly $^{16}\mathrm{O}(\mathrm{d},\mathrm{n})^{17}\mathrm{F}$, have negative Q-values; others, such as $^{27}\mathrm{Al}(\mathrm{d},\mathrm{n})^{28}\mathrm{Si}$ which has a Q-value of 9.36 MeV, have cross sections orders of magnitudes lower than that for $^{7}\mathrm{Li}(\mathrm{d},\mathrm{n})^{8}\mathrm{Be}$ at the low energies of these experiments. All gammas generated by reactions of concern, such as $^{16}\mathrm{O}(\mathrm{d},\gamma)^{17}\mathrm{F}$ and $^{2}\mathrm{H}(\mathrm{d},\gamma)^{4}\mathrm{He}$, occur above 7 MeV and are eliminated with the pulse-shape discrimination electronics.

Ideally, the raw neutron spectrum for each angle was fitted with a combination of the measured n_0, n_1, n_2, and $^{2}\mathrm{H}(\mathrm{d},\mathrm{n})^{3}\mathrm{He}$ response functions, described in Section 2.3.3, in a given region of interest as shown in Figure 3.3. However, because of disentanglement issues with the n_2 and $^{2}\mathrm{H}(\mathrm{d},\mathrm{n})^{3}\mathrm{He}$ states, extraction of results for the n_2 state was extremely difficult. For the analyzing power results given in Chapter 4 and the cross-section and S-factor results given in Chapter 6, only the n_0 and n_1 states were considered. Therefore, each raw neutron spectrum was ultimately fitted at each angle with just a combination of the measured n_0 and n_1 response functions in the region between approximately 6 MeV and 14 MeV where the n_2 and $^{2}\mathrm{H}(\mathrm{d},\mathrm{n})^{3}\mathrm{He}$ states, as well as any γ-ray background which may have escaped the PSD cuts, should have little effect on the data. Each fit consisted of four free parameters to be varied: the gain and scale (height) of each of the two response functions. The gain was adjusted manually as its approximate value could be discerned by where the n_0 and n_1 peaks should be located on the spectrum. The value of the gain was then "fine-tuned" to get the lowest χ^2. MINUIT then minimized the scaling parameter to ensure the lowest χ^2 was obtained.

After the events were sorted into specific spectra for each run, runs with the

same energy and detector threshold and voltage parameters were added together to maximize statistics for each detector. The analyzing power measurements rely on asymmetries in spin states, so when analyzing these data sets, the total spectra including both spin states was fitted first because it had the most statistics. Then, the parameter values used in that fit were applied to each spin-state spectra. To obtain the n_0 yield, the n_1 response spectrum was subtracted from the region of interest and the remainder summed. To obtain the n_1 yield, the n_0 response spectrum was subtracted to leave only the n_1 state.

A rough energy calibration was done for each detector, primarily for presentation purposes, and was determined by pinpointing the channel corresponding to the 14 MeV endpoint energy of the n_0 state, dividing that channel number by the energy to obtain a calibration factor, and applying that calibration factor linearly to all channels in the spectrum. After the calibration was done, the location of the n_1 endpoint was compared to the actual value to establish the accuracy of the calibration; the uncertainty was found to be no more than $\pm$ 0.5 MeV.

3.4 Error Analysis

The errors associated with the yields extracted from the fits were calculated as follows:

$$(\Delta Y)^2 = (\Delta Y_{raw})^2 + Y_{raw}^2 \left((\Delta scale_{n_0})^2 + (\Delta scale_{n_1})^2 \right) \tag{3.1}$$

where $\Delta Y_{raw} = \sqrt{Y_{raw}}$ is the statistical error associated with the yields and where $\Delta scale_{n_n}$ corresponds to the errors given by Minuit for the n_0 and n_1 scaling parameters.

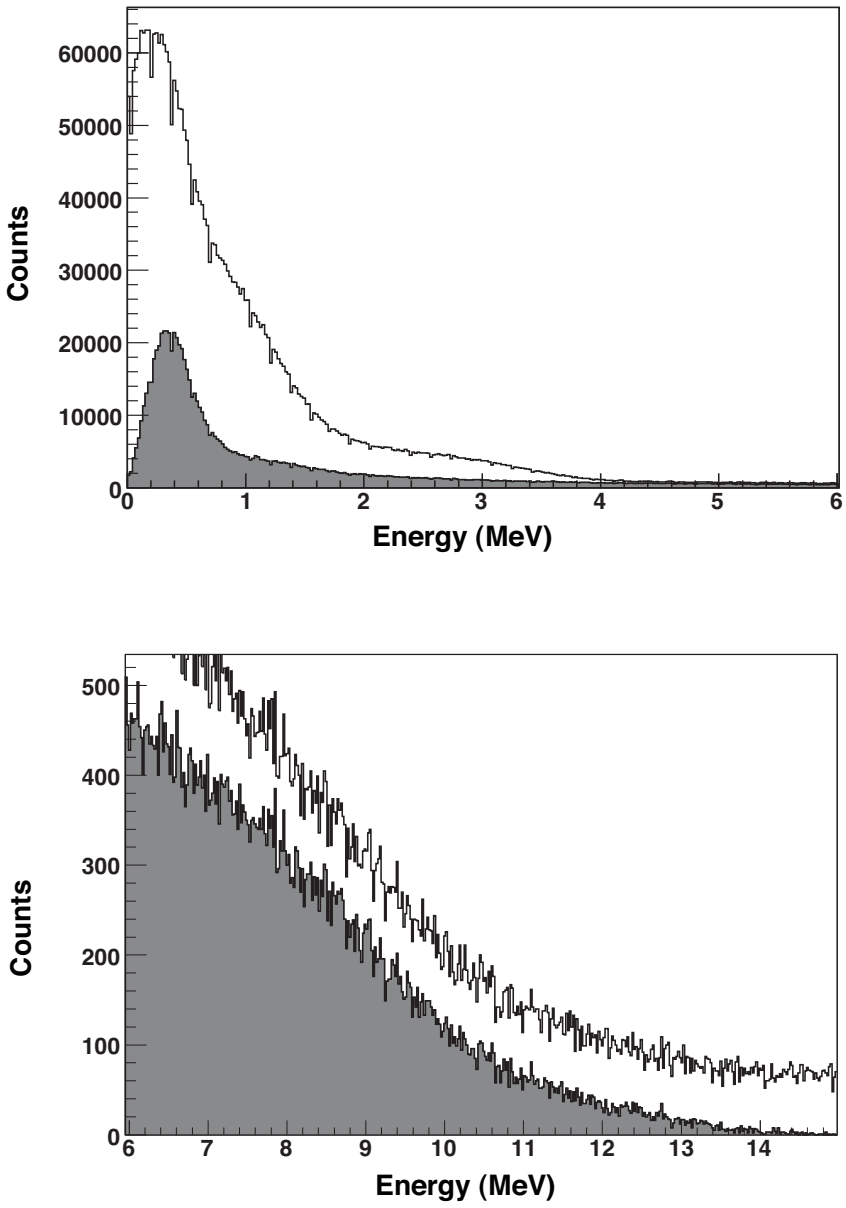

Figure 3.2: The effect of the software PSD cut on a typical energy spectrum at E_d = 80 keV. The shaded histogram is the spectrum with the γ-ray events eliminated by the PSD cut. The top figure shows the low energy end of the spectrum, whereas the bottom figure shows the high-energy region of interest for the n_0 and n_1 states.

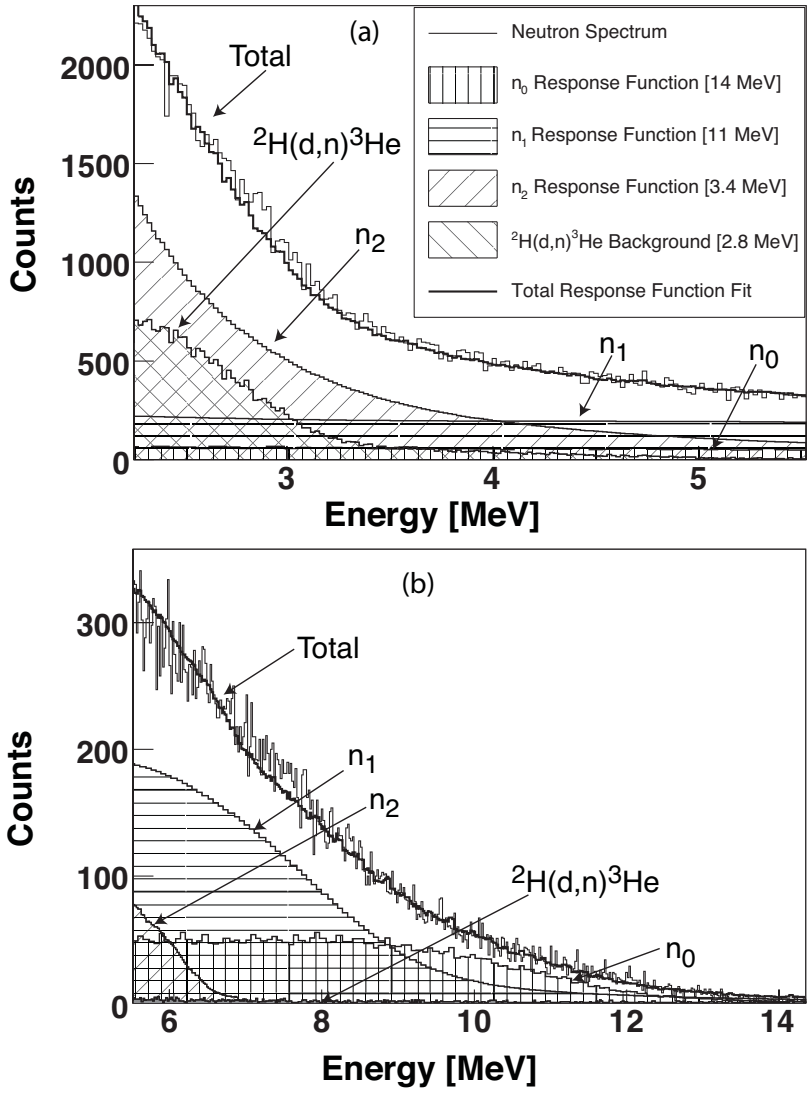

Figure 3.3: The measured total neutron spectrum for the ^{7}Li(d, n)^{8}Be reaction at an incident deuteron energy of 80 keV in the fitting region between 2 MeV and 14 MeV. (a) shows the low energy end of the fitting region, and (b) shows the high energy end. The legend in (b) is the same as that in (a).

Chapter 4

Polarization Observables

The angular distributions of the polarization observables are determined largely by differences in neutron yields for different spin states. This chapter will cover the extraction of the differential cross section $\sigma(\theta)$, the vector analyzing power $iT_{11}(\theta)$, and the tensor analyzing powers $T_{20}(\theta)$, $T_{21}(\theta)$, and $T_{22}(\theta)$ from the yields determined from the spectral analysis in Chapter 3.

4.1 Analyzing Powers

The differential cross section for a reaction initiated by a beam with tensor components t_{kq} is given by

$$\sigma = \sigma_0 \sum_{k,q} t_{kq} T^*_{kq}, \tag{4.1}$$

where σ_0 is the cross section for unpolarized beam and $\mathrm{T}^*_{kq} = (-1)^q \mathrm{T}_{k-q}$ are the tensor analyzing powers. Parity conservation demands that $\mathrm{T}_{10}= 0$, that T_{11} is purely imaginary, and that the T_{2q} are real. For a spin-one beam in the coordinate system of the Madison Convention discussed in Section 2.1.1 and shown in Figure 2.1, the cross section can be written as

$$\sigma(\theta) = \sigma_0(\theta)\Big(1 + 2\Re\left(i\mathrm{t}_{11}\right) i\mathrm{T}_{11}(\theta) + \mathrm{t}_{20}\mathrm{T}_{20}(\theta) + 2\Re\left(\mathrm{t}_{21}\right)\mathrm{T}_{21}(\theta) + 2\Re\left(\mathrm{t}_{22}\right)\mathrm{T}_{22}(\theta)\Big), \quad (4.2)$$

where $\Re$ signifies the real part.

It is more convenient to express the beam polarization with respect to an internal coordinate system in which the third axis is the spin-symmetry axis of the beam $\hat{\zeta}$. In this system, most of the polarization moments p_κ and $\mathrm{p}_{\kappa\lambda}$ (or the corresponding spherical tensors $\tau_{\kappa\lambda}$) vanish to leave only p_ζ and $\mathrm{p}_{\zeta\zeta}$ (τ_{10} and τ_{20}). The ABPIS produces polarized beams with specific values of p_ζ and $\mathrm{p}_{\zeta\zeta}$, while allowing the spin-symmetry axis $\hat{\zeta}$ to be rotated by the Wien filter.

Using a rotational matrix $\mathcal{D}$ to change from the coordinate system of τ_{kq} to that of t_{kq} [Edm74], the tensor t_{kq} is obtained through

$$\mathrm{t}_{kq} = \sum_{q'=-k}^{k} \tau_{kq'} \mathcal{D}^{(k)}_{q'q}. \quad (4.3)$$

Figure 4.1 illustrates this transformation between the internal coordinate system and that of the Madison Convention. The Euler angles defining this rotation are $0°$, $-\beta$, and $-(90° - \phi)$. The final beam moments of Equation 4.2 can then be written in terms of p_ζ, $\mathrm{p}_{\zeta\zeta}$, and the spin-symmetry axis direction angles β and ϕ. The beam tensor moments, described in Chapter 2,

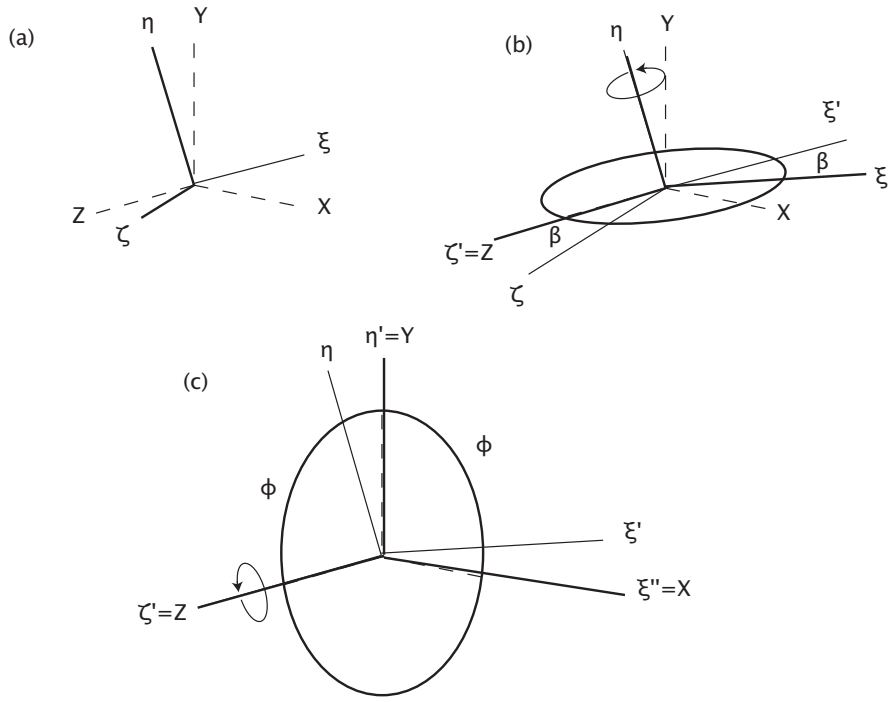

Figure 4.1: Rotation of the internal coordinate system $\xi\eta\zeta$ into the Madison Convention coordinate system XYZ. (a) The first Euler angle is 0° as the ζ-axis is already in the X-Z plane. (b) The second rotation is around the *line of nodes*, the η-axis with a rotation of $-\beta°$ from the ξ-axis to the ζ-axis. This brings the ξ-axis into the X-Y plane and the ζ-axis along Z. (c) The final rotation is around the ζ = Z-axis, or the *figure axis*. This corresponds to an angle of $-(90-\phi)°$ and a clockwise rotation in the ξ-ζ plane. This brings the η axis along Y and the ξ axis along X.

$$\tau_{10} = \sqrt{\frac{3}{2}}\mathrm{p}_\zeta, \quad \tau_{20} = \frac{\mathrm{p}_{\zeta\zeta}}{\sqrt{2}}, \tag{4.4}$$

become

$$\begin{aligned}
\mathrm{t}_{11} &= -i\tau_{10}\frac{\sin\beta e^{i\phi}}{\sqrt{2}}, \\
\mathrm{t}_{20} &= \frac{\tau_{20}}{2}\left(3\cos^2\beta - 1\right), \\
\mathrm{t}_{21} &= -i\tau_{20}\sqrt{\frac{3}{2}}\sin\beta\cos\beta e^{i\phi}, \text{ and} \\
\mathrm{t}_{22} &= -\tau_{20}\sqrt{\frac{3}{8}}\sin^2\beta e^{2i\phi},
\end{aligned} \tag{4.5}$$

and when put into Equation 4.2, give the following expression for the polarized cross section:

$$\begin{aligned}
\sigma(\theta) = \sigma_0(\theta)\Big(1 + \sqrt{3}\mathrm{p}_\zeta i\mathrm{T}_{11}(\theta)\sin\beta\cos\phi + \frac{1}{2\sqrt{2}}\mathrm{p}_{\zeta\zeta}\mathrm{T}_{20}(\theta)\left(3\cos^2\beta - 1\right) + \\
\sqrt{3}\mathrm{p}_{\zeta\zeta}\mathrm{T}_{21}(\theta)\sin\beta\cos\beta\sin\phi - \frac{\sqrt{3}}{2}\mathrm{p}_{\zeta\zeta}\mathrm{T}_{22}(\theta)\sin^2\beta\cos 2\phi\Big).
\end{aligned} \tag{4.6}$$

Through appropriate selection of specific beam polarizations and polarization axis alignments, the above equation can be used to extract an analyzing power of interest. Each observable is described in more detail below.

4.1.1 $iT_{11}(\theta)$

To measure the vector analyzing power $i\mathrm{T}_{11}(\theta)$, the polarization of the beam $\mathrm{p}_{\zeta\zeta}$ was set to 0 to eliminate all tensor observables in Equation 4.6. This was achieved by using the transitions labeled 1 and 2 in Table 2.1. Unfortunately, these states only

yield a theoretical maximum for p_ζ of $\frac{2}{3}$, and no choice of β or ϕ will eliminate all three tensor moments. Therefore, the beam polarization axis was set to $\beta = 90°$ and $\phi = 0°$. Using these values and noting that $\sigma(\theta)$ is proportional to the yield $Y(\theta)$, Equation 4.6 becomes:

$$Y(\theta) = Y_0(\theta)\Big(1 + \sqrt{3}p_\zeta iT_{11}(\theta)\Big) \tag{4.7}$$

where θ is the angular position of the detector and Y_0 is the yield for unpolarized beam. If the polarization $p_\zeta = p_z^+$ for transition state 1 in Table 2.1 and $p_\zeta = -p_z^-$ for state 2, with p_z^+ and p_z^- being positive quantities, then the previous equation can be solved for $iT_{11}(\theta)$ such that

$$iT_{11} = \frac{1}{\sqrt{3}} \frac{Y_+(\theta) - Y_-(\theta)}{Y_+(\theta)p_z^- + Y_-(\theta)p_z^+}, \tag{4.8}$$

where Y_- and Y_+ are the yields for transition states 1 and 2 respectively. Propagation of errors gives

$$\begin{aligned}(\Delta iT_{11}(\theta))^2 = \frac{1}{3}\Bigg((\Delta Y_+)^2 \left(\frac{1}{Y_+p_z^- + Y_-p_z^+} + \frac{p_z^-(Y_+ - Y_-)}{(Y_+p_z^- + Y_-p_z^+)^2}\right)^2 + \\ (\Delta Y_-)^2 \left(\frac{-1}{Y_+p_z^- + Y_-p_z^+} + \frac{p_z^+(Y_+ - Y_-)}{(Y_+p_z^- + Y_-p_z^+)^2}\right)^2 + \\ \left(\Delta p_z^+\right)^2 \left(\frac{Y_-(Y_+ - Y_-)}{(Y_+p_z^- + Y_-p_z^+)^2}\right)^2 + \left(\Delta p_z^-\right)^2 \left(\frac{Y_+(Y_+ - Y_-)}{(Y_+p_z^- + Y_-p_z^+)^2}\right)^2\Bigg)\end{aligned} \tag{4.9}$$

The values for $iT_{11}(\theta)$ for $^7\mathrm{Li}(\vec{d}, n)^8\mathrm{Be}$ at E_d=160-0 keV and 130-0 keV are given in Table A.1 for the n_0 state and Table A.2 for the n_1 state and shown in Figure 4.2 and Figure 4.3. Note that the values given have been transformed into the center-of-mass system. Unfortunately, due to an electronics error, the data set at E_d=80-0 keV could not be analyzed.

As described in Section 2.1.3, the p_z value was given an error of 5%; errors for the yields were calculated by taking the error in the fit parameters for n_0 and n_1 added in quadrature with the statistical error, as given in Equation 3.1 and detailed in Section 3.4.

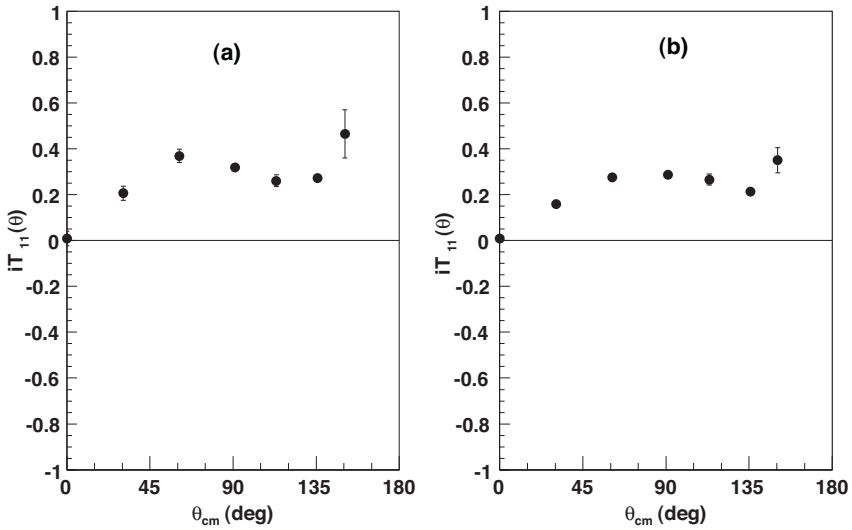

Figure 4.2: The measured $iT_{11}(\theta)$ at (a) E_d= 160-0 keV and (b) E_d= 130-0 keV for the $^7Li(\vec{d}, n_0)^8Be$ reaction. The errors shown consist of both statistical and systematic uncertainties. Error bars that are not visible in the figure are smaller than the point itself.

4.1.2 $T_{20}(\theta)$

From Equation 4.6, it is apparent that by setting $\beta = 0^\circ$ all terms are eliminated except that which contains $T_{20}(\theta)$:

$$Y(\theta) = Y_0(\theta)\left(1 + \frac{1}{\sqrt{2}} p_{\zeta\zeta} T_{20}(\theta)\right). \tag{4.10}$$

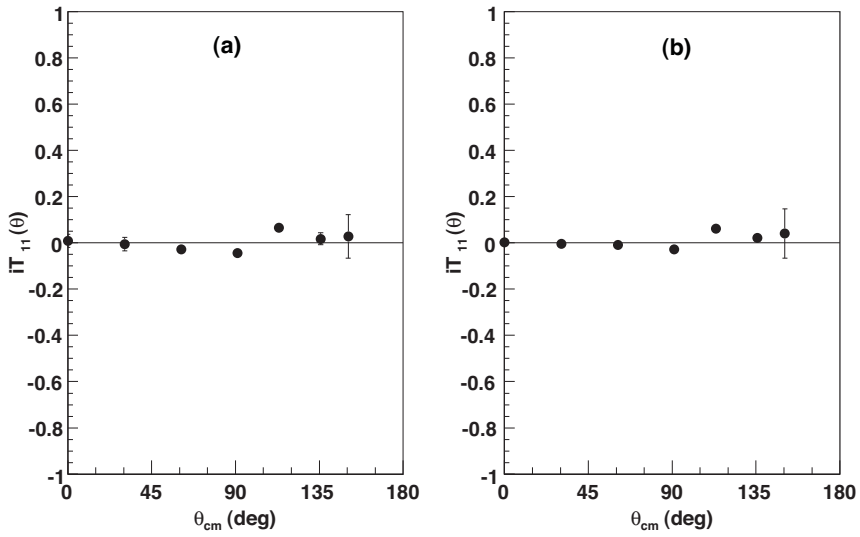

Figure 4.3: The measured $iT_{11}(\theta)$ at (a) E_d= 160-0 keV and (b) E_d= 130-0 keV for the ^{7}Li$(\vec{d}, n_1)^8$Be reaction. The errors shown consist of both statistical and systematic uncertainties. Error bars that are not visible in the figure are smaller than the point itself.

$T_{20}(\theta)$ can be determined from the above equation by setting the ABPIS to flip between states 3 and 4 in Table 2.1 and setting ϕ arbitrarily to 90°. By designating $p_{\zeta\zeta} = p^+_{zz}$ for transition state 4 and $p_{\zeta\zeta} = -p^-_{zz}$ for state 3, with both p^+_{zz} and p^-_{zz} being positive quantities,

$$T_{20}(\theta) = \sqrt{2}\left(\frac{Y_+(\theta) - Y_-(\theta)}{Y_+(\theta)p^-_{zz} + Y_-(\theta)p^+_{zz}}\right), \tag{4.11}$$

where Y_+ corresponds to the yield measured in state 4 and Y_- to the yield in state 3. Propagation of errors gives

$$\begin{aligned}(\Delta T_{20}(\theta))^2 = 2\Bigg((\Delta Y_+)^2\left(\frac{1}{Y_+p^-_{zz} + Y_-p^+_{zz}} + \frac{p^-_{zz}(Y_+ - Y_-)}{(Y_+p^-_{zz} + Y_-p^+_{zz})^2}\right)^2 + \\ (\Delta Y_-)^2\left(\frac{-1}{Y_+p^-_{zz} + Y_-p^+_{zz}} + \frac{p^+_{zz}(Y_+ - Y_-)}{(Y_+p^-_{zz} + Y_-p^+_{zz})^2}\right)^2 + \\ \left(\Delta p^+_{zz}\right)^2\left(\frac{Y_-(Y_+ - Y_-)}{(Y_+p^-_{zz} + Y_-p^+_{zz})^2}\right)^2 + \left(\Delta p^-_{zz}\right)^2\left(\frac{Y_+(Y_+ - Y_-)}{(Y_+p^-_{zz} + Y_-p^+_{zz})^2}\right)^2\Bigg).\end{aligned} \tag{4.12}$$

The experimentally measured values of $T_{20}(\theta)$ in the center-of-mass system are given in Table A.3 and shown in Figure 4.4 for the ^{7}Li$(\vec{d}, n_0)^8$Be reaction and in Table A.4 and Figure 4.5 for the ^{7}Li$(\vec{d}, n_1)^8$Be reaction at E_d= 160-0 keV, 130-0 keV, and 80-0 keV. The errors on the points were determined in the same manner as those for $iT_{11}(\theta)$.

4.1.3 $T_{21}(\theta)$

The observable $T_{21}(\theta)$ is the hardest of the five observables to measure. An asymmetry between left and right detectors for three spin states was required: transition states 3 and 4 from Table 2.1 and an unpolarized ($p_{\zeta\zeta}$= 0) state. The angle β was

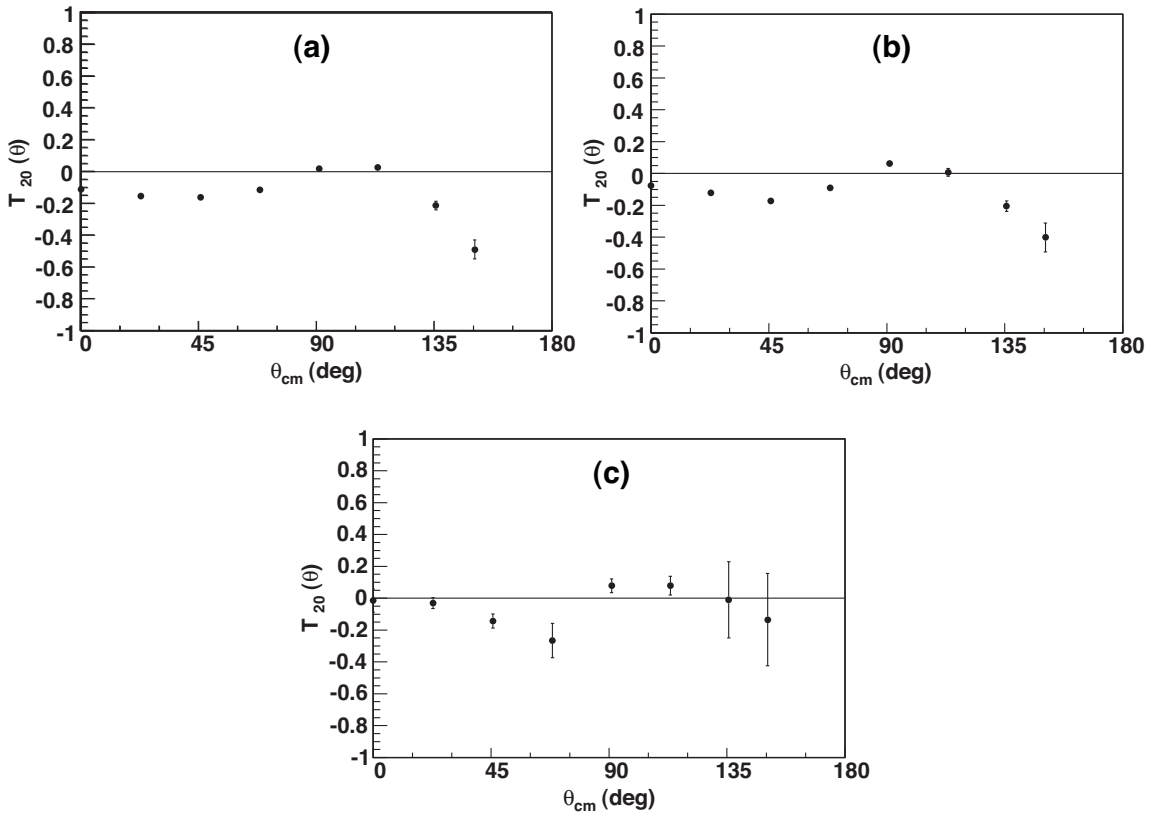

Figure 4.4: The measured $T_{20}(\theta)$ at (a) E_d= 160-0 keV, (b) E_d= 130-0 keV, and (c) E_d= 80-0 keV for the ^{7}Li$(\vec{d}, n_0)^8$Be reaction. The errors shown consist of both statistical and systematic uncertainties. Error bars that are not visible in the figure are smaller than the point itself.

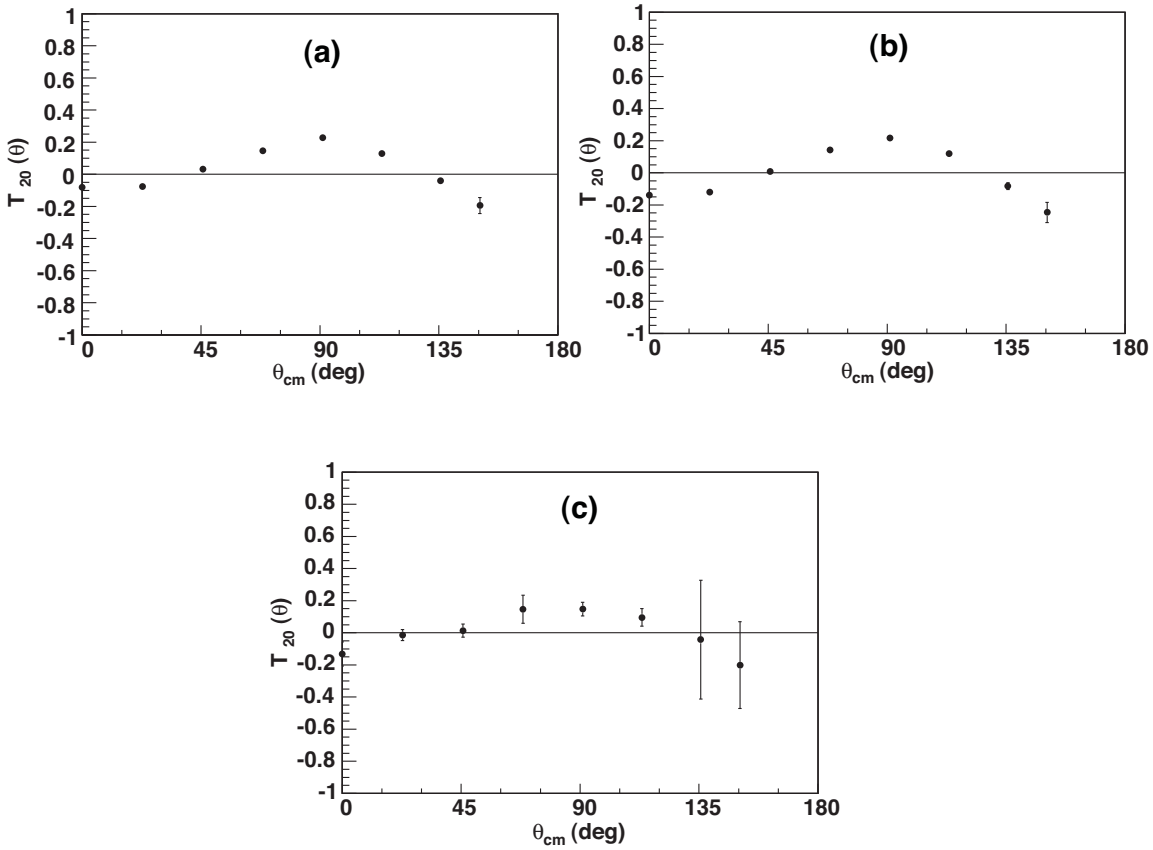

Figure 4.5: The measured $T_{20}(\theta)$ at (a) E_d= 160-0 keV, (b) E_d= 130-0 keV, and (c) E_d= 80-0 keV for the ^{7}Li$(\vec{d}, n_1)^8$Be reaction. The errors shown consist of both statistical and systematic uncertainties. Error bars that are not visible in the figure are smaller than the point itself.

set to 45°, and detectors at beam right had $\phi = 90°$ and those on beam left had $\phi = -90°$. Equation 4.6 then becomes

$$L(\theta) = \frac{Y(\theta, -90°)}{Y_0(\theta)} = 1 + \frac{1}{4\sqrt{2}} \mathrm{p}_{\zeta\zeta} \mathrm{T}_{20}(\theta) - \frac{\sqrt{3}}{2} \mathrm{p}_{\zeta\zeta} \mathrm{T}_{21}(\theta) + \frac{\sqrt{3}}{4} \mathrm{p}_{\zeta\zeta} \mathrm{T}_{22}(\theta) \qquad (4.13)$$

and

$$R(\theta) = \frac{Y(\theta, 90°)}{Y_0(\theta)} = 1 + \frac{1}{4\sqrt{2}} \mathrm{p}_{\zeta\zeta} \mathrm{T}_{20}(\theta) + \frac{\sqrt{3}}{2} \mathrm{p}_{\zeta\zeta} \mathrm{T}_{21}(\theta) + \frac{\sqrt{3}}{4} \mathrm{p}_{\zeta\zeta} \mathrm{T}_{22}(\theta), \qquad (4.14)$$

where $L(\theta)$ and $R(\theta)$ correspond to the yields for the beam left and beam right detectors respectively, and $Y(\theta, \pm 90°)$ and $Y_0(\theta)$ are the polarized and unpolarized yields, respectively for the detector at angle θ. Solving these two equations for $\mathrm{T}_{21}(\theta)$ gives

$$\mathrm{T}_{21}(\theta) = \frac{1}{\sqrt{3}} \frac{R(\theta) - L(\theta)}{\mathrm{p}_{\zeta\zeta}}. \qquad (4.15)$$

Detector pairs were periodically swapped from beam left to beam right to reduce systematic errors. In addition, the $\mathrm{T}_{21}(\theta)$ for state 3 and state 4 were averaged. Propogation of errors for Equation 4.15 gives

$$(\Delta \mathrm{T}_{21}(\theta))^2 = \frac{1}{3}\Bigg((\Delta R(\theta))^2 \left(\frac{1}{\mathrm{p}_{\zeta\zeta}}\right)^2 + (\Delta L(\theta))^2 \left(\frac{1}{\mathrm{p}_{\zeta\zeta}}\right)^2 + (\Delta \mathrm{p}_{\zeta\zeta})^2 \left(\frac{R(\theta) - L(\theta)}{\mathrm{p}_{\zeta\zeta}^2}\right)^2 \Bigg), \qquad (4.16)$$

where

$$(\Delta R(\theta))^2 = (\Delta L(\theta))^2 = (\Delta Y(\theta, \pm 90°))^2 \left(\frac{1}{Y_0(\theta)}\right)^2 + (\Delta Y_0(\theta))^2 \left(\frac{Y(\theta, \pm 90°)}{Y_0^2(\theta)}\right)^2.$$

The experimentally measured values of $T_{21}(\theta)$, transformed to the center-of-mass system, are given in Table A.5 and shown in Figure 4.6 for the ^{7}Li($\vec{d}$, n_0)^{8}Be reaction and in Table A.6 and Figure 4.7 for the ^{7}Li($\vec{d}$, n_1)^{8}Be reaction at E_d= 160-0 keV, 130-0 keV, and 80-0 keV. Only a partial angular distribution for the E_d= 80-0 keV was taken due to time constraints and experimental difficulties. The errors on the points were determined in the same manner as those for the previous observables.

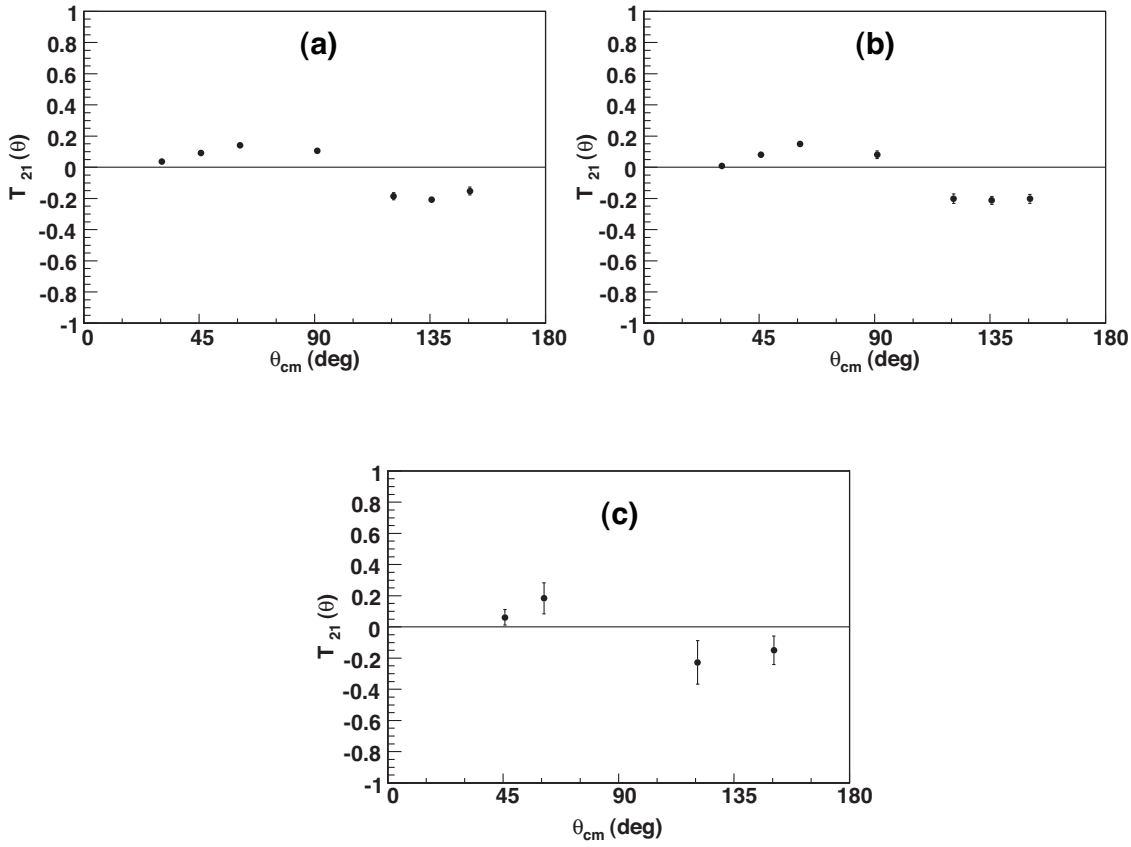

Figure 4.6: The measured $T_{21}(\theta)$ at (a) E_d= 160-0 keV, (b) E_d= 130-0 keV, and (c) E_d= 80-0 keV for the ^{7}Li($\vec{d}$, n_0)^{8}Be reaction. The errors shown consist of both statistical and systematic uncertainties. Error bars that are not visible in the figure are smaller than the point itself.

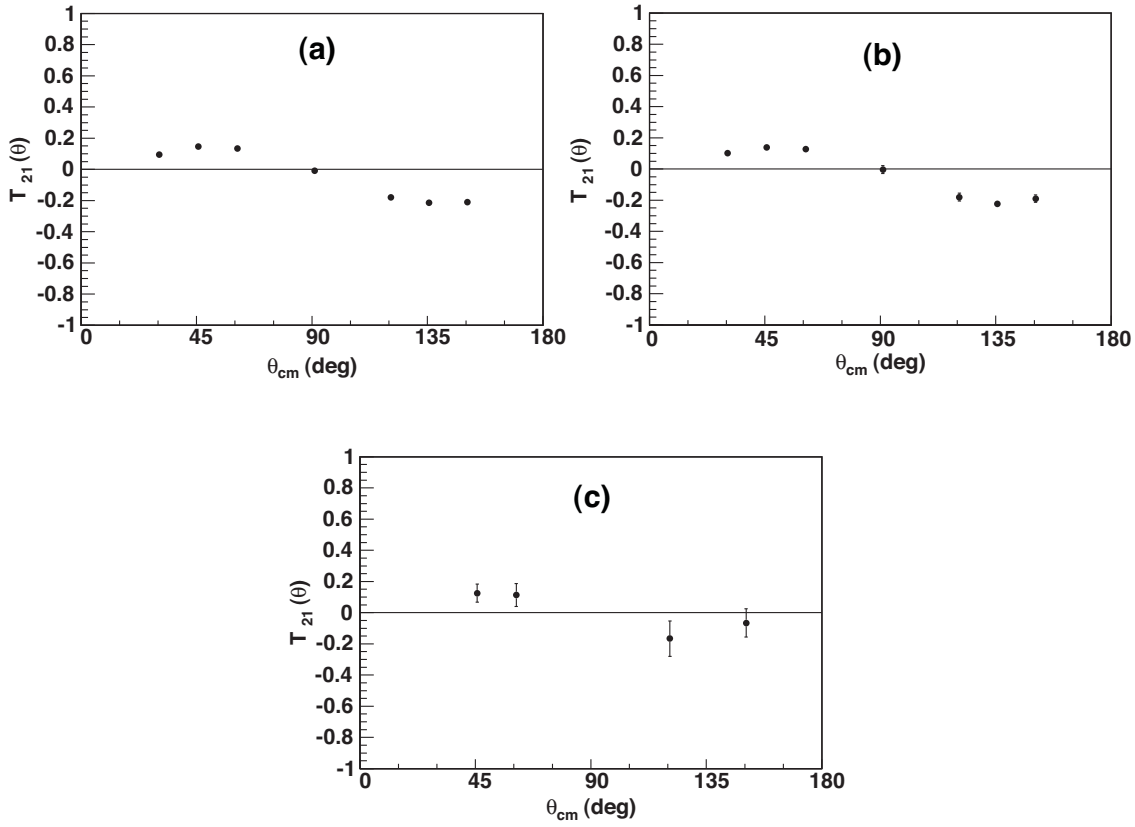

Figure 4.7: The measured $T_{21}(\theta)$ at (a) E_d= 160-0 keV, (b) E_d= 130-0 keV, and (c) E_d= 80-0 keV for the ^{7}Li$(\vec{d}, n_1)^8$Be reaction. The errors shown consist of both statistical and systematic uncertainties. Error bars that are not visible in the figure are smaller than the point itself.

4.1.4 $T_{22}(\theta)$

The observable $T_{22}(\theta)$ can be measured by choosing a pure tensor polarized beam, transitions 5 and 6 in Table 2.1 with $\beta = 54.7°$ and $\phi = 0°$. This choice sets $p_\zeta = 0$ and reduces Equation 4.6 to

$$Y(\theta) = Y_0(\theta)\left(1 - \frac{1}{\sqrt{3}} p_{\zeta\zeta} T_{22}(\theta)\right). \tag{4.17}$$

By designating $p_{\zeta\zeta} = p^+_{zz}$ for state 5 and $p_{\zeta\zeta} = -p^-_{zz}$ for state 6, with both p^+_{zz} and p^-_{zz} being positive quantities, $T_{22}(\theta)$ can be found as

$$T_{22}(\theta) = -\sqrt{3}\frac{Y_+(\theta) - Y_-(\theta)}{Y_+(\theta)p^-_{zz} + Y_-(\theta)p^+_{zz}}, \tag{4.18}$$

where Y_+ is the yield in state 5 and Y_- is the yield from state 6.

Unfortunately, as is evident from Table 2.1, these states which yield $p_{\zeta\zeta} = 1$ for number 5 and $p_{\zeta\zeta} = -2$ for number 6, reduce the overall intensity of the beam by a factor of $\frac{1}{3}$. This takes place because the second quadrupole removes this portion of the beam during the polarization process.

Propogation of errors for Equation 4.18 gives

$$\begin{aligned}(\Delta T_{22}(\theta))^2 = 3\Bigg((\Delta Y_+)^2 &\left(\frac{1}{Y_+p^-_{zz} + Y_-p^+_{zz}} + \frac{p^-_{zz}(Y_+ - Y_-)}{(Y_+p^-_{zz} + Y_-p^+_{zz})^2}\right)^2 + \\ (\Delta Y_-)^2 &\left(\frac{-1}{Y_+p^-_{zz} + Y_-p^+_{zz}} + \frac{p^+_{zz}(Y_+ - Y_-)}{(Y_+p^-_{zz} + Y_-p^+_{zz})^2}\right)^2 + \\ \left(\Delta p^+_{zz}\right)^2 &\left(\frac{Y_-(Y_+ - Y_-)}{(Y_+p^-_{zz} + Y_-p^+_{zz})^2}\right)^2 + \left(\Delta p^-_{zz}\right)^2\left(\frac{Y_+(Y_+ - Y_-)}{(Y_+p^-_{zz} + Y_-p^+_{zz})^2}\right)^2\Bigg)\end{aligned} \tag{4.19}$$

The experimentally measured values of $T_{22}(\theta)$ in the center-of-mass system are given in Table A.7 and shown in Figure 4.8 for the $^7\mathrm{Li}(\vec{\mathrm{d}}, \mathrm{n}_0)^8\mathrm{Be}$ reaction and in Table

A.8 and Figure 4.9 for the ^{7}Li($\vec{d}$, n_1)^{8}Be reaction at E_d= 160-0 keV, 130-0 keV, and 80-0 keV. The errors on the points were determined in the same manner as those for the previous observables.

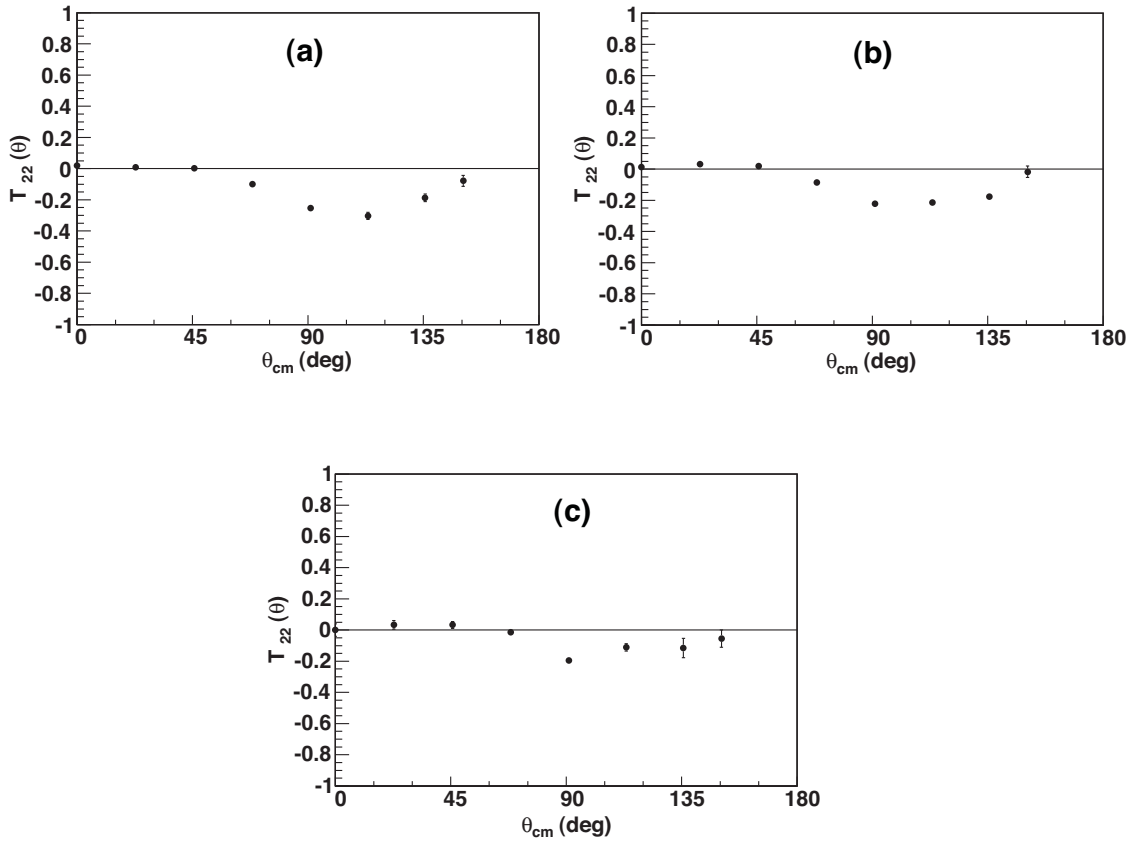

Figure 4.8: The measured $T_{22}(\theta)$ at (a) E_d= 160-0 keV, (b) E_d= 130-0 keV, and (c) E_d= 80-0 keV for the ^{7}Li($\vec{d}$, n_0)^{8}Be reaction. The errors shown consist of both statistical and systematic uncertainties. Error bars that are not visible in the figure are smaller than the point itself.

4.2 Differential Cross Section

Both the differential and absolute cross sections were measured for the ^{7}Li($\vec{d}$, n_0)^{8}Be and ^{7}Li($\vec{d}$, n_1)^{8}Be reactions. The absolute cross section was measured with unpolar-

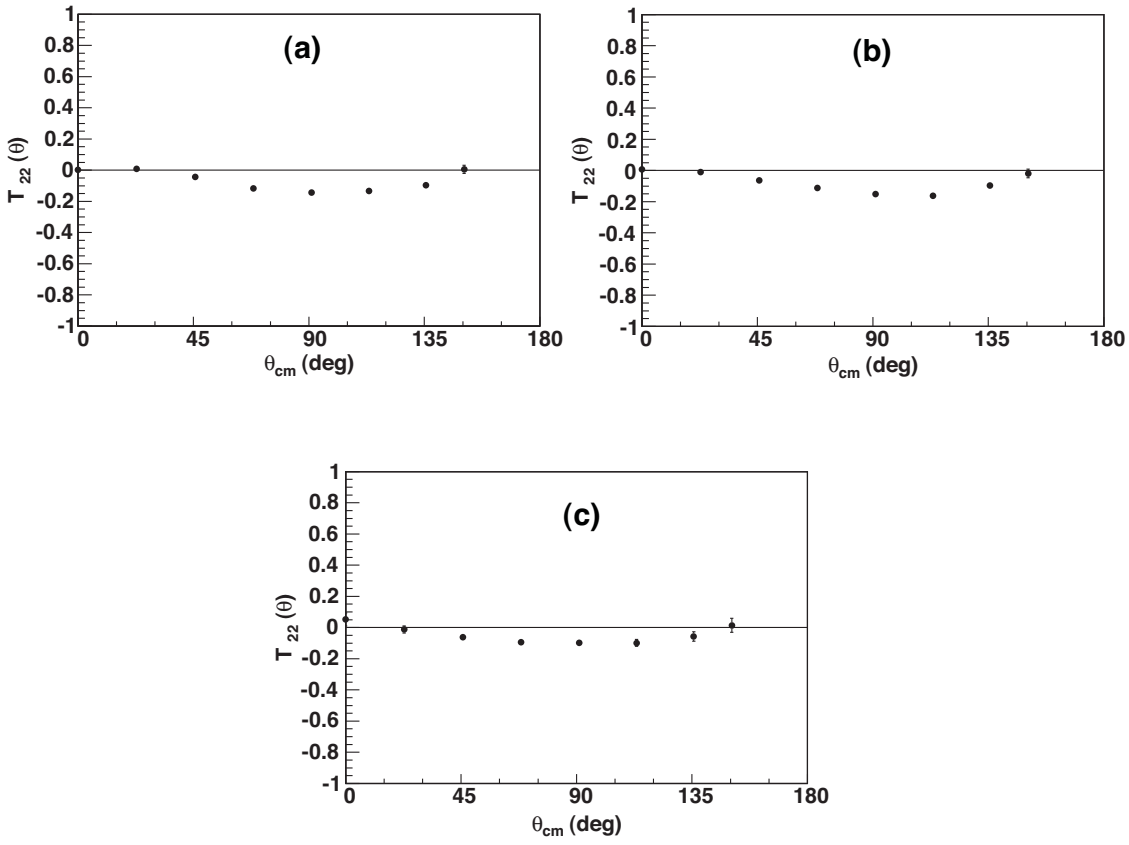

Figure 4.9: The measured $T_{22}(\theta)$ at (a) E_d= 160-0 keV, (b) E_d= 130-0 keV, and (c) E_d= 80-0 keV for the ^{7}Li$(\vec{d}, n_1)^8$Be reaction. The errors shown consist of both statistical and systematic uncertainties. Error bars that are not visible in the figure are smaller than the point itself.

ized beams of 80 keV, 60 keV, and 45 keV; these measurements as well as the absolute cross section and S-factor results are detailed in Chapter 6. The differential cross section, which was used in the Transition Matrix Element analysis described in Chapter 5, is discussed here.

The differential cross section was measured during the $T_{20}(\theta)$ run. When the beam is set such that $\beta = 0°$, the cross section in Equation 4.6 becomes

$$\sigma(\theta) = \sigma_0(\theta)\left(1 + \frac{1}{\sqrt{2}}T_{20}(\theta)\right) \tag{4.20}$$

for a given polarization state $p_{\zeta\zeta}$. With the transitions designated as in Section 4.1.2, the differential cross section can be found to be

$$\sigma_0 = \frac{1}{2}\left(\sigma_+ + \sigma_-\right). \tag{4.21}$$

Initially, at E_d= 160 keV, the five beam-left detectors and the detector at 113°, as shown in Figure 2.4 were moved to the side, and the detector at 150° was used to take data at the five beam-left angles between 0° and 90° and at the beam-right angles of 113° and 150°. The beam-right detectors at 90° and 135° were used as beam current monitors. The differential cross section at $E_d = 160$ keV was then determined using these runs from this one detector.

The detectors were then replaced in their original locations and the normal running continued. The data for the sum of the polarization states at $E_d = 160$ keV with all detectors in place was normalized to the angular correlation data described above to obtain a scaling factor between all detectors. This factor was then applied to the data at $E_d = 130$ keV and that at $E_d = 80$ keV. These cross sections, after being transformed to the center-of-mass system, are given in Table A.9 and Figure 4.10 for

the ^{7}Li($\vec{\mathrm{d}}$, n_0)^{8}Be reaction and in Table A.10 and Figure 4.11 for the ^{7}Li($\vec{\mathrm{d}}$, n_1)^{8}Be reaction. The error in each point is given by the error in the scale factor for that angle, which is the error in the angular correlation yields, added in quadrature with the error in the yield for that angle and energy.

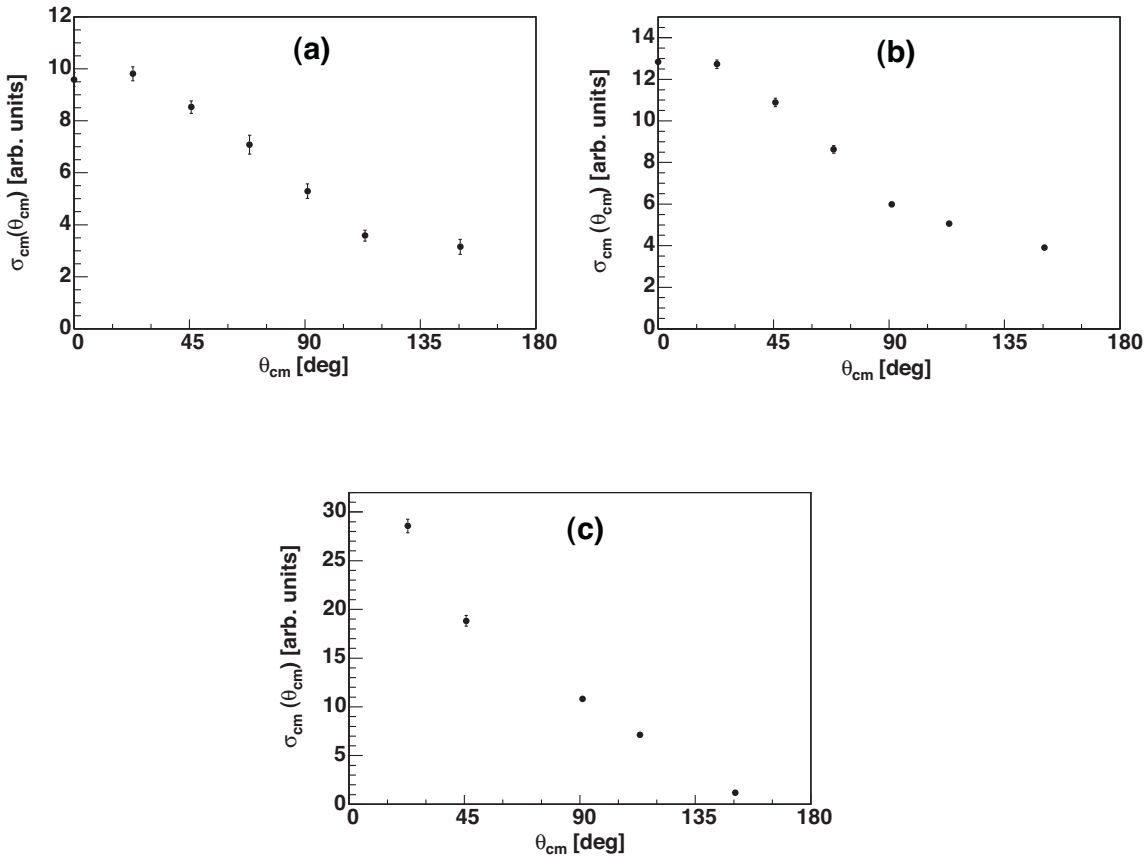

Figure 4.10: The measured $\sigma_{\mathrm{c.m.}}(\theta)$ at (a) $\mathrm{E_d}$= 160-0 keV, (b) $\mathrm{E_d}$= 130-0 keV, and (c) $\mathrm{E_d}$= 80-0 keV for the ^{7}Li($\vec{\mathrm{d}}$, n_0)^{8}Be reaction. The errors shown consist of both statistical and systematic uncertainties. Error bars that are not visible in the figure are smaller than the point itself.

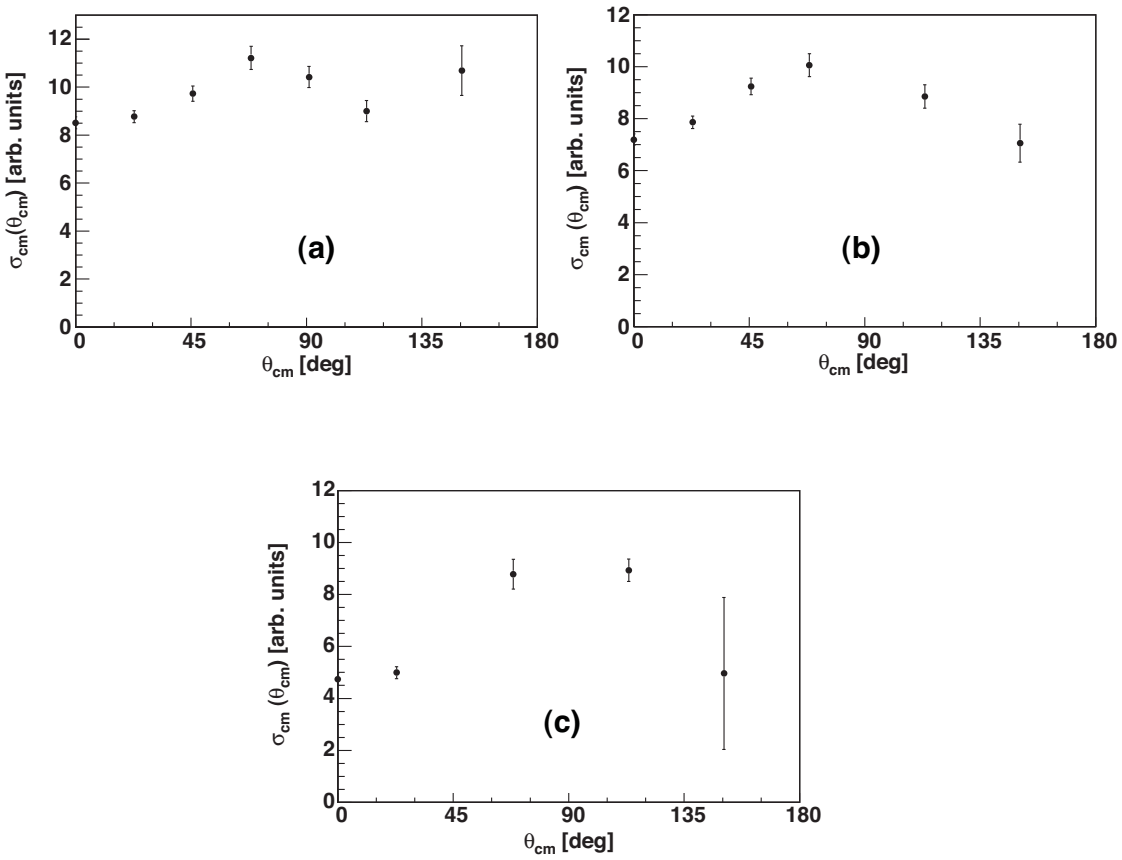

Figure 4.11: The measured $\sigma_{\mathrm{c.m.}}(\theta)$ at (a) E_d= 160-0 keV, (b) E_d= 130-0 keV, and (c) E_d= 80-0 keV for the $^7\mathrm{Li}(\vec{\mathrm{d}}, \mathrm{n}_1)^8\mathrm{Be}$ reaction. The errors shown consist of both statistical and systematic uncertainties.

Chapter 5

Transition Matrix Element Analysis

The observables presented in Chapter 4 can be compared directly to the observables predicted by theoretical calculations. However, this comparison only reveals differences between theory and experiment; greater insight can be obtained by investigating the origins of these differences. One powerful way to do this is to expand the observables in terms of the complex Transition Matrix Elements (TMEs). The TMEs can then be fitted to the measured data to obtain the amplitudes and phases of the TMEs that best represent the data. This provides a deeper insight into the nature of the reaction and, by comparing these TMEs with those calculated from theory, as shown in Chapter 7, critical information about why the theory and experiment may differ can be gleaned.

5.1 Legendre Polynomial Expansion

The polarization observables can be expressed in terms of Legendre polynomials. The Legendre polynomial expansion can be related to an expansion in transition matrix elements (TMEs), discussed further in Section 5.2. The significance of individual Legendre polynomials in the expansion gives a hint as to which transitions will be involved in the reaction.

The unpolarized cross section σ_0 can be expanded in terms of Legendre polynomials to be

$$\sigma_0(\theta) = \left(\frac{\lambda\!\!\!^{-2}}{4\,(2x+1)\,(2a+1)}\right) \sum_{k=0}^{n} \mathrm{Q}_k \mathrm{a}_k \mathrm{P}_k(\cos\theta), \tag{5.1}$$

where Q_0 and P_0 are both defined to be 1, $\lambda\!\!\!^{-}$ is the reduced wavelength of the incident particle, x is the spin of the incident particle, and a is the spin of the target nucleus. The Q_k are the finite geometry correction factors, which will be discussed in Section 5.1.1, a_k are the Legendre polynomial coefficients, and P_k are the Legendre polynomials.

The total cross section σ_T is found by integrating Equation 5.1 over all angles θ and ϕ to obtain

$$\sigma_T = \int_0^{2\pi}\int_0^{\pi} \sigma_0(\theta)\sin\theta d\theta d\phi = 4\pi\left(\frac{\lambda\!\!\!^{-2}}{4\,(2x+1)\,(2a+1)}\right)\mathrm{a}_0. \tag{5.2}$$

In addition, if an A_0 coefficient is defined such that it is the absolute cross section normalization constant:

$$\mathrm{A}_0 = \left(\frac{\lambda\!\!\!^{-2}}{4\,(2x+1)\,(2a+1)}\right)\mathrm{a}_0, \tag{5.3}$$

then the total cross section becomes

$$\sigma_T = 4\pi \mathrm{A}_0. \tag{5.4}$$

The polarized cross section can then be written in terms of Legendre polynomials according to the formalism of [Sey79] such that

$$\sigma_p(\theta) = \mathrm{A}_0 \sum_k \Big(\mathrm{a}_k \mathrm{P}_k(\cos\theta) + \mathrm{b}_k \mathrm{P}^1_k(\cos\theta)\mathrm{p}_y + \mathrm{c}_k \mathrm{P}_k(\cos\theta)\mathrm{t}_{20} + \mathrm{d}_k \mathrm{P}^1_k(\cos\theta)\Re\left(\mathrm{t}_{21}\right) + \mathrm{e}_k \mathrm{P}^2_k(\cos\theta)\Re\left(\mathrm{t}_{22}\right)\Big). \tag{5.5}$$

By comparing this equation with Equation 4.2, a relation can be developed between the associated Legendre polynomial coefficients a_k, b_k, c_k, d_k, and e_k and the observables. This results in

$$i\mathrm{T}_{11}(\theta)\ \sigma_0(\theta) = \frac{\mathrm{A}_0}{\sqrt{3}} \sum_k \mathrm{Q}_k \mathrm{b}_k \mathrm{P}^1_k(\cos\theta), \tag{5.6}$$

$$\mathrm{T}_{20}(\theta)\ \sigma_0(\theta) = \mathrm{A}_0 \sum_k \mathrm{Q}_k \mathrm{c}_k \mathrm{P}_k(\cos\theta), \tag{5.7}$$

$$\mathrm{T}_{21}(\theta)\ \sigma_0(\theta) = \frac{\mathrm{A}_0}{2} \sum_k \mathrm{Q}_k \mathrm{d}_k \mathrm{P}^1_k(\cos\theta), \tag{5.8}$$

and

$$\mathrm{T}_{22}(\theta)\ \sigma_0(\theta) = \frac{\mathrm{A}_0}{2} \sum_k \mathrm{Q}_k \mathrm{e}_k \mathrm{P}^2_k(\cos\theta). \tag{5.9}$$

5.1.1 The Q_k Coefficients

Because of the mathematical properties of the Legendre polynomials, a set of coefficients, namely the Q_k coefficients shown in Equation 5.1 and in Equation 5.6 through Equation 5.9, can correct for the finite geometry of the detector. As detailed in [Ros53] and [Fer65], the Q_k coefficients are defined as

$$Q_k = \frac{J_k}{J_0}, \tag{5.10}$$

where

$$J_k = \int_{-1}^{1} \epsilon(\beta)\ P_k(\cos\beta)\ d(\cos\beta), \tag{5.11}$$

where β is the angle of the incident neutrons with respect to the detector's symmetry axis, and where $\epsilon(\beta)$ is the probability of neutron detection at that angle.

As outlined in [Ros53], the simplest method for calculating the Q_k coefficients is by calculating $\epsilon(\beta)$ such that

$$\epsilon(\beta) = 1 - e^{-\Sigma x(\beta)}, \tag{5.12}$$

where Σ is the neutron attenuation coefficient for the detector material and $x(\beta)$ is the path length through the detector at an angle β. The path length $x(\beta)$ is determined in the following way for a detector with radius r and thickness t a distance d from the target:

$$\begin{aligned} x(\beta) &= \frac{t}{\cos\beta} \quad \text{when } \tan\beta < \frac{r}{d+t}, \\ x(\beta) &= \frac{r}{\sin\beta} - \frac{d}{\cos\beta} \quad \text{when } \tan\beta < \frac{r}{d} \text{ and } \tan\beta > \frac{r}{d+t}, \\ \text{and } \ x(\beta) &= 0 \quad \text{when } \tan\beta > \frac{r}{d}. \end{aligned} \tag{5.13}$$

As is evident from the above equations, the Q_k value approaches 1 as the detector is moved farther from the target, subtending a more and more shallow angle β, i.e. in

the limit of a point detector. The Q_k values for this experiment are listed in Table 5.1. Although the Σ value in Equation 5.12 is energy dependent, the difference between the Q_k values for the 11-MeV n_1 neutrons and the 14-MeV n_0 neutrons detected in this experiment is less than 8.6×10^{-5}. Also, the difference in the Q_k values for the 12.7-cm and 11.4-cm detectors used in this experiment is less than 0.01.

k	Q_k
0	1.0
1	0.99
2	0.98
3	0.97
4	0.95
5	0.93

Table 5.1: The Q_k values used in this experiment.

5.1.2 Legendre Polynomial Fits to Data

The data were fitted to Equations 5.6 through 5.9 using a least-squares fit method as described in detail in [Bev03]. The results of these fits are listed in Table B.1 and Table B.2 and are shown in Figure 5.1, Figure 5.2, and Figure 5.3 for the n_0 state and in Figure 5.4, Figure 5.5, and Figure 5.6 for the n_1 state.

General expressions for the reaction cross section in terms of Legendre Polynomials and the contributing TMEs show that, on the basis of angular momentum coupling theory, the highest order polynomial which appears in the expansion is given by $k_{max} \leq 2l$ or $k_{max} \leq 2l'$, whichever is smaller [AS60]. The best fit of the $^7\mathrm{Li}(\vec{\mathrm{d}}, \mathrm{n}_0)^8\mathrm{Be}$ data to a Legendre polynomial expansion went to order $k = 4$ for all observables except $\sigma_{c.m.}$, for which an expansion to $k = 3$ was sufficient. The need to expand to $k = 4$ indicates that some d-waves (l=2) will need to be included in the

TME expansion for this channel, which will be covered in Section 5.2. An expansion to order $k = 2$, however, was sufficient to fit the $^7\mathrm{Li}(\vec{\mathrm{d}}, \mathrm{n}_1)^8\mathrm{Be}$ data. This indicates that only s- and p-waves ($l \leq 1$) need be considered in the TME expansion for this channel.

5.2 Transition Matrix Element Expansion

The Legendre polynomial expansion coefficients of the previous section can be expressed in terms of a set of transition matrix elements (TMEs). The initial TMEs for the $^7\mathrm{Li}(\vec{\mathrm{d}}, \mathrm{n}_0)^8\mathrm{Be}$ and $^7\mathrm{Li}(\vec{\mathrm{d}}, \mathrm{n}_1)^8\mathrm{Be}$ reactions were determined as outlined in Section 5.2.1 and constrained according to the provisions in Section 5.2.3. The FORTRAN code FATSO, which is described in Section 5.2.2, was used to obtain the coefficients which related the TMEs to the Legendre polynomial coefficients.

5.2.1 TMEs for the $^7\mathrm{Li}(\vec{\mathrm{d}}, \mathrm{n})^8\mathrm{Be}$ Reaction

The expansion of the Legendre polynomial coefficients in terms of reaction TMEs is done according to the formalism of [Sey79] where each TME is written in terms of $\mathrm{R} = |\mathrm{R}|\mathrm{e}^{i\phi}$ where $|\mathrm{R}|$ is the TME amplitude and ϕ is the phase.

The angular momenta of a reaction can be specified by

$$\boldsymbol{a}(\boldsymbol{x}, \boldsymbol{L})\boldsymbol{c}, \tag{5.14}$$

where $\boldsymbol{a}$ is the target spin, $\boldsymbol{x}$ is the projectile spin which also carries an orbital angular momentum of $\boldsymbol{l}$, $\boldsymbol{L}$ is the spin of the detected particle which carries orbital angular momentum $\boldsymbol{l'}$, and $\boldsymbol{c}$ is the spin of the residual nucleus. In the channel spin coupling

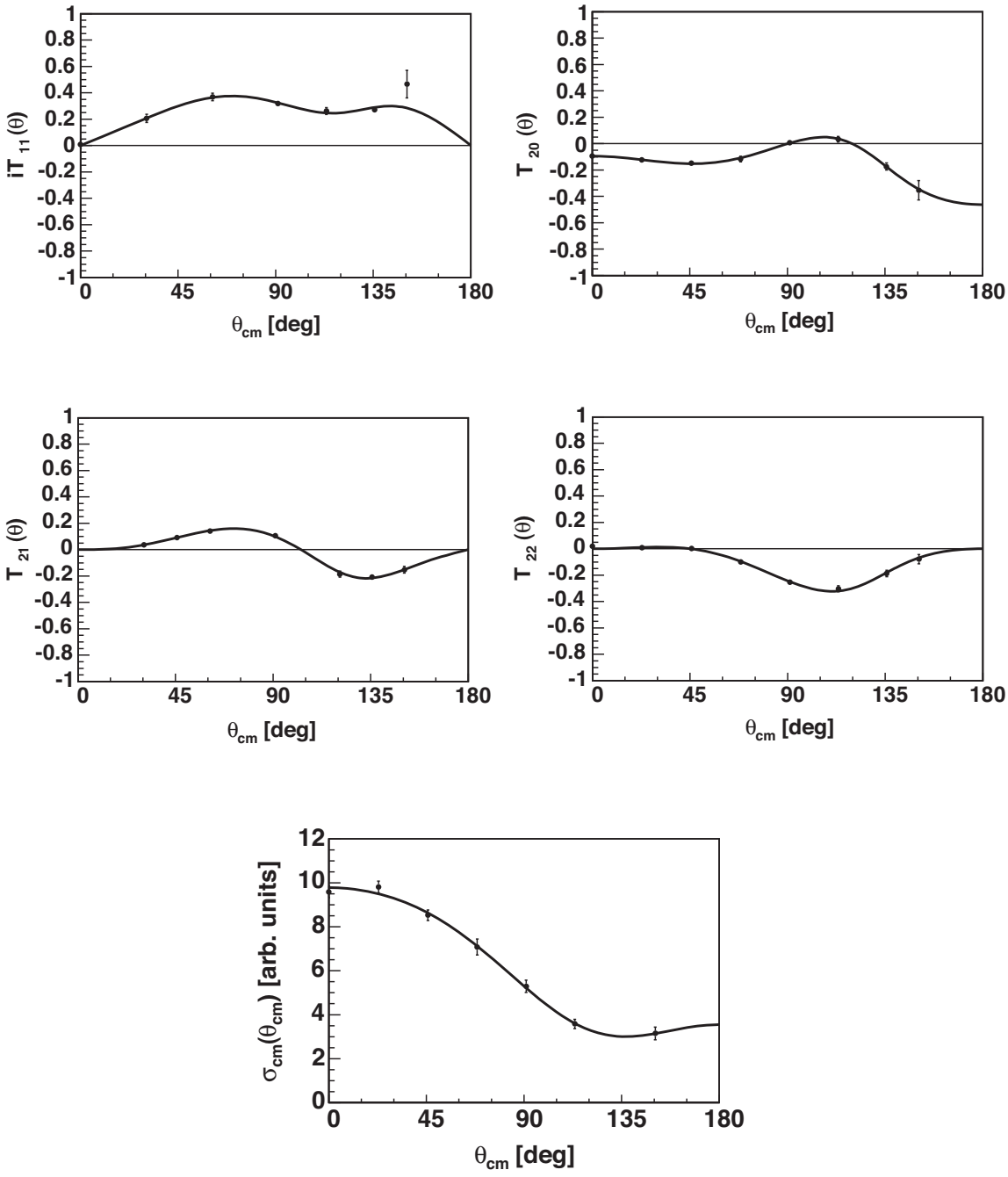

Figure 5.1: Legendre polynomial fits of order $k = 4$ (solid lines) to the ^{7}Li$(\vec{\mathrm{d}}, \mathrm{n}_0)^8$Be data at $\mathrm{E_d}$= 160 keV. The errors bars represent the statistical and systematic uncertainties.

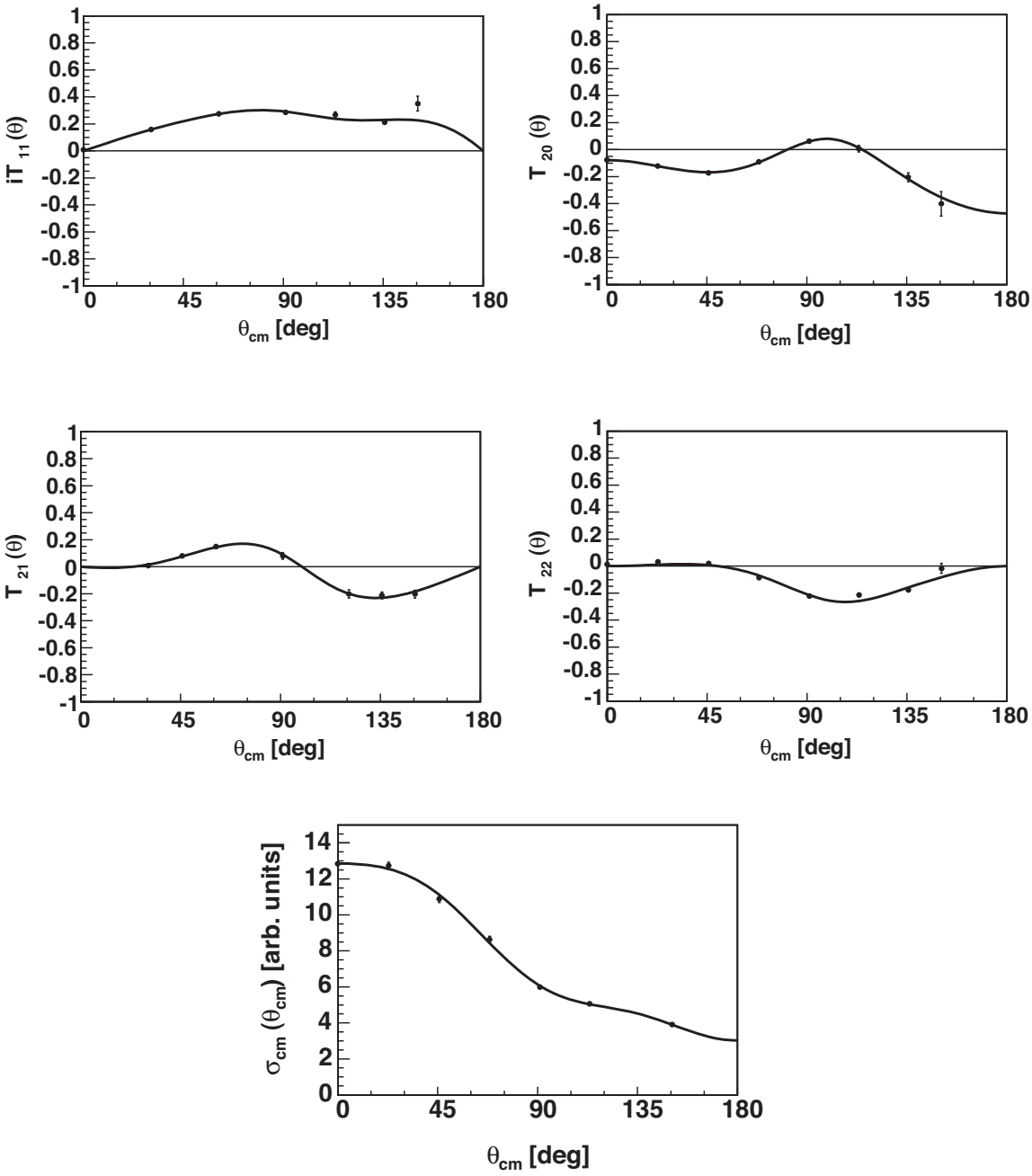

Figure 5.2: Legendre polynomial fits of order $k = 4$ (solid lines) to the ^{7}Li$(\vec{\mathrm{d}}, \mathrm{n}_0)^8$Be data at $\mathrm{E_d}$= 130 keV. The errors bars represent the statistical and systematic uncertainties.

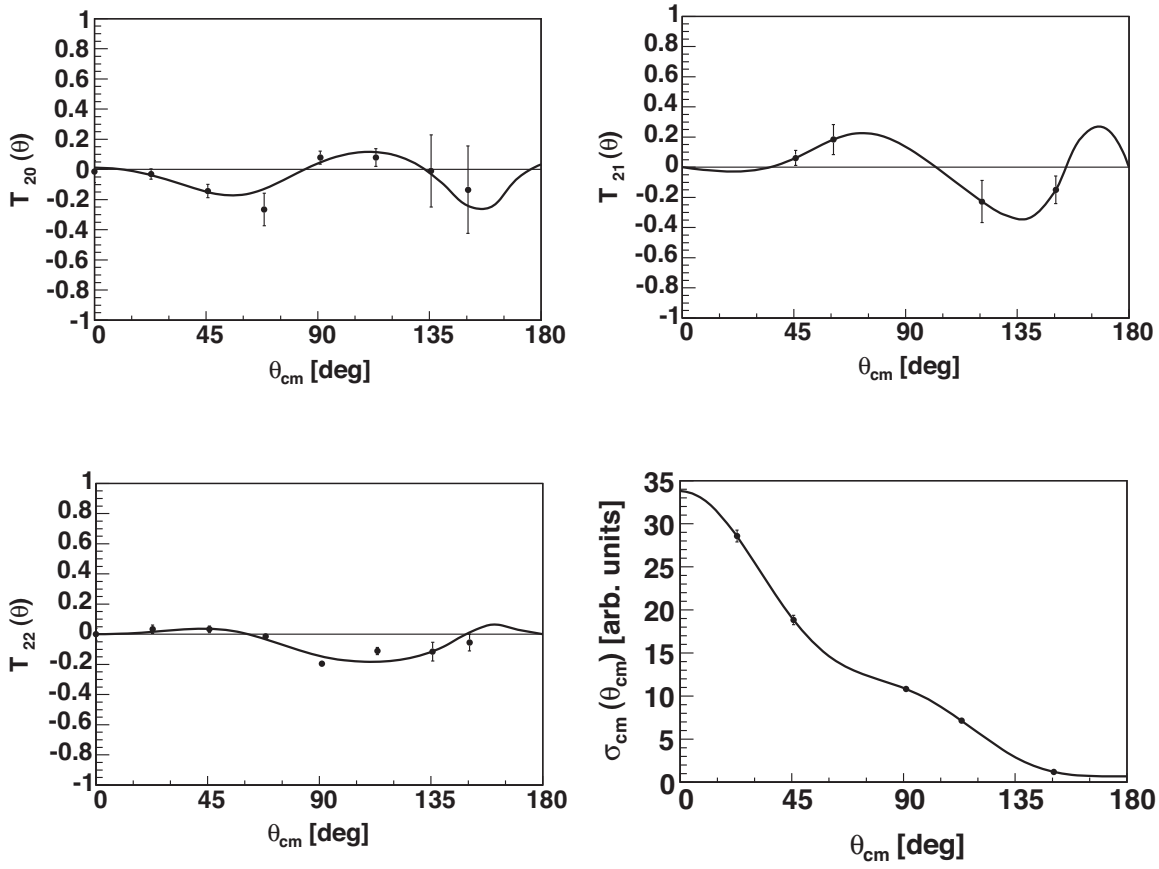

Figure 5.3: Legendre polynomial fits of order $k = 4$ (solid lines) to the $^7\mathrm{Li}(\vec{\mathrm{d}}, \mathrm{n}_0)^8\mathrm{Be}$ data at $\mathrm{E_d}$= 80 keV. The errors bars represent the statistical and systematic uncertainties.

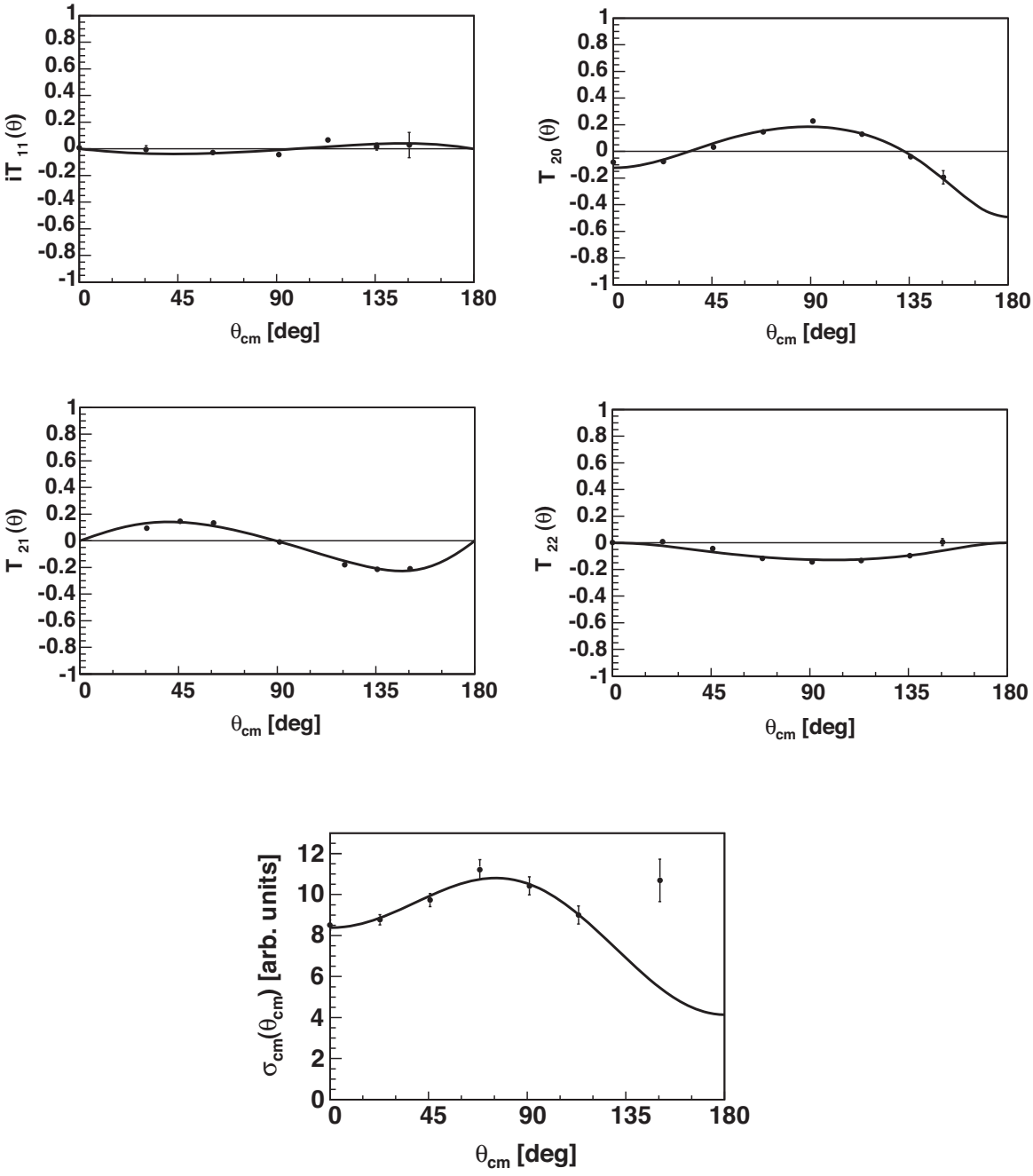

Figure 5.4: Legendre polynomial fits of order $k = 2$ (solid lines) to the $^7\mathrm{Li}(\vec{\mathrm{d}}, \mathrm{n}_1)^8\mathrm{Be}$ data at $\mathrm{E_d}$= 160 keV. The errors bars represent the statistical and systematic uncertainties.

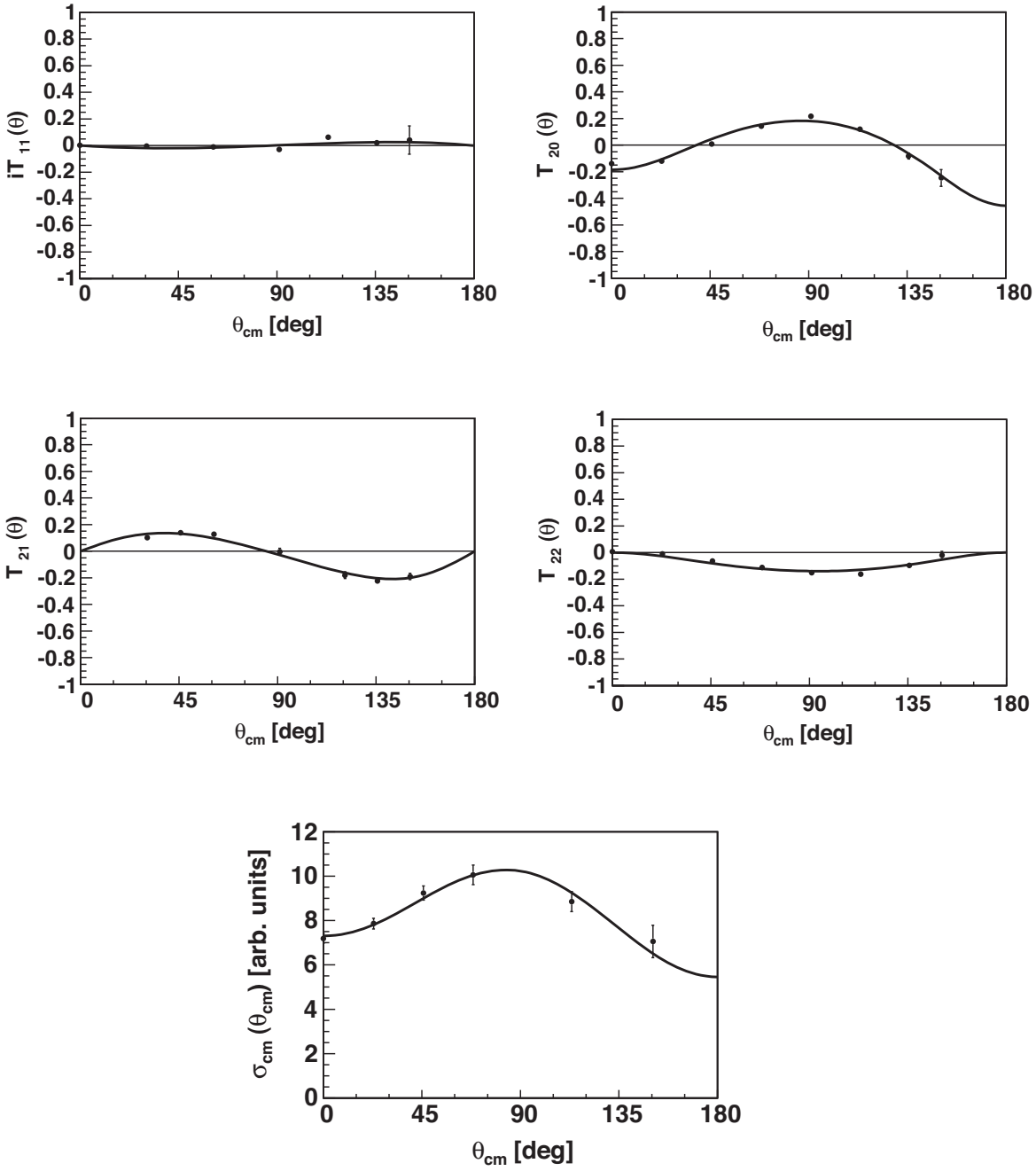

Figure 5.5: Legendre polynomial fits of order $k = 2$ (solid lines) to the $^7\mathrm{Li}(\vec{\mathrm{d}}, \mathrm{n}_1)^8\mathrm{Be}$ data at $\mathrm{E_d}$= 130 keV. The errors bars represent the statistical and systematic uncertainties.

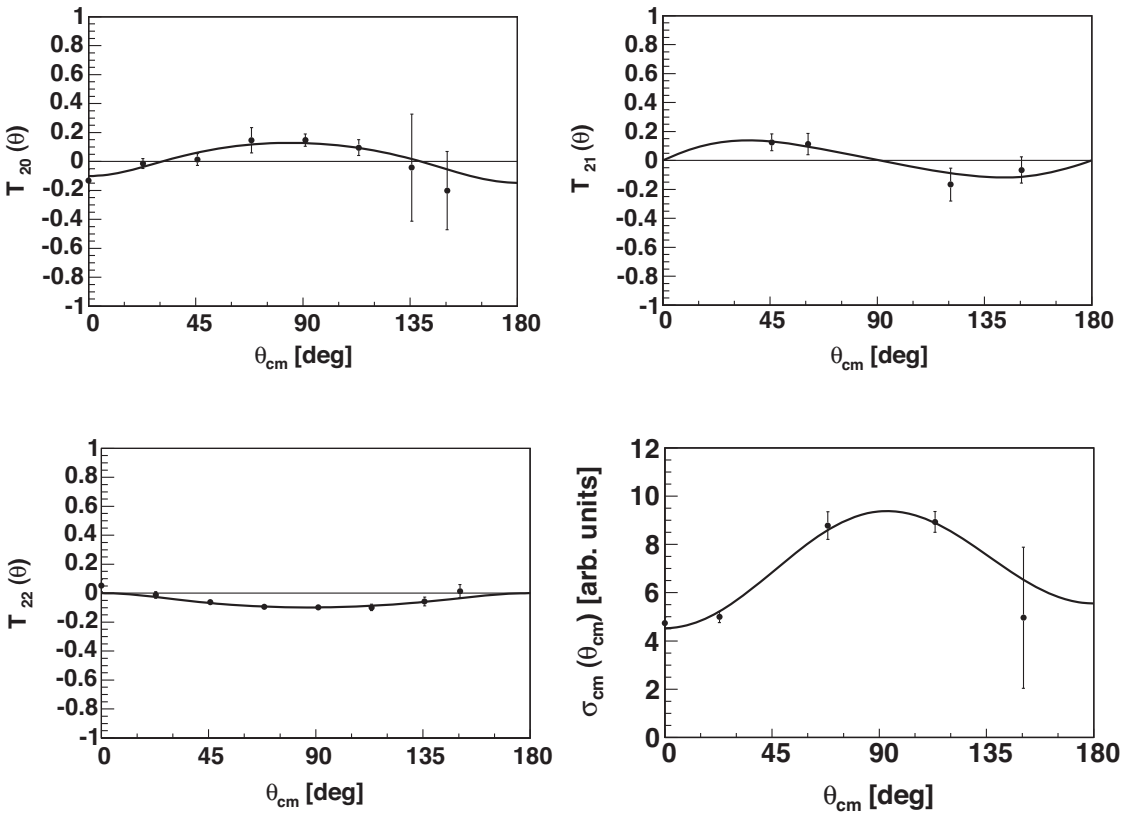

Figure 5.6: Legendre polynomial fits of order $k = 2$ (solid lines) to the ^{7}Li$(\vec{\mathrm{d}}, \mathrm{n}_1)^8$Be data at $\mathrm{E_d}$= 80 keV. The errors bars represent the statistical and systematic uncertainties.

scheme, angular momentum coupling occurs in the following order:

$$\boldsymbol{x} + \boldsymbol{a} = \boldsymbol{s} \tag{5.15}$$

$$\boldsymbol{l} + \boldsymbol{s} = \boldsymbol{J} \tag{5.16}$$

$$\boldsymbol{L} + \boldsymbol{c} = \boldsymbol{s'} \tag{5.17}$$

$$\boldsymbol{l'} + \boldsymbol{s'} = \boldsymbol{J}. \tag{5.18}$$

Each matrix element can then be identified by its quantum numbers $\boldsymbol{J}$, $\boldsymbol{l}$, $\boldsymbol{s}$, $\boldsymbol{l'}$, and $\boldsymbol{s'}$ and written in the $^{2s+1}l_{2J+1}$ notation.

In the case of the $^{7}\mathrm{Li}(\vec{\mathrm{d}},\mathrm{n}_0)^{8}\mathrm{Be}$ reaction, $\boldsymbol{x} = 1^+$, $\boldsymbol{a} = 3/2^-$, $\boldsymbol{L} = 1/2^+$, and $\boldsymbol{c} = 0^+$, resulting in $\boldsymbol{s} = 1/2^-$, $3/2^-$, and $5/2^-$ and $\boldsymbol{s'} = 1/2^+$. As shown in Section 5.1.2, the entrance channel can be limited to s-, p-, and d-waves, i.e. $\boldsymbol{l} = 0$, 1, and 2. The initial TMEs were further constrained by limiting $\boldsymbol{l'} \leq 3$ since higher values of $\boldsymbol{l'}$ are expected to be smaller on the basis of angular momentum barrier effects. The resulting twenty matrix elements are given in Table 5.2.

For $^{7}\mathrm{Li}(\vec{\mathrm{d}},\mathrm{n}_1)^{8}\mathrm{Be}$, $\boldsymbol{x}$, $\boldsymbol{a}$, and $\boldsymbol{L}$ are the same as in the n_0 case, but $\boldsymbol{c} = 2^+$. This gives the same $\boldsymbol{s}$ values, but $\boldsymbol{s'} = 3/2^+$ and $5/2^+$. As shown in Section 5.1.2, only s- and p-waves need to be considered in the entrance channel, i.e. $\boldsymbol{l} = 0$ and 1. The initial set of TMEs were further constrained by limiting $\boldsymbol{l'} \leq 2$ and $\boldsymbol{J} \leq 5/2$, again since higher values of $\boldsymbol{l'}$ and $\boldsymbol{J}$ are expected to be smaller on the basis of angular momentum barrier effects. The resulting twenty-four matrix elements are given in Table 5.3. The TMEs are written in $^{2s+1}l_{2J+1}$ notation. To facilitate reference to individual TMEs in the subsequent chapters, a number appears in parenthesis after a TME when more than one TME have the same notation.

TME	l	s	J^π	s'	l'
$^2s_2$	0	1/2	$1/2^-$	1/2	1
$^4s_4$		3/2	$3/2^-$		1
$^6s_6$		5/2	$5/2^-$		3
$^2p_2$	1	1/2	$1/2^+$	1/2	0
$^4p_2$		3/2	$1/2^+$		0
$^2p_4$		1/2	$3/2^+$		2
$^4p_4$		3/2	$3/2^+$		2
$^6p_4$		5/2	$3/2^+$		2
$^4p_6$		3/2	$5/2^+$		2
$^6p_6$		5/2	$5/2^+$		2
$^4d_2$	2	3/2	$1/2^-$	1/2	1
$^6d_2$		5/2	$1/2^-$	1/2	1
$^2d_4$		1/2	$3/2^-$		1
$^4d_4$		3/2	$3/2^-$		1
$^6d_4$		5/2	$3/2^-$		1
$^2d_6$		1/2	$5/2^-$		3
$^4d_6$		3/2	$5/2^-$		3
$^6d_6$		5/2	$5/2^-$		3
$^4d_8$		3/2	$7/2^-$		3
$^6d_8$		5/2	$7/2^-$		3

Table 5.2: Original TMEs for the $^7\mathrm{Li}(\vec{\mathrm{d}}, \mathrm{n}_0)^8\mathrm{Be}$ reaction.

5.2.2 FATSO code

The output of the FORTRAN program FATSO was used to relate the TMEs given in Table 5.2 and Table 5.3 to the Legendre polynomial coefficients. This program calculates the expressions which relate the Legendre polynomial coefficients of each observable (see Section 5.1) to the various TMEs specified by the user [Sei74].

The polarization observable theory of Chapter 4 can be generalized further such that for a two-body nuclear reaction involving polarized particles, the most general observable quantity is

$$t'_{k'q'K'Q'} = \sum_{k,q,K,Q} t_{kq} t_{KQ} \mathrm{e}^{-\mathrm{i}(q+Q)\phi} A^{k'q'K'Q'}_{kqKQ}(\theta) \tag{5.19}$$

TME	l	s	J^π	s'	l'
$^2s_2$	0	1/2	$1/2^-$	3/2	1
$^4s_4$ (1)		3/2	$3/2^-$	3/2	1
$^4s_4$ (2)		3/2	$3/2^-$	5/2	1
$^6s_6$ (1)		5/2	$5/2^-$	3/2	1
$^6s_6$ (2)		5/2	$5/2^-$	5/2	1
$^2p_4$ (1)	1	1/2	$3/2^+$	3/2	0
$^4p_4$ (1)		3/2	$3/2^+$	3/2	0
$^6p_4$ (1)		5/2	$3/2^+$	3/2	0
$^4p_6$ (1)		3/2	$5/2^+$	5/2	0
$^6p_6$ (1)		5/2	$5/2^+$	5/2	0
$^2p_2$ (1)		1/2	$1/2^+$	3/2	2
$^2p_2$ (2)		1/2	$1/2^+$	5/2	2
$^4p_2$ (1)		3/2	$1/2^+$	3/2	2
$^4p_2$ (2)		3/2	$1/2^+$	5/2	2
$^2p_4$ (2)		1/2	$3/2^+$	3/2	2
$^2p_4$ (3)		1/2	$3/2^+$	5/2	2
$^4p_4$ (2)		3/2	$3/2^+$	3/2	2
$^4p_4$ (3)		3/2	$3/2^+$	5/2	2
$^6p_4$ (2)		5/2	$3/2^+$	3/2	2
$^6p_4$ (3)		5/2	$3/2^+$	5/2	2
$^4p_6$ (2)		3/2	$5/2^+$	3/2	2
$^4p_6$ (3)		3/2	$5/2^+$	5/2	2
$^6p_6$ (2)		5/2	$5/2^+$	3/2	2
$^6p_6$ (3)		5/2	$5/2^+$	5/2	2

Table 5.3: Original TMEs for the $^7\mathrm{Li}(\vec{\mathrm{d}}, \mathrm{n}_1)^8\mathrm{Be}$ reaction.

where the tensor moments t_{kq} are defined by the Madison Convention and where the primed quantities correspond to the outgoing channel. For the outgoing channel, the fully correlated tensor moment for both particles appears; however, the incoming beam and target polarizations t_{kq} and t_{KQ}, respectively, can be written as a direct product due an absence of any correlation [Sei74]. By explicitly writing out the dependence on the azimuthal angle ϕ, a coordinate system fixed in the laboratory rather than in the Madison convention can be defined, as described in Chapter 4.

The $A_{kqKQ}^{k'q'K'Q'}(\theta)$ are the coefficients which relate the TMEs to the Legendre poly-

nomial coefficients and are defined as [Sei74]

$$A_{kqKQ}^{k'q'K'Q'}(\theta) = \frac{\lambda\!\!\!^{-2}\hat{i}'\hat{I}'}{4\hat{i}\hat{I}} \sum_{L} d^{(L)}_{q+Q,q'+Q'}(\theta) \sum_{\mu,\nu} F(kq, KQ; \mu, \nu; L) F'(k'q', K'Q'; \mu, \nu; L) \left\{ {}^{\mathrm{Re}}_{\mathrm{i\ Im}}(R_\mu R^*_\nu) \right\} \tag{5.20}$$

for $k' + K' + k + K = \{^{\mathrm{even}}_{\mathrm{odd}}\}$, and where $\lambda\!\!\!^{-}$ is the reduced wavelength for the incoming channel, i and I are the projectile and target spins, $\hat{i} \equiv \sqrt{(2i+1)}$, L is the order of the Legendre polynomial, and $d^{(L)}_{m'm}(\theta)$ are the reduced rotation matrices. The reaction matrix elements R_ν are defined as

$$R_\nu = \langle l'_\nu s'_\nu J^\pi_\nu \,|R|\, l_\nu s_\nu J^\pi_\nu \rangle \tag{5.21}$$

for channels ν and ν' characterized by orbital angular momentum l_ν, channel spin s_ν, and total angular momentum and parity J^π_ν. The angular momentum functions F and F' are defined as

$$F(kq, KQ; 1, 2; L) = (-)^{l_1+L} \hat{J}_1 \hat{J}_2 \hat{l}_1 \hat{l}_2 \hat{s}_1 \hat{s}_2 \hat{k} \hat{K} \sum_{\lambda} \hat{\lambda}(l_1 l_2 00|\lambda 0) \sum_{\tau} \hat{\tau}(\lambda\tau 0\ q+Q|L\ q+Q) (kKqQ|\tau\ q+Q) \begin{Bmatrix} i & I & s_1 \\ k & K & \tau \\ i & I & s_2 \end{Bmatrix} \begin{Bmatrix} l_1 & s_1 & J_1 \\ \lambda & \tau & L \\ l_2 & s_2 & J_2 \end{Bmatrix} \tag{5.22}$$

where τ is the tensor rank and where $\vec{\lambda} = \vec{l_1} + \vec{l_2}$.

The reaction specifics and matrix elements given in Table 5.2 and Table 5.3 are inputed into the program and the values of the expansion coefficients $A_{kqKQ}^{k'q'K'Q'}(\theta)$ are output in matrix format.

5.2.3 Constraining the Fit

The original TMEs given in Table 5.2 and Table 5.3 and their relative phases result in thirty-nine free parameters for the n_0 transition and forty-seven free parameters for the n_1 transition. A unique fit for this many parameters would be hard to find, even with the quantity of data collected, necessitating further constraint if possible. These simplifications are necessary in order to be able to obtain solutions given the number of knowns and unknowns in the problem. The simplification will ultimately be justified if well-behaved solutions are obtained.

For the n_0 state, elements with the same $\boldsymbol{s}$, $\boldsymbol{l}$, $\boldsymbol{s'}$, and $\boldsymbol{l'}$ values but different $\boldsymbol{J}$ values were added together. This is done assuming that the coupling of $\boldsymbol{l}$ and $\boldsymbol{s}$ or $\boldsymbol{l'}$ and $\boldsymbol{s'}$ is small compared to the $\boldsymbol{l}$ and $\boldsymbol{s}$ dependence itself. Most of this arises for the spin-orbit effects which are small compared to the $\boldsymbol{l}$-dependent interaction. Finally, the phases are assumed to be determined from the $\boldsymbol{l}$-values and were therefore limited to a relative p- to s-wave phase ϕ_{p-s} and a relative d- to p-wave phase ϕ_{d-p}, as well as a phase δ^s between s-wave elements with $\boldsymbol{l'} = 1$ and $\boldsymbol{l'} = 3$, a phase δ^p between p-wave elements with $\boldsymbol{l'} = 0$ and $\boldsymbol{l'} = 2$, and a phase δ^d between d-wave elements with $\boldsymbol{l'} = 1$ and $\boldsymbol{l'} = 3$. Spin-dependent effects are neglected by doing this since these are expected to be less important than the $\boldsymbol{l}$ effects. As shown in Table 5.4, this results in fourteen TMEs and five phases for a total of nineteen independent parameters to fit to the data.

For the same reasons given for the n_0 state TME reduction, the n_1 state TMEs were constrained by adding all elements with the same $\boldsymbol{s}$, $\boldsymbol{l}$, $\boldsymbol{s'}$,and $\boldsymbol{l'}$ values. In addition, only two phases were considered: a relative p- to s-wave phase ϕ_{p-s} and a phase δ^p between p-wave elements with $\boldsymbol{l'} = 0$ and $\boldsymbol{l'} = 2$. This results in a total of

nine TMEs and two phases for a total of eleven independent parameters to fit to the data, as shown in Table 5.5.

new TME	old TMEs	l	s	J^π	s'	l'
$^2s_2$		0	1/2	$1/2^-$	1/2	1
$^4s_4$			3/2	$3/2^-$		1
$^6s_6$			5/2	$5/2^-$		3
$^2p_2$		1	1/2	$1/2^+$	1/2	0
$^4p_2$			3/2	$1/2^+$		0
$^2p_4$			1/2	$3/2^+$		2
$^4p_{10}$	$^4p_4 + {}^4p_6$		3/2	$3/2^+$, $5/2^+$		2
$^6p_{10}$	$^6p_4 + {}^6p_6$		5/2	$3/2^+$, $5/2^+$		2
$^2d_4$		2	1/2	$3/2^-$	1/2	1
$^4d_6$	$^4d_2 + {}^4d_4$		3/2	$1/2^-$, $3/2^-$		1
$^6d_6$	$^6d_2 + {}^6d_4$		5/2	$1/2^-$, $3/2^-$		1
$^2d_6$			1/2	$5/2^-$		3
$^4d_{14}$	$^4d_6 + {}^4d_8$		3/2	$5/2^-$, $7/2^-$		3
$^6d_{14}$	$^6d_6 + {}^6d_8$		5/2	$5/2^-$, $7/2^-$		3
Phases						
ϕ_{p-s}	Relative p- to s-wave phase					
ϕ_{d-p}	Relative d- to p-wave phase					
δ^s	l'=1 to l'=3 phase for s-waves					
δ^p	l'=0 to l'=2 phase for p-waves					
δ^d	l'=1 to l'=3 phase for d-waves					

Table 5.4: Constrained TMEs for the $^7\mathrm{Li}(\vec{\mathrm{d}}, \mathrm{n}_0)^8\mathrm{Be}$ reaction.

5.2.4 Performing the TME Fit

The expansion of the Legendre polynomial coefficients in terms of the output of the FATSO code and in terms of the constrained TMEs and phases are given in Appendix C. These equations are then fitted to the data to optimize the amplitudes and phases to obtain expressions for the observables that describe the measured data the best. This is done by performing a least-square minimization procedure to all

new TME	old TMEs	l	s	J^π	s'	l'
$^2s_2$		0	1/2	$1/2^-$	3/2	1
$^4s_8$	$^4s_4(1)+(2)$		3/2	$3/2^-$	3/2, 5/2	1
$^6s_6$	$^6s_6$ (1)+(2)		5/2	$5/2^-$	3/2, 5/2	1
$^2p_4$		1	1/2	$3/2^+$	3/2	0
$^4p_{10}$	$^4p_4(1)$ +		3/2	$3/2^+$	3/2	0
	$^4p_6(1)$			$5/2^+$	5/2	0
$^6p_{10}$	$^6p_4(1)$ +		5/2	$3/2^+$	3/2	0
	$^6p_6(1)$			$5/2^+$	5/2	0
$^2p_{12}$	$^2p_2((1)+(2))+$		1/2	$1/2^+$	3/2, 5/2	2
	$^2p_4((2)+(3))$			$3/2^+$	3/2, 5/2	2
$^4p_{24}$	$^4p_2((1)+(2))+$		3/2	$1/2^+$	3/2, 5/2	2
	$^4p_4((2)+(3))+$			$3/2^+$	3/2, 5/2	2
	$^4p_6((2)+(3))$			$5/2^+$	3/2, 5/2	2
$^6p_{20}$	$^6p_4((2)+(3))+$		5/2	$3/2^+$	3/2, 5/2	2
	$^6p_6((2)+(3))$			$5/2^+$	3/2, 5/2	2
Phases						
ϕ_{p-s}	Relative p- to s-wave phase					
δ^p	l'=0 to l'=2 phase for p-waves					

Table 5.5: Constrained TMEs for the $^7\mathrm{Li}(\vec{\mathrm{d}},\mathrm{n}_1)^8\mathrm{Be}$ reaction.

data points. The total χ^2 function is given by a sum of the individual χ^2 functions for each observable, e. g.

$$\chi^2_{T_{kq}} = \sum_i \left(\frac{F_{T_{kq}}(\theta_i) - T_{kq}(\theta_i)}{\Delta T_{kq}(\theta_i)} \right)^2 , \tag{5.23}$$

where $T_{kq}(\theta_i)$ are the measured observables, $\Delta T_{kq}(\theta_i)$ are their errors, and $F_{T_{kq}}(\theta_i)$ is the expression of $T_{kq}(\theta_i)$ via the Legendre polynomials for each angle θ_i. The minimization routine calls the MINUIT fitting package [Jam71] and is available as a C++ code which utilizes the built-in class TMinuit of the data analysis package ROOT.

Grid searches for the best fit of the TME amplitudes and phases to the full data set at $\mathrm{E_d}$ = 160 keV were performed. Each amplitude was set to 100% while the other amplitudes were set to zero. Then the phases were varied in 60° steps for that

combination of amplitudes. The resulting solutions with the lowest total χ^2 were searched on again, varying the amplitudes and phases in each case. The best five to ten solutions from the $E_d = 160$ keV searches were then searched on at $E_d = 130$ keV and 80 keV. For both the $^7\mathrm{Li}(\vec{d}, n_0)^8\mathrm{Be}$ and $^7\mathrm{Li}(\vec{d}, n_1)^8\mathrm{Be}$ data sets, a single solution to the TME fits had the best χ^2. These solutions are described in more detail in Section 5.3.

5.3 TME Analysis Results

The results of the TME fits to the $^7\mathrm{Li}(\vec{d}, n_0)^8\mathrm{Be}$ data are given in Table 5.6 and shown as a function of energy in Figure 5.7. A graph of each observable and the TME fit to the data is shown in Figure 5.8 for $E_d = 160$ keV, Figure 5.9 for $E_d = 130$ keV, and Figure 5.10 for $E_d = 80$ keV. P-waves comprise over 70% of the solution, with the $^2p_2$ matrix element dominating. S-wave and D-wave components make up about 10% each of the total solution for E_d= 160 keV, but at the lower beam energies, the D-wave component falls to less than 5% and the P-wave component rises to over 80%.

Table 5.7 and Figure 5.11 show the results of the TME fits to the $^7\mathrm{Li}(\vec{d}, n_1)^8\mathrm{Be}$ data as a function of energy. Each observable is graphed with the TME fit to the data in Figure 5.12 for $E_d = 160$ keV, in Figure 5.13 for $E_d = 130$ keV, and in Figure 5.14 for $E_d = 80$ keV. As can be seen from these figures and Table 5.7, P-waves dominate the solution, especially at 80 keV, where it comprises almost 100% of the total contribution. The $^6p_{10}$ matrix elements dominates. However, the increase in the χ^2 for higher energies could indicate that an inclusion of D-waves is necessary to obtain a satisfactory fit to the data. In addition, an over-simplification of the

	E_d = 160 keV	E_d = 130 keV	E_d = 80 keV
TME	Strength (%)		
$^2s_2$	11±2	8±1	11±1
$^2p_2$	49±8	61±9	62±3
$^4p_2$	12±3	11±3	4±1
$^4p_{10}$	12±2	12±2	14±1
$^6p_{10}$	1±0.4	1±0.8	4±1
$^2d_6$	13±4	4±2	3±0.3
	Phase (°)		
ϕ_{p-s}	-75±4	-78±4	-46±1
ϕ_{d-p}	174±4	172±4	118±2
δ^s	0±525	0±538	0±537
δ^p	-44±10	-46±14	-47±6
δ^d	-20±35	150±38	0±50
χ^2_ν	1.0	0.9	1.6

Table 5.6: Results of the TME fits to the $^7\mathrm{Li}(\vec{\mathrm{d}},\mathrm{n}_0)^8\mathrm{Be}$ data.

matrix elements may have resulted in the large error bars on some of the amplitudes. Unfortunately, due to the large volume of possible unconstrained matrix elements, this is hard to avoid.

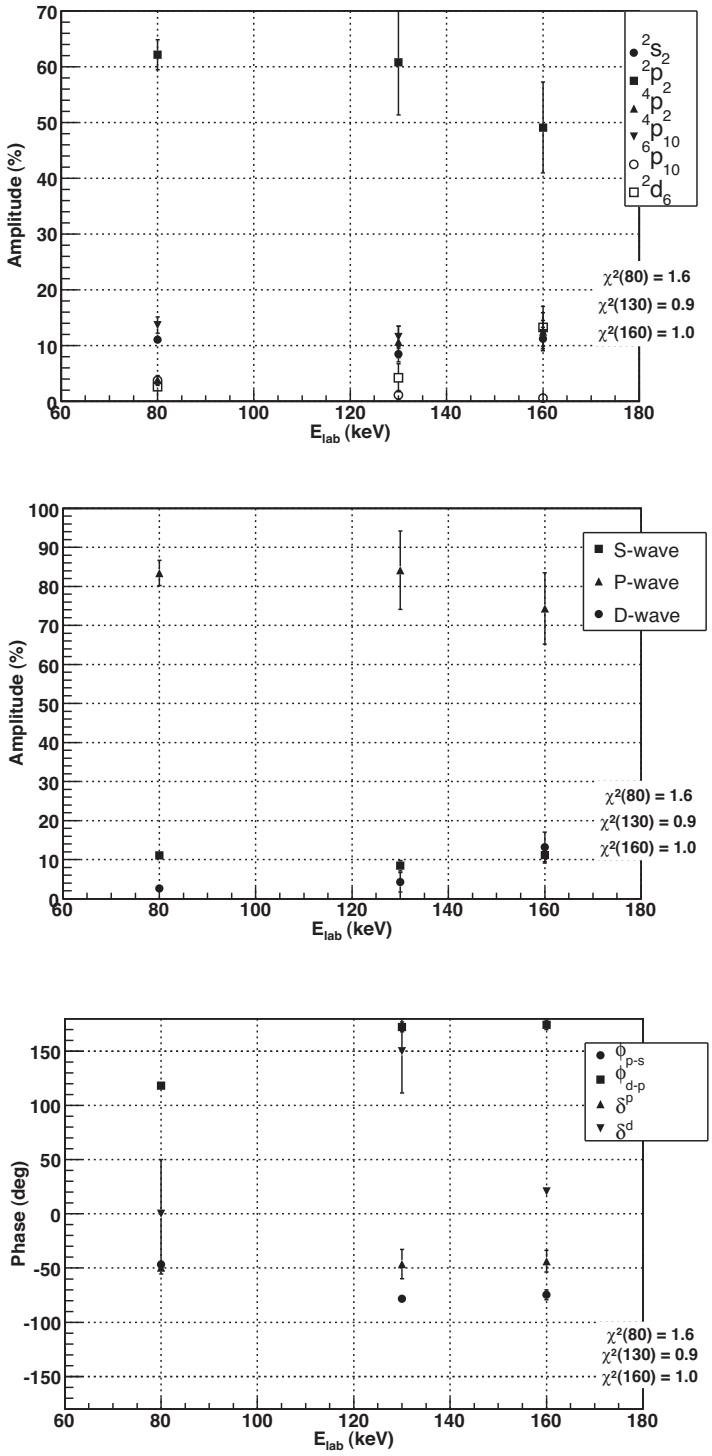

Figure 5.7: TME fit results to the $^{7}\mathrm{Li}(\vec{\mathrm{d}},\mathrm{n}_0)^{8}\mathrm{Be}$ data. The error bars are those generated by the fit.

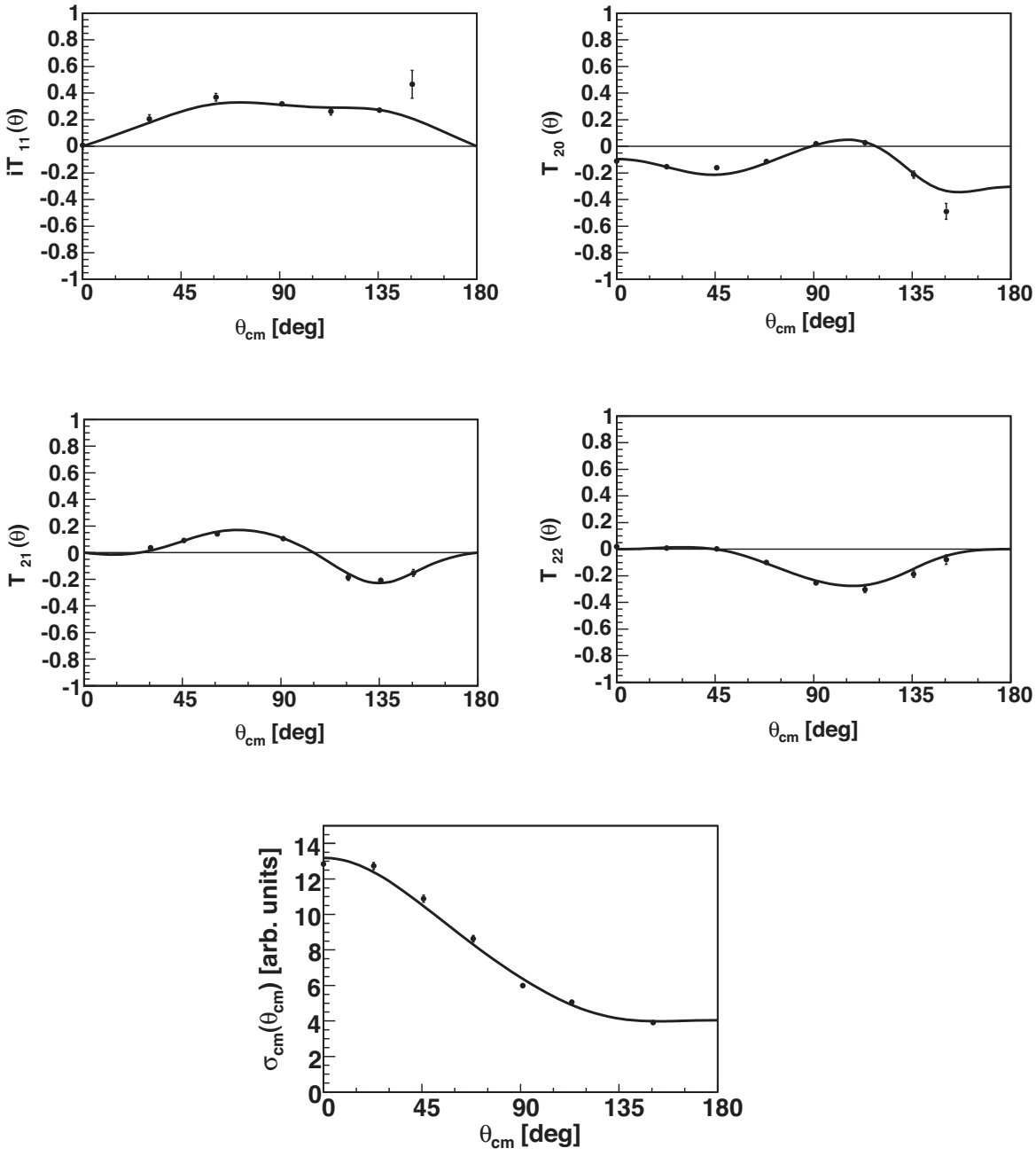

Figure 5.8: TME fits to the ^{7}Li$(\vec{\mathrm{d}}, \mathrm{n}_0)^{8}$Be data at $\mathrm{E_d}$= 160 keV. The errors bars represent the statistical and systematic uncertainties.

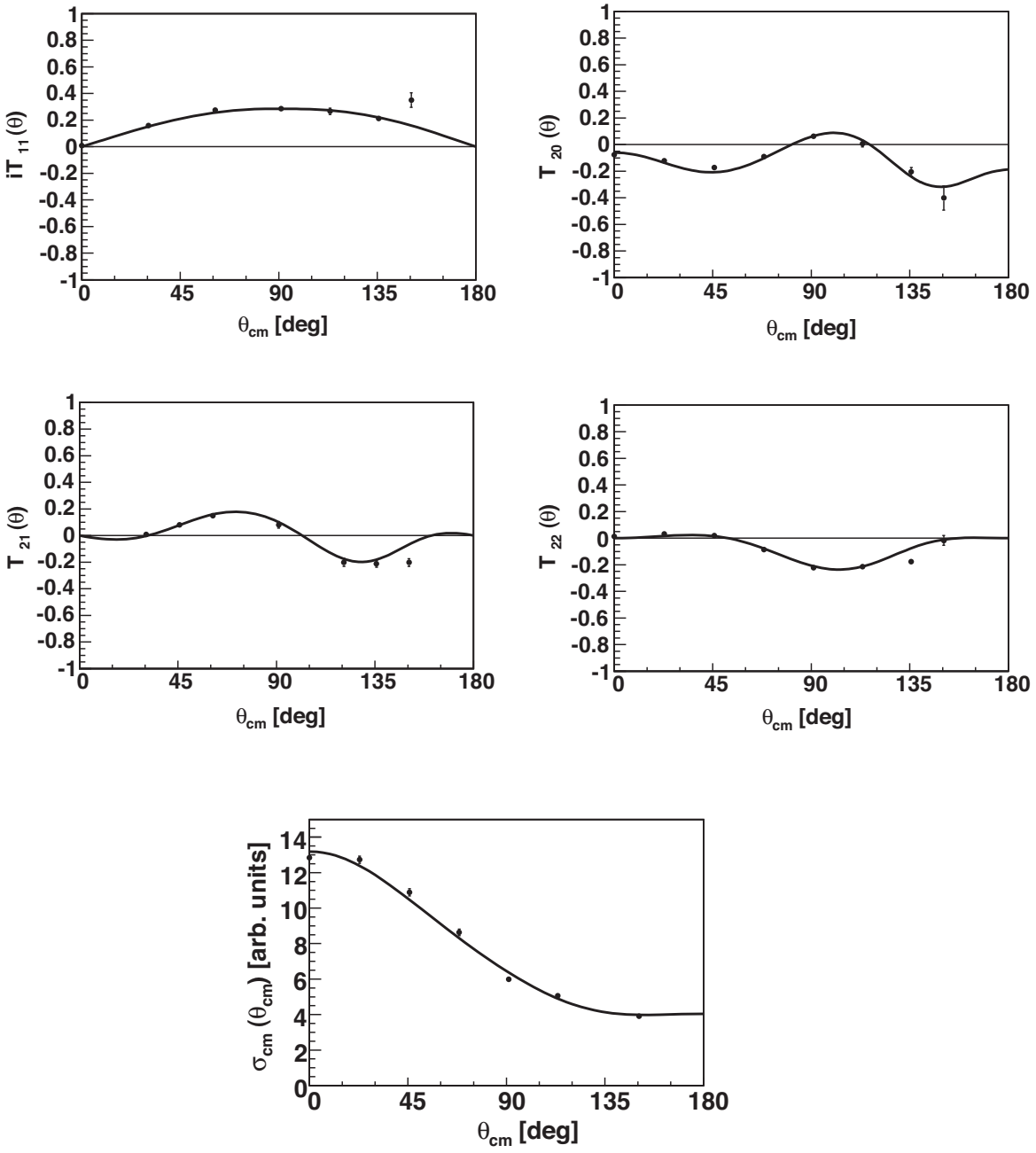

Figure 5.9: TME fits to the $^{7}\mathrm{Li}(\vec{\mathrm{d}},\mathrm{n}_0)^{8}\mathrm{Be}$ data at $\mathrm{E_d}$= 130 keV. The errors bars represent the statistical and systematic uncertainties.

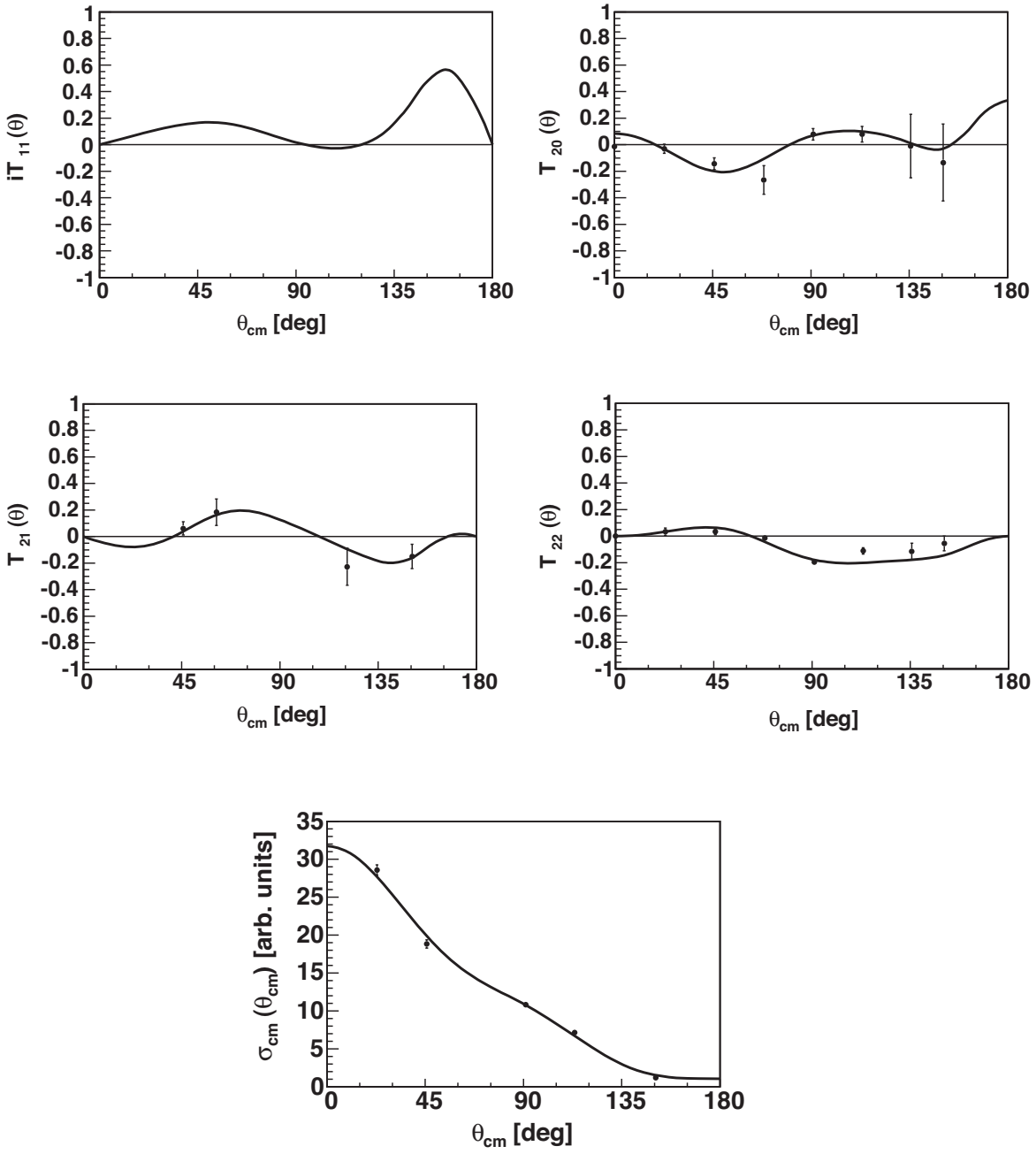

Figure 5.10: TME fits to the ^{7}Li$(\vec{\mathrm{d}}, \mathrm{n}_0)^{8}$Be data at $\mathrm{E_d}$= 80 keV. The errors bars represent the statistical and systematic uncertainties.

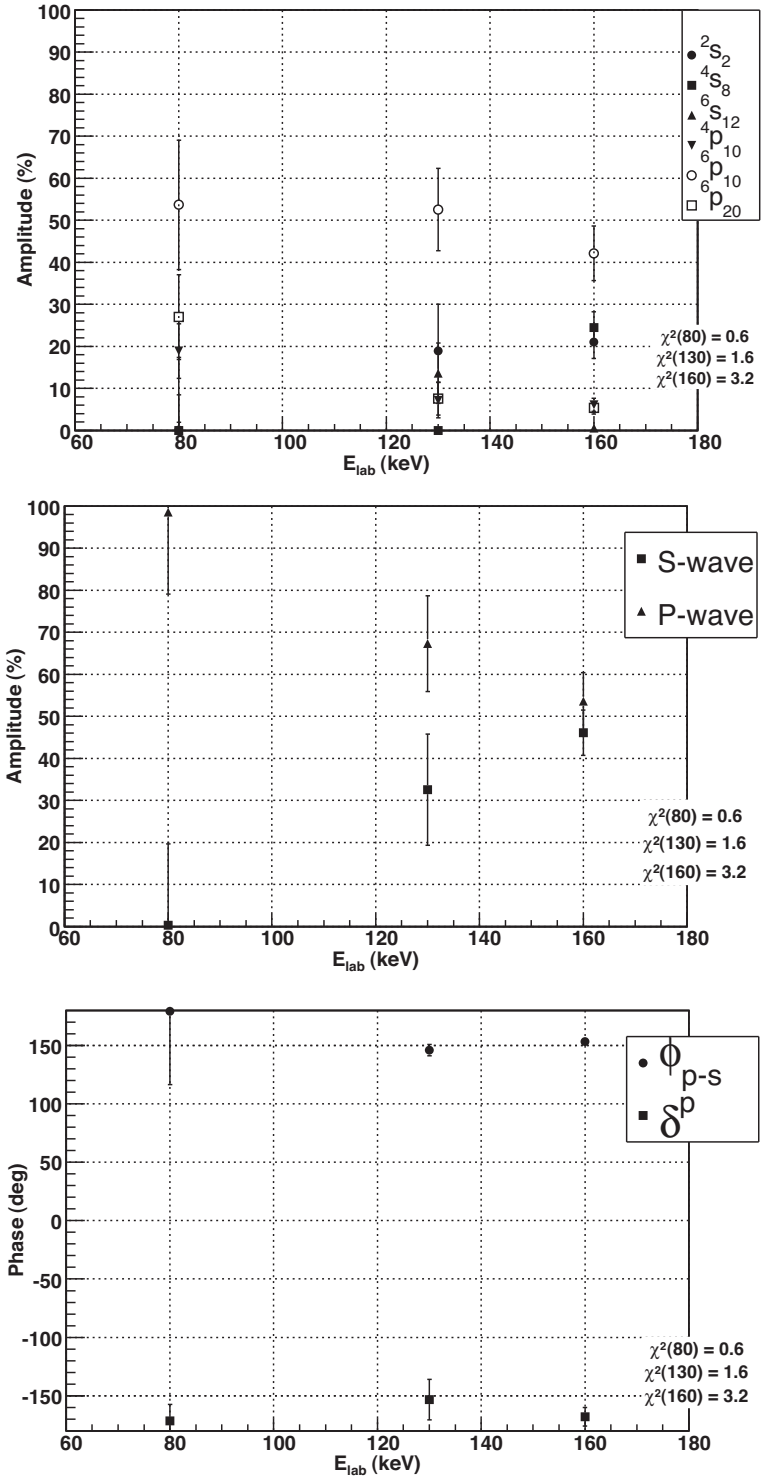

Figure 5.11: TME fit results to the $^{7}\mathrm{Li}(\vec{\mathrm{d}},\mathrm{n}_1)^{8}\mathrm{Be}$ data. The error bars are those generated by the fit.

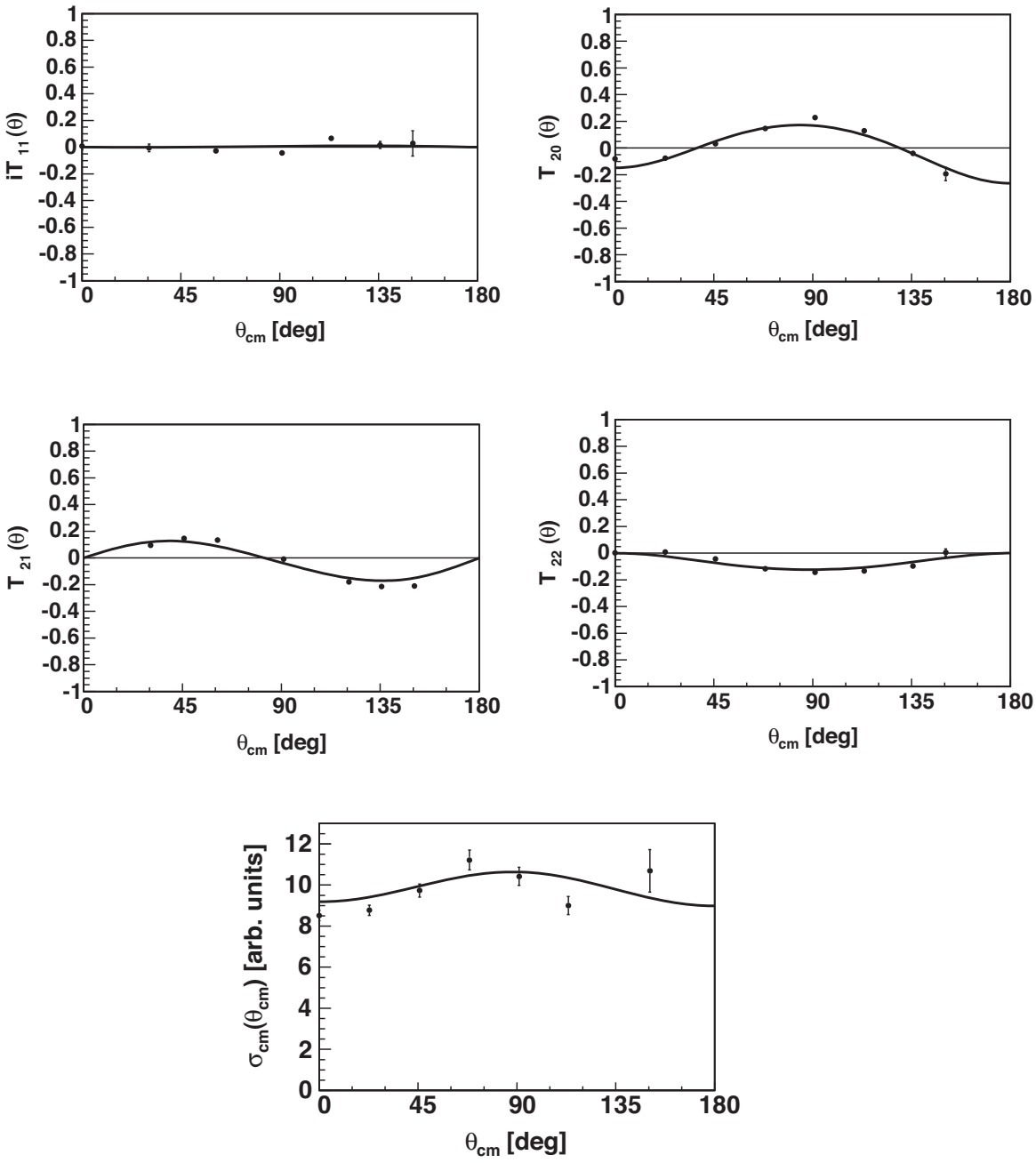

Figure 5.12: TME fits to the $^{7}\mathrm{Li}(\vec{\mathrm{d}},\mathrm{n}_1)^{8}\mathrm{Be}$ data at $\mathrm{E_d}$= 160 keV. The errors bars represent the statistical and systematic uncertainties.

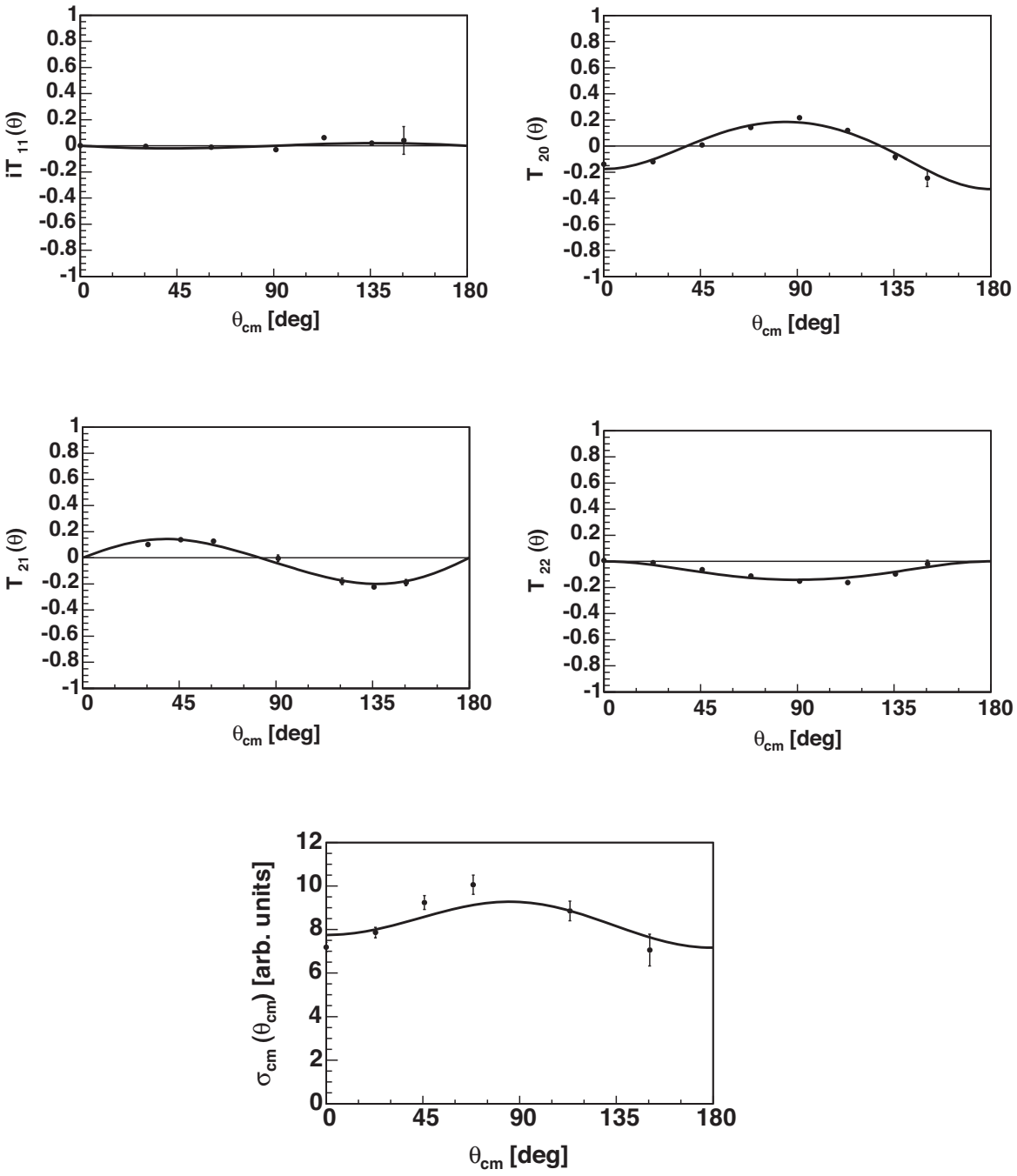

Figure 5.13: TME fits to the $^{7}\mathrm{Li}(\vec{\mathrm{d}},\mathrm{n}_1)^{8}\mathrm{Be}$ data at $\mathrm{E_d}$= 130 keV. The errors bars represent the statistical and systematic uncertainties.

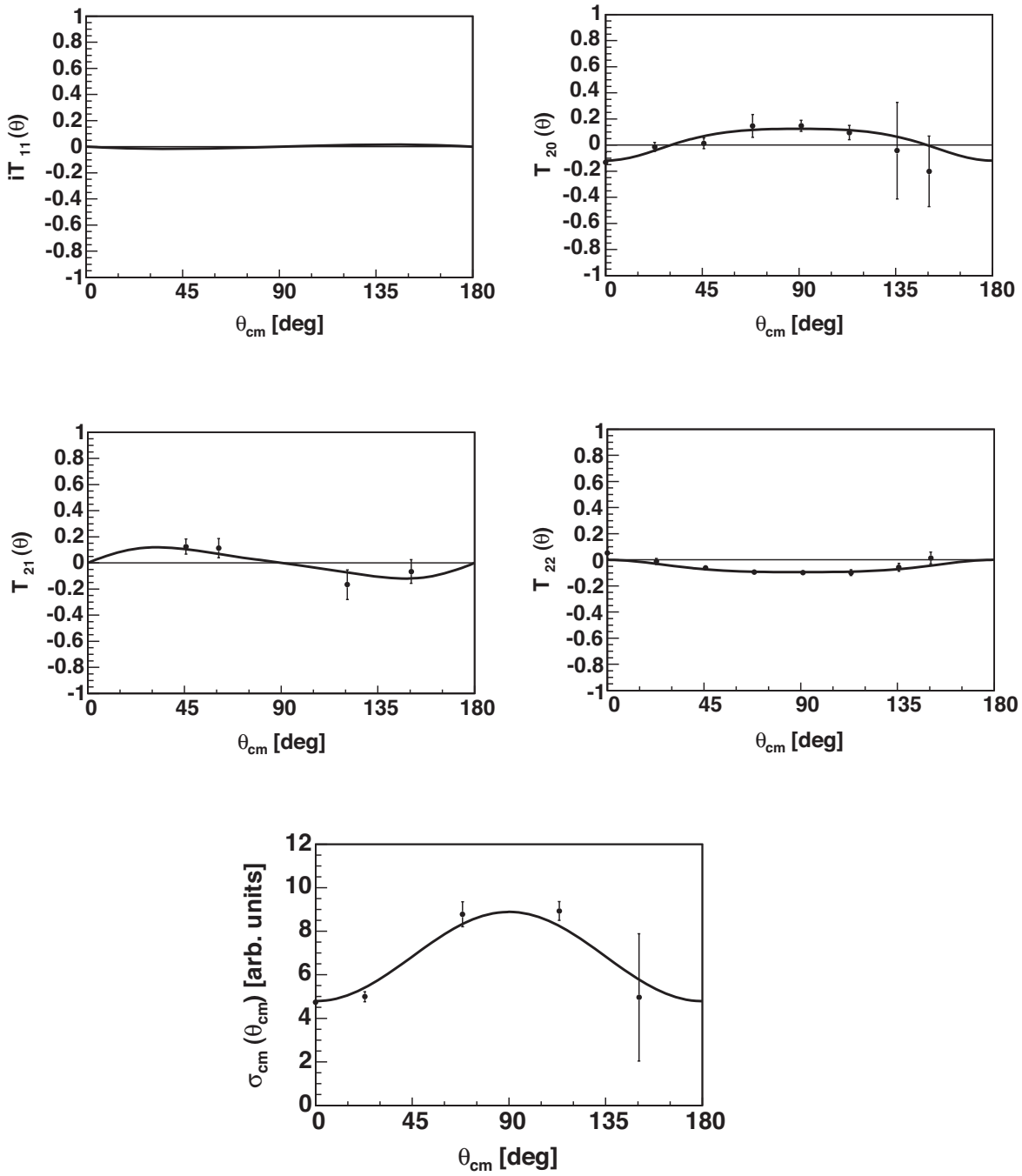

Figure 5.14: TME fits to the $^{7}\mathrm{Li}(\vec{\mathrm{d}},\mathrm{n}_1)^{8}\mathrm{Be}$ data at $\mathrm{E_d}$= 80 keV. The errors bars represent the statistical and systematic uncertainties.

	E_d = 160 keV	E_d = 130 keV	E_d = 80 keV
TME	Strength (%)		
$^2s_2$	21±4	18±11	0.2±2
$^4s_8$	24±4	0.01±0.3	0.02±17
$^6s_{12}$	0.6±0.3	14±7	0.2±8
$^4p_{10}$	6±2	7±4	18±6
$^6p_{10}$	42±6	52±10	54±15
$^6p_{20}$	5±1	8±4	27±10
	Phase (°)		
ϕ_{p-s}	153±3	146±5	179±63
δ^p	-168±8	-153±17	-171±14
χ^2_ν	3.2	1.6	0.6

Table 5.7: Results of the TME fits to the $^7\mathrm{Li}(\vec{\mathrm{d}}, \mathrm{n}_1)^8\mathrm{Be}$ data.

Chapter 6

S Factor and Cross Section

The primordial abundance of ^{7}Li is one of the more important diagnostics of the degree of baryon inhomogeneity in early universe models [Boy93]. The ^{7}Li yield is determined from a balance between production and destruction reactions. An accurate knowledge of both types of reactions is necessary for cosmological model calculations to be reliable. For one set of destruction reactions, the ^{7}Li+d reactions, recent primordial nucleosynthesis codes have incorporated resonant terms at 280 keV and 600 keV in addition to the direct term [Boy93]. These reaction rates were calculated for the Big Bang Nucleosynthesis temperature region $T = 0.12 \times 10^9$ to 10^{10} K, corresponding to an energy region of $E_{c.m.}$= 10 to 900 keV, using measured astrophysical S factors. However, the direct term for energies below the 280-keV resonance was *assumed* to have zero slope on the basis of (d,n) and (d,p) data taken between 1.6 to 2.0 MeV [Ser04, Boy93, Sla57].

The cross section for the (d,n) channel, which is dominant over the (d,p) channel, has been studied below a center-of-mass (c.m.) energy of 280 keV [Hof01, Bag52]

and has been measured at c.m. energies down to 50 keV [Hof01]. The S factor was experimentally determined at effective c.m. energies of 50 keV, 83.5 keV, and 100 keV [Hof01] which indicated that the slope of the S factor is non-zero and negative.

The present measurements were undertaken to determine the slope and absolute value of the S factor and the absolute cross section for the $^{7}\mathrm{Li}(\mathrm{d},\mathrm{n})^{8}\mathrm{Be}$ reaction at c.m. energies below 70 keV for the n_0 transition to the 0^+ ground state of ^{8}Be and for the n_1 transition to the 2^+ first excited state. An investigation of the n_2 transition to the 4^+ second excited state was also undertaken, but the spectrum in this region was too complicated to extract reliable results. The present results indicate that the S factor for the n_0 transition has a slope consistent with zero, whereas the S factor for the n_1 transition has a small negative slope at c.m. energies below 70 keV which can be attributed to electron screening effects. The bare nucleus results are in agreement with the zero-slope S-factor assumption of [Boy93]. The present results have been published; that paper is presented in full in Appendix D.

6.1 Experimental Details and Data Analysis Issues

For these measurements, the ABPIS produced unpolarized deuteron beams at energies $\mathrm{E_d}$ = 45 keV, 60 keV, and 80 keV. Beam currents averaged about 40 μA. Data sets at 80 keV and 60 keV were taken at the beginning and end of the week-long run with the 45-keV set taken in the middle.

As illustrated in Section 3.3, the raw neutron spectrum for each angle was fitted with a combination of the measured the n_0, n_1, n_2, and $^{2}\mathrm{H}(\mathrm{d},\mathrm{n})^{3}\mathrm{He}$ response functions. To obtain the raw n_0 yields, the n_1, n_2, and $^{2}\mathrm{H}(\mathrm{d},\mathrm{n})^{3}\mathrm{He}$ functions were subtracted from the spectrum; a similar procedure was performed to obtain the n_1 and n_2 yields.

Then, in each case, the remaining spectrum was summed from approximately 2 MeV to 14 MeV. Because the entire spectral region was not summed, a correction factor was obtained to determine the absolute cross section by dividing the number of counts in the corresponding summation region of the response spectrum by the entire number of counts in the response spectrum. For the n_0 and n_1 states this ratio was generally on the order of 60%. However, for the n_2 state this ratio was 10% on average. More of the spectrum could not be used due to the efficiency of the detectors changing rapidly below 3 MeV. The small percentage of the spectrum that was usable and disentanglement issues with the neutrons from the $^2H(d,n)^3He$ reaction made the n_2 data extraction difficult and unreliable.

In addition, each raw neutron spectrum was ultimately fitted at each angle with just a combination of the measured n_0 and n_1 response functions in the region between approximately 6 MeV and 14 MeV, where the n_2 and $^2H(d,n)^3He$ states should have little effect on the data. These yield results agreed with the yield results from the full fits as described above. For these cases, the ratio of the number of counts in the summed region to those of the entire spectrum was generally 30-50%.

The angular distributions of the yield at each energy for each state were fitted with a Legendre polynomial, as described in Section 5.1, so that the total yield at each energy could be found according to Equation 5.4. The angular distributions of the yields with their Legendre polynomial fits are shown in Figure 6.1 and Figure 6.2. The data are given in Table A.11 and Table A.12 in Appendix A for the n_0 and n_1 states respectively. The values of the coefficients of the Legendre polynomials fits are given in Table B.5 and Table B.6 in Appendix B. The total integrated yields are given in Table 6.1.

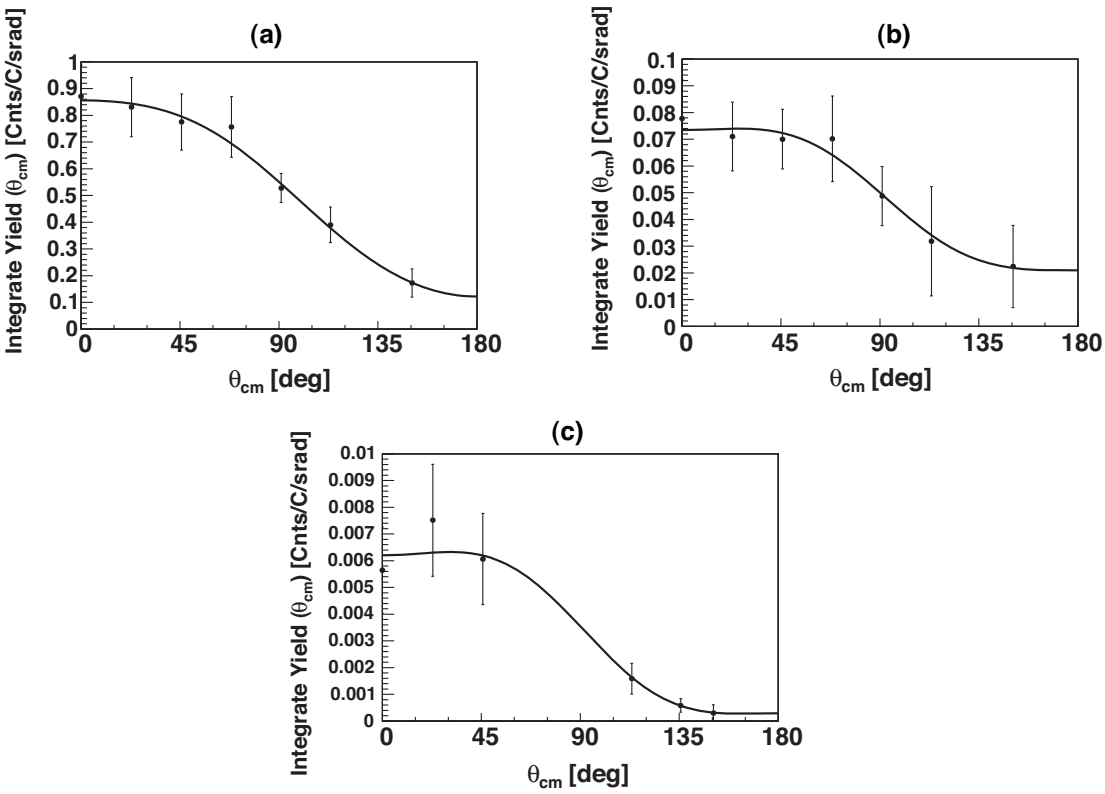

Figure 6.1: The measured integrated yields for the S-factor data at (a) E_d= 80 keV, (b) E_d= 60 keV, and (c) E_d= 45 keV for the ^{7}Li(d, n_0)^{8}Be reaction. The data points are given in Table A.11. The error bars represent the statistical and systematic errors as discussed in Section 4.2. The solid line is a Legendre polynomial fit to the data points; the coefficients for the fits are given in Table B.5.

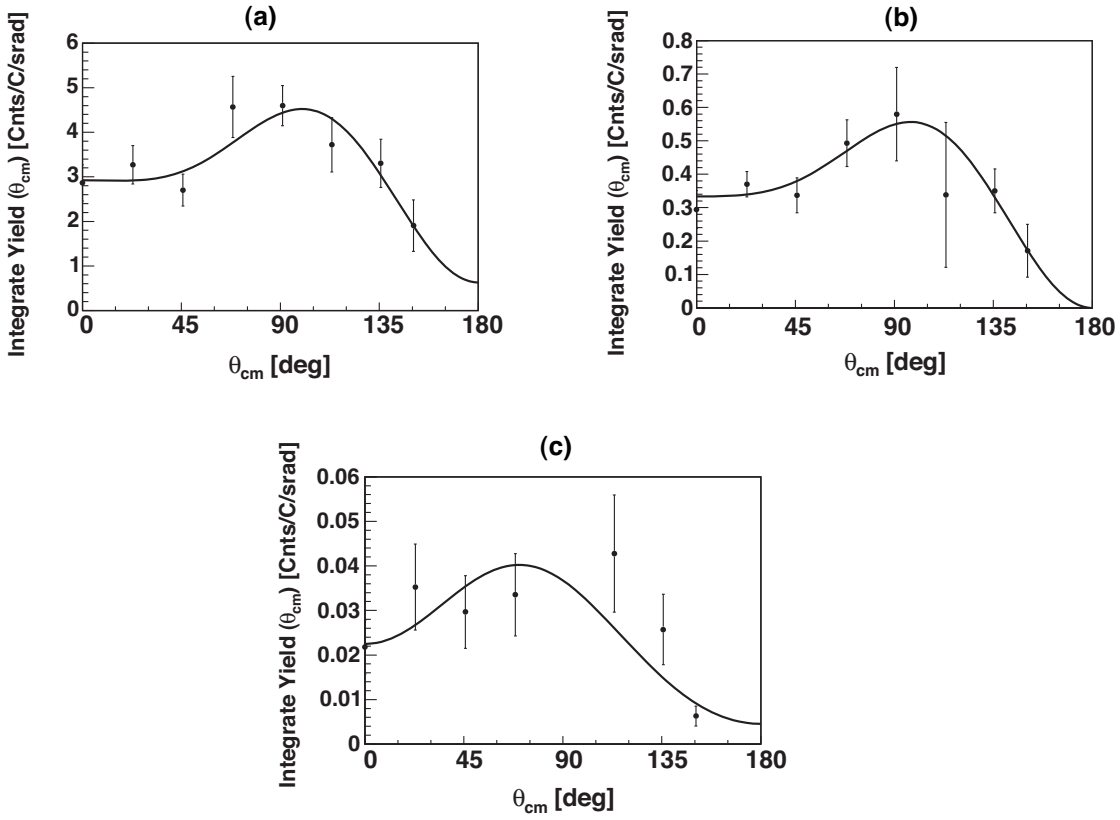

Figure 6.2: The measured integrated yields for the S-factor data at (a) E_d= 80 keV, (b) E_d= 60 keV, and (c) E_d= 45 keV for the ^{7}Li(d, n_1)^{8}Be reaction. The data points are given in Table A.12. The error bars represent the statistical and systematic errors as discussed in Section 4.2. The solid line is a Legendre polynomial fit to the data points; the coefficients for the fits are given in Table B.6.

	n_0 (Counts/C)	n_1 (Counts/C)
$Y(80)$	6.607 ± 1.122	44.48 ± 7.552
$Y(60)$	0.6119 ± 0.2157	5.297 ± 1.460
$Y(45)$	0.04272 ± 0.01741	0.3513 ± 0.1135

Table 6.1: Total integrated yields at incident beam energies of E_d= 80 keV, 60 keV, and 45 keV for the ^{7}Li(d, n)^{8}Be reaction.

6.1.1 Thick Target Analysis

Because the target is thick enough to stop the deuteron beam, the yield that is measured is not simply at one energy but rather over a range of energies. As the beam penetrates the target a distance dx, the change in energy can be calculated using known stopping powers, such that $dE = \frac{dE}{dx}dx = -STP(E)dx$, where $STP(E) = -\frac{dE}{dx}(E)$ is the stopping power for the projectile in the target. Therefore, for every slice of target dx, the cross section $\sigma(E)$ is determined. When the target is thick enough to stop the beam completely, the observed yield is the total yield from the beam energy to 0 and can be written as:

$$Y(E_d) = C \int_{E_d}^{0} \frac{\sigma(E) f}{STP(E)} dE, \tag{6.1}$$

where E_d is the deuteron beam energy, $\sigma(E)$ is the energy-dependent cross section, f is the atomic fraction of the target, and $STP(E)$ is the stopping power of the target for deuterons. The constant C is the total number of incident deuterons times the detector solid angle and efficiency. The raw yield for each angle was normalized by this constant.

The stopping powers are parametrized for different projectile energies. Below 10 keV,

$$STP(E) = A_0\sqrt{E}. \tag{6.2}$$

In the region between 10 keV and 1 MeV,

$$\begin{aligned} S_{low}(E) &= A_1 E^{0.45}, \\ S_{high}(E) &= \frac{A_2}{E} \log\left(1.0 + \frac{A_3}{E} + A_4 E\right), \\ \text{and} \quad STP(E) &= \left(\frac{1}{S_{low}} + \frac{1}{S_{high}}\right)^{-1}. \end{aligned} \tag{6.3}$$

The element-specific coefficients A_i are given in [And77] for an incident hydrogen beam. Conversion to a deuteron beam requires that the energy E in the calculations is one-half the value for hydrogen.

When the target is composed of a mixture of elements, as is the case for deuterons on a $^7Li_2O$ target, the stopping power calculations should take into account the relative weights of the components:

$$STP(E)_{total} = \sum_i w_i STP(E)_i, \tag{6.4}$$

where w_i is the relative weight of the individual component and $STP(E)_i$ is the stopping power for that element. The coefficients A_i for oxygen and ^{7}Li are given in Table 6.2.

A_i	Oxygen	^{7}Li
A_0	2.652	1.411
A_1	3.0	1.6
A_2	1920.0	725.6
A_3	2000.0	3013.0
A_4	0.0223	0.04578

Table 6.2: Coefficients for the stopping power of hydrogen in oxygen and in ^{7}Li.

6.2 Astrophysical S Factor

The importance of the S factor was described in detail in Section 1.2.2. There, in Equation 1.2, the nonresonant cross section was written in terms of the S factor. At the low energies of this experiment, the S factor can be assumed to be linear with energy:

$$S\left(E_{c.m.}\right) = S_0 + S_1 E_{c.m.}. \tag{6.5}$$

The yield in Equation 6.1 can then be calculated for a given beam energy from the values of S_0 and S_1 with the help of Equation 1.2.

6.2.1 Yield Ratios

As a preliminary evaluation of our data, the ratios of the experimental yields at each energy were compared to the ratios predicted given a constant S factor, i.e. $S_1 = 0$ in Equation 6.5. This comparison is shown in Table 6.3 and indicates that the slope of the S factor is consistent with zero for the n_0 case but not for the n_1 case.

	Theoretical	Experimental	
	constant S(E)	n_0	n_1
$Y(80)/Y(60)$	10	11 ± 1.5	8.4 ± 0.91
$Y(60)/Y(45)$	15	14 ± 3.9	15 ± 2.6

Table 6.3: Comparison of the n_0 and n_1 neutron yield ratios to a theoretical calculation assuming $S(E)$ is constant. $Y(80)$, $Y(60)$, and $Y(45)$ are the experimental yields at a beam energy of 80 keV, 60 keV, and 45 keV, respectively.

6.2.2 Determining S_0 and S_1

To determine the slope, the integral in Equation 6.1 was evaluated numerically, and the three measured yields were fitted simultaneously. In this calculation, the target was divided into 1-μg/cm^2 layers corresponding to less than 1-keV energy loss in the target material. The stopping power of the target was calculated using Anderson and Ziegler's energy loss equations [And77] as described in Section 6.1.1. Using Equation 6.5 as the form of $S(E)$ and starting with arbitrary values for S_0 and S_1, the yield and energy loss for the first layer was calculated. The yield calculation was then repeated for the next layer at the decreased energy. This process was repeated until the yield of a subsequent layer was less than 0.1% of the yield in the first layer. The sum of the yields from all layers of the target equaled the total yield at the beam energy. This process was performed at all three beam energies and repeated iteratively, continuously adjusting the values of S_0 and S_1, until the best fit to the measured yields was obtained.

The errors in S_0 and S_1 arise from the statistical uncertainties associated with the experimental yields and the systematic errors from the response function fits to the spectra, from the S-factor fits to the three yields, and from the parameters necessary to determine the absolute scale. These errors are broken down into their components in Table 6.4. The errors were added in quadrature to get the final errors in the S_0 and S_1 parameters.

The constant C in Equation 6.1 allows an absolute scale to be included in the yield calculation and thus in the S-factor and cross-section determination. This scale factor was folded into the S-factor result, giving it units of keV b. Using the results of the S factor derived from the yields, the absolute cross section for each energy was

Source of Error	n_0	n_1
Statistical	15%	15%
Systematic		
Response Function Fits	23%	16%
BCI	1%	1%
Solid Angle	2%	2%
Detector Efficiency	3%	3%
S-Factor Fits:		
S_0	5%	20%
S_1	–	51%
Total Errors:		
S_0	28%	30%
S_1	–	57%

Table 6.4: Statistical and systematic uncertainties contributing to the final S-factor results for the ^{7}Li(d, n)^{8}Be reaction. As noted in Section 6.3, a constant S factor was found to best represent the n_0 state, and thus no error is listed for the S_1 parameter.

then determined.

6.3 Experimental Results and Discussion

The measured yields as a function of beam energy for the ground-state and first-excited-state transitions are shown in Figure 6.3. The error bars represent the statistical errors from the raw yields and the systematic errors from fitting the response functions to the spectra. The two curves shown in each plot are the best fits to the experimental results assuming the S factor is constant with energy (dotted line) or varies linearly (non-zero slope, solid line). The numerical results and the corresponding χ^2 values are given in Table 6.5. As seen in Figure 6.3 and the χ^2 values in Table 6.5, the linear fit is much better than the constant fit for the n_1 transition, but the addition of a non-zero slope in the n_0 case changes little. Therefore, for the n_0 case,

the data are consistent with a slope of zero to an accuracy of $S_1/S_0 = 0.002 \pm 0.008$.

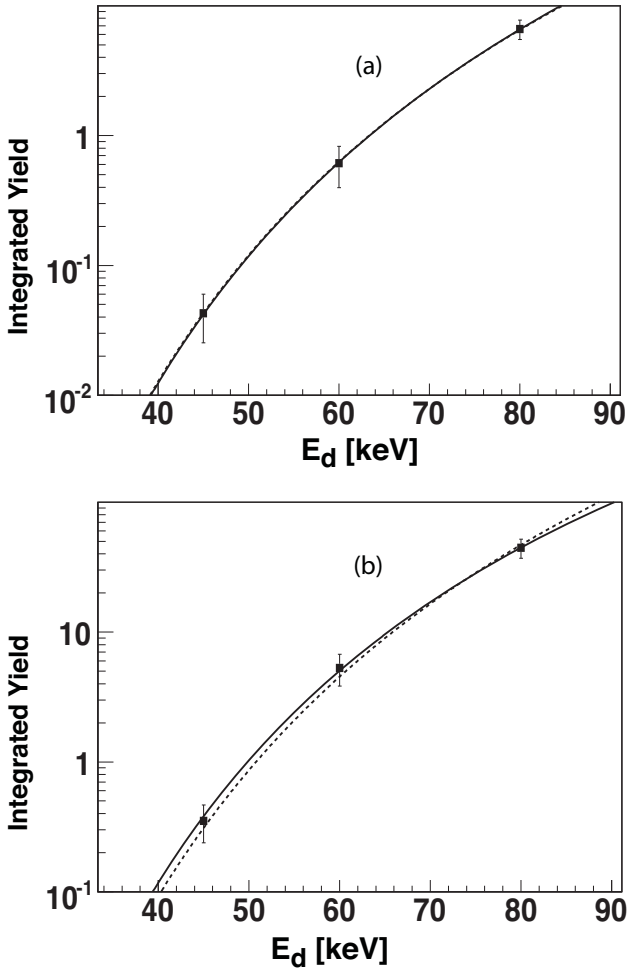

Figure 6.3: Measured energy-integrated yields for (a) ^{7}Li(d, n_0)^{8}Be and (b) ^{7}Li(d, n_1)^{8}Be plotted at the incident beam energy. The error bars include statistical and systematic uncertainties. The solid lines were obtained by assuming an S factor that varies linearly with deuteron energy; the dashed lines were obtained by assuming a constant S factor (zero slope).

For the n_1 transitions, this negative, nonzero slope makes a significant difference in the $S(0)$ value, as is shown in Figure 6.4. The $S(0)$ value for the linear $S(E)$ is a factor of 1.6 greater than that for a constant $S(E)$ for the n_1 neutron group.

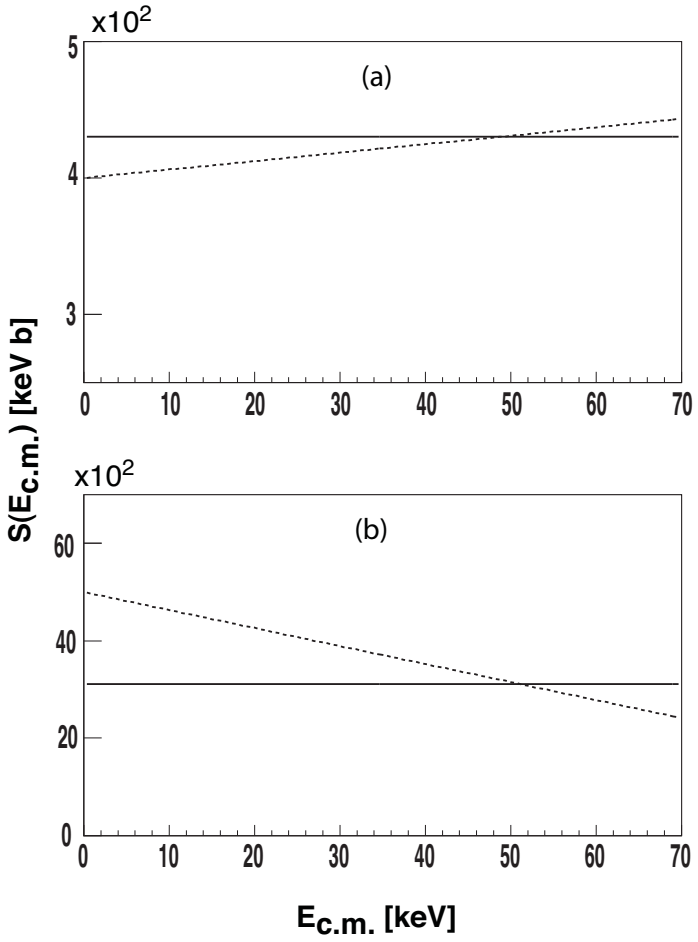

Figure 6.4: Comparison of the constant $S(E)$ result (solid line) and the linear, non-zero-slope $S(E)$ result (dotted line) for the (a) n_0 and (b) n_1 groups. In the n_1 case, the slope of the S factor makes a significant difference in the value of $S(0)$. The errors on the non-zero-slope value for n_0 make that result indistinguishable from the constant slope result.

state	$S(E) = S_0 + S_1 E$ [keV b]	χ^2/ν
n_0	$S(E) = 430(\pm 120)$	0.032
	$S(E) = 400(\pm 200) + 0.62(\pm 3.3)E$	0.030
n_1	$S(E) = 3100(\pm 750)$	2.2
	$S(E) = 5000(\pm 1500) - 37(\pm 21)E$	0.62

Table 6.5: Numerical values for the constant and linear $S(E)$ fits to the experimental yields along with the χ^2 per degree of freedom ν values obtained from the fits.

6.3.1 Electron Screening Effects

As shown in Equation 1.2, the cross section can be separated into its geometrical, nuclear, and Coulomb barrier components. This separation assumes that the Coulomb barrier is that resulting from bare nuclei, i.e. projectile and target nuclei with no electron clouds present. In the laboratory setting, however, especially at low energies, this ceases to be a valid assumption, as the electrons can screen the Coloumb repulsion between the bare nuclei, invalidate the energy dependence expected with a constant $S(E)$, and significantly raise the measured cross section over that due to bare nuclei [Ali00, Sho93].

The classical turning radius for a head-on collision is $r_t = Z_1 Z_2 e^2/E$ and, even for very low energy cross sections, is well inside the electron cloud of the target. In the simplest sense, electron screening provides a constant additional energy U_e to the center-of-mass energy of the colliding nuclei [Sho93]. U_e is the electron screening potential energy, which is the difference in the electron binding energies of the atoms in the entrance channel and of the composite atom in the adiabatic limit [Ass87]. Using the expression for the cross section in terms of the S factor in Equation 1.2 with the energy-dependence of the Sommerfeld parameter $\eta(E)$ explicitly written out, the cross section enhancement is then [Sho93]:

$$
\begin{aligned}
f_{lab}(E) &\equiv \frac{\sigma(E+U_e)}{\sigma(E)} \\
&= \frac{S(E+U_e)}{S(E)} \frac{E}{E+U_e} \frac{\exp\left[-2\pi\eta(E+U_e)\right]}{\exp\left[-2\pi\eta(E)\right]}.
\end{aligned}
\tag{6.6}
$$

When $U_e \ll E$, the parameter $2\pi\eta(E+U_e)$ given by Equation 1.4 becomes

$$
\begin{aligned}
2\pi\eta(E+U_e) &= 31.29 Z_1 Z_2 \sqrt{\frac{\mu}{E+U_e}} \\
&\approx 31.29 Z_1 Z_2 \sqrt{\frac{\mu}{E}} \left(1 - \frac{1}{2}\frac{U_e}{E}\right).
\end{aligned}
\tag{6.7}
$$

If S is also essentially energy independent, this approximation makes Equation 6.6 [Ali00]

$$
f_{lab}(E) = \frac{E}{E+U_e} \exp\left(\pi\eta(E)\frac{U_e}{E}\right). \tag{6.8}
$$

The bare-nucleus S factor for the ^{7}Li(p, α)^{8}Be reaction was extracted using the Trojan Horse Method by Lattuada, *et al.* [Lat01]. The Trojan Horse Method extracts the cross section of an astrophyically relevant two-body reaction such as ^{7}Li+$p \rightarrow \alpha+\alpha$ at low energies from a suitably chosen three-body reaction, ^{7}Li+$d \rightarrow \alpha+\alpha+n$. This method overcomes experimental difficulties of using extremely low energy protons, for example, by substituting them with higher energy deuterons. The proton, carried in by the deuteron, is now "transferred" to the ^{7}Li inside the Coulomb field generated by the electrons. By using this method, Lattuada, *et al.*, determined the value for the electron-screening potential $U_e = 330 \pm 40$ eV for protons incident on ^{7}Li.

Electron screening effects are expected to be negligible at energies $E/U_e \geq 100$ [Lat01]. For the U_e for protons on ^{7}Li given above, screening effects are not expected to be noticeable for c.m. energies $E_{c.m.}$ above 33 keV. However, if this is applied to a deuteron on ^{7}Li, electron screening effects become an issue for $E_{c.m.} < 66$ keV. This means that for the data taken at $E_d = 60$ keV and 45 keV, electron screening effects

need to be considered. In addition, as discussed in Section 6.1.1, the thick ^{7}Li target slows the incident deuterons from beam energy to zero. However, the cross section decreases exponentially with decreasing deuteron energy, so most of the yield will occur for the initial higher energies in the target. For the deuteron beams used in these experiments, the lab energy at which 50% of the yield is produced E_{50} and that at which 90% of the yield is produced E_{90} are given in Table 6.6.

E_d (keV)	E_{50} (keV)	E_{90} (keV)	$S_1'(E_{50})$ (keV^{-1})	$S_1'(E_{90})$ (keV^{-1})
45	43.0	36.6	-0.0046	-0.0071
60	55.3	46.4	-0.0024	-0.0038
80	72.7	59.3	-0.0012	-0.0020

Table 6.6: Laboratory values for the energies at which 50% of the yield is produced in the target (E_{50}) and at which 90% of the yield is produced (E_{90}) for a given incident beam energy E_d, as well as the values of the relative S-factor slope S_1' at E_{50} and at E_{90}.

From Equation 1.2, Equation 6.5, and Equation 6.8, it is possible to calculate the slope of the cross section ratio due to screening effects, which is also the slope of the S factor at a specific energy. The value of the relative slope $S_1' = S_1/\ S_0$ is given in Table 6.6 for E_{50} and E_{90}. In comparison, our measured negative relative slope of the (d, n_1) channel is $S_1' = -0.007 \pm 0.005$ keV^{-1}. It can be concluded that the negative slope we observe can be attributed to electron screening effects. Although the relative slope for the (d, n_0) channel is consistent with zero ($S_1' = 0.002 \pm 0.008$ keV^{-1}), the uncertainty also allows for a slope compatible with screening effects.

6.3.2 Comparison with Previous Results

Figure 6.5 shows the S-factor results of the present measurement along with previous results for ^{7}Li(d, n)^{8}Be. The solid line is the linear $S(E)$ result obtained from the analysis discussed above. The S factor for $n_0 + n_1$ is $S(E) = 5400(\pm 1500) - 37(\pm 21)E$ keV b. The negative value of the slope is consistent with the value expected from an estimate of the effects due to electron screening. We therefore recommend that this slope should not be included in determining the S factor at zero energy. The data points of [Hof01] and [Bag52] and the line representing the assumptions of [Boy93] are for all three neutron groups. Therefore, the present measurement can only act as a lower limit on these measurements. However, the small slope of the present result is in reasonable agreement with the zero-slope assumption of [Boy93]. Boyd *et al.* examined cross-section data measured by [Sla57] and found that values obtained for $S(E)$ from those data were fairly constant from 1.6 to 2.0 MeV. They then assumed this constant value for the S factor and extrapolated it down to zero energy . In order to compare the slope of the present data with that of [Hof01], their data points at $E_{c.m.} = 50$ and 83.5 keV were fitted to a line with slope equal to our slope of -37 b. The best fit resulted in a line equal to our line plus 75000 keV b, or $80000 - 37E$ keV b. This line is shown in Figure 6.5 as the dot-dashed line and indicates that the slope of the S factor at higher energies, as seen in the Hofstee *et al.* data, appears to be more negative than the slope of the present result. Note, however, that the present result does not include the n_2 neutron group.

Figure 6.6 shows the corresponding comparison of the total cross sections. The points representing these present measurements are plotted at the effective center of mass energy, i.e. the energy at which half the yield is deposited in the target, and are the results for $n_0 + n_1$; these results are given in Table 6.7. The present work lies

	$\sigma_{Total}(E_{c.m.,eff})[\mu\text{b}]$	
$E_{c.m.,eff}$ [keV]	n_0	n_1
33	0.017 ± 0.0047	0.15 ± 0.066
43	0.17 ± 0.047	1.3 ± 0.67
57	1.3 ± 0.39	9.1 ± 6.0

Table 6.7: Numerical values for the absolute cross section for n_0 and n_1 as computed from the S factors $S(E) = 430(\pm 120)$ keV b and $S(E) = 5000(\pm 1500) - 37(\pm 21)E$ keV b, respectively.

below the (d,n) cross section calculated from the S factor given by [Boy93], which is to be expected due to the absence of the n_2 group in the present results. Hofstee *et al.* measured the branching ratio of the $^7\text{Li}(\text{d},\text{n})^8\text{Be} \rightarrow 2\alpha$ yields with respect to the yield of the ^{6}Li(d, p_0+p_1) reaction and noted that contributions from ^{6}Li reactions complicated the spectra [Hof01].

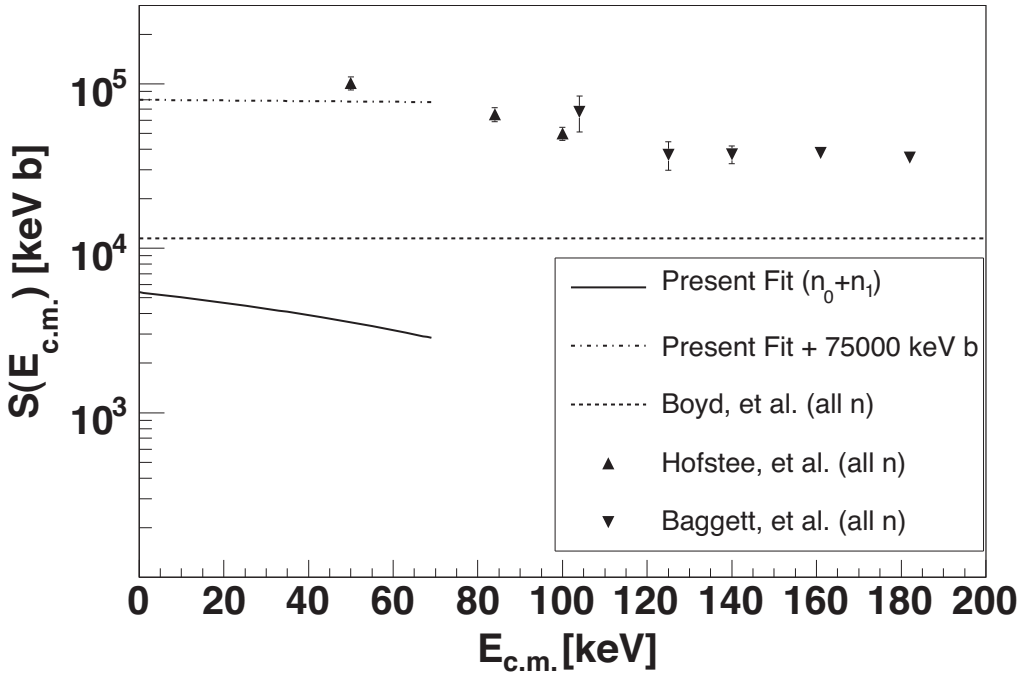

Figure 6.5: Results of the present measurement (solid line) along with the previous data of [Boy93], [Hof01], and [Bag52]. The line assumed by [Boy93] is based on data from [Sla57]. The points for [Bag52] were computed by assuming their differential cross section data at 90° was isotropic, multiplying it by 4π to get the total cross section, and finally using the total cross section to deduce the S factor. It should be noted that the data for [Boy93], [Hof01], and [Bag52] include all neutron groups whereas the present result is for the n_0 and n_1 groups only. The dot-dashed line is the present result + 75000 keV b, resulting from the best fit of a line with slope equal to the present slope of -37 b to the two lower energy points of [Hof01].

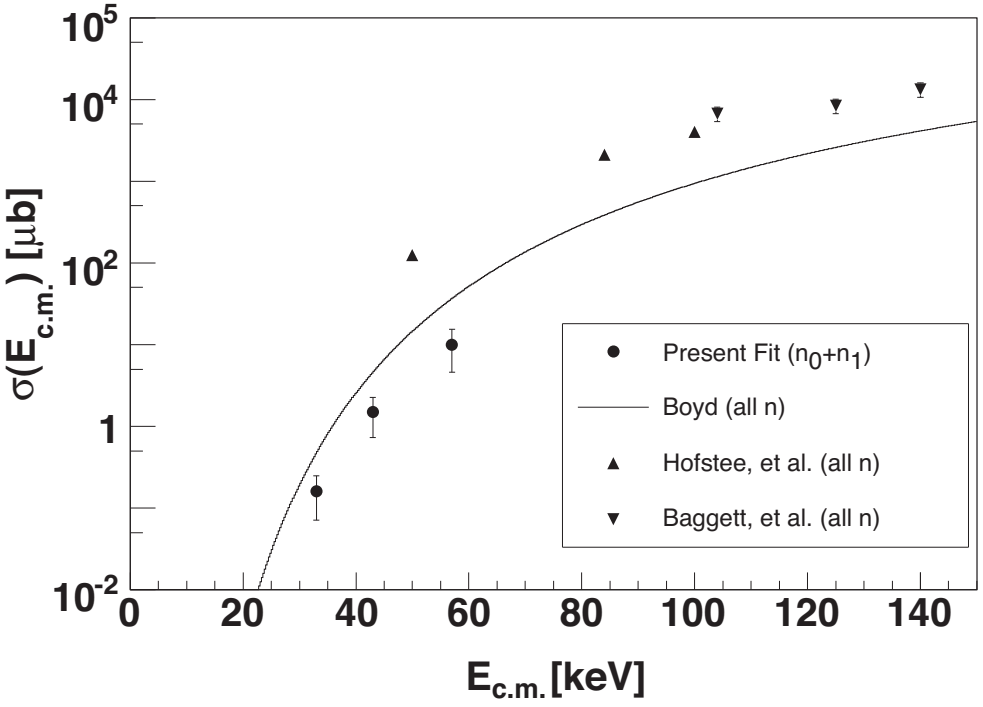

Figure 6.6: Results of the present measurement (circular points) along with the previous data of [Boy93], [Hof01], and [Bag52]. The points for [Bag52] were computed by assuming their differential cross section data at 90° was isotropic and then multiplying it by 4π to get the total cross section. The line representing [Boy93] was obtained by using the S-factor result they presented to compute the cross section. It should be noted that the data for [Boy93], [Hof01], and [Bag52] include all neutron groups whereas the present result is for the n_0 and n_1 groups only.

Chapter 7

Comparison of Experimental Results with Theory

Previous low-energy studies at 450 keV [Gal84] have compared the experimental data to the results of a Distorted-Wave Born Approximation (DWBA) calculation which assumes the reaction mechanism is a direct stripping reaction. The elementary picture of a direct reaction is one in which the proton is "stripped" from the incoming deuteron, leaving the remaining neutron relatively undisturbed. Direct reactions are generally characterized by surface processes, involving a transition directly from the initial to final state without forming a compound state in the interim [Sat83].

This chapter will discuss two methods of calculating direct reactions: the DWBA method and the broader coupled reaction channels (CRC) method which uses a multistep direct reaction process. The predictions of these models will be compared with the experimental results given in Chapters 5 and 6.

7.1 Distorted Wave Born Approximation

Distorted-wave theories start with the concept that the most important event that occurs between two colliding nuclei is elastic scattering. Elastic scattering includes absorption or the removal of flux into many other reaction channels even if the sum total of the results in complete absorption of the incident flux to the nuclear interior. These many couplings to other channels can be represented on average by using a complex optical potential. In addition, it is assumed that the couplings to individual reaction channels are weak and not strongly correlated with each other in any way [Sat83].

With these assumptions and within the limitations of simple optical models, an attempt is made to describe the elastic scattering exactly and treat other reactions as perturbations or transitions between elastic scattering states. For a reaction $A(a,b)B$ induced by an interaction V, the transition amplitude is [Sat83]

$$T_{DWBA} = \int \chi^{(-)}(\mathbf{k}_b, \mathbf{r}_b)^* (\psi_B \psi_b | V | \psi_A \psi_a) \chi^{(+)}(\mathbf{k}_a, \mathbf{r}_a) \mathrm{d}\mathbf{r}_a \mathrm{d}\mathbf{r}_b, \tag{7.1}$$

where $\mathbf{k}_a$ is the relative momentum, $\mathbf{r}_a$ is the separation of the centers of mass of nuclei a and A, and $\mathbf{k}_b$ and $\mathbf{r}_b$ are the corresponding quantities for the final channel $b + B$. The internal state of the ith nucleus is represented by ψ_i. The wave functions that describe the corresponding elastic scattering are the distorted waves $\chi(\mathbf{k}, \mathbf{r})$ and have the form [Sat83]

$$\chi(\mathbf{k}, \mathbf{r}) = \mathrm{e}^{i\mathbf{k}\cdot\mathbf{r}} + \psi_{scatt}. \tag{7.2}$$

The $(+)$ and $(-)$ superscripts on the distorted waves in Equation 7.1 represent the incoming and outgoing waves, respectively. The distorted waves are generated using optical potentials whose parameters have been adjusted to fit observed elastic scattering at an appropriate energy.

The nuclear matrix element $(\psi_B\psi_b|V|\psi_A\psi_a)$ contains all the nuclear structure information carried by this description of the reaction. When a zero-range form of the matrix element is used ($\mathbf{r}_b = \mathbf{r}_a$), as in the DWBA calculation code DWUCK4 described in Section 7.1.1, the matrix element can be written in the form of $(\psi_B\psi_b|V|\psi_A\psi_a) \propto \sum_{l,m} f_l(r)Y_l^m(\theta,\phi)$, where Y_l^m are the spherical harmonics and $f_l(r)$ are the radial form factors [Sat83]. Using this form, very general computer codes can be written to evaluate the distorted-wave amplitude in Equation 7.1 with a variety of options for the form factor. However, even after the nuclear matrix element is evaluated, it remains a function of the two channel coordinates $\mathbf{r}_b$ and $\mathbf{r}_a$, and evaluation of Equation 7.1 requires a six-dimensional integral [Sat83]. Partial wave expansions can transform this problem into sums of two-dimensional radial integrals, as is done in the code DWUCK4.

In the case of a stripping reaction, where $a = b + x$ and $B = A + x$, the quantity ψ_B can be rewritten as:

$$\psi_B = C^{J_A l J_B}_{m_A m m_B}\sqrt{S_{lj}}\psi_A\phi^l_m(\mathbf{r}_x), \tag{7.3}$$

where

$$C^{J_A l J_B}_{m_A m m_B} = C(J_A m_A l m|J_B m_B) \tag{7.4}$$

is the Clebsch-Gordan coefficient, S_{lj} is the spectroscopic factor, and $\phi^l_m(\mathbf{r}_x)$ is the single particle wave function for particle x. The transition amplitude is then

$$T_{DWBA} = \sqrt{S_{lj}}C^{J_A l J_B}_{m_A m m_B}B_{lm}. \tag{7.5}$$

For deuteron stripping ($a = d$, $b = n$, and $x = p$), the quantity B_{lm} is defined to be

$$B_{lm} = \int \mathrm{d}\mathbf{r}_n \mathrm{d}\mathbf{r}_p \chi^{(-)}(\mathbf{r}_p)\phi^l_m(\mathbf{r}_p)V_{np}(\mathbf{r}_{np})\phi_d(\mathbf{r}_{np})\chi^{(+)}(\mathbf{r}_d). \tag{7.6}$$

The deuteron wave function can be written as

$$\phi_d(r_{np}) = \frac{\mathrm{e}^{-\gamma r_{np}}}{r_{np}}\sqrt{\frac{\gamma}{2\pi}}, \tag{7.7}$$

where the binding energy $(\hbar^2\gamma^2)/(2m) = 2.2$ MeV. In the zero-range approximation,

$$V_{np}\phi_d = -(T-E)\phi_d = -\frac{\hbar^2}{2m_d}(\nabla^2-\gamma^2)\sqrt{\frac{\gamma}{2\pi}}\frac{\mathrm{e}^{-\gamma r_{np}}}{r_{np}} = -\frac{\hbar^2}{2m_d}\sqrt{\frac{\gamma}{2\pi}}\delta(\mathbf{r}_n-\mathbf{r}_p). \tag{7.8}$$

This makes

$$B_{lm} = \frac{\hbar^2}{2m_d}\sqrt{\frac{\gamma}{2\pi}}\int \mathrm{d}\mathbf{r}\chi^{(-)}(\mathbf{r})\phi_m^l(\mathbf{r})\chi^{(+)}(\mathbf{r}). \tag{7.9}$$

The differential cross section for the reaction then is

$$\begin{aligned}\frac{\mathrm{d}\sigma}{\mathrm{d}\Omega} &= \frac{m_{A+d}m_{B+n}}{(2\pi\hbar^2)^2}\,\frac{k_{B+n}}{k_{A+d}}\,|T|^2 \\ &= \frac{m_n m_d}{(2\pi\hbar^2)^2}\,\frac{k_n}{k_d}\,\frac{2J_B+1}{2J_A+1}\sum_m \frac{1}{(2l+1)}S_{lj}\,|B_{lm}|^2\,.\end{aligned} \tag{7.10}$$

7.1.1 DWUCK4

The FORTRAN code DWUCK4 [Kun] calculates the scattering and reaction observables for a binary nuclear reaction using DWBA and a zero-range interaction. The code is written for projectiles with any combination of spins 0, 1/2, or 1 and computes both the cross section and polarization observables.

The following input parameters are needed to do the calculations:

1. The optical model potential for a deuteron on ^{7}Li to generate the incoming distorted wave $\chi^{(+)}(\mathbf{k}_a, \mathbf{r}_a)$.

2. The optical model potential for a neutron on ^{8}Be to generate the outgoing distorted wave $\chi^{(-)}(\mathbf{k}_b, \mathbf{r}_b)$.

3. The binding energy, quantum numbers, and starting parameters of a Wood-Saxon potential (real and spin-orbit terms) for the final single particle state to generate the single-particle wave function $\phi_m^l(\mathbf{r})$.

Using the potentials described in [Gal84] as a starting point, the input parameters used to run DWUCK4 for the ^{7}Li$(\vec{\mathrm{d}}, \mathrm{n}_0)^8$Be reaction at $\mathrm{E_d} = 160$ keV, 130 keV, and 80 keV are given in Table 7.1 [Kun03]. The values in column four represent the optical model potential for a deuteron incident on ^{7}Li, and those in column five represent the potential for a neutron on ^{8}Be. The values in the sixth column are for the single particle state. The real potential depth value is the starting value which DWUCK4 then searches on to give the proper binding energy of the single particle state, i.e. the well-depth of the potential is varied to generate the correct ϕ_m^l; the value for the depth in parentheses is the best fit. In addition, the coulomb potential is included in all cases with the specified radius. The values used for the binding energy, the orbital angular momentum l, the total angular momentum J, and the number of nodes (excluding the origin and infinity) for the single particle state are also given in Table 7.1. The final well-depth value for the transferred proton could be larger than the starting value because the radius is small. These values were used because of the success Galloway, *et al.* obtained when fitting cross section data below 500 keV to DWBA calculations using these parameters.

The cross section σ_{DW}^{lsj} DWUCK4 outputs can be related to that in Equation 7.10 by

$$\frac{\mathrm{d}\sigma(\theta)}{\mathrm{d}\Omega} = \frac{2J_B+1}{2J_A+1}\,\frac{S_{lj}}{2j+1}\,\frac{D_0^2}{10^4}\,\sigma_{DW}^{lsj}(\theta), \tag{7.11}$$

where the parameter D_0^2 is the zero-range approximation of the overlap function. For deuterons, $D_0^2 \approx 1.5 \times 10^4$ MeV^2 fm^3 [Sat83].

Unfortunately, the results of the calculation did not represent the ^{7}Li($\vec{\mathrm{d}}$, n_0)^{8}Be experimental data, as can be seen in Figures 7.1, 7.2, and 7.3 for $\mathrm{E_d}$ = 160 keV, 130 keV, and 80 keV, respectively. Because the code so inadequately described the data, the ^{7}Li($\vec{\mathrm{d}}$, n_1)^{8}Be reaction was not run and a new method was sought to explain the data.

Potential			Incident d	Emitted n	Transferred p
Real					
Depth	V	(MeV)	140	46.3	55.0 (81.6)
Radius	r	(fm)	1.80	1.32	1.20
Diffuseness	a	(fm)	1.40	0.66	0.70
Volume imaginary					
Depth	W	(MeV)	30.0	0.75	
Radius	r_w	(fm)	0.84	1.26	
Diffuseness	a_w	(fm)	0.85	0.58	
Surface imaginary					
Depth	W_D	(MeV)	6.87	8.10	
Radius	r_D	(fm)	1.98	1.26	
Diffuseness	a_D	(fm)	0.59	0.48	
Spin-orbit					
Real depth	V_s	(MeV)	4.25	9.00	6.25
Radius	r_s	(fm)	1.00	1.01	1.20
Diffuseness	a_s	(fm)	0.94	0.75	0.70
Coulomb radius	R_c	(fm)	1.30	1.30	1.27
Binding Energy		(MeV)			17.254
Orbital ang. mom.	l				1
Total ang. mom.	J				3/2
Number of nodes					0

Table 7.1: Input parameters for the DWBA code DWUCK4 for the ^{7}Li($\vec{\mathrm{d}}$, n_0)^{8}Be reaction. The real potential well-depth value in the "Transferred p" column is the starting value. DWUCK4 searched on the starting value in order to obtain the proper binding energy of the single particle state; the value in parentheses is the best fit.

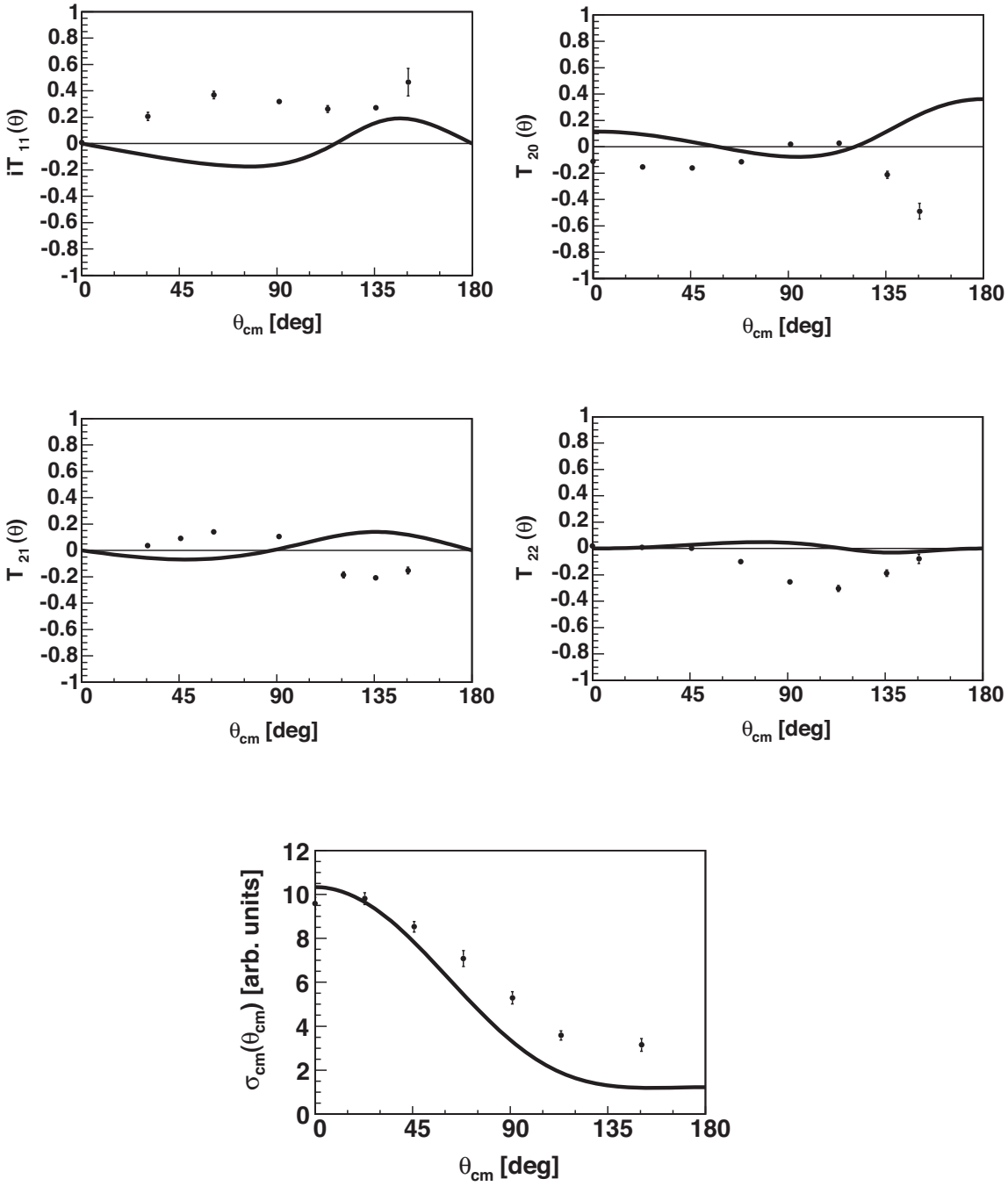

Figure 7.1: Comparison of the DWUCK4 calculation with the ^{7}Li($\vec{\mathrm{d}}$, n$_0$)^{8}Be experimental data at E$_\mathrm{d}$= 160 keV. The error bars represent statistical and systematic uncertainties.

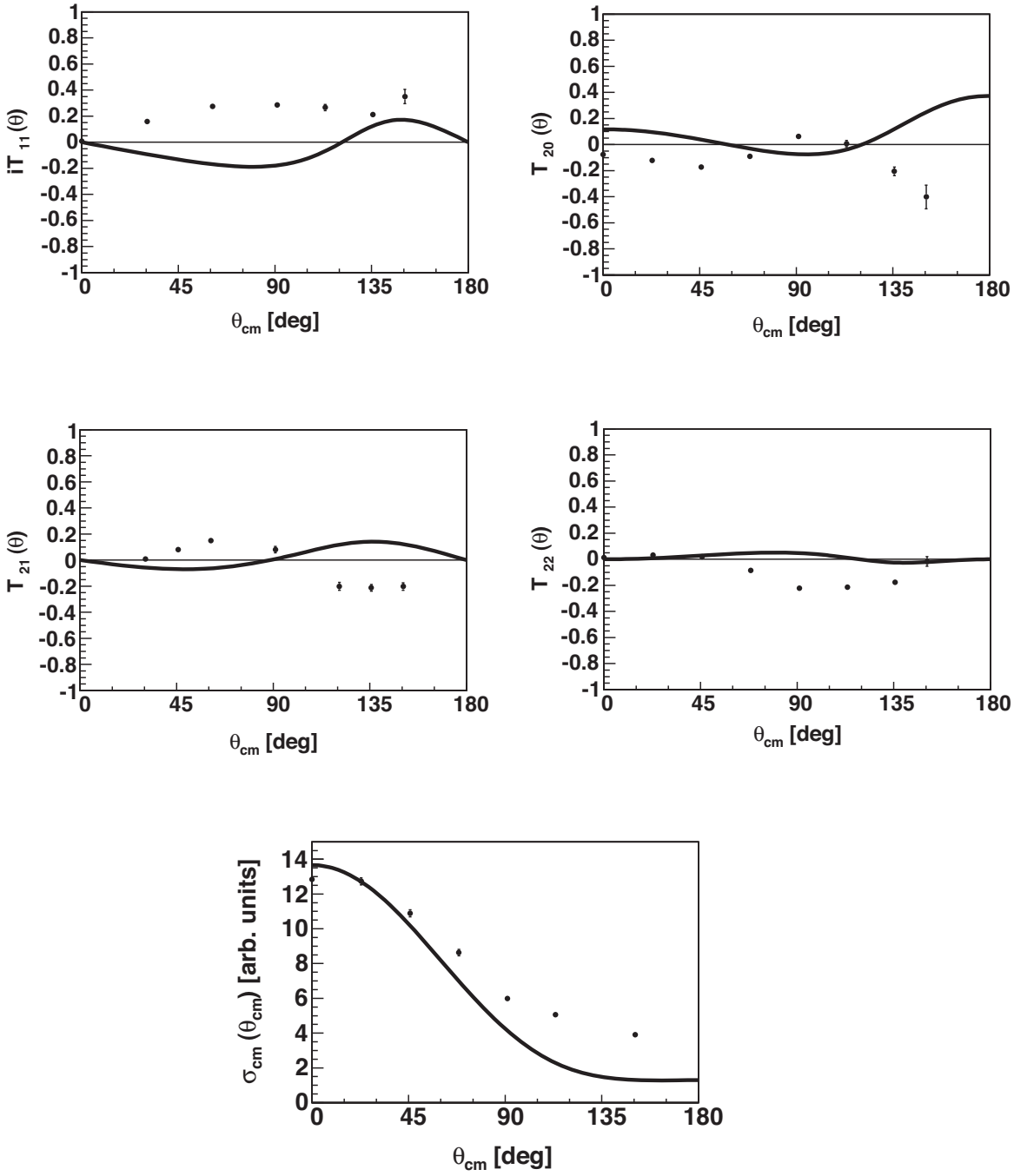

Figure 7.2: Comparison of the DWUCK4 calculation with the ^{7}Li$(\vec{\mathrm{d}}, \mathrm{n}_0)^{8}$Be experimental data at $\mathrm{E_d}$= 130 keV. The error bars represent statistical and systematic uncertainties.

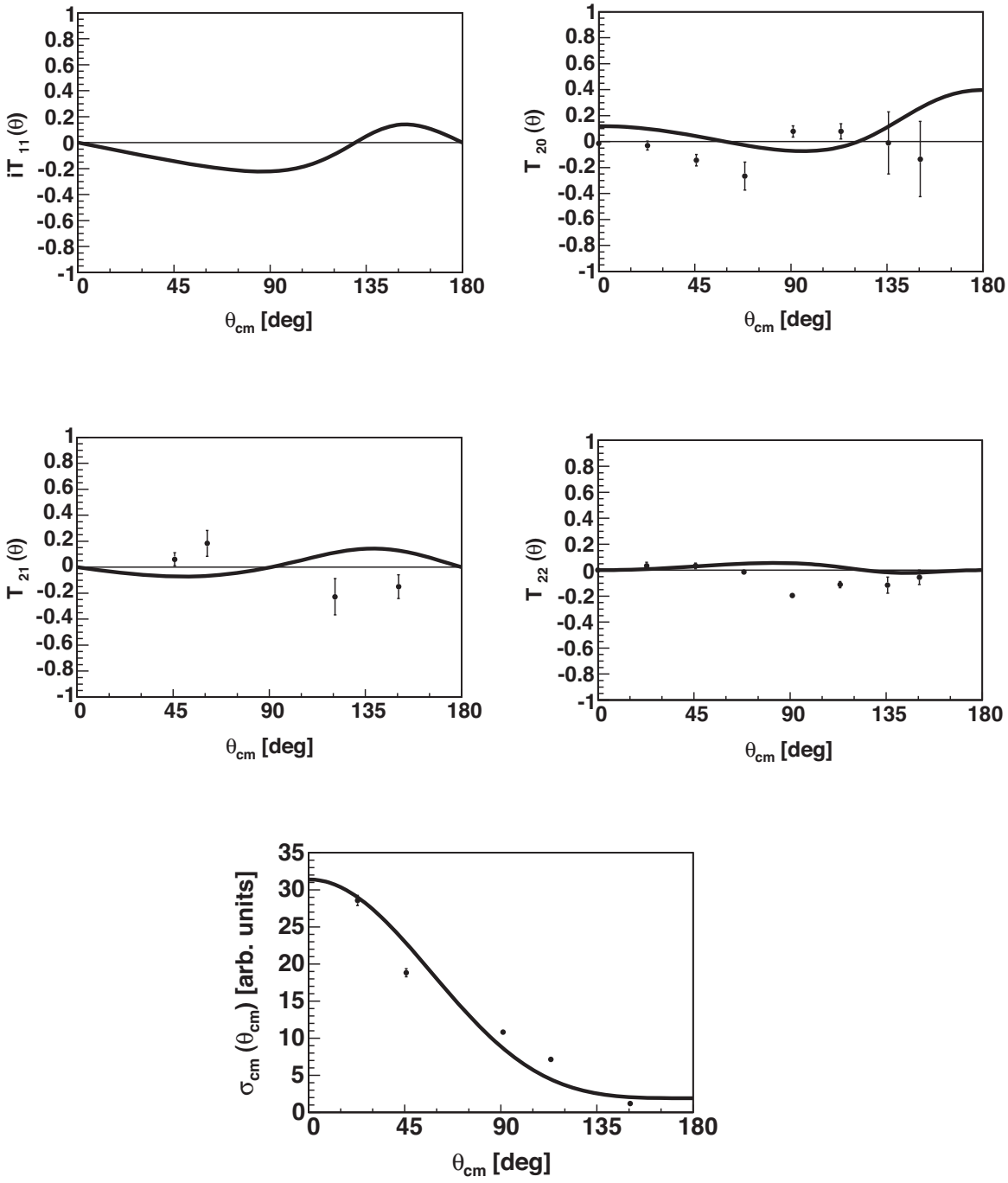

Figure 7.3: Comparison of the DWUCK4 calculation with the $^{7}\mathrm{Li}(\vec{\mathrm{d}},\mathrm{n}_0)^{8}\mathrm{Be}$ experimental data at $\mathrm{E_d}$= 80 keV. The error bars represent statistical and systematic uncertainties.

7.2 Coupled Reaction Channels

To first approximation, when two nuclei approach one another, they may be regarded as clusters of nucleons whose primary interaction results from the inter-nucleon two-body force. This has an average effect found by folding the force over the internal configurations of the clusters. The configurations are usually not static, and one or more rearrangement process may occur during the collision. In addition to elastic scattering where the target and projectile will remain in their ground states, other nonelastic interactions will have time to occur. For example, when one or both nuclei are deformed, inelastic excitations may occur and higher-energy states may become populated. Or, a particle in one nucleus may become excited from its initial bound state to another state (bound or unbound) during the reaction. Nucleons may also transfer from one nucleus to the other singly or as a simultaneous event [Tho88]. Calculations to deal with all of these rearrangements or transfer reactions are called "coupled reaction channels," or CRC, methods. This method introduces a new feature to traditional DWBA calculations: the inital and final channels in the rearrangement collision are not fully orthogonal, i.e. $(\psi_B\psi_b|\psi_A\psi_a) \neq 0$, leading to nonorthogonality corrections in the equations [Sat83].

As described in detail in Section 7.1, the distorted-waves method is built on the idea that elastic scattering is dominant and must be treated fully while nonelastic events can be treated with perturbation theory. However, a particular nonelastic channel may be sufficiently excited to make perturbation theory inadequate [Sat83].

In a special case of the CRC method, a two-step process becomes important in which a transfer or rearrangement is preceded or followed by an inelastic excitation. This calculation can be carried out to second order in the DWBA and is called the

"two-step" DWBA. In many cases, the elastic distorted waves are replaced by the solutions of the coupled-channels problem to include both elastic and inelastic waves, although the transfer is still treated to first order in the interaction. The reaction may proceed to a given final state along several paths, so the interference between contributions becomes important [Sat83].

A general n-step DWBA approximation feeds flux "forward" in the sequence $1 \rightarrow 2 \rightarrow \ldots \rightarrow n+1$ neglecting back couplings. The total wave function $\overline{\Psi}$ is projected onto a product of the projectile and target nuclear basis states ϕ_i with the wave functions describing their relative motion $\psi_i(\mathbf{R}_i)$ [Tho88]:

$$P\overline{\Psi} \equiv \Psi = \sum_{i}^{N} \phi_i \psi_i(\mathbf{R}_i), \tag{7.12}$$

where $\mathbf{R}_i$ is the radial separation of the interacting nuclei pair. In many cases, the coupled equations take the form

$$[E_i - H_i]\psi_i(\mathbf{R}_i) = \sum_{j=1}^{j=i-1} \langle \phi_i | \mathcal{H} - E | \phi_j \rangle \psi_j(\mathbf{R}_j), \tag{7.13}$$

where E_i is the asymptotic kinetic energy in the ith channel. The channel-projected Hamiltonian $H_i = T_i + U_i$, where T_i is the kinetic energy of the projectile-target relative motion [Tho88]

$$T_i = -\frac{\hbar^2}{2\mu_i}\left(\frac{d^2}{dR_i^2} - \frac{L(L+1)}{R_i^2}\right) \tag{7.14}$$

and U_i is the diagonal optical potential with nuclear and Coulomb (U_c) components, where [Sat83]

$$\begin{aligned} U_c(r) &= \frac{Z_a Z_A e^2}{r} \qquad r \geq R_{ch} \\ &= \frac{Z_a Z_A e^2}{2R_{ch}}\left(3 - \frac{r^2}{R_{ch}^2}\right) \qquad r \leq R_{ch} \end{aligned} \tag{7.15}$$

with R_{ch} being the charge radius and Z_a and Z_A being the projectile and target charges. The total Hamiltonian $\mathcal{H}$ is given by [Tho88]

$$\mathcal{H} - E = H_i - E_i + V_i, \tag{7.16}$$

where V_i are the interaction potentials between channels which have vanishing diagonal elements $\langle \phi_i | V_i | \phi_i \rangle = 0$.

One way to expand the matrix element $\langle \phi_i | \mathcal{H} - E | \phi_j \rangle$ in Equation 7.13 gives $\mathcal{H} - E = H_j - E_j + V_j$, so that

$$\langle \phi_i | \mathcal{H} - E | \phi_j \rangle = \langle \phi_i | V_j | \phi_j \rangle + \langle \phi_i | \phi_j \rangle [H_j - E_j]. \tag{7.17}$$

Using this expansion for the two-step DWBA referred to earlier, the coupled equations from Equation 7.13 are, for the inital channel:

$$[E_1 - H_1]\psi_1(\mathbf{R}_1) = 0 \tag{7.18}$$

and for the second channel:

$$\begin{aligned} [E_2 - H_2]\psi_2(\mathbf{R}_2) &= \langle \phi_2 | \mathcal{H} - E | \phi_1 \rangle \psi_1(\mathbf{R}_1) \\ &= \langle \phi_2 | V_1 | \phi_1 \rangle \psi_1 + \langle \phi_2 | \phi_1 \rangle [H_1 - E_1] \psi_1. \end{aligned} \tag{7.19}$$

7.2.1 FRESCO

The coupled-channels code FRESCO can calculate finite-range transfer interactions among any number of mass partitions and any number of nuclear excitations in each of those partitions [Tho04]. Kernels of the non-local interactions are calculated before the coupled-channels set is solved iteratively. The stored kernels are used at each iteration to integrate the wave functions to generate the source terms for the next iteration. FRESCO can also generate local couplings for the rotational

or single-particle excitations of the projectile or the target. The local form factors for zero-range or local-energy-approximation can also be used. In the case of multistep DWBA, these local interactions may also be included iteratively [Tho04].

For the ^{7}Li$(\vec{\mathrm{d}}, \mathrm{n}_0)^8$Be and ^{7}Li$(\vec{\mathrm{d}}, \mathrm{n}_1)^8$Be reactions, the entrance channel was modeled with a potential containing volume, surface imaginary, and spin-orbit terms, as in Galloway, *et al.*, [Gal84]. However, this did not allow for a correct description of the polarization observables. Inclusion of a target spin-orbit interaction $\mathbf{L} \cdot \mathbf{J}_t$, where L is the orbital angular momentum and J_t is the target spin, in the complete Hamiltonian $\mathcal{H}$ provided improvement in describing these observables. The same result can be achieved by including a coupling to the first excited state of the target [Nis82]. Inclusion of target excitations involves tensor interactions which arise naturally from the deformation of the target. In the present work, these two mechanisms were both included and adjusted to provide the best fit and the most physical parameters. The resulting values for the potentials that best fit the experimental data are given in Table 7.2, as well as the deformation parameter β. The value of β was allowed to vary to fit the data; the final value of 1.3 given in Table 7.2 is nearly two times larger than the previously determined value of 0.75 [Bel05].

The target spin-orbit potential depth is very large, nearly 8 MeV. Because the interaction strength is proportional to $(\hbar/(2m))^2$, the term would normally be expected to be on the order of 1-2 MeV, given the spin-orbit terms for the other particles. This large spin-orbit strength is unusual but was the only way to reproduce the positive $i\mathrm{T}_{11}(\theta)$ values observed in the experiment. (See Figure 7.5).

A two-step DWBA approach, utilizing FRESCO, was used where excitations to the $J^\pi = 1/2^-$ state of ^{7}Li were considered as well as couplings to the $J^\pi = 2^+$ first excited state of ^{8}Be [Bra05b]. An illustration of this coupling scheme is shown in

Figure 7.4. The results of the calculation compared with the experimental data are shown in Figures 7.5 through 7.9 for each polarization observable. The total cross section at E_d = 80 keV, 60 keV, and 45 keV is compared with the experimental data in Figure 7.10. It is obvious from these figures that although the FRESCO code is able to qualitatively describe the data, serious discrepancies remain. A comparison of the experimental TMEs with those generated by FRESCO, as described below, confirms this.

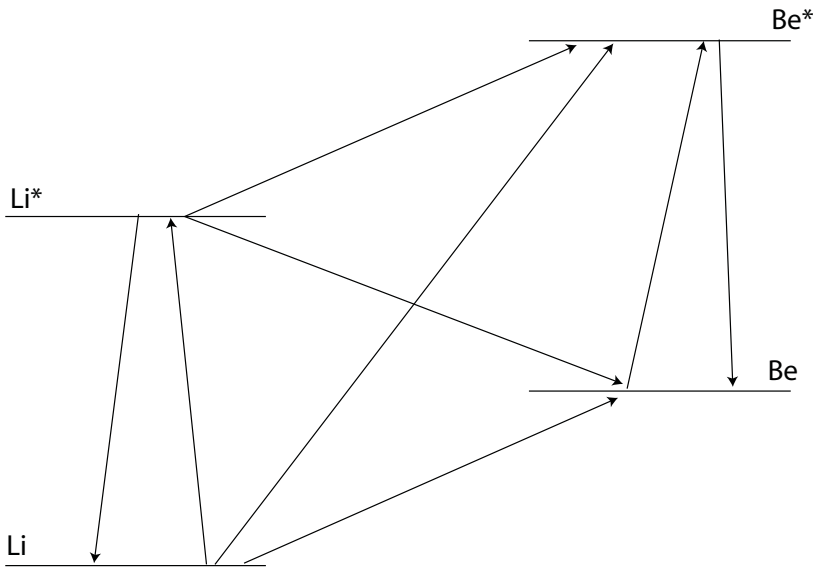

Figure 7.4: Diagram depicting the coupled channels considered in the code FRESCO.

Scattering amplitude analysis reveals that for the $^7\mathrm{Li}(\vec{\mathrm{d}}, \mathrm{n}_0)^8\mathrm{Be}$ reaction, the most important contributions in the energy range E_d = 80 keV to E_d = 160 keV are from the ($L = 2,\ j = 3,\ J^\pi = \frac{3}{2}^-$), ($L = 0,\ j = 1,\ J^\pi = \frac{3}{2}^-$), and ($L = 1,\ j =$

Potential			Incident d	Emitted n	Transferred p	Target spin-orbit
Real						
Depth	V	(MeV)	149.9	46.3	55.0	
Radius	r	(fm)	2.06	1.32	1.20	
Diffuseness	a	(fm)	0.83	0.66	0.70	
Volume imaginary						
Depth	W	(MeV)	2.30	0.75		
Radius	r_w	(fm)	0.10	1.26		
Diffuseness	a_w	(fm)	0.07	0.58		
Surface imaginary						
Depth	W_D	(MeV)	6.87	8.10	2.70	
Radius	r_D	(fm)	1.98	1.26	0.68	
Diffuseness	a_D	(fm)	0.59	0.48	0.08	
Spin-orbit						
Real depth	V_s	(MeV)	8.50	9.00	3.05	7.91
Radius	r_s	(fm)	1.00	1.01	1.73	0.71
Diffuseness	a_s	(fm)	0.94	0.75	0.70	0.43
Deformation	β	(fm)				1.32

Table 7.2: Values of the potentials used in the CRC code FRESCO for the ^{7}Li$(\vec{\mathrm{d}}, \mathrm{n}_0)^8$Be and ^{7}Li$(\vec{\mathrm{d}}, \mathrm{n}_1)^8$Be reactions that best reproduced the experimental data [Bra05a].

2, $J^\pi = \frac{1}{2}^+$) channels, in the j-j coupling scheme. The ($L = 1,\ j = 2,\ J^\pi = \frac{1}{2}^+$) channel becomes the most significant as energy decreases in this range. The most important contributions in the ^{7}Li$(\vec{\mathrm{d}}, \mathrm{n}_1)^8$Be reaction in this energy range are from the ($L = 1,\ j = 2,\ J^\pi = \frac{5}{2}^+$), ($L = 2,\ j = 3,\ J^\pi = \frac{3}{2}^-$), and ($L = 1,\ j = 1,\ J^\pi = \frac{5}{2}^+$) channels [Bra05b].

The results of the overall s-, p-, and d-wave contributions for each reaction for the calculation and experiment are compared in Table 7.3 and Table 7.4. For the ^{7}Li$(\vec{\mathrm{d}}, \mathrm{n}_0)^8$Be reaction, FRESCO predicts large d-wave contributions which are dominant at $\mathrm{E_d}$ = 160 keV and 130 keV. However, the experimental results indicate that the reaction proceeds primarily by p-waves in the entrance channel. In the case of

the ^{7}Li$(\vec{d}, n_1)^8$Be reaction, both FRESCO and the experimental results indicate that the reaction mechanism is predominantly p-waves in the entrance channel. FRESCO and the experiment are in good agreement at E_d= 80 keV, with the FRESCO result of 93% p-waves lying within the experimental error bars of 99±19%. However, the CRC method predicts that there may be a d-wave contribution, particularly at E_d = 160 keV. The higher χ^2 value for the E_d = 160 keV fits to the data, as mentioned in Section 5.3, could indicate that a d-wave contribution should be considered in the fits.

	E_d = 160 keV		E_d = 130 keV		E_d = 80 keV	
	Strength (%)					
Transition	TME fit	CRC	TME fit	CRC	TME fit	CRC
S-wave	11 ± 2	17	8 ± 1	18	11 ± 1	20
P-wave	75 ± 10	26	86 ± 10	34	84 ± 3	46
D-wave	14 ± 4	57	6 ± 3	48	5 ± 1	34

Table 7.3: Comparison of the TME fits to the ^{7}Li$(\vec{d}, n_0)^8$Be data to the results of a coupled reaction channels (CRC) calculation done by FRESCO [Bra05a].

	E_d = 160 keV		E_d = 130 keV		E_d = 80 keV	
	Strength (%)					
Transition	TME fit	CRC	TME fit	CRC	TME fit	CRC
S-wave	46 ± 5	9	33 ± 13	2	1 ± 19	3
P-wave	54 ± 7	64	67 ± 11	93	99 ± 19	93
D-wave	–	27	–	5	–	4

Table 7.4: Comparison on the TME fits to the ^{7}Li$(\vec{d}, n_1)^8$Be data to the results of a coupled reaction channels (CRC) calculation done by FRESCO [Bra05a].

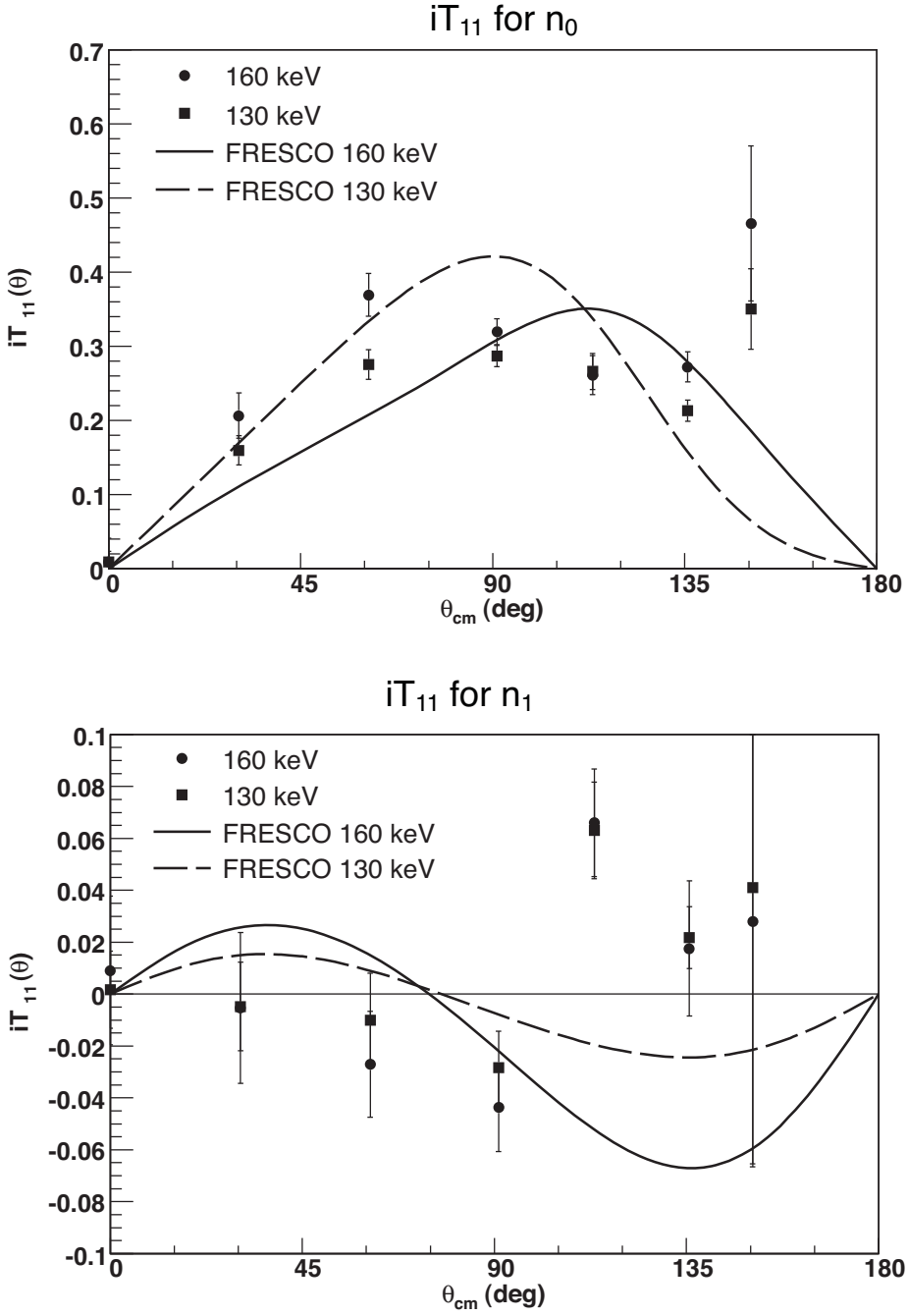

Figure 7.5: Comparison of the CRC calculation for iT_{11} with the ^{7}Li$(\vec{d}, n_0)^8$Be and ^{7}Li$(\vec{d}, n_1)^8$Be experimental data at E_d= 160 keV (circles, solid line) and 130 keV (squares, dashed line). The error bars represent statistical and systematic uncertainties.

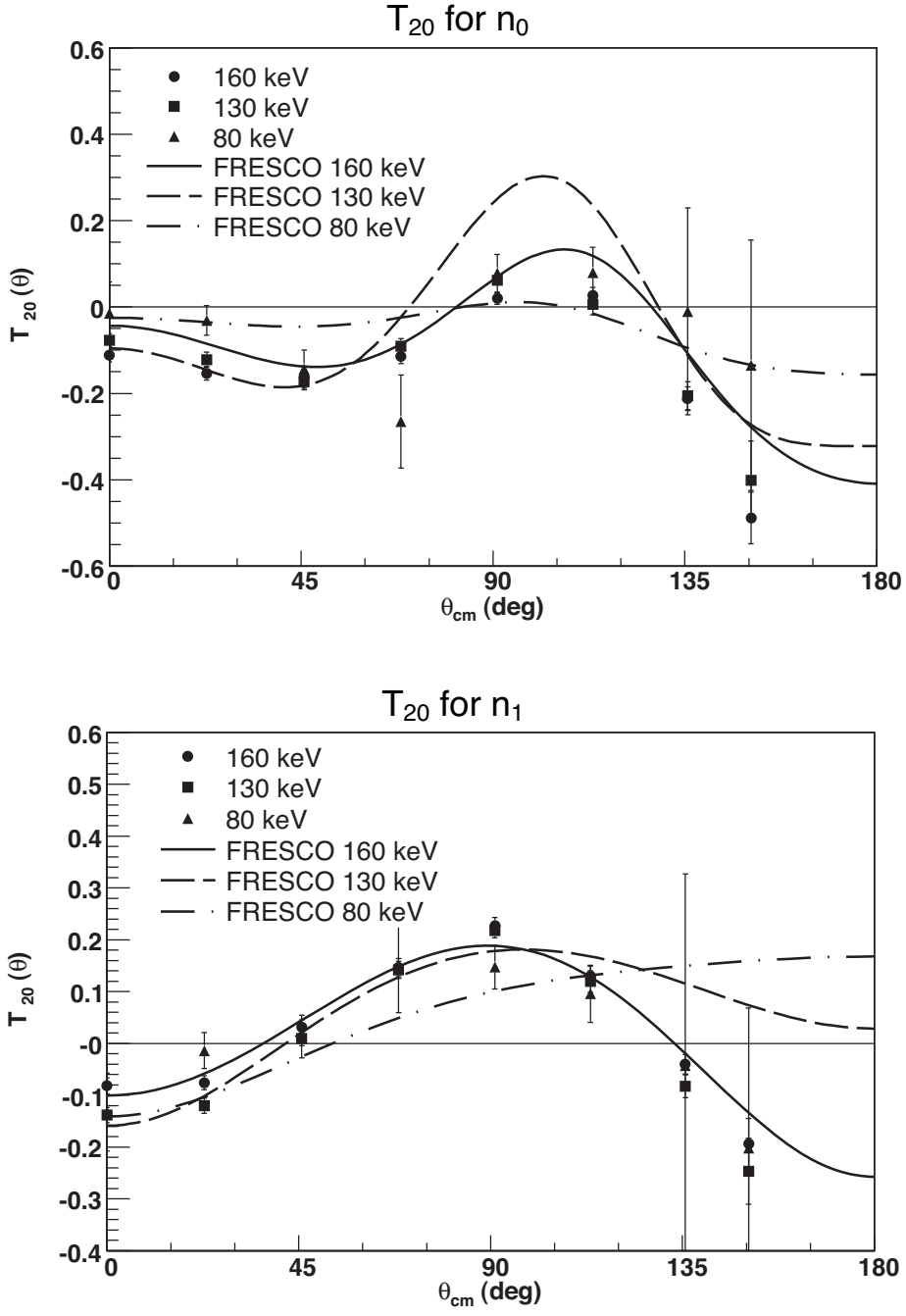

Figure 7.6: Comparison of the CRC calculation for T_{20} with the $^{7}\mathrm{Li}(\vec{\mathrm{d}},\mathrm{n}_0)^{8}\mathrm{Be}$ and $^{7}\mathrm{Li}(\vec{\mathrm{d}},\mathrm{n}_1)^{8}\mathrm{Be}$ experimental data at $\mathrm{E_d}$= 160 keV (circles, solid line), 130 keV (squares, dashed line), and 80 keV (triangles, dot-dashed line). The error bars represent statistical and systematic uncertainties.

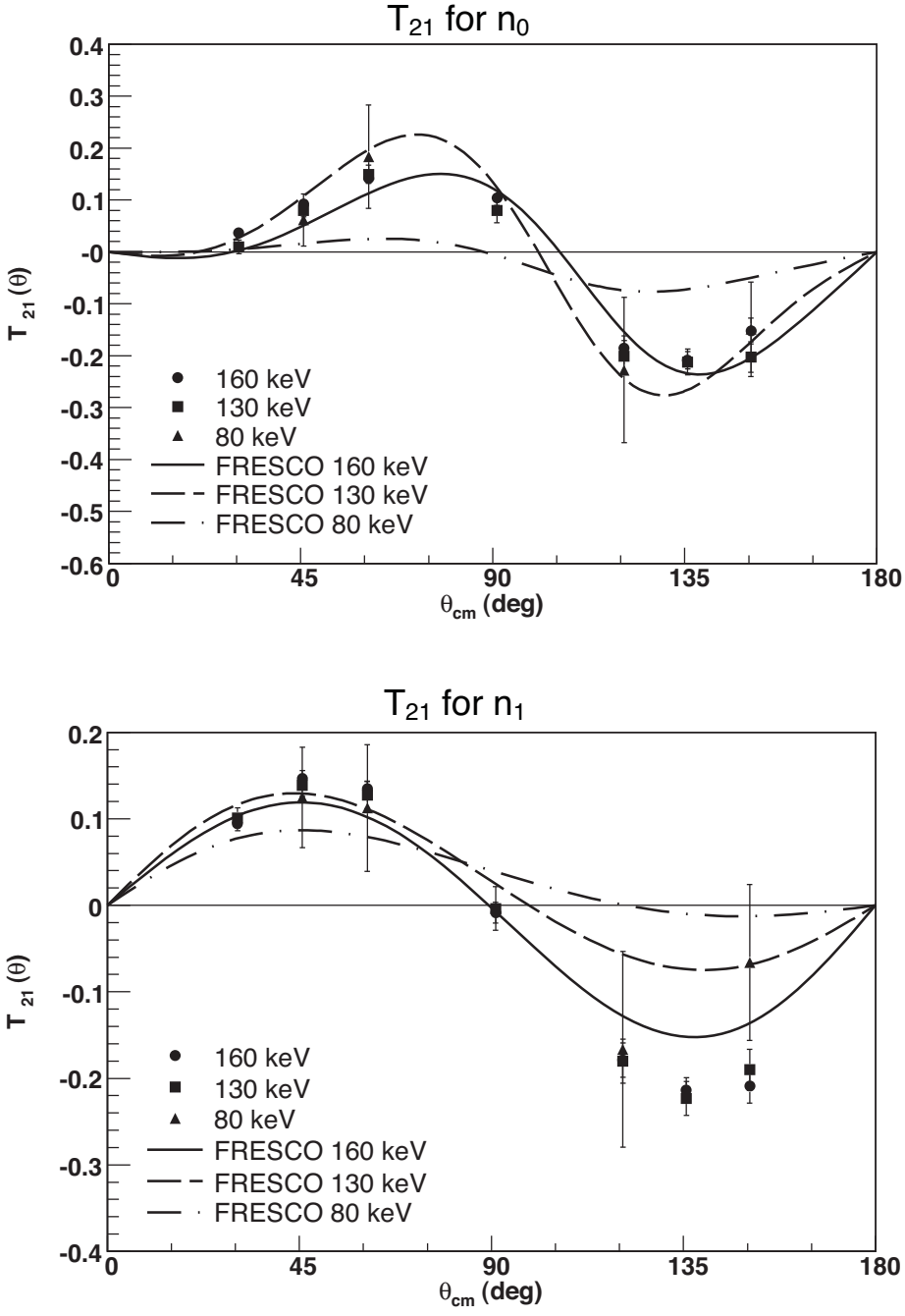

Figure 7.7: Comparison of the CRC calculation for T_{21} with the $^7\mathrm{Li}(\vec{\mathrm{d}},\mathrm{n}_0)^8\mathrm{Be}$ and $^7\mathrm{Li}(\vec{\mathrm{d}},\mathrm{n}_1)^8\mathrm{Be}$ experimental data at $\mathrm{E_d}$= 160 keV (circles, solid line), 130 keV (squares, dashed line), and 80 keV (triangles, dot-dashed line). The error bars represent statistical and systematic uncertainties.

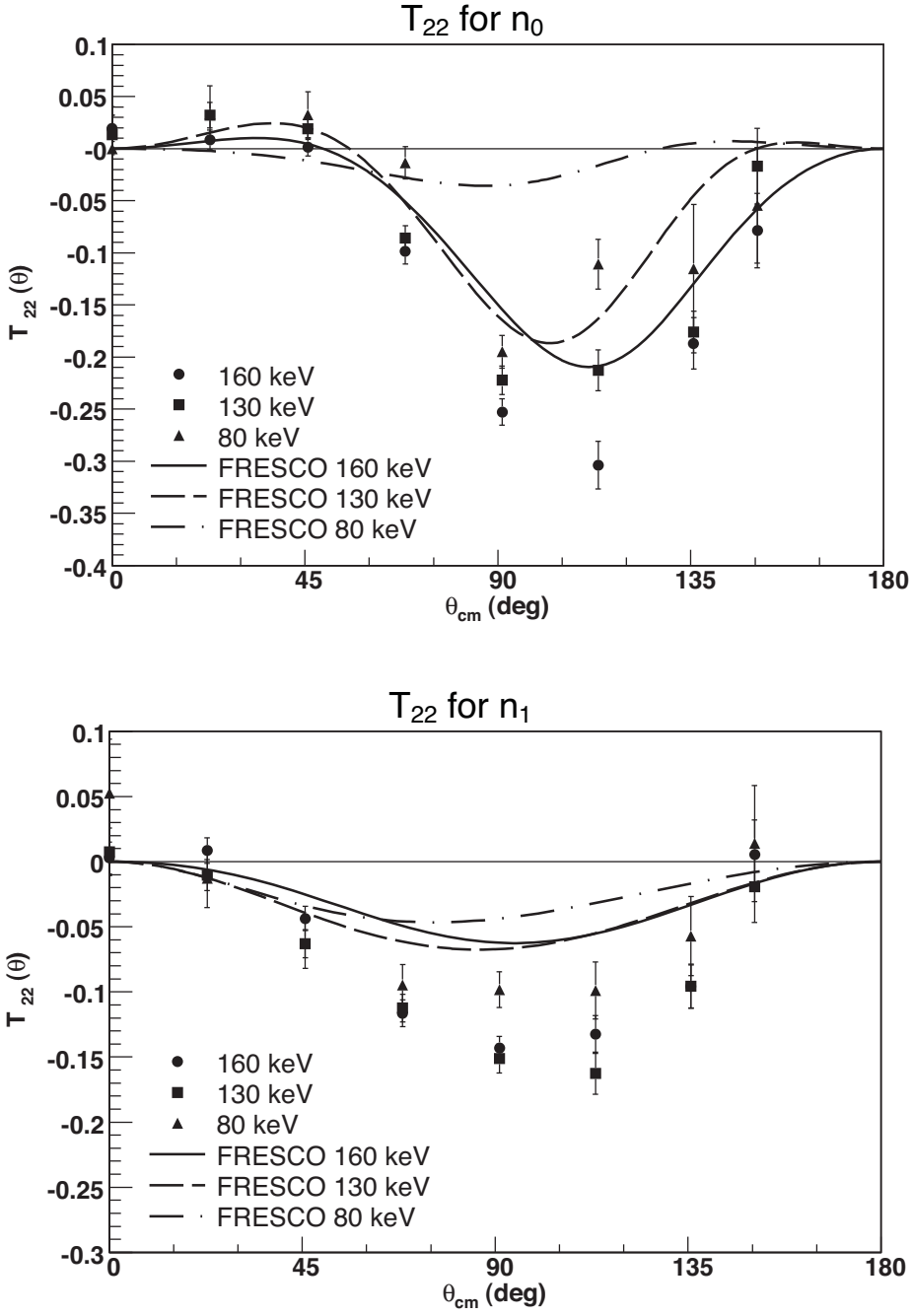

Figure 7.8: Comparison of the CRC calculation for T_{22} with the $^{7}\mathrm{Li}(\vec{\mathrm{d}},\mathrm{n}_0)^{8}\mathrm{Be}$ and $^{7}\mathrm{Li}(\vec{\mathrm{d}},\mathrm{n}_1)^{8}\mathrm{Be}$ experimental data at $\mathrm{E_d}$= 160 keV (circles, solid line), 130 keV (squares, dashed line), and 80 keV (triangles, dot-dashed line). The error bars represent statistical and systematic uncertainties.

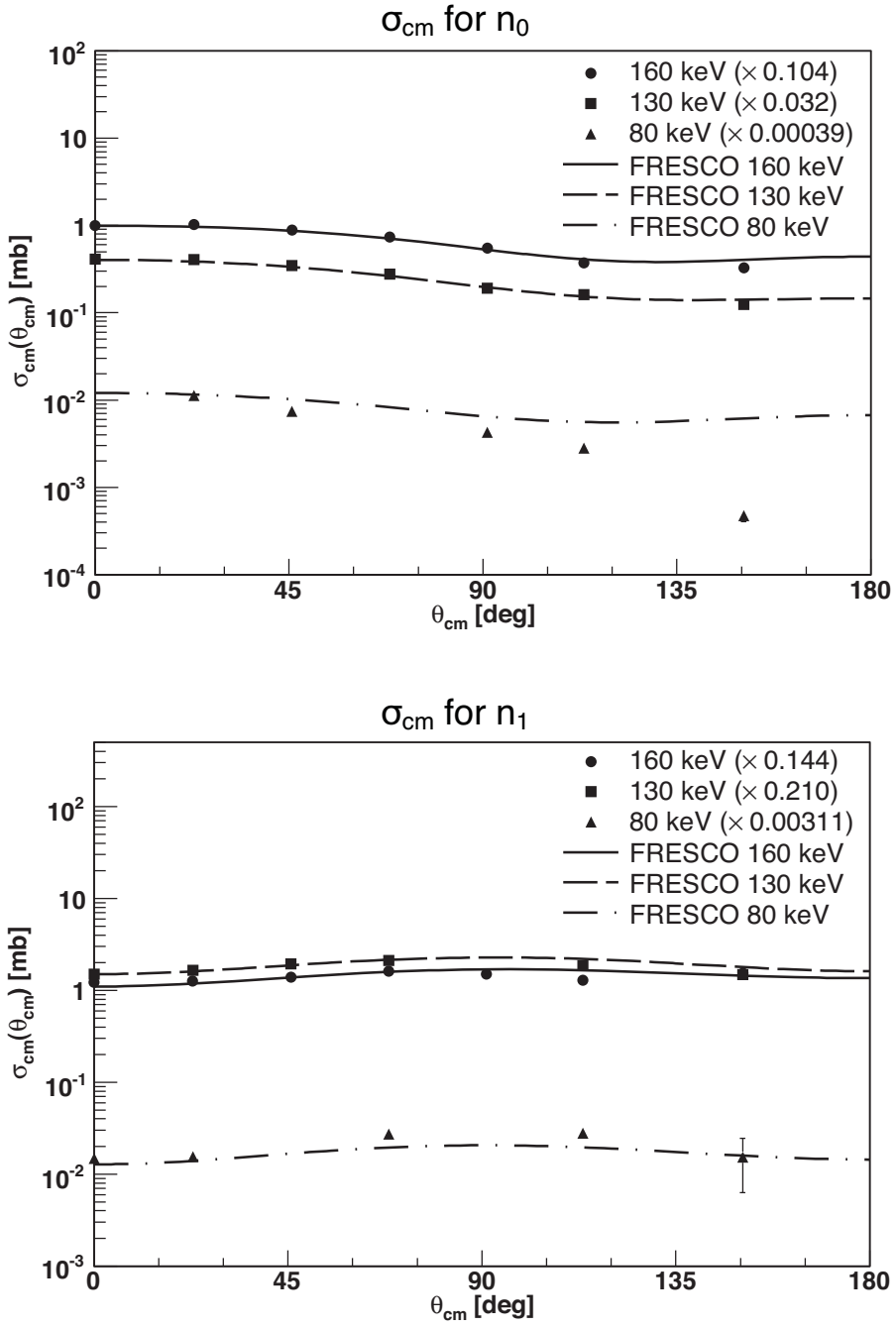

Figure 7.9: Comparison of the CRC calculation for the differential cross section with the ^{7}Li$(\vec{d}, n_0)^8$Be and ^{7}Li$(\vec{d}, n_1)^8$Be experimental data at E_d= 160 keV (circles, solid line), 130 keV (squares, dashed line), and 80 keV (triangles, dot-dashed line). The error bars represent statistical and systematic uncertainties. The experimental data have been multiplied by the number in parenthesis to normalize them to the calculation results.

7.3 Astrophysical S Factor

The experimental results for the astrophysical S factor presented in Chapter 6 were also compared with the predictions of the DWBA and CRC calculations. The values for the absolute cross section are given in Table 7.5, and both the cross section and S factor are shown in Figure 7.10. Although the DWBA model was not able to reproduce the polarization observables for the n_0 state, the predicted values for the absolute cross section are in reasonable agreement with the measured absolute cross section for the ^{7}Li(d, n_0)^{8}Be and ^{7}Li(d, n_1)^{8}Be reactions (solid line and dotted line in Figure 7.10).

The FRESCO code predictions for the ^{7}Li(d, n_0)^{8}Be and ^{7}Li(d, n_1)^{8}Be S factors in this energy region do not agree with the experimental results, as shown in Table 7.5 and Figure 7.10. The absolute cross section values predicted by FRESCO for the n_1 state (dot-dashed line in Figure 7.10) lie within the error bars of the ^{7}Li(d, n_1)^{8}Be experimental data. However, the values predicted for the n_0 state (dashed line) are significantly higher. In both cases, FRESCO predicts an S factor with a positive slope and possibly some higher-order energy dependence. Therefore, it is recommended that this theory not be used to extrapolate the S factor to lower energies.

	$\sigma(E_{c.m.})$					
	n_0			n_1		
$E_{c.m.}$ [keV]	Exp.	DWBA	CRC	Exp.	DWBA	CRC
33	0.017 ± 0.0047	0.031	0.041	0.15 ± 0.066	0.10	0.072
43	0.17 ± 0.047	0.32	0.59	1.3 ± 0.67	1.0	1.1
57	1.3 ± 0.39	2.5	7.1	9.1 ± 6.0	7.9	14.0

Table 7.5: Comparison of the experimental values for the absolute cross section for the ^{7}Li(d, n_0)^{8}Be and ^{7}Li(d, n_1)^{8}Be reactions with the values given by the DWBA and CRC models.

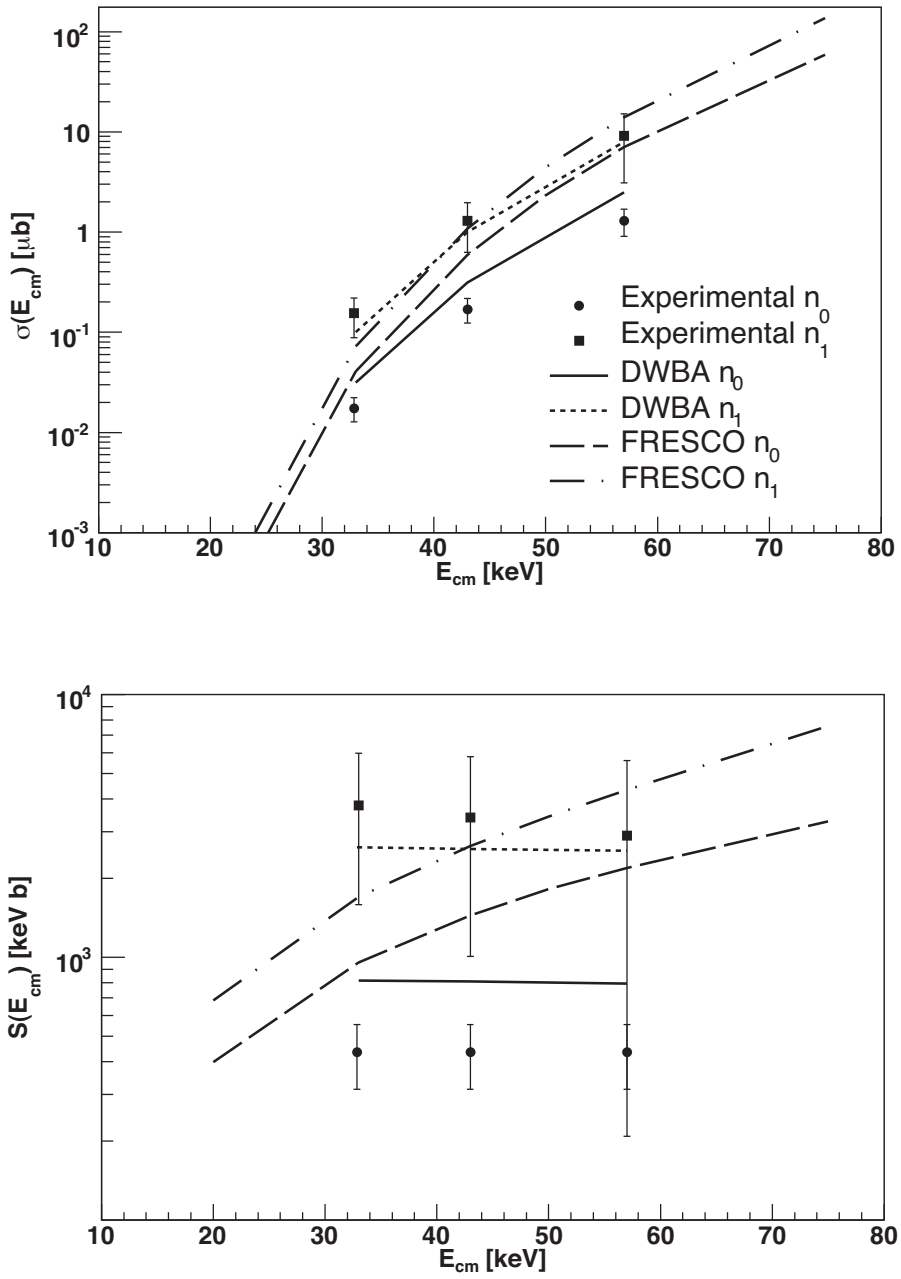

Figure 7.10: Comparison of FRESCO and DWBA calculations for the total cross section and S factor with the $^7\mathrm{Li}(\vec{\mathrm{d}},\mathrm{n}_0)^8\mathrm{Be}$ and $^7\mathrm{Li}(\vec{\mathrm{d}},\mathrm{n}_1)^8\mathrm{Be}$ experimental data at $\mathrm{E_d}$= 80 keV, 60 keV, and 45 keV. The error bars represent statistical and systematic uncertainties.

Chapter 8

Conclusions

This experimental study of the ^{7}Li(d, n)^{8}Be reaction succeeded in providing the most complete picture to date of the ^{7}Li(d, n_0)^{8}Be and ^{7}Li(d, n_1)^{8}Be reactions in the region between $E_{c.m.}$= 33 keV and 124 keV. The polarization observables $iT_{11}(\theta)$, $T_{20}(\theta)$, $T_{21}(\theta)$, $T_{22}(\theta)$, and the differential cross section were measured for both ^{7}Li($\vec{d}$, n_0)^{8}Be and ^{7}Li($\vec{d}$, n_1)^{8}Be at E_d= 80 keV, 130 keV, and 160 keV. Complex transition matrix elements (TMEs), listed in Tables 5.4 and 5.5, were fit to the observables. The experimental polarization observables were compared with both Distorted Wave Born Approximation (DWBA) and coupled reaction channels (CRC) calculations. Because the CRC calculation gave a reasonable description of the polarization observables, the theory's prediction for the behavior of the contributing TMEs was compared with those that were obtained from the TME analysis of the experimental data. In addition, the absolute cross section and S factor were measured for both the ^{7}Li(d, n_0)^{8}Be and ^{7}Li(d, n_1)^{8}Be reactions at $E_{c.m.}$= 33 keV, 43 keV, and 57 keV. These results were used to extrapolate the S factor down to zero energy, were compared with previous measurements, and were compared with the predictions of

the DWBA and CRC calculations.

8.1 Review of Results

The results of the polarization observable measurements for $^{7}\mathrm{Li}(\vec{\mathrm{d}},\mathrm{n}_0)^{8}\mathrm{Be}$ and $^{7}\mathrm{Li}(\vec{\mathrm{d}},\mathrm{n}_1)^{8}\mathrm{Be}$ are given in Chapter 4 and Appendix A. A TME analysis yielded a unique, dominant p-wave solution in both the n_0 and n_1 cases. The solution for the n_0 transition corresponded to an average of 82% p-waves in the entrance channel, 10% s-waves, and 8% d-waves, with the $^{2}\mathrm{p}_2$ element carrying over 50% of the total strength. The n_1 solution was dominated by an average of 73% p-waves and 27% s-waves, with the $^{6}\mathrm{p}_4$ and $^{6}\mathrm{p}_6$ elements carrying over 40% of the total amplitude.

A distorted-waves Born approximation (DWBA) calculation was compared with the experimental data but was unable to reproduce the angular distributions of the analyzing powers. The CRC calculation using the code FRESCO provided a better description of the experimental results than the DWBA calculation once a large target spin-orbit potential and coupling to the first excited state of the target was included in the calculation (see Chapter 7). However, although the FRESCO result was in qualitative agreement with the experimental data, serious discrepancies remained. As detailed in Chapter 7, a more demanding comparison of the experimentally determined TMEs with the theoretical ones indicated that the theory fails to reproduce the significant features of the data. As shown in Tables 7.3 and 7.4, the FRESCO calculations produced a TME solution for the n_0 state consisting of an average of 46% d-wave contribution in the entrance channel, 35% p-waves, and 18% s-waves and a solution for the n_1 state of an average of 83% p-waves, 12% d-waves, and 5% s-waves. Although the n_1 solution is similar to the experimental result with a dominant p-wave

solution (no d-waves were fit to the experimental data), the n_0 solution is distinctly different with its dominant d-wave solution as opposed to the experimental data's dominant p-wave solution.

Absolute cross section and S-factor results for the ^{7}Li(d, n_0)^{8}Be and ^{7}Li(d, n_1)^{8}Be reactions are given in Chapter 6. From these experimental data, the total S factor for the ^{7}Li(d, $n_0 + n_1$)^{8}Be reaction was found to be $S(E) = 5400(\pm 1500) - 37(\pm 21)E$ keV b, with the slope being attributed to electron screening effects. Because only the n_0 and n_1 states could be measured, this value only sets a lower limit on the total S factor.

8.2 Discussion of Astrophysical Significance

The importance of the astrophysical S factor for nuclear reaction rates, and hence light element production in the Big Bang, was discussed in Chapters 1 and 6. As was pointed out there, in present reaction rate calculations for ^{7}Li+d in the BBN energy ($E = 10{-}900$ keV) and temperature ($T = 0.12{\times}10^9{-}10^{10}$ K) regions, the nonresonant contribution has been determined using an S factor from experimental data taken at $E_{c.m.}$= 1.6 to 2.0 MeV, assumed to be constant, and extrapolated to lower energies. The purpose of the present experimental work, which covers the energy region of $E_{c.m.}$= 33 to 124 keV corresponding to the temperature region $T = 0.4 \times 10^9$ to 1.4×10^9 K, was to test that assumption and provide data in the region of interest ($E_{c.m.}$= 20 - 200 keV) for a more reliable extrapolation of the S factor.

The absolute cross section and S-factor measurements in the energy region $E_{c.m.}$= 33 keV to 57 keV partially accomplished this goal. Because only the ^{7}Li(d, n_0)^{8}Be and ^{7}Li(d, n_1)^{8}Be reactions could be measured, these results can only set a lower

limit on the total value (which includes an n_2 value as well as the n_0 and n_1 values). However, the n_0+n_1 results indicate that the S factor is constant in the energy region between $E_{c.m.}$= 30 keV and 60 keV, which agrees well with the assumption used by [Boy93] in their reaction rate calculations. Although the present value for n_0+ n_1 of $4 \times 10^3(\pm 1 \times 10^3)$ keV b is a factor of 3 lower than the value used by Boyd, *et al.* (See Figure 6.5), because the present value does not include the n_2 state, the result is consistent with their assumption.

The TME analysis of the polarization observable data can be used to test how well we understand the reaction dynamics. This has an impact on the reliability of the extrapolated values of the S factor. In the present case, the CRC calculations (FRESCO) were able to qualitatively reproduce the experimental data. However, the S factor obtained by using this model does not agree with the experimental results, and a comparison of the TMEs obtained from our data with those predicted by FRESCO indicates some serious discrepancies, especially in the case of the (d,n_0) channel. We therefore recommend that the CRC theory not but used to extrapolate the S factor to lower energies.

The DWBA model predicts a constant S factor for the n_0 and n_1 states which agrees very well with the experimental value. Based on this and the experimental results, it is recommended that the constant value be used for the S factor in these energy regions.

8.3 In Closing

The measurement of the absolute cross section, S factor, and polarization observables for the $^7\mathrm{Li}(\mathrm{d}, \mathrm{n}_0)^8\mathrm{Be}$ and $^7\mathrm{Li}(\mathrm{d}, \mathrm{n}_1)^8\mathrm{Be}$ reactions is the most complete mea-

surement of these reactions in these energy regions to date. The extracted and extrapolated values of the S factors are the most reliable obtained, although a careful examination indicates that our theoretical understanding of the reaction dynamics is incomplete. Hopefully, the difficulty of our present theoretical models to fully explain the data will spark interest in investigating and developing new theoretical models to understand the reaction dynamics in greater detail.

Appendix A

Data Tables

A.1 $iT_{11}(\theta)$

The $iT_{11}(\theta)$ experimental results as described in Section 4.1.1 are shown in Figure 4.2 for the n_0 state and in Figure 4.3 for the n_1 state and are given in Table A.1 and Table A.2, respectively. The errors are calculated as described in that section.

	E_d=160-0 keV		E_d=130-0 keV	
$\theta_{c.m.}$	$iT_{11}(\theta)$	$\Delta iT_{11}(\theta)$	$iT_{11}(\theta)$	$\Delta iT_{11}(\theta)$
0°	0.0093	0.0319	0.0089	0.0144
30.5°	0.2064	0.0306	0.1594	0.0197
60.9°	0.3691	0.0289	0.2753	0.0202
91.0°	0.3194	0.0174	0.2867	0.0145
113.4°	0.2612	0.0262	0.2660	0.0242
135.7°	0.2721	0.0204	0.2132	0.0144
150.5°	0.4654	0.1046	0.3503	0.0544

Table A.1: The measured $iT_{11}(\theta)$ at E_d=160-0 keV and E_d= 130-0 keV for $^7Li(\vec{d}, n_0)^8Be$. Error bars include the statistical and systematic uncertainties.

	E_d=160-0 keV		E_d=130-0 keV	
$\theta_{c.m.}$	$iT_{11}(\theta)$	$\Delta iT_{11}(\theta)$	$iT_{11}(\theta)$	$\Delta iT_{11}(\theta)$
0°	0.0091	0.0286	0.0017	0.0148
30.5°	-0.0053	0.0291	-0.0048	0.0171
60.9°	-0.0271	0.0204	-0.0101	0.0182
91.0°	-0.0437	0.0169	-0.0283	0.0140
113.4°	0.0660	0.0208	0.0630	0.0186
135.7°	0.0176	0.0261	0.0218	0.0119
150.5°	0.0279	0.0944	0.0410	0.1064

Table A.2: The measured $iT_{11}(\theta)$ at E_d=160-0 keV and E_d= 130-0 keV for $^7Li(\vec{d}, n_1)^8Be$. Error bars include the statistical and systematic uncertainties.

A.2 $T_{20}(\theta)$

The $T_{20}(\theta)$ experimental data for the n_0 and n_1 states are given in Table A.3 and Table A.4 and were shown in Figure 4.4 and Figure 4.5. These data and their errors were described in Section 4.1.2.

	E_d=160-0 keV		E_d=130-0 keV		E_d= 80-0 keV	
$\theta_{c.m.}$	$T_{20}(\theta)$	$\Delta T_{20}(\theta)$	$T_{20}(\theta)$	$\Delta T_{20}(\theta)$	$T_{20}(\theta)$	$\Delta T_{20}(\theta)$
0°	-0.1109	0.0164	-0.0767	0.0150	-0.0148	0.0725
22.8°	-0.1535	0.0154	-0.1222	0.0177	-0.0310	0.0343
45.7°	-0.1609	0.0154	-0.1728	0.0192	-0.1440	0.0439
68.4°	-0.1145	0.0164	-0.0912	0.0179	-0.2651	0.1077
91.0°	0.0195	0.0130	0.0619	0.0125	0.0783	0.0433
113.4°	0.0270	0.0184	0.0064	0.0246	0.0792	0.0589
135.7°	-0.2121	0.0273	-0.2051	0.0322	-0.0104	0.2395
150.5°	-0.4886	0.0600	-0.4012	0.0907	-0.1346	0.2898

Table A.3: The measured $T_{20}(\theta)$ at E_d=160-0 keV, E_d= 130-0 keV, and E_d= 80-0 keV for $^7Li(\vec{d}, n_0)^8Be$. Error bars include the statistical and systematic uncertainties.

	E_d=160-0 keV		E_d=130-0 keV		E_d= 80-0 keV	
$\theta_{c.m.}$	$T_{20}(\theta)$	$\Delta T_{20}(\theta)$	$T_{20}(\theta)$	$\Delta T_{20}(\theta)$	$T_{20}(\theta)$	$\Delta T_{20}(\theta)$
0°	-0.0818	0.0152	-0.1381	0.0149	-0.1323	0.0753
22.8°	-0.0757	0.0132	-0.1203	0.0144	-0.0138	0.0345
45.7°	0.0320	0.0132	0.0095	0.0138	0.0131	0.0411
68.4°	0.1465	0.0178	0.1421	0.0162	0.1465	0.0871
91.0°	0.2273	0.0157	0.2175	0.0134	0.1473	0.0418
113.4°	0.1301	0.0191	0.1196	0.0209	0.0960	0.0550
135.7°	-0.0400	0.0188	-0.0828	0.0219	-0.0427	0.3696
150.5°	-0.1940	0.0497	-0.2468	0.0635	-0.2015	0.2700

Table A.4: The measured $T_{20}(\theta)$ at E_d=160-0 keV, E_d= 130-0 keV, and E_d= 80-0 keV for ^{7}Li($\vec{d}, n_1$)^{8}Be. Error bars include the statistical and systematic uncertainties.

A.3 $T_{21}(\theta)$

The experimental data and their associated errors described in Section 4.1.3 for $T_{21}(\theta)$ are given in Table A.5 for the n_0 state and in Table A.6 for the n_1 state. These data were shown in Figures 4.6 and 4.7.

	E_d=160-0 keV		E_d=130-0 keV		E_d= 80-0 keV	
$\theta_{c.m.}$	$T_{21}(\theta)$	$\Delta T_{21}(\theta)$	$T_{21}(\theta)$	$\Delta T_{21}(\theta)$	$T_{21}(\theta)$	$\Delta T_{21}(\theta)$
30.5°	0.0364	0.0076	0.0095	0.0133		
45.7°	0.0924	0.0088	0.0801	0.0121	0.0617	0.0503
60.9°	0.1415	0.0088	0.1494	0.0175	0.1835	0.0992
91.0°	0.1045	0.0148	0.0801	0.0242		
120.8°	-0.1854	0.0234	-0.2011	0.0303	-0.2276	0.1397
135.7°	-0.2085	0.0169	-0.2121	0.0251		
150.5°	-0.1522	0.0250	-0.2027	0.0292	-0.1491	0.0913

Table A.5: The measured $T_{21}(\theta)$ at E_d=160-0 keV, E_d= 130-0 keV, and E_d= 80-0 keV for ^{7}Li($\vec{d}, n_0$)^{8}Be. Error bars include the statistical and systematic uncertainties.

	E_d=160-0 keV		E_d=130-0 keV		E_d= 80-0 keV	
$\theta_{c.m.}$	$T_{21}(\theta)$	$\Delta T_{21}(\theta)$	$T_{21}(\theta)$	$\Delta T_{21}(\theta)$	$T_{21}(\theta)$	$\Delta T_{21}(\theta)$
30.5°	0.0945	0.0081	0.1012	0.0115		
45.7°	0.1465	0.0093	0.1387	0.0128	0.1249	0.0580
60.9°	0.1348	0.0081	0.1273	0.0162	0.1125	0.0734
91.0°	-0.0086	0.0120	-0.0037	0.0251		
120.8°	-0.1788	0.0198	-0.1803	0.0254	-0.1665	0.1130
135.7°	-0.2134	0.0139	-0.2233	0.0195		
150.5°	-0.2093	0.0193	-0.1902	0.0237	-0.0659	0.0902

Table A.6: The measured $T_{21}(\theta)$ at E_d=160-0 keV, E_d= 130-0 keV, and E_d= 80-0 keV for ^{7}Li($\vec{d}, n_1$)^{8}Be. Error bars include the statistical and systematic uncertainties.

A.4 $T_{22}(\theta)$

The experimental data and their errors for $T_{22}(\theta)$ was described in Section 4.1.4 and shown in Figures 4.8 and 4.9 for the n_0 and n_1 states, respectively. Those data are given in Tables A.7 and A.8.

	E_d=160-0 keV		E_d=130-0 keV		E_d= 80-0 keV	
$\theta_{c.m.}$	$T_{22}(\theta)$	$\Delta T_{22}(\theta)$	$T_{22}(\theta)$	$\Delta T_{22}(\theta)$	$T_{22}(\theta)$	$\Delta T_{22}(\theta)$
0°	0.0196	0.0127	0.0132	0.0189	0.0001	0.0404
22.8°	0.0085	0.0094	0.0322	0.0123	0.0332	0.0272
45.7°	0.0014	0.0086	0.0193	0.0105	0.0326	0.0221
68.4°	-0.0985	0.0121	-0.0858	0.0118	-0.0136	0.0155
91.0°	-0.2527	0.0126	-0.2223	0.0136	-0.1949	0.0156
113.4°	-0.3036	0.0228	-0.2128	0.0195	-0.1108	0.0238
135.7°	-0.1869	0.0247	-0.1761	0.0200	-0.1152	0.0615
150.5°	-0.0786	0.0356	-0.0169	0.0363	-0.0545	0.0555

Table A.7: The measured $T_{22}(\theta)$ at E_d=160-0 keV, E_d= 130-0 keV, and E_d= 80-0 keV for ^{7}Li($\vec{d}, n_0$)^{8}Be. Error bars include the statistical and systematic uncertainties.

	E_d=160-0 keV		E_d=130-0 keV		E_d= 80-0 keV	
$\theta_{c.m.}$	$T_{22}(\theta)$	$\Delta T_{22}(\theta)$	$T_{22}(\theta)$	$\Delta T_{22}(\theta)$	$T_{22}(\theta)$	$\Delta T_{22}(\theta)$
0°	0.0028	0.0121	0.0076	0.0182	0.0526	0.0416
22.8°	0.0085	0.0099	-0.0104	0.0119	-0.0126	0.0227
45.7°	-0.0436	0.0092	-0.0629	0.0108	-0.0620	0.0198
68.4°	-0.1165	0.0103	-0.1124	0.0107	-0.0947	0.0158
91.0°	-0.1430	0.0088	-0.1512	0.0111	-0.0982	0.0137
113.4°	-0.1326	0.0145	-0.1625	0.0162	-0.0988	0.0219
135.7°	-0.0956	0.0170	-0.0958	0.0166	-0.0571	0.0303
150.5°	0.0056	0.0264	-0.0193	0.0273	0.0139	0.0447

Table A.8: The measured $T_{22}(\theta)$ at E_d=160-0 keV, E_d= 130-0 keV, and E_d= 80-0 keV for ^{7}Li$(\vec{d}, n_1)^8$Be. Error bars include the statistical and systematic uncertainties.

A.5 Differential Cross Section

The angular distribution of the differential cross section and its errors, as described in Section 4.2, are given in Table A.9 for the n_0 state and in Table A.10 for the n_1 state. These cross section data were used in the TME calculations of Chapter 5 and are shown in Figures 4.10 and 4.11.

	E_d=160-0 keV		E_d=130-0 keV		E_d= 80-0 keV	
$\theta_{c.m.}$	$\sigma(\theta)$	$\Delta\sigma(\theta)$	$\sigma(\theta)$	$\Delta\sigma(\theta)$	$\sigma(\theta)$	$\Delta\sigma(\theta)$
0°	9.59	0.270	12.84	0.10		
22.8°	9.81	0.27	12.73	0.20	28.56	0.68
45.7°	8.53	0.24	10.89	0.20	18.82	0.55
68.4°	7.08	0.36	8.63	0.18		
91.0°	5.29	0.28	5.99	0.13	10.82	0.30
113.4°	3.58	0.21	5.06	0.12	7.14	0.28
150.5°	3.15	0.29	3.90	0.12	1.20	0.18

Table A.9: The measured $\sigma(\theta)$ at E_d=160-0 keV, E_d= 130-0 keV, and E_d= 80-0 keV for ^{7}Li$(\vec{d}, n_0)^8$Be. The $\sigma(\theta)$ for each incident deuteron energy have been normalized independently from one another and from the ^{7}Li$(\vec{d}, n_1)^8$Be sets and have arbitrary units. Error bars include the statistical and systematic uncertainties.

	E_d=160-0 keV		E_d=130-0 keV		E_d= 80-0 keV	
$\theta_{c.m.}$	$\sigma(\theta)$	$\Delta\sigma(\theta)$	$\sigma(\theta)$	$\Delta\sigma(\theta)$	$\sigma(\theta)$	$\Delta\sigma(\theta)$
0°	8.51	0.25	7.19	0.22	4.74	0.24
22.8°	8.77	0.25	7.86	0.24	4.99	0.23
45.7°	9.73	0.32	9.24	0.32		
68.4°	11.22	0.48	10.06	0.44	8.78	0.57
91.0°	10.42	0.44				
113.4°	9.00	0.44	8.85	0.45	8.93	0.43
150.5°	10.69	1.03	7.06	0.73	4.96	2.92

Table A.10: The measured $\sigma(\theta)$ at E_d=160-0 keV, E_d= 130-0 keV, and E_d= 80-0 keV for ^{7}Li$(\vec{d}, n_1)^8$Be. The $\sigma(\theta)$ for each incident deuteron energy have been normalized independently from one another and from the ^{7}Li$(\vec{d}, n_0)^8$Be sets and have arbitrary units. Error bars include the statistical and systematic uncertainties.

A.6 Integrated Yields for the S-Factor Calculation

The angular distributions of the integrated yields in Section 6.2 shown in Figure 6.1 for the n_0 state and Figure 6.2 for the n_1 state are given in Tables A.11 and A.12. These angular distributions were fit to a Legendre polynomial distribution then integrated over all angles to obtain the total integrated yield values used to determine the S factor.

	E_d=80-0 keV		E_d=60-0 keV		E_d= 45-0 keV	
$\theta_{c.m.}$	$Y_{80}(\theta)$	$\Delta Y_{80}(\theta)$	$Y_{60}(\theta)$	$\Delta Y_{60}(\theta)$	$Y_{45}(\theta)$	$\Delta Y_{45}(\theta)$
0°	0.871	0.117	0.0778	0.0147	0.00565	0.00162
22.8°	0.831	0.110	0.0710	0.0129	0.00751	0.00210
45.7°	0.775	0.105	0.0700	0.0112	0.00606	0.00171
68.4°	0.756	0.114	0.0702	0.0160		
91.0°	0.528	0.054	0.0488	0.0111		
113.4°	0.390	0.066	0.0318	0.0204	0.00159	0.00058
135.7°					0.00059	0.00025
150.5°	0.173	0.053	0.0224	0.0154	0.00030	0.00031

Table A.11: The measured integrated yield $Y(\theta)$ at E_d=80-0 keV, E_d= 60-0 keV, and E_d= 45-0 keV for $^7Li(d, n_0)^8Be$. The yields have been normalized by BCI, detector efficiency, solid angle, percentage of the spectrum summed over, and dead time. Error bars include the statistical and systematic uncertainties.

	E_d=80-0 keV		E_d=60-0 keV		E_d= 45-0 keV	
$\theta_{c.m.}$	$Y_{80}(\theta)$	$\Delta Y_{80}(\theta)$	$Y_{60}(\theta)$	$\Delta Y_{60}(\theta)$	$Y_{45}(\theta)$	$\Delta Y_{45}(\theta)$
0°	2.864	0.407	0.294	0.057	0.0218	0.0060
22.8°	3.271	0.432	0.370	0.038	0.0352	0.0097
45.7°	2.703	0.358	0.337	0.052	0.0297	0.0082
68.4°	4.568	0.686	0.493	0.070	0.0335	0.0092
91.0°	4.597	0.451	0.580	0.140		
113.4°	3.720	0.610	0.338	0.217	0.0428	0.0131
135.7°	3.303	0.541	0.350	0.065	0.0257	0.0079
150.5°	1.904	0.580	0.171	0.079	0.0063	0.0022

Table A.12: The measured integrated yield $Y(\theta)$ at E_d=80-0 keV, E_d= 60-0 keV, and E_d= 45-0 keV for $^7Li(d, n_1)^8Be$. The yields have been normalized by BCI, detector efficiency, solid angle, percentage of the spectrum summed over, and dead time. Error bars include the statistical and systematic uncertainties.

Appendix B

Legendre Polynomial Coefficients

In Chapter 5 and Chapter 6, it was necessary to expand the observables in terms of Legendre polynomials. The results of those expansions are given here.

B.1 Individual Legendre Polynomial Fits

The cross section and analyzing powers were expanded in terms of Legendre polynomials according the formalism described in Section 5.1 for both the $^7\mathrm{Li}(\vec{\mathrm{d}},\mathrm{n}_0)^8\mathrm{Be}$ and $^7\mathrm{Li}(\vec{\mathrm{d}},\mathrm{n}_1)^8\mathrm{Be}$ reactions. To obtain the best fit, it was necessary to expand the $^7\mathrm{Li}(\vec{\mathrm{d}},\mathrm{n}_0)^8\mathrm{Be}$ reaction to order $k = 4$ and the $^7\mathrm{Li}(\vec{\mathrm{d}},\mathrm{n}_1)^8\mathrm{Be}$ reaction to order $k = 2$. The values of the coefficients from those expansions are given in Table B.1 and Table B.2. In both cases, there are no b coefficients for $\mathrm{E_d}$= 80 keV because there was no $i\mathrm{T}_{11}(\theta)$ data at that energy.

Coefficient	160 keV	130 keV	80 keV
A_0	5.676 ± 0.113	7.170 ± 0.063	11.389 ± 0.194
a_1	0.681 ± 0.035	0.670 ± 0.016	1.105 ± 0.033
a_2	0.154 ± 0.042	0.215 ± 0.016	0.272 ± 0.034
a_3	-0.129 ± 0.056	0.024 ± 0.023	0.371 ± 0.052
a_4	0.024 ± 0.064	-0.109 ± 0.029	0.261 ± 0.063
b_1	0.624 ± 0.030	0.505 ± 0.019	
b_2	0.196 ± 0.023	0.123 ± 0.015	
b_3	0.059 ± 0.017	0.045 ± 0.011	
b_4	-0.042 ± 0.016	-0.014 ± 0.012	
c_0	-0.101 ± 0.009	-0.098 ± 0.009	-0.051 ± 0.024
c_1	-0.070 ± 0.018	-0.067 ± 0.020	-0.135 ± 0.038
c_2	-0.171 ± 0.020	-0.202 ± 0.022	-0.074 ± 0.044
c_3	0.136 ± 0.027	0.099 ± 0.030	0.154 ± 0.063
c_4	0.045 ± 0.028	0.132 ± 0.029	0.149 ± 0.056
d_1	0.131 ± 0.016	0.084 ± 0.023	0.162 ± 0.199
d_2	0.186 ± 0.010	0.198 ± 0.013	0.164 ± 0.060
d_3	-0.046 ± 0.008	-0.059 ± 0.011	-0.069 ± 0.119
d_4	-0.042 ± 0.008	-0.054 ± 0.011	-0.100 ± 0.073
e_2	-0.129 ± 0.007	-0.105 ± 0.005	-0.061 ± 0.007
e_3	0.019 ± 0.003	0.022 ± 0.003	0.018 ± 0.004
e_4	0.010 ± 0.002	0.007 ± 0.002	0.014 ± 0.002

Table B.1: Legendre polynomial fits of order $k = 4$ to the $^7\mathrm{Li}(\vec{\mathrm{d}}, \mathrm{n}_0)^8\mathrm{Be}$ data.

B.2 TME Fits

Once the TME fits had been performed to the data sets, each solution gave values of Legendre polynomial coefficients for that solution. These coefficients can be compared with those obtained from the individual Legendre polynomial expansions given in the previous section. By virtue of the $9 - j$ symbol in Equation 5.22 and the input parameters, the FATSO code expanded the $^7\mathrm{Li}(\vec{\mathrm{d}}, \mathrm{n}_0)^8\mathrm{Be}$ equations to order $k = 4$ for the a and b coefficients and to order $k = 6$ for the c, d, and e coefficients. In addition, the $^7\mathrm{Li}(\vec{\mathrm{d}}, \mathrm{n}_1)^8\mathrm{Be}$ equations were expanded for the same reasons to order $k = 4$ for the c, d, and e coefficients. It should be noted, however, that in both cases,

Coefficient	160 keV	130 keV	80 keV
A_0	9.117 ± 0.275	8.946 ± 0.232	7.925 ± 0.286
a_1	0.235 ± 0.074	0.104 ± 0.042	-0.065 ± 0.098
a_2	-0.319 ± 0.063	-0.292 ± 0.044	-0.371 ± 0.099
b_1	-0.018 ± 0.021	-0.003 ± 0.016	
b_2	-0.041 ± 0.016	-0.025 ± 0.010	
c_0	0.086 ± 0.008	0.066 ± 0.008	0.073 ± 0.032
c_1	0.056 ± 0.011	0.064 ± 0.013	0.023 ± 0.075
c_2	-0.260 ± 0.017	-0.287 ± 0.017	-0.157 ± 0.067
d_1	-0.006 ± 0.015	-0.057 ± 0.020	0.007 ± 0.114
d_2	0.210 ± 0.011	0.208 ± 0.012	0.150 ± 0.060
e_2	-0.099 ± 0.006	-0.108 ± 0.006	-0.079 ± 0.008

Table B.2: Legendre polynomial fits of order $k = 2$ to the $^7\mathrm{Li}(\vec{\mathrm{d}}, \mathrm{n}_1)^8\mathrm{Be}$ data.

the coefficients of order higher than those expanded in the individual fits were very close to 0. The coefficients for the $^7\mathrm{Li}(\vec{\mathrm{d}}, \mathrm{n}_0)^8\mathrm{Be}$ reaction are given in Table B.3, and those for the $^7\mathrm{Li}(\vec{\mathrm{d}}, \mathrm{n}_1)^8\mathrm{Be}$ reaction are given in Table B.4.

B.3 S-factor Yield Fits

In chapter Chapter 6, the angular distribution of the yields for each energy for the $^7\mathrm{Li}(\vec{\mathrm{d}}, \mathrm{n}_0)^8\mathrm{Be}$ and $^7\mathrm{Li}(\vec{\mathrm{d}}, \mathrm{n}_1)^8\mathrm{Be}$ reactions were fit with a Legendre polynomial to obtain an integrable, functional form. This Legendre polynomial, when integrated over all angles, would give the total cross section for that energy. The Legendre polynomial coefficients from the fits are given in Table B.5 for the $^7\mathrm{Li}(\vec{\mathrm{d}}, \mathrm{n}_0)^8\mathrm{Be}$ reaction and in Table B.6 for the $^7\mathrm{Li}(\vec{\mathrm{d}}, \mathrm{n}_1)^8\mathrm{Be}$ reaction. The total cross section, as given in Equation 5.4, $\sigma_T = 4\pi \mathrm{A}_0$.

Coefficient	160-0 keV	130-0 keV	80-0 keV
A_0	5.600	7.067	11.602
a_1	0.620	0.646	1.104
a_2	0.109	0.197	0.250
a_3	0.004	0.005	0.229
a_4	0.126	0.026	0.176
b_1	0.579	0.491	0.178
b_2	0.133	0.107	0.144
b_3	0.027	0.026	0.102
b_4	-0.010	0.001	-0.001
c_0	-0.115	-0.101	-0.053
c_1	-0.110	-0.099	-0.156
c_2	-0.187	-0.205	-0.079
c_3	0.116	0.098	0.163
c_4	0.101	0.175	0.239
c_5	0.001	0.001	0.103
c_6	0.026	0.030	0.037
d_1	0.135	0.121	0.166
d_2	0.176	0.166	0.096
d_3	-0.064	-0.054	-0.090
d_4	-0.048	-0.074	-0.101
d_5	-0.000	-0.000	-0.034
d_6	-0.007	-0.008	-0.010
e_2	-0.127	-0.095	-0.067
e_3	0.016	0.014	0.023
e_4	0.012	0.013	0.018
e_5	0.000	0.000	0.004
e_6	0.001	0.001	0.001

Table B.3: Legendre polynomial coefficients from the TME fit to the $^{7}\mathrm{Li}(\vec{\mathrm{d}},\mathrm{n}_0)^{8}\mathrm{Be}$ data.

Coefficient	160-0 keV	130-0 keV	80-0 keV
A_0	10.118	8.660	7.52101
a_1	0.010	0.034	0.000
a_2	-0.104	-0.141	-0.369
b_1	0.012	0.000	0.000
b_2	-0.006	-0.023	-0.017
c_0	0.061	0.062	0.086
c_1	0.056	0.063	0.000
c_2	-0.242	-0.274	-0.142
c_3	-0.006	-0.006	-0.000
c_4	-0.008	-0.007	-0.024
d_1	-0.069	-0.008	-0.000
d_2	0.193	0.220	0.126
d_3	0.003	0.003	0.000
d_4	0.003	0.003	0.010
e_2	-0.089	-0.103	-0.079
e_3	-0.001	-0.001	-0.000
e_4	-0.000	-0.000	-0.002

Table B.4: Legendre polynomial coefficients from the TME fit to the ^{7}Li($\vec{\mathrm{d}}$, n_1)^{8}Be data.

Coefficient	80-0 keV	60-0 keV	45-0 keV
A_0	0.526 ± 0.030	0.0487 ± 0.0060	0.00340 ± 0.00081
a_1	0.738 ± 0.111	0.663 ± 0.224	1.105 ± 0.355
a_2	-0.078 ± 0.101	-0.039 ± 0.237	-0.058 ± 0.300
a_3	-0.040 ± 0.162	-0.126 ± 0.302	-0.244 ± 0.357

Table B.5: Legendre polynomial fits of order $k = 3$ to the ^{7}Li(d, n_0)^{8}Be S-factor yields.

Coefficient	80-0 keV	60-0 keV	45-0 keV
A_0	3.539 ± 0.201	0.421 ± 0.039	0.0290 ± 0.0040
a_1	0.070 ± 0.085	0.134 ± 0.096	0.457 ± 0.144
a_2	-0.509 ± 0.127	-0.618 ± 0.222	-0.545 ± 0.196
a_3	0.263 ± 0.138	0.272 ± 0.206	-0.148 ± 0.156

Table B.6: Legendre polynomial fits of order $k = 3$ to the ^{7}Li(d, n_1)^{8}Be S-factor yields.

Appendix C

Observable Equations

The observable analysis described in Chapter 5 used the TMEs listed in Table 5.4 and Table 5.5 which had been constrained from the TMEs listed in Table 5.2 and Table 5.3. The coefficients in the following equations were calculated using the FORTRAN code FATSO. The $9-j$ symbol, in Equation 5.22 restricts the value of k. For the $^{7}\mathrm{Li}(\vec{\mathrm{d}},\mathrm{n}_0)^{8}\mathrm{Be}$ reaction, k was limited to 4 for the a and b coefficients and to 6 for the others. For the $^{7}\mathrm{Li}(\vec{\mathrm{d}},\mathrm{n}_1)^{8}\mathrm{Be}$ reaciton, k was limited to 2 for the a and b coefficients and to 4 for the rest.

C.1 Equations for the $^{7}\mathrm{Li}(\vec{\mathrm{d}},\mathrm{n}_0)^{8}\mathrm{Be}$ Reaction

C.1.1 Cross Section

Using Equation 5.1 and the constrained TMEs, the formula for cross section in terms of the Legendre polynomials is

$$\sigma(\theta) = \mathrm{A}_0\left(\mathrm{a}_0 + \mathrm{Q}_1\mathrm{a}_1\mathrm{P}_1(\cos\theta) + \mathrm{Q}_2\mathrm{a}_2\mathrm{P}_2(\cos\theta) + \mathrm{Q}_3\mathrm{a}_3\mathrm{P}_3(\cos\theta) + \mathrm{Q}_4\mathrm{a}_4\mathrm{P}_4(\cos\theta)\right), \tag{C.1}$$

where the coefficients can be expanded as

$$\begin{aligned}
\mathrm{a}_0 = \; & 2\left|{}^{2}\mathrm{s}_2\right|^2 + 4\left|{}^{4}\mathrm{s}_4\right|^2 + 6\left|{}^{6}\mathrm{s}_6\right|^2 \\
& + 2\left|{}^{2}\mathrm{p}_2\right|^2 + 2\left|{}^{4}\mathrm{p}_2\right|^2 + 4\left|{}^{2}\mathrm{p}_4\right|^2 + 10\left|{}^{4}\mathrm{p}_{10}\right|^2 + 10\left|{}^{6}\mathrm{p}_{10}\right|^2 \\
& + 4\left|{}^{2}\mathrm{d}_4\right|^2 + 6\left|{}^{4}\mathrm{d}_6\right|^2 + 6\left|{}^{6}\mathrm{d}_6\right|^2 + 6\left|{}^{2}\mathrm{d}_6\right|^2 + 14\left|{}^{4}\mathrm{d}_{14}\right|^2 + 14\left|{}^{6}\mathrm{d}_{14}\right|^2,
\end{aligned} \tag{C.2}$$

$$\begin{aligned}
\mathrm{a}_1 = \; & 4\left|{}^{2}\mathrm{s}_2\right|\left|{}^{2}\mathrm{p}_2\right|\cos\left(\phi_{p-s}\right) + 8\left|{}^{2}\mathrm{s}_2\right|\left|{}^{2}\mathrm{p}_4\right|\cos\left(\phi_{p-s}\right) \\
& - 5.6568\left|{}^{4}\mathrm{s}_4\right|\left|{}^{4}\mathrm{p}_2\right|\cos\left(\phi_{p-s}\right) + 16.7231\left|{}^{4}\mathrm{s}_4\right|\left|{}^{4}\mathrm{p}_{10}\right|\cos\left(\phi_{p-s}\right) \\
& - 7.2199\left|{}^{6}\mathrm{s}_6\right|\left|{}^{6}\mathrm{p}_{10}\right|\cos\left(\phi_{p-s}\right) + 8\left|{}^{2}\mathrm{p}_2\right|\left|{}^{2}\mathrm{d}_4\right|\cos\left(\phi_{d-p}\right) \\
& + 9.65683\left|{}^{4}\mathrm{p}_2\right|\left|{}^{4}\mathrm{d}_6\right|\cos\left(\phi_{d-p}\right) + 1.6\left|{}^{2}\mathrm{p}_4\right|\left|{}^{2}\mathrm{d}_4\right|\cos\left(\phi_{d-p}\right) \\
& + 14.4\left|{}^{2}\mathrm{p}_4\right|\left|{}^{2}\mathrm{d}_6\right|\cos\left(\phi_{d-p}\right) - 2.2968\left|{}^{4}\mathrm{p}_{10}\right|\left|{}^{4}\mathrm{d}_6\right|\cos\left(\phi_{d-p}\right) \\
& + 34.0297\left|{}^{4}\mathrm{p}_{10}\right|\left|{}^{4}\mathrm{d}_{14}\right|\cos\left(\phi_{d-p}\right) + -9.3576\left|{}^{6}\mathrm{p}_{10}\right|\left|{}^{6}\mathrm{d}_6\right|\cos\left(\phi_{d-p}\right) \\
& + 26.9712\left|{}^{6}\mathrm{p}_{10}\right|\left|{}^{6}\mathrm{d}_{14}\right|\cos\left(\phi_{d-p}\right),
\end{aligned} \tag{C.3}$$

$$
\begin{aligned}
\mathrm{a}_2 = {} & 8\left|{}^2\mathrm{s}_2\right|\left|{}^2\mathrm{d}_4\right|\cos\left(\phi_{d-p}+\phi_{p-s}\right)+12\left|{}^2\mathrm{s}_2\right|\left|{}^2\mathrm{d}_6\right|\cos\left(\phi_{d-p}+\phi_{p-s}\right) \\
& -13.6569\left|{}^4\mathrm{s}_4\right|\left|{}^4\mathrm{d}_6\right|\cos\left(\phi_{d-p}+\phi_{p-s}\right)+24.5566\left|{}^4\mathrm{s}_4\right|\left|{}^4\mathrm{d}_{14}\right|\cos\left(\phi_{d-p}+\phi_{p-s}\right) \\
& +1.691\left|{}^6\mathrm{s}_6\right|\left|{}^6\mathrm{d}_6\right|\cos\left(\phi_{d-p}+\phi_{p-s}\right)-6.7811\left|{}^6\mathrm{s}_6\right|\left|{}^6\mathrm{d}_{14}\right|\cos\left(\phi_{d-p}+\phi_{p-s}\right) \\
& +8\left|{}^2\mathrm{p}_2\right|\left|{}^2\mathrm{p}_4\right|\cos\left(\delta^p\right)-11.825\left|{}^4\mathrm{p}_2\right|\left|{}^4\mathrm{p}_{10}\right|\cos\left(\delta^p\right) \\
& +4\left|{}^2\mathrm{p}_4\right|^2+7.4788\left|{}^4\mathrm{p}_{10}\right|^2-7.828\left|{}^6\mathrm{p}_{10}\right|^2 \\
& +4\left|{}^2\mathrm{d}_4\right|^2+3.4286\left|{}^2\mathrm{d}_4\right|\left|{}^2\mathrm{d}_6\right|\cos\left(\delta^d\right)+5.6568\left|{}^4\mathrm{d}_6\right|^2 \\
& -5.1375\left|{}^4\mathrm{d}_6\right|\left|{}^4\mathrm{d}_{14}\right|\cos\left(\delta^d\right)-5.8809\left|{}^6\mathrm{d}_6\right|^2-15.5872\left|{}^6\mathrm{d}_6\right|\left|{}^6\mathrm{d}_{14}\right|\cos\left(\delta^d\right) \\
& +6.8571\left|{}^2\mathrm{d}_6\right|^2+14.7683\left|{}^4\mathrm{d}_{14}\right|^2+2.8368\left|{}^6\mathrm{d}_{14}\right|^2,
\end{aligned}
\tag{C.4}
$$

$$
\begin{aligned}
\mathrm{a}_3 = {} & 12\left|{}^2\mathrm{p}_2\right|\left|{}^2\mathrm{d}_6\right|\cos\left(\phi_{d-p}\right)-17.3641\left|{}^4\mathrm{p}_2\right|\left|{}^4\mathrm{d}_{14}\right|\cos\left(\phi_{d-p}\right) \\
& +14.4\left|{}^2\mathrm{p}_4\right|\left|{}^2\mathrm{d}_4\right|\cos\left(\phi_{d-p}\right)+9.6\left|{}^2\mathrm{p}_4\right|\left|{}^2\mathrm{d}_6\right|\cos\left(\phi_{d-p}\right) \\
& -26.2513\left|{}^4\mathrm{p}_{10}\right|\left|{}^4\mathrm{d}_6\right|\cos\left(\phi_{d-p}\right)+17.3028\left|{}^4\mathrm{p}_{10}\right|\left|{}^4\mathrm{d}_{14}\right|\cos\left(\phi_{d-p}\right) \\
& +8.3402\left|{}^6\mathrm{p}_{10}\right|\left|{}^6\mathrm{d}_6\right|\cos\left(\phi_{d-p}\right)-22.8912\left|{}^6\mathrm{p}_{10}\right|\left|{}^6\mathrm{d}_{14}\right|\cos\left(\phi_{d-p}\right),
\end{aligned}
\tag{C.5}
$$

and

$$
\begin{aligned}
\mathrm{a}_4 = {} & 20.5714\left|{}^2\mathrm{d}_4\right|\left|{}^2\mathrm{d}_6\right|\cos\left(\delta^d\right)-36.7832\left|{}^4\mathrm{d}_6\right|\left|{}^4\mathrm{d}_{14}\right|\cos\left(\delta^d\right) \\
& +14.6316\left|{}^6\mathrm{d}_6\right|\left|{}^6\mathrm{d}_{14}\right|\cos\left(\delta^d\right)+5.1429\left|{}^2\mathrm{d}_6\right|^2+8.9075\left|{}^4\mathrm{d}_{14}\right|^2 \\
& -14.9207\left|{}^6\mathrm{d}_{14}\right|^2.
\end{aligned}
\tag{C.6}
$$

C.1.2 $i\mathrm{T}_{11}$

From Equation 5.6, the expansion of $i\mathrm{T}_{11}(\theta)$is

$$
\frac{i\mathrm{T}_{11}(\theta)\ \sigma(\theta)}{\mathrm{A}_0}=\mathrm{Q}_1\mathrm{b}_1\mathrm{P}_1^1(\cos\theta)+\mathrm{Q}_2\mathrm{b}_2\mathrm{P}_2^1(\cos\theta)+\mathrm{Q}_3\mathrm{b}_3\mathrm{P}_3^1(\cos\theta)+\mathrm{Q}_4\mathrm{b}_4\mathrm{P}_4^1(\cos\theta). \tag{C.7}
$$

The coefficients are:

$$
\begin{aligned}
\mathrm{b}_1 = & -2.3094\left|{}^2\mathrm{s}_2\right|\left|{}^2\mathrm{p}_2\right|\sin\left(\phi_{p-s}\right) - 2.5820\left|{}^2\mathrm{s}_2\right|\left|{}^4\mathrm{p}_2\right|\sin\left(\phi_{p-s}\right) \\
& + 2.3094\left|{}^2\mathrm{s}_2\right|\left|{}^2\mathrm{p}_4\right|\sin\left(\phi_{p-s}\right) - 8.1649\left|{}^2\mathrm{s}_2\right|\left|{}^4\mathrm{p}_{10}\right|\sin\left(\phi_{p-s}\right) \\
& + 3.6515\left|{}^4\mathrm{s}_4\right|\left|{}^2\mathrm{p}_2\right|\sin\left(\phi_{p-s}\right) - 3.266\left|{}^4\mathrm{s}_4\right|\left|{}^4\mathrm{p}_2\right|\sin\left(\phi_{p-s}\right) \\
& - 3.6515\left|{}^4\mathrm{s}_4\right|\left|{}^2\mathrm{p}_4\right|\sin\left(\phi_{p-s}\right) - 3.7274\left|{}^4\mathrm{s}_4\right|\left|{}^4\mathrm{p}_{10}\right|\sin\left(\phi_{p-s}\right) \\
& - 12.7106\left|{}^4\mathrm{s}_4\right|\left|{}^6\mathrm{p}_{10}\right|\sin\left(\phi_{p-s}\right) + 4.042\left|{}^6\mathrm{s}_6\right|\left|{}^4\mathrm{p}_{10}\right|\sin\left(\phi_{p-s}\right) \\
& - 11.7962\left|{}^6\mathrm{s}_6\right|\left|{}^6\mathrm{p}_{10}\right|\sin\left(\phi_{p-s}\right) - 2.3094\left|{}^2\mathrm{p}_2\right|\left|{}^2\mathrm{d}_4\right|\sin\left(\phi_{d-p}\right) \\
& - 4.721\left|{}^2\mathrm{p}_2\right|\left|{}^4\mathrm{d}_6\right|\sin\left(\phi_{d-p}\right) - 2.582\left|{}^4\mathrm{p}_2\right|\left|{}^2\mathrm{d}_4\right|\sin\left(\phi_{d-p}\right) \\
& + 2.5007\left|{}^4\mathrm{p}_2\right|\left|{}^4\mathrm{d}_6\right|\sin\left(\phi_{d-p}\right) - 7.5775\left|{}^4\mathrm{p}_2\right|\left|{}^6\mathrm{d}_6\right|\sin\left(\phi_{d-p}\right) \\
& - 1.8475\left|{}^2\mathrm{p}_4\right|\left|{}^2\mathrm{d}_4\right|\sin\left(\phi_{d-p}\right) - 1.8517\left|{}^2\mathrm{p}_4\right|\left|{}^4\mathrm{d}_6\right|\sin\left(\phi_{d-p}\right) \\
& + 4.1569\left|{}^2\mathrm{p}_4\right|\left|{}^2\mathrm{d}_6\right|\sin\left(\phi_{d-p}\right) - 12.2964\left|{}^2\mathrm{p}_4\right|\left|{}^4\mathrm{d}_{14}\right|\sin\left(\phi_{d-p}\right) \\
& + 1.3138\left|{}^4\mathrm{p}_{10}\right|\left|{}^2\mathrm{d}_4\right|\sin\left(\phi_{d-p}\right) - 3.4551\left|{}^4\mathrm{p}_{10}\right|\left|{}^4\mathrm{d}_6\right|\sin\left(\phi_{d-p}\right) \\
& - 5.8804\left|{}^4\mathrm{p}_{10}\right|\left|{}^6\mathrm{d}_6\right|\sin\left(\phi_{d-p}\right) - 9.4788\left|{}^4\mathrm{p}_{10}\right|\left|{}^2\mathrm{d}_6\right|\sin\left(\phi_{d-p}\right) \\
& - 7.302\left|{}^4\mathrm{p}_{10}\right|\left|{}^4\mathrm{d}_{14}\right|\sin\left(\phi_{d-p}\right) - 23.1688 - 7.302\left|{}^4\mathrm{p}_{10}\right|\left|{}^6\mathrm{d}_{14}\right|\sin\left(\phi_{d-p}\right) \\
& + 4.4174\left|{}^6\mathrm{p}_{10}\right|\left|{}^4\mathrm{d}_6\right|\sin\left(\phi_{d-p}\right) - 15.2802\left|{}^6\mathrm{p}_{10}\right|\left|{}^6\mathrm{d}_6\right|\sin\left(\phi_{d-p}\right) \\
& - 9.2139\left|{}^6\mathrm{p}_{10}\right|\left|{}^4\mathrm{d}_{14}\right|\sin\left(\phi_{d-p}\right) - 7.5894\left|{}^6\mathrm{p}_{10}\right|\left|{}^6\mathrm{d}_{14}\right|\sin\left(\phi_{d-p}\right),
\end{aligned}
\tag{C.8}
$$

$$
\begin{aligned}
\mathrm{b}_2 = & -2.3094\left|{}^2\mathrm{s}_2\right|\left|{}^2\mathrm{d}_4\right|\sin\left(\phi_{d-p}+\phi_{p-s}\right) - 3.6515\left|{}^2\mathrm{s}_2\right|\left|{}^4\mathrm{d}_6\right|\sin\left(\phi_{d-p}+\phi_{p-s}\right) \\
& + 2.3094\left|{}^2\mathrm{s}_2\right|\left|{}^2\mathrm{d}_6\right|\sin\left(\phi_{d-p}+\phi_{p-s}\right) - 6.8313\left|{}^2\mathrm{s}_2\right|\left|{}^4\mathrm{d}_{14}\right|\sin\left(\phi_{d-p}+\phi_{p-s}\right) \\
& + 3.6515\left|{}^4\mathrm{s}_4\right|\left|{}^2\mathrm{d}_4\right|\sin\left(\phi_{d-p}+\phi_{p-s}\right) - 3.8071\left|{}^4\mathrm{s}_4\right|\left|{}^4\mathrm{d}_6\right|\sin\left(\phi_{d-p}+\phi_{p-s}\right) \\
& + 3.5721\left|{}^4\mathrm{s}_4\right|\left|{}^6\mathrm{d}_6\right|\sin\left(\phi_{d-p}+\phi_{p-s}\right) - 3.6515\left|{}^4\mathrm{s}_4\right|\left|{}^2\mathrm{d}_6\right|\sin\left(\phi_{d-p}+\phi_{p-s}\right) \\
& - 3.9429\left|{}^4\mathrm{s}_4\right|\left|{}^4\mathrm{d}_{14}\right|\sin\left(\phi_{d-p}+\phi_{p-s}\right) - 10.4185\left|{}^4\mathrm{s}_4\right|\left|{}^6\mathrm{d}_{14}\right|\sin\left(\phi_{d-p}+\phi_{p-s}\right)
\end{aligned}
\tag{C.9}
$$

$$
\begin{aligned}
&+ 0.497 \left|{}^6\mathrm{s}_6\right| \left|{}^4\mathrm{d}_6\right| \sin\left(\phi_{d-p} + \phi_{p-s}\right) + 2.274 \left|{}^6\mathrm{s}_6\right| \left|{}^6\mathrm{d}_6\right| \sin\left(\phi_{d-p} + \phi_{p-s}\right) \\
&+ 2.877 \left|{}^6\mathrm{s}_6\right| \left|{}^4\mathrm{d}_{14}\right| \sin\left(\phi_{d-p} + \phi_{p-s}\right) - 4.7931 \left|{}^6\mathrm{s}_6\right| \left|{}^6\mathrm{d}_{14}\right| \sin\left(\phi_{d-p} + \phi_{p-s}\right) \\
&+ 2.3094 \left|{}^2\mathrm{p}_2\right| \left|{}^2\mathrm{p}_4\right| \sin\left(\delta^p\right) - 5.266 \left|{}^2\mathrm{p}_2\right| \left|{}^4\mathrm{p}_{10}\right| \sin\left(\delta^p\right) \\
&+ 2.582 \left|{}^4\mathrm{p}_2\right| \left|{}^2\mathrm{p}_4\right| \sin\left(\delta^p\right) + 3.1543 \left|{}^4\mathrm{p}_2\right| \left|{}^4\mathrm{p}_{10}\right| \sin\left(\delta^p\right) \\
&+ 2.9959 \left|{}^4\mathrm{p}_2\right| \left|{}^6\mathrm{p}_{10}\right| \sin\left(\delta^p\right) + 1.6496 \left|{}^2\mathrm{d}_4\right| \left|{}^2\mathrm{d}_6\right| \sin\left(\delta^d\right) \\
&- 2.2265 \left|{}^2\mathrm{d}_4\right| \left|{}^4\mathrm{d}_{14}\right| \sin\left(\delta^d\right) + 1.5387 \left|{}^4\mathrm{d}_6\right| \left|{}^2\mathrm{d}_6\right| \sin\left(\delta^d\right) \\
&+ 2.909 \left|{}^4\mathrm{d}_6\right| \left|{}^4\mathrm{d}_{14}\right| \sin\left(\delta^d\right) - 1.754 \left|{}^4\mathrm{d}_6\right| \left|{}^6\mathrm{d}_{14}\right| \sin\left(\delta^d\right) \\
&+ 2.6395 \left|{}^6\mathrm{d}_6\right| \left|{}^4\mathrm{d}_{14}\right| \sin\left(\delta^d\right) + 9.8968 \left|{}^6\mathrm{d}_6\right| \left|{}^6\mathrm{d}_{14}\right| \sin\left(\delta^d\right),
\end{aligned}
$$

$$
\begin{aligned}
\mathrm{b}_3 = {} & 2.3094 \left|{}^2\mathrm{p}_2\right| \left|{}^2\mathrm{d}_6\right| \sin\left(\phi_{d-p}\right) - 5.2837 \left|{}^2\mathrm{p}_2\right| \left|{}^4\mathrm{d}_{14}\right| \sin\left(\phi_{d-p}\right) \\
& + 2.582 \left|{}^4\mathrm{p}_2\right| \left|{}^2\mathrm{d}_6\right| \sin\left(\phi_{d-p}\right) + 3.0649 \left|{}^4\mathrm{p}_2\right| \left|{}^4\mathrm{d}_{14}\right| \sin\left(\phi_{d-p}\right) \\
& + 3.6835 \left|{}^4\mathrm{p}_2\right| \left|{}^6\mathrm{d}_{14}\right| \sin\left(\phi_{d-p}\right) - 2.7713 \left|{}^2\mathrm{p}_4\right| \left|{}^2\mathrm{d}_4\right| \sin\left(\phi_{d-p}\right) \\
& - 4.3818 \left|{}^2\mathrm{p}_4\right| \left|{}^4\mathrm{d}_6\right| \sin\left(\phi_{d-p}\right) + 0.4619 \left|{}^2\mathrm{p}_4\right| \left|{}^2\mathrm{d}_6\right| \sin\left(\phi_{d-p}\right) \\
& - 2.9138 \left|{}^2\mathrm{p}_4\right| \left|{}^4\mathrm{d}_{14}\right| \sin\left(\phi_{d-p}\right) + 6.3192 \left|{}^4\mathrm{p}_{10}\right| \left|{}^2\mathrm{d}_4\right| \sin\left(\phi_{d-p}\right) \\
& - 4.4638 \left|{}^4\mathrm{p}_{10}\right| \left|{}^4\mathrm{d}_6\right| \sin\left(\phi_{d-p}\right) + 4.6187 \left|{}^4\mathrm{p}_{10}\right| \left|{}^6\mathrm{d}_6\right| \sin\left(\phi_{d-p}\right) \\
& + 1.8458 \left|{}^4\mathrm{p}_{10}\right| \left|{}^2\mathrm{d}_6\right| \sin\left(\phi_{d-p}\right) - 0.9972 \left|{}^4\mathrm{p}_{10}\right| \left|{}^4\mathrm{d}_{14}\right| \sin\left(\phi_{d-p}\right) \\
& - 6.6471 \left|{}^4\mathrm{p}_{10}\right| \left|{}^6\mathrm{d}_{14}\right| \sin\left(\phi_{d-p}\right) - 4.5022 \left|{}^6\mathrm{p}_{10}\right| \left|{}^4\mathrm{d}_6\right| \sin\left(\phi_{d-p}\right) \\
& + 2.1397 \left|{}^6\mathrm{p}_{10}\right| \left|{}^6\mathrm{d}_6\right| \sin\left(\phi_{d-p}\right) + 7.1729 \left|{}^6\mathrm{p}_{10}\right| \left|{}^4\mathrm{d}_{14}\right| \sin\left(\phi_{d-p}\right) \\
& + 1.5958 \left|{}^6\mathrm{p}_{10}\right| \left|{}^6\mathrm{d}_{14}\right| \sin\left(\phi_{d-p}\right),
\end{aligned}
\tag{C.10}
$$

and

$$
\begin{aligned}
\mathrm{b_4} = {} & 2.9692\left|{}^2\mathrm{d_4}\right|\left|{}^2\mathrm{d_6}\right|\sin\left(\delta^d\right) - 6.7934\left|{}^2\mathrm{d_4}\right|\left|{}^4\mathrm{d_{14}}\right|\sin\left(\delta^d\right) \\
& + 4.6948\left|{}^4\mathrm{d_6}\right|\left|{}^2\mathrm{d_6}\right|\sin\left(\delta^d\right) + 4.6524\left|{}^4\mathrm{d_6}\right|\left|{}^4\mathrm{d_{14}}\right|\sin\left(\delta^d\right) \\
& + 5.9461\left|{}^4\mathrm{d_6}\right|\left|{}^6\mathrm{d_{14}}\right|\sin\left(\delta^d\right) - 3.3305\left|{}^6\mathrm{d_6}\right|\left|{}^4\mathrm{d_{14}}\right|\sin\left(\delta^d\right) \\
& - 2.7862\left|{}^6\mathrm{d_6}\right|\left|{}^6\mathrm{d_{14}}\right|\sin\left(\delta^d\right).
\end{aligned}
\tag{C.11}
$$

C.1.3 $\mathrm{T_{20}}$

Equation 5.7 gives

$$
\begin{aligned}
\frac{\mathrm{T_{20}}(\theta)\ \sigma(\theta)}{\mathrm{A_0}} = {} & \mathrm{c_0} + \mathrm{Q_1 c_1 P_1}(\cos\theta) + \mathrm{Q_2 c_2 P_2}(\cos\theta) + \mathrm{Q_3 c_3 P_3}(\cos\theta) \\
& + \mathrm{Q_4 c_4 P_4}(\cos\theta) + \mathrm{Q_5 c_5 P_5}(\cos\theta) + \mathrm{Q_6 c_6 P_6}(\cos\theta),
\end{aligned}
\tag{C.12}
$$

where the coefficients are

$$
\begin{aligned}
\mathrm{c_0} = {} & -1.2649\left|{}^2\mathrm{s_2}\right|\left|{}^4\mathrm{d_6}\right|\cos\left(\phi_{d-p}+\phi_{p-s}\right) + 3.7947\left|{}^2\mathrm{s_2}\right|\left|{}^6\mathrm{d_6}\right|\cos\left(\phi_{d-p}+\phi_{p-s}\right) \\
& + 1.7889\left|{}^4\mathrm{s_4}\right|\left|{}^2\mathrm{d_4}\right|\cos\left(\phi_{d-p}+\phi_{p-s}\right) - 4.5255\left|{}^4\mathrm{s_4}\right|\left|{}^4\mathrm{d_6}\right|\cos\left(\phi_{d-p}+\phi_{p-s}\right) \\
& + 6.3498\left|{}^4\mathrm{s_4}\right|\left|{}^6\mathrm{d_6}\right|\cos\left(\phi_{d-p}+\phi_{p-s}\right) + 6.5727\left|{}^6\mathrm{s_6}\right|\left|{}^2\mathrm{d_6}\right|\cos\left(\phi_{d-p}+\phi_{p-s}\right) \\
& - 7.7769\left|{}^6\mathrm{s_6}\right|\left|{}^4\mathrm{d_{14}}\right|\cos\left(\phi_{d-p}+\phi_{p-s}\right) + 6.3498\left|{}^6\mathrm{s_6}\right|\left|{}^6\mathrm{d_{14}}\right|\cos\left(\phi_{d-p}+\phi_{p-s}\right) \\
& - 1.2649\left|{}^2\mathrm{p_2}\right|\left|{}^4\mathrm{p_2}\right| + 1.1314\left|{}^4\mathrm{p_2}\right|^2 + 0.8\left|{}^2\mathrm{p_4}\right|\left|{}^4\mathrm{p_{10}}\right| - 5.8788\left|{}^2\mathrm{p_4}\right|\left|{}^6\mathrm{p_{10}}\right| \\
& - 1.1314\left|{}^4\mathrm{p_{10}}\right|^2 + 1.1536\left|{}^4\mathrm{p_{10}}\right|\left|{}^6\mathrm{p_{10}}\right| + 1.1314\left|{}^6\mathrm{p_{10}}\right|^2 - 1.7889\left|{}^2\mathrm{d_4}\right|\left|{}^4\mathrm{d_6}\right| \\
& - 2.8685\left|{}^2\mathrm{d_4}\right|\left|{}^6\mathrm{d_6}\right| + 1.1314\left|{}^4\mathrm{d_6}\right|^2 + 6.2326\left|{}^4\mathrm{d_6}\right|\left|{}^6\mathrm{d_6}\right| + 1.4343\left|{}^2\mathrm{d_6}\right|\left|{}^4\mathrm{d_6}\right| \\
& - 1.9395\left|{}^6\mathrm{d_6}\right|^2 + 1.4343\left|{}^2\mathrm{d_6}\right|\left|{}^4\mathrm{d_{14}}\right| - 7.0265\left|{}^2\mathrm{d_6}\right|\left|{}^6\mathrm{d_{14}}\right| - 1.1314\left|{}^4\mathrm{d_{14}}\right|^2 \\
& - 4.1569\left|{}^4\mathrm{d_{14}}\right|\left|{}^6\mathrm{d_{14}}\right| + 3.9598\left|{}^6\mathrm{d_{14}}\right|^2,
\end{aligned}
\tag{C.13}
$$

$$
\begin{aligned}
c_1 = & -1.2649\left|{}^2s_2\right|\left|{}^4p_2\right|\cos\left(\phi_{p-s}\right)+0.8\left|{}^2s_2\right|\left|{}^4p_{10}\right|\cos\left(\phi_{p-s}\right)\\
& -5.8788\left|{}^2s_2\right|\left|{}^6p_{10}\right|\cos\left(\phi_{p-s}\right)+1.7889\left|{}^4s_4\right|\left|{}^2p_2\right|\cos\left(\phi_{p-s}\right)\\
& -3.2\left|{}^4s_4\right|\left|{}^4p_2\right|\cos\left(\phi_{p-s}\right)+0.3578\left|{}^4s_4\right|\left|{}^2p_4\right|\cos\left(\phi_{p-s}\right)\\
& -0.1319\left|{}^4s_4\right|\left|{}^4p_{10}\right|\cos\left(\phi_{p-s}\right)-2.5088\left|{}^4s_4\right|\left|{}^6p_{10}\right|\cos\left(\phi_{p-s}\right)\\
& +7.8872\left|{}^6s_6\right|\left|{}^2p_4\right|\cos\left(\phi_{p-s}\right)-9.174\left|{}^6s_6\right|\left|{}^4p_{10}\right|\cos\left(\phi_{p-s}\right)\\
& +5.84\left|{}^6s_6\right|\left|{}^6p_{10}\right|\cos\left(\phi_{p-s}\right)-3.0538\left|{}^2p_2\right|\left|{}^4d_6\right|\cos\left(\phi_{d-p}\right)\\
& +0.9262\left|{}^2p_2\right|\left|{}^6d_6\right|\cos\left(\phi_{d-p}\right)-2.5298\left|{}^4p_2\right|\left|{}^2d_4\right|\cos\left(\phi_{d-p}\right)\\
& +5.4627\left|{}^4p_2\right|\left|{}^4d_6\right|\cos\left(\phi_{d-p}\right)+0.4142\left|{}^4p_2\right|\left|{}^6d_6\right|\cos\left(\phi_{d-p}\right)\\
& -2.8876\left|{}^2p_4\right|\left|{}^4d_6\right|\cos\left(\phi_{d-p}\right)+7.0158\left|{}^2p_4\right|\left|{}^6d_6\right|\cos\left(\phi_{d-p}\right)\\
& +1.7211\left|{}^2p_4\right|\left|{}^4d_{14}\right|\cos\left(\phi_{d-p}\right)-8.4318\left|{}^2p_4\right|\left|{}^6d_{14}\right|\cos\left(\phi_{d-p}\right)\\
& +3.6873\left|{}^4p_{10}\right|\left|{}^2d_4\right|\cos\left(\phi_{d-p}\right)-10.8911\left|{}^4p_{10}\right|\left|{}^4d_6\right|\cos\left(\phi_{d-p}\right)\\
& +12.3324\left|{}^4p_{10}\right|\left|{}^6d_6\right|\cos\left(\phi_{d-p}\right)+1.692\left|{}^4p_{10}\right|\left|{}^2d_6\right|\cos\left(\phi_{d-p}\right)\\
& -2.5078\left|{}^4p_{10}\right|\left|{}^4d_{14}\right|\cos\left(\phi_{d-p}\right)-5.3489\left|{}^4p_{10}\right|\left|{}^6d_{14}\right|\cos\left(\phi_{d-p}\right)\\
& +1.1334\left|{}^6p_{10}\right|\left|{}^2d_4\right|\cos\left(\phi_{d-p}\right)-4.4211\left|{}^6p_{10}\right|\left|{}^4d_6\right|\cos\left(\phi_{d-p}\right)\\
& +4.144\left|{}^6p_{10}\right|\left|{}^6d_6\right|\cos\left(\phi_{d-p}\right)-10.4169\left|{}^6p_{10}\right|\left|{}^2d_6\right|\cos\left(\phi_{d-p}\right)\\
& +0.3129\left|{}^6p_{10}\right|\left|{}^4d_{14}\right|\cos\left(\phi_{d-p}\right)+3.8821\left|{}^6p_{10}\right|\left|{}^6d_{14}\right|\cos\left(\phi_{d-p}\right),
\end{aligned}
\tag{C.14}
$$

$$
\begin{aligned}
c_2 = & \ 1.7889\left|{}^2s_2\right|\left|{}^4s_4\right|+6.5727\left|{}^2s_2\right|\left|{}^6s_6\right|\cos\left(\delta^s\right)\\
& -1.7889\left|{}^2s_2\right|\left|{}^4d_6\right|\cos\left(\phi_{d-p}+\phi_{p-s}\right)-2.8685\left|{}^2s_2\right|\left|{}^6d_6\right|\cos\left(\phi_{d-p}+\phi_{p-s}\right)\\
& +1.4343\left|{}^2s_2\right|\left|{}^4d_{14}\right|\cos\left(\phi_{d-p}+\phi_{p-s}\right)-7.0265\left|{}^2s_2\right|\left|{}^6d_{14}\right|\cos\left(\phi_{d-p}+\phi_{p-s}\right)\\
& +2.2627\left|{}^4s_4\right|^2-4.1569\left|{}^4s_4\right|\left|{}^6s_6\right|\cos\left(\delta^s\right)+1.7889\left|{}^4s_4\right|\left|{}^2d_4\right|\cos\left(\phi_{d-p}+\phi_{p-s}\right)
\end{aligned}
\tag{C.15}
$$

$$
\begin{aligned}
&- 3.2\left|{}^4\mathrm{s}_4\right|\left|{}^4\mathrm{d}_6\right|\cos\left(\phi_{d-p}+\phi_{p-s}\right) - 6.9356\left|{}^4\mathrm{s}_4\right|\left|{}^6\mathrm{d}_6\right|\cos\left(\phi_{d-p}+\phi_{p-s}\right)\\
&+ 0.7666\left|{}^4\mathrm{s}_4\right|\left|{}^2\mathrm{d}_6\right|\cos\left(\phi_{d-p}+\phi_{p-s}\right) - 0.3405\left|{}^4\mathrm{s}_4\right|\left|{}^4\mathrm{d}_{14}\right|\cos\left(\phi_{d-p}+\phi_{p-s}\right)\\
&- 6.4932\left|{}^4\mathrm{s}_4\right|\left|{}^6\mathrm{d}_{14}\right|\cos\left(\phi_{d-p}+\phi_{p-s}\right) - 3.3941\left|{}^6\mathrm{s}_6\right|^2\\
&+ 1.8779\left|{}^6\mathrm{s}_6\right|\left|{}^2\mathrm{d}_4\right|\cos\left(\phi_{d-p}+\phi_{p-s}\right) - 0.0299\left|{}^6\mathrm{s}_6\right|\left|{}^4\mathrm{d}_6\right|\cos\left(\phi_{d-p}+\phi_{p-s}\right)\\
&- 2.8611\left|{}^6\mathrm{s}_6\right|\left|{}^6\mathrm{d}_6\right|\cos\left(\phi_{d-p}+\phi_{p-s}\right) + 7.5116\left|{}^6\mathrm{s}_6\right|\left|{}^2\mathrm{d}_6\right|\cos\left(\phi_{d-p}+\phi_{p-s}\right)\\
&- 5.8677\left|{}^6\mathrm{s}_6\right|\left|{}^4\mathrm{d}_{14}\right|\cos\left(\phi_{d-p}+\phi_{p-s}\right) - 0.5148\left|{}^6\mathrm{s}_6\right|\left|{}^6\mathrm{d}_{14}\right|\cos\left(\phi_{d-p}+\phi_{p-s}\right)\\
&+ 3.7394\left|{}^2\mathrm{p}_2\right|\left|{}^4\mathrm{p}_{10}\right|\cos\left(\delta^p\right) - 3.9545\left|{}^2\mathrm{p}_2\right|\left|{}^6\mathrm{p}_{10}\right|\cos\left(\delta^p\right)\\
&- 2.5298\left|{}^4\mathrm{p}_2\right|\left|{}^2\mathrm{p}_4\right|\cos\left(\delta^p\right) - 6.6892\left|{}^4\mathrm{p}_2\right|\left|{}^4\mathrm{p}_{10}\right|\cos\left(\delta^p\right)\\
&- 1.7685\left|{}^4\mathrm{p}_2\right|\left|{}^6\mathrm{p}_{10}\right|\cos\left(\delta^p\right) + 1.6398\left|{}^2\mathrm{p}_4\right|\left|{}^4\mathrm{p}_{10}\right| - 5.329\left|{}^2\mathrm{p}_4\right|\left|{}^6\mathrm{p}_{10}\right|\\
&+ 1.8268\left|{}^4\mathrm{p}_{10}\right|^2 - 10.3379\left|{}^4\mathrm{p}_{10}\right|\left|{}^6\mathrm{p}_{10}\right| - 4.9989\left|{}^6\mathrm{p}_{10}\right|^2 - 4.3187\left|{}^2\mathrm{d}_4\right|\left|{}^4\mathrm{d}_6\right|\\
&+ 4.7209\left|{}^2\mathrm{d}_4\right|\left|{}^6\mathrm{d}_6\right| + 5.6256\left|{}^2\mathrm{d}_4\right|\left|{}^4\mathrm{d}_{14}\right|\cos\left(\delta^d\right) + 2.2512\left|{}^2\mathrm{d}_4\right|\left|{}^6\mathrm{d}_{14}\right|\cos\left(\delta^d\right)\\
&+ 5.4627\left|{}^4\mathrm{d}_6\right|^2 - 5.2327\left|{}^4\mathrm{d}_6\right|\left|{}^6\mathrm{d}_6\right| - 4.5614\left|{}^4\mathrm{d}_6\right|\left|{}^2\mathrm{d}_6\right|\cos\left(\delta^d\right)\\
&- 16.457\left|{}^4\mathrm{d}_6\right|\left|{}^4\mathrm{d}_{14}\right|\cos\left(\delta^d\right) - 8.2117\left|{}^4\mathrm{d}_6\right|\left|{}^6\mathrm{d}_{14}\right|\cos\left(\delta^d\right)\\
&+ 1.8721\left|{}^6\mathrm{d}_6\right|^2 + 11.4612\left|{}^6\mathrm{d}_6\right|\left|{}^4\mathrm{d}_{14}\right|\cos\left(\delta^d\right) + 5.7272\left|{}^6\mathrm{d}_6\right|\left|{}^6\mathrm{d}_{14}\right|\cos\left(\delta^d\right)\\
&+ 2.2187\left|{}^2\mathrm{d}_6\right|\left|{}^4\mathrm{d}_{14}\right| - 7.5571\left|{}^2\mathrm{d}_6\right|\left|{}^6\mathrm{d}_{14}\right| + 0.4645\left|{}^4\mathrm{d}_{14}\right|^2\\
&- 7.4686\left|{}^4\mathrm{d}_{14}\right|\left|{}^6\mathrm{d}_{14}\right| - 2.7809\left|{}^6\mathrm{d}_{14}\right|^2,
\end{aligned}
$$

$$
\begin{aligned}
\mathrm{c}_3 = {}& 2.9394\left|{}^2\mathrm{s}_2\right|\left|{}^4\mathrm{p}_{10}\right|\cos\left(\phi_{p-s}\right) + 1.9243\left|{}^2\mathrm{s}_2\right|\left|{}^6\mathrm{p}_{10}\right|\cos\left(\phi_{p-s}\right)\\
&+ 3.2199\left|{}^4\mathrm{s}_4\right|\left|{}^2\mathrm{p}_4\right|\cos\left(\phi_{p-s}\right) + 9.5919\left|{}^4\mathrm{s}_4\right|\left|{}^4\mathrm{p}_{10}\right|\cos\left(\phi_{p-s}\right)\\
&+ 5.01\left|{}^4\mathrm{s}_4\right|\left|{}^6\mathrm{p}_{10}\right|\cos\left(\phi_{p-s}\right) + 6.5727\left|{}^6\mathrm{s}_6\right|\left|{}^2\mathrm{p}_2\right|\cos\left(\phi_{p-s}\right)\\
&+ 2.9394\left|{}^6\mathrm{s}_6\right|\left|{}^4\mathrm{p}_2\right|\cos\left(\phi_{p-s}\right) + 5.2582\left|{}^6\mathrm{s}_6\right|\left|{}^2\mathrm{p}_4\right|\cos\left(\phi_{p-s}\right)\\
&+ 0.4845\left|{}^6\mathrm{s}_6\right|\left|{}^4\mathrm{p}_{10}\right|\cos\left(\phi_{p-s}\right) - 1.7558\left|{}^6\mathrm{s}_6\right|\left|{}^6\mathrm{p}_{10}\right|\cos\left(\phi_{p-s}\right)\\
&+ 5.491\left|{}^2\mathrm{p}_2\right|\left|{}^4\mathrm{d}_{14}\right|\cos\left(\phi_{d-p}\right) - 3.7141\left|{}^2\mathrm{p}_2\right|\left|{}^6\mathrm{d}_{14}\right|\cos\left(\phi_{d-p}\right)
\end{aligned}
\tag{C.16}
$$

$$
\begin{aligned}
&- 3.7947\left|{}^4\mathrm{p}_2\right|\left|{}^2\mathrm{d}_6\right|\cos\left(\phi_{d-p}\right) - 9.8226\left|{}^4\mathrm{p}_2\right|\left|{}^4\mathrm{d}_{14}\right|\cos\left(\phi_{d-p}\right)\\
&- 1.661\left|{}^4\mathrm{p}_2\right|\left|{}^6\mathrm{d}_{14}\right|\cos\left(\phi_{d-p}\right) - 3.2199\left|{}^2\mathrm{p}_4\right|\left|{}^4\mathrm{d}_6\right|\cos\left(\phi_{d-p}\right)\\
&- 5.1634\left|{}^2\mathrm{p}_4\right|\left|{}^6\mathrm{d}_6\right|\cos\left(\phi_{d-p}\right) + 2.4997\left|{}^2\mathrm{p}_4\right|\left|{}^4\mathrm{d}_{14}\right|\cos\left(\phi_{d-p}\right)\\
&- 4.5171\left|{}^2\mathrm{p}_4\right|\left|{}^6\mathrm{d}_{14}\right|\cos\left(\phi_{d-p}\right) + 3.7915\left|{}^4\mathrm{p}_{10}\right|\left|{}^2\mathrm{d}_4\right|\cos\left(\phi_{d-p}\right)\\
&- 5.2582\left|{}^4\mathrm{p}_{10}\right|\left|{}^4\mathrm{d}_6\right|\cos\left(\phi_{d-p}\right) - 13.5568\left|{}^4\mathrm{p}_{10}\right|\left|{}^6\mathrm{d}_6\right|\cos\left(\phi_{d-p}\right)\\
&+ 2.5277\left|{}^4\mathrm{p}_{10}\right|\left|{}^2\mathrm{d}_6\right|\cos\left(\phi_{d-p}\right) + 6.4023\left|{}^4\mathrm{p}_{10}\right|\left|{}^4\mathrm{d}_{14}\right|\cos\left(\phi_{d-p}\right)\\
&- 6.8897\left|{}^4\mathrm{p}_{10}\right|\left|{}^6\mathrm{d}_{14}\right|\cos\left(\phi_{d-p}\right) - 9.0424\left|{}^6\mathrm{p}_{10}\right|\left|{}^2\mathrm{d}_4\right|\cos\left(\phi_{d-p}\right)\\
&+ 0.1515\left|{}^6\mathrm{p}_{10}\right|\left|{}^4\mathrm{d}_6\right|\cos\left(\phi_{d-p}\right) - 3.5685\left|{}^6\mathrm{p}_{10}\right|\left|{}^6\mathrm{d}_6\right|\cos\left(\phi_{d-p}\right)\\
&- 6.0282\left|{}^6\mathrm{p}_{10}\right|\left|{}^2\mathrm{d}_6\right|\cos\left(\phi_{d-p}\right) - 6.4304\left|{}^6\mathrm{p}_{10}\right|\left|{}^4\mathrm{d}_{14}\right|\cos\left(\phi_{d-p}\right)\\
&- 15.2401\left|{}^6\mathrm{p}_{10}\right|\left|{}^6\mathrm{d}_{14}\right|\cos\left(\phi_{d-p}\right),
\end{aligned}
$$

$$
\begin{aligned}
\mathrm{c}_4 = {}& 4.0567\left|{}^2\mathrm{s}_2\right|\left|{}^4\mathrm{d}_{14}\right|\cos\left(\phi_{d-p}+\phi_{p-s}\right) + 3.3123\left|{}^2\mathrm{s}_2\right|\left|{}^6\mathrm{d}_{14}\right|\cos\left(\phi_{d-p}+\phi_{p-s}\right)\\
&+ 4.6\left|{}^4\mathrm{s}_4\right|\left|{}^2\mathrm{d}_6\right|\cos\left(\phi_{d-p}+\phi_{p-s}\right) + 13.5508\left|{}^4\mathrm{s}_4\right|\left|{}^4\mathrm{d}_{14}\right|\cos\left(\phi_{d-p}+\phi_{p-s}\right)\\
&+ 8.8422\left|{}^4\mathrm{s}_4\right|\left|{}^6\mathrm{d}_{14}\right|\cos\left(\phi_{d-p}+\phi_{p-s}\right) + 11.2674\left|{}^6\mathrm{s}_6\right|\left|{}^2\mathrm{d}_4\right|\cos\left(\phi_{d-p}+\phi_{p-s}\right)\\
&+ 7.1262\left|{}^6\mathrm{s}_6\right|\left|{}^4\mathrm{d}_6\right|\cos\left(\phi_{d-p}+\phi_{p-s}\right) + 1.9045\left|{}^6\mathrm{s}_6\right|\left|{}^6\mathrm{d}_6\right|\cos\left(\phi_{d-p}+\phi_{p-s}\right)\\
&+ 5.6337\left|{}^6\mathrm{s}_6\right|\left|{}^2\mathrm{d}_6\right|\cos\left(\phi_{d-p}+\phi_{p-s}\right) + 0.8846\left|{}^6\mathrm{s}_6\right|\left|{}^4\mathrm{d}_{14}\right|\cos\left(\phi_{d-p}+\phi_{p-s}\right)\\
&- 1.9991\left|{}^6\mathrm{s}_6\right|\left|{}^6\mathrm{d}_{14}\right|\cos\left(\phi_{d-p}+\phi_{p-s}\right) + 5.0389\left|{}^2\mathrm{p}_4\right|\left|{}^4\mathrm{p}_{10}\right| + 3.2988\left|{}^2\mathrm{p}_4\right|\left|{}^6\mathrm{p}_{10}\right|\\
&+ 9.192\left|{}^4\mathrm{p}_{10}\right|^2 + 8.303\left|{}^4\mathrm{p}_{10}\right|\left|{}^6\mathrm{p}_{10}\right| + 2.6389\left|{}^6\mathrm{p}_{10}\right|^2 + 5.3564\left|{}^2\mathrm{d}_4\right|\left|{}^4\mathrm{d}_{14}\right|\cos\left(\delta^d\right)\\
&- 9.6795\left|{}^2\mathrm{d}_4\right|\left|{}^6\mathrm{d}_{14}\right|\cos\left(\delta^d\right) - 4.6\left|{}^4\mathrm{d}_6\right|\left|{}^2\mathrm{d}_6\right|\cos\left(\delta^d\right)\\
&- 7.2569\left|{}^4\mathrm{d}_6\right|\left|{}^4\mathrm{d}_{14}\right|\cos\left(\delta^d\right) + 4.2017\left|{}^4\mathrm{d}_6\right|\left|{}^6\mathrm{d}_{14}\right|\cos\left(\delta^d\right)\\
&- 12.7896\left|{}^6\mathrm{d}_6\right|\left|{}^4\mathrm{d}_{14}\right|\cos\left(\delta^d\right) - 5.1867\left|{}^6\mathrm{d}_6\right|\left|{}^6\mathrm{d}_{14}\right|\cos\left(\delta^d\right) + 3.6002\left|{}^2\mathrm{d}_6\right|\left|{}^4\mathrm{d}_{14}\right|\\
&- 4.0869\left|{}^2\mathrm{d}_6\right|\left|{}^6\mathrm{d}_{14}\right| + 5.1116\left|{}^4\mathrm{d}_{14}\right|^2 - 8.6197\left|{}^4\mathrm{d}_{14}\right|\left|{}^6\mathrm{d}_{14}\right| - 9.8767\left|{}^6\mathrm{d}_{14}\right|^2,
\end{aligned}
\tag{C.17}
$$

$$
\begin{aligned}
c_5 = {} & 6.7612 \left|{}^2p_4\right| \left|{}^4d_{14}\right| \cos\left(\phi_{d-p}\right) + 5.5205 \left|{}^2p_4\right| \left|{}^6d_{14}\right| \cos\left(\phi_{d-p}\right) \\
& + 6.9985 \left|{}^4p_{10}\right| \left|{}^2d_6\right| \cos\left(\phi_{d-p}\right) + 25.1435 \left|{}^4p_{10}\right| \left|{}^4d_{14}\right| \cos\left(\phi_{d-p}\right) \\
& + 17.149 \left|{}^4p_{10}\right| \left|{}^6d_{14}\right| \cos\left(\phi_{d-p}\right) + 4.5816 \left|{}^6p_{10}\right| \left|{}^2d_6\right| \cos\left(\phi_{d-p}\right) \\
& + 13.7947 \left|{}^6p_{10}\right| \left|{}^4d_{14}\right| \cos\left(\phi_{d-p}\right) + 9.0502 + 13.7947 \left|{}^6p_{10}\right| \left|{}^6d_{14}\right| \cos\left(\phi_{d-p}\right),
\end{aligned}
\tag{C.18}
$$

and

$$
\begin{aligned}
c_6 = {} & 9.2199 \left|{}^2d_6\right| \left|{}^4d_{14}\right| + 7.528 \left|{}^2d_6\right| \left|{}^6d_{14}\right| + 16.8755 \left|{}^4d_{14}\right|^2 \\
& + 17.3778 \left|{}^4d_{14}\right| \left|{}^6d_{14}\right| + 7.614 \left|{}^6d_{14}\right|^2.
\end{aligned}
\tag{C.19}
$$

C.1.4 T_{21}

Equation 5.8 yields

$$
\begin{aligned}
\frac{T_{21}(\theta)\ \sigma(\theta)}{A_0} = {} & Q_1 d_1 P_1^1(\cos\theta) + Q_2 d_2 P_2^1(\cos\theta) + Q_3 d_3 P_3^1(\cos\theta) \\
& + Q_4 d_4 P_4^1(\cos\theta) + Q_5 d_5 P_5^1(\cos\theta) + Q_6 d_6 P_6^1(\cos\theta).
\end{aligned}
\tag{C.20}
$$

The coefficients can be expanded as follows:

$$
\begin{aligned}
\mathrm{d}_1 = {} & 1.5492 \left|{}^2\mathrm{s}_2\right| \left|{}^4\mathrm{p}_2\right| \cos\left(\phi_{p-s}\right) - 0.9798 \left|{}^2\mathrm{s}_2\right| \left|{}^4\mathrm{p}_{10}\right| \cos\left(\phi_{p-s}\right) \\
& + 7.2 \left|{}^2\mathrm{s}_2\right| \left|{}^6\mathrm{p}_{10}\right| \cos\left(\phi_{p-s}\right) - 2.1909 \left|{}^4\mathrm{s}_4\right| \left|{}^2\mathrm{p}_2\right| \cos\left(\phi_{p-s}\right) \\
& + 3.9192 \left|{}^4\mathrm{s}_4\right| \left|{}^4\mathrm{p}_2\right| \cos\left(\phi_{p-s}\right) - 0.4382 \left|{}^4\mathrm{s}_4\right| \left|{}^2\mathrm{p}_4\right| \cos\left(\phi_{p-s}\right) \\
& + 0.1615 \left|{}^4\mathrm{s}_4\right| \left|{}^4\mathrm{p}_{10}\right| \cos\left(\phi_{p-s}\right) + 3.0727 \left|{}^4\mathrm{s}_4\right| \left|{}^6\mathrm{p}_{10}\right| \cos\left(\phi_{p-s}\right) \\
& - 9.6598 \left|{}^6\mathrm{s}_6\right| \left|{}^2\mathrm{p}_4\right| \cos\left(\phi_{p-s}\right) + 11.2359 \left|{}^6\mathrm{s}_6\right| \left|{}^4\mathrm{p}_{10}\right| \cos\left(\phi_{p-s}\right) \\
& - 7.1525 \left|{}^6\mathrm{s}_6\right| \left|{}^6\mathrm{p}_{10}\right| \cos\left(\phi_{p-s}\right) - 1.5492 \left|{}^2\mathrm{p}_2\right| \left|{}^4\mathrm{d}_6\right| \cos\left(\phi_{d-p}\right) \\
& + 2.757 \left|{}^2\mathrm{p}_2\right| \left|{}^6\mathrm{d}_6\right| \cos\left(\phi_{d-p}\right) - 1.5492 \left|{}^4\mathrm{p}_2\right| \left|{}^2\mathrm{d}_4\right| \cos\left(\phi_{d-p}\right) \\
& + 3.9192 \left|{}^4\mathrm{p}_2\right| \left|{}^4\mathrm{d}_6\right| \cos\left(\phi_{d-p}\right) - 6.3446 \left|{}^4\mathrm{p}_2\right| \left|{}^6\mathrm{d}_6\right| \cos\left(\phi_{d-p}\right) \\
& + 2.8637 \left|{}^2\mathrm{p}_4\right| \left|{}^4\mathrm{d}_6\right| \cos\left(\phi_{d-p}\right) - 0.6491 \left|{}^2\mathrm{p}_4\right| \left|{}^6\mathrm{d}_6\right| \cos\left(\phi_{d-p}\right) \\
& - 1.054 \left|{}^2\mathrm{p}_4\right| \left|{}^4\mathrm{d}_{14}\right| \cos\left(\phi_{d-p}\right) + 5.1634 \left|{}^2\mathrm{p}_4\right| \left|{}^6\mathrm{d}_{14}\right| \cos\left(\phi_{d-p}\right) \\
& - 2.6202 \left|{}^4\mathrm{p}_{10}\right| \left|{}^2\mathrm{d}_4\right| \cos\left(\phi_{d-p}\right) + 9.7311 \left|{}^4\mathrm{p}_{10}\right| \left|{}^4\mathrm{d}_6\right| \cos\left(\phi_{d-p}\right) \\
& - 8.1378 \left|{}^4\mathrm{p}_{10}\right| \left|{}^6\mathrm{d}_6\right| \cos\left(\phi_{d-p}\right) - 0.5143 \left|{}^4\mathrm{p}_{10}\right| \left|{}^2\mathrm{d}_6\right| \cos\left(\phi_{d-p}\right) \\
& - 0.934 \left|{}^4\mathrm{p}_{10}\right| \left|{}^4\mathrm{d}_{14}\right| \cos\left(\phi_{d-p}\right) + 7.8126 \left|{}^4\mathrm{p}_{10}\right| \left|{}^6\mathrm{d}_{14}\right| \cos\left(\phi_{d-p}\right) \\
& - 4.7135 \left|{}^6\mathrm{p}_{10}\right| \left|{}^2\mathrm{d}_4\right| \cos\left(\phi_{d-p}\right) + 11.6048 \left|{}^6\mathrm{p}_{10}\right| \left|{}^4\mathrm{d}_6\right| \cos\left(\phi_{d-p}\right) \\
& - 12.0494 \left|{}^6\mathrm{p}_{10}\right| \left|{}^6\mathrm{d}_6\right| \cos\left(\phi_{d-p}\right) - 5.1799 \left|{}^6\mathrm{p}_{10}\right| \left|{}^2\mathrm{d}_6\right| \cos\left(\phi_{d-p}\right) \\
& + 5.5347 \left|{}^6\mathrm{p}_{10}\right| \left|{}^4\mathrm{d}_{14}\right| \cos\left(\phi_{d-p}\right) - 1.6001 \left|{}^6\mathrm{p}_{10}\right| \left|{}^6\mathrm{d}_{14}\right| \cos\left(\phi_{d-p}\right),
\end{aligned}
\tag{C.21}
$$

$$
\begin{aligned}
\mathrm{d}_2 = {} & - 1.4606 \left|{}^2\mathrm{s}_2\right| \left|{}^4\mathrm{s}_4\right| - 5.3664 \left|{}^2\mathrm{s}_2\right| \left|{}^6\mathrm{s}_6\right| \cos\left(\delta^s\right) \\
& + 0.7303 \left|{}^2\mathrm{s}_2\right| \left|{}^4\mathrm{d}_6\right| \cos\left(\phi_{d-p} + \phi_{p-s}\right) + 1.1711 \left|{}^2\mathrm{s}_2\right| \left|{}^6\mathrm{d}_6\right| \cos\left(\phi_{d-p} + \phi_{p-s}\right) \\
& - 0.5856 \left|{}^2\mathrm{s}_2\right| \left|{}^4\mathrm{d}_{14}\right| \cos\left(\phi_{d-p} + \phi_{p-s}\right) + 2.8685 \left|{}^2\mathrm{s}_2\right| \left|{}^6\mathrm{d}_{14}\right| \cos\left(\phi_{d-p} + \phi_{p-s}\right) \\
& - 1.8475 \left|{}^4\mathrm{s}_4\right|^2 + 3.3941 \left|{}^4\mathrm{s}_4\right| \left|{}^6\mathrm{s}_6\right| \cos\left(\delta^s\right) - 0.7303 \left|{}^4\mathrm{s}_4\right| \left|{}^2\mathrm{d}_4\right| \cos\left(\phi_{d-p} + \phi_{p-s}\right)
\end{aligned}
\tag{C.22}
$$

$$
\begin{aligned}
&+ 1.3064 \left|{}^4\mathrm{s}_4\right| \left|{}^4\mathrm{d}_6\right| \cos\left(\phi_{d-p} + \phi_{p-s}\right) + 2.8314 \left|{}^4\mathrm{s}_4\right| \left|{}^6\mathrm{d}_6\right| \cos\left(\phi_{d-p} + \phi_{p-s}\right) \\
&- 0.313 \left|{}^4\mathrm{s}_4\right| \left|{}^2\mathrm{d}_6\right| \cos\left(\phi_{d-p} + \phi_{p-s}\right) - 0.139 \left|{}^4\mathrm{s}_4\right| \left|{}^4\mathrm{d}_{14}\right| \cos\left(\phi_{d-p} + \phi_{p-s}\right) \\
&+ 2.6508 \left|{}^4\mathrm{s}_4\right| \left|{}^6\mathrm{d}_{14}\right| \cos\left(\phi_{d-p} + \phi_{p-s}\right) + 2.7713 \left|{}^6\mathrm{s}_6\right|^2 \\
&- 0.7667 \left|{}^6\mathrm{s}_6\right| \left|{}^2\mathrm{d}_4\right| \cos\left(\phi_{d-p} + \phi_{p-s}\right) + 0.0122 \left|{}^6\mathrm{s}_6\right| \left|{}^4\mathrm{d}_6\right| \cos\left(\phi_{d-p} + \phi_{p-s}\right) \\
&+ 1.168 \left|{}^6\mathrm{s}_6\right| \left|{}^6\mathrm{d}_6\right| \cos\left(\phi_{d-p} + \phi_{p-s}\right) - 3.0666 \left|{}^6\mathrm{s}_6\right| \left|{}^2\mathrm{d}_6\right| \cos\left(\phi_{d-p} + \phi_{p-s}\right) \\
&+ 2.3954 \left|{}^6\mathrm{s}_6\right| \left|{}^4\mathrm{d}_{14}\right| \cos\left(\phi_{d-p} + \phi_{p-s}\right) + 0.2101 \left|{}^6\mathrm{s}_6\right| \left|{}^6\mathrm{d}_{14}\right| \cos\left(\phi_{d-p} + \phi_{p-s}\right) \\
&- 2 \left|{}^2\mathrm{p}_2\right| \left|{}^4\mathrm{p}_{10}\right| \cos\left(\delta^p\right) + 1.3814 \left|{}^2\mathrm{p}_2\right| \left|{}^6\mathrm{p}_{10}\right| \cos\left(\delta^p\right) \\
&+ 1.5492 \left|{}^4\mathrm{p}_2\right| \left|{}^2\mathrm{p}_4\right| \cos\left(\delta^p\right) + 4.6149 \left|{}^4\mathrm{p}_2\right| \left|{}^4\mathrm{p}_{10}\right| \cos\left(\delta^p\right) \\
&+ 3.6137 \left|{}^4\mathrm{p}_2\right| \left|{}^6\mathrm{p}_{10}\right| \cos\left(\delta^p\right) - 1.7226 \left|{}^2\mathrm{p}_4\right| \left|{}^4\mathrm{p}_{10}\right| + 4.023 \left|{}^2\mathrm{p}_4\right| \left|{}^6\mathrm{p}_{10}\right| \\
&- 1.134 \left|{}^4\mathrm{p}_{10}\right|^2 + 8.9443 \left|{}^4\mathrm{p}_{10}\right| \left|{}^6\mathrm{p}_{10}\right| \\
&+ 2.8723 \left|{}^6\mathrm{p}_{10}\right|^2 - 2.2795 \left|{}^2\mathrm{d}_4\right| \left|{}^4\mathrm{d}_6\right| + 1.5859 \left|{}^2\mathrm{d}_4\right| \left|{}^6\mathrm{d}_6\right| \\
&- 2.7295 \left|{}^2\mathrm{d}_4\right| \left|{}^4\mathrm{d}_{14}\right| \cos\left(\delta^d\right) - 3.4069 \left|{}^2\mathrm{d}_4\right| \left|{}^6\mathrm{d}_{14}\right| \cos\left(\delta^d\right) \\
&+ 3.1539 \left|{}^4\mathrm{d}_6\right|^2 - 5.3819 \left|{}^4\mathrm{d}_6\right| \left|{}^6\mathrm{d}_6\right| + 2.8011 \left|{}^4\mathrm{d}_6\right| \left|{}^2\mathrm{d}_6\right| \cos\left(\delta^d\right) \\
&+ 9.1897 \left|{}^4\mathrm{d}_6\right| \left|{}^4\mathrm{d}_{14}\right| \cos\left(\delta^d\right) + 10.4434 \left|{}^4\mathrm{d}_6\right| \left|{}^6\mathrm{d}_{14}\right| \cos\left(\delta^d\right) \\
&- 0.2556 \left|{}^6\mathrm{d}_6\right|^2 - 0.7199 \left|{}^6\mathrm{d}_6\right| \left|{}^4\mathrm{d}_{14}\right| \cos\left(\delta^d\right) - 8.4994 \left|{}^6\mathrm{d}_6\right| \left|{}^6\mathrm{d}_{14}\right| \cos\left(\delta^d\right) \\
&- 1.6347 \left|{}^2\mathrm{d}_6\right| \left|{}^4\mathrm{d}_{14}\right| + 2.2362 \left|{}^2\mathrm{d}_6\right| \left|{}^6\mathrm{d}_{14}\right| - 1.2164 \left|{}^4\mathrm{d}_{14}\right|^2 + 11.2898 \left|{}^4\mathrm{d}_{14}\right| \left|{}^6\mathrm{d}_{14}\right| \\
&+ 2.4023 \left|{}^6\mathrm{d}_{14}\right|^2,
\end{aligned}
$$

$$
\begin{aligned}
\mathrm{d}_3 = \; &- 1.6 \left|{}^2\mathrm{s}_2\right| \left|{}^4\mathrm{p}_{10}\right| \cos\left(\phi_{p-s}\right) - 1.0475 \left|{}^2\mathrm{s}_2\right| \left|{}^6\mathrm{p}_{10}\right| \cos\left(\phi_{p-s}\right) \\
&- 1.7527 \left|{}^4\mathrm{s}_4\right| \left|{}^2\mathrm{p}_4\right| \cos\left(\phi_{p-s}\right) - 5.2212 \left|{}^4\mathrm{s}_4\right| \left|{}^4\mathrm{p}_{10}\right| \cos\left(\phi_{p-s}\right) \\
&- 2.727 \left|{}^4\mathrm{s}_4\right| \left|{}^6\mathrm{p}_{10}\right| \cos\left(\phi_{p-s}\right) - 3.5777 \left|{}^6\mathrm{s}_6\right| \left|{}^2\mathrm{p}_2\right| \cos\left(\phi_{p-s}\right) \\
&- 1.6 \left|{}^6\mathrm{s}_6\right| \left|{}^4\mathrm{p}_2\right| \cos\left(\phi_{p-s}\right) - 2.8621 \left|{}^6\mathrm{s}_6\right| \left|{}^2\mathrm{p}_4\right| \cos\left(\phi_{p-s}\right) \\
&- 0.2637 \left|{}^6\mathrm{s}_6\right| \left|{}^4\mathrm{p}_{10}\right| \cos\left(\phi_{p-s}\right) + 0.9557 \left|{}^6\mathrm{s}_6\right| \left|{}^6\mathrm{p}_{10}\right| \cos\left(\phi_{p-s}\right)
\end{aligned}
\tag{C.23}
$$

$$
\begin{aligned}
&- 1.9322\left|{}^{2}\mathrm{p}_{2}\right|\left|{}^{4}\mathrm{d}_{14}\right|\cos\left(\phi_{d-p}\right) - 0.3141\left|{}^{2}\mathrm{p}_{2}\right|\left|{}^{6}\mathrm{d}_{14}\right|\cos\left(\phi_{d-p}\right)\\
&+ 1.5492\left|{}^{4}\mathrm{p}_{2}\right|\left|{}^{2}\mathrm{d}_{6}\right|\cos\left(\phi_{d-p}\right) + 4.5637\left|{}^{4}\mathrm{p}_{2}\right|\left|{}^{4}\mathrm{d}_{14}\right|\cos\left(\phi_{d-p}\right)\\
&+ 3.543\left|{}^{4}\mathrm{p}_{2}\right|\left|{}^{6}\mathrm{d}_{14}\right|\cos\left(\phi_{d-p}\right) + 0.8763\left|{}^{2}\mathrm{p}_{4}\right|\left|{}^{4}\mathrm{d}_{6}\right|\cos\left(\phi_{d-p}\right)\\
&+ 1.4053\left|{}^{2}\mathrm{p}_{4}\right|\left|{}^{6}\mathrm{d}_{6}\right|\cos\left(\phi_{d-p}\right) - 1.5308\left|{}^{2}\mathrm{p}_{4}\right|\left|{}^{4}\mathrm{d}_{14}\right|\cos\left(\phi_{d-p}\right)\\
&+ 1.5026\left|{}^{2}\mathrm{p}_{4}\right|\left|{}^{6}\mathrm{d}_{14}\right|\cos\left(\phi_{d-p}\right) - 0.8\left|{}^{4}\mathrm{p}_{10}\right|\left|{}^{2}\mathrm{d}_{4}\right|\cos\left(\phi_{d-p}\right)\\
&+ 2.0178\left|{}^{4}\mathrm{p}_{10}\right|\left|{}^{4}\mathrm{d}_{6}\right|\cos\left(\phi_{d-p}\right) + 4.0425\left|{}^{4}\mathrm{p}_{10}\right|\left|{}^{6}\mathrm{d}_{6}\right|\cos\left(\phi_{d-p}\right)\\
&- 1.7798\left|{}^{4}\mathrm{p}_{10}\right|\left|{}^{2}\mathrm{d}_{6}\right|\cos\left(\phi_{d-p}\right) - 2.823\left|{}^{4}\mathrm{p}_{10}\right|\left|{}^{4}\mathrm{d}_{14}\right|\cos\left(\phi_{d-p}\right)\\
&+ 3.9896\left|{}^{4}\mathrm{p}_{10}\right|\left|{}^{6}\mathrm{d}_{14}\right|\cos\left(\phi_{d-p}\right) + 2.7051\left|{}^{6}\mathrm{p}_{10}\right|\left|{}^{2}\mathrm{d}_{4}\right|\cos\left(\phi_{d-p}\right)\\
&+ 3.0175\left|{}^{6}\mathrm{p}_{10}\right|\left|{}^{4}\mathrm{d}_{6}\right|\cos\left(\phi_{d-p}\right) + 2.6382\left|{}^{6}\mathrm{p}_{10}\right|\left|{}^{6}\mathrm{d}_{6}\right|\cos\left(\phi_{d-p}\right)\\
&+ 3.4475\left|{}^{6}\mathrm{p}_{10}\right|\left|{}^{2}\mathrm{d}_{6}\right|\cos\left(\phi_{d-p}\right) + 6.3177\left|{}^{6}\mathrm{p}_{10}\right|\left|{}^{4}\mathrm{d}_{14}\right|\cos\left(\phi_{d-p}\right)\\
&+ 5.9659\left|{}^{6}\mathrm{p}_{10}\right|\left|{}^{6}\mathrm{d}_{14}\right|\cos\left(\phi_{d-p}\right),
\end{aligned}
$$

$$
\begin{aligned}
\mathrm{d}_{4} = \; &- 1.6561\left|{}^{2}\mathrm{s}_{2}\right|\left|{}^{4}\mathrm{d}_{14}\right|\cos\left(\phi_{d-p}+\phi_{p-s}\right) - 1.3523\left|{}^{2}\mathrm{s}_{2}\right|\left|{}^{6}\mathrm{d}_{14}\right|\cos\left(\phi_{d-p}+\phi_{p-s}\right)\\
&- 1.8779\left|{}^{4}\mathrm{s}_{4}\right|\left|{}^{2}\mathrm{d}_{6}\right|\cos\left(\phi_{d-p}+\phi_{p-s}\right) - 5.5321\left|{}^{4}\mathrm{s}_{4}\right|\left|{}^{4}\mathrm{d}_{14}\right|\cos\left(\phi_{d-p}+\phi_{p-s}\right)\\
&- 3.6098\left|{}^{4}\mathrm{s}_{4}\right|\left|{}^{6}\mathrm{d}_{14}\right|\cos\left(\phi_{d-p}+\phi_{p-s}\right) - 4.5999\left|{}^{6}\mathrm{s}_{6}\right|\left|{}^{2}\mathrm{d}_{4}\right|\cos\left(\phi_{d-p}+\phi_{p-s}\right)\\
&- 2.9092\left|{}^{6}\mathrm{s}_{6}\right|\left|{}^{4}\mathrm{d}_{6}\right|\cos\left(\phi_{d-p}+\phi_{p-s}\right) - 0.7775\left|{}^{6}\mathrm{s}_{6}\right|\left|{}^{6}\mathrm{d}_{6}\right|\cos\left(\phi_{d-p}+\phi_{p-s}\right)\\
&- 2.3\left|{}^{6}\mathrm{s}_{6}\right|\left|{}^{2}\mathrm{d}_{6}\right|\cos\left(\phi_{d-p}+\phi_{p-s}\right) - 0.3612\left|{}^{6}\mathrm{s}_{6}\right|\left|{}^{4}\mathrm{d}_{14}\right|\cos\left(\phi_{d-p}+\phi_{p-s}\right)\\
&+ 0.8161\left|{}^{6}\mathrm{s}_{6}\right|\left|{}^{6}\mathrm{d}_{14}\right|\cos\left(\phi_{d-p}+\phi_{p-s}\right) - 2.0471\left|{}^{2}\mathrm{p}_{4}\right|\left|{}^{4}\mathrm{p}_{10}\right|\\
&- 1.3467\left|{}^{2}\mathrm{p}_{4}\right|\left|{}^{6}\mathrm{p}_{10}\right| - 3.7526\left|{}^{4}\mathrm{p}_{10}\right|^{2} - 3.3897\left|{}^{4}\mathrm{p}_{10}\right|\left|{}^{6}\mathrm{p}_{10}\right| - 1.0773\left|{}^{6}\mathrm{p}_{10}\right|^{2}\\
&- 0.8281\left|{}^{2}\mathrm{d}_{4}\right|\left|{}^{4}\mathrm{d}_{14}\right|\cos\left(\delta^{d}\right) + 0.9484\left|{}^{2}\mathrm{d}_{4}\right|\left|{}^{6}\mathrm{d}_{14}\right|\cos\left(\delta^{d}\right)\\
&+ 0.939\left|{}^{4}\mathrm{d}_{6}\right|\left|{}^{2}\mathrm{d}_{6}\right|\cos\left(\delta^{d}\right)
\end{aligned}
\tag{C.24}
$$

$$
\begin{aligned}
&+ 2.1525\left|{}^4\mathrm{d}_6\right|\left|{}^4\mathrm{d}_{14}\right|\cos\left(\delta^d\right) + 2.3315\left|{}^4\mathrm{d}_6\right|\left|{}^6\mathrm{d}_{14}\right|\cos\left(\delta^d\right)\\
&+ 2.2508\left|{}^6\mathrm{d}_6\right|\left|{}^4\mathrm{d}_{14}\right|\cos\left(\delta^d\right) + 3.0475\left|{}^6\mathrm{d}_6\right|\left|{}^6\mathrm{d}_{14}\right|\cos\left(\delta^d\right) - 1.753\left|{}^2\mathrm{d}_6\right|\left|{}^4\mathrm{d}_{14}\right|\\
&+ 1.2469\left|{}^2\mathrm{d}_6\right|\left|{}^6\mathrm{d}_{14}\right| - 1.8768\left|{}^4\mathrm{d}_6\right|^2 + 3.3785\left|{}^4\mathrm{d}_{14}\right|\left|{}^6\mathrm{d}_{14}\right| + 2.8687\left|{}^6\mathrm{d}_{14}\right|,
\end{aligned}
$$

$$
\begin{aligned}
\mathrm{d}_5 = \; &- 2.2082\left|{}^2\mathrm{p}_4\right|\left|{}^4\mathrm{d}_{14}\right|\cos\left(\phi_{d-p}\right) - 1.803\left|{}^2\mathrm{p}_4\right|\left|{}^6\mathrm{d}_{14}\right|\cos\left(\phi_{d-p}\right)\\
&- 2.2857\left|{}^4\mathrm{p}_{10}\right|\left|{}^2\mathrm{d}_6\right|\cos\left(\phi_{d-p}\right) - 8.2118\left|{}^4\mathrm{p}_{10}\right|\left|{}^4\mathrm{d}_{14}\right|\cos\left(\phi_{d-p}\right)\\
&- 5.6008\left|{}^4\mathrm{p}_{10}\right|\left|{}^6\mathrm{d}_{14}\right|\cos\left(\phi_{d-p}\right) - 1.4964\left|{}^6\mathrm{p}_{10}\right|\left|{}^2\mathrm{d}_6\right|\cos\left(\phi_{d-p}\right)\\
&- 4.5053\left|{}^6\mathrm{p}_{10}\right|\left|{}^4\mathrm{d}_{14}\right|\cos\left(\phi_{d-p}\right) - 2.9558\left|{}^6\mathrm{p}_{10}\right|\left|{}^6\mathrm{d}_{14}\right|\cos\left(\phi_{d-p}\right),
\end{aligned}
\tag{C.25}
$$

and

$$
\begin{aligned}
\mathrm{d}_6 = \; &- 2.5093\left|{}^2\mathrm{d}_6\right|\left|{}^4\mathrm{d}_{14}\right| - 2.0489\left|{}^2\mathrm{d}_6\right|\left|{}^6\mathrm{d}_{14}\right| - 4.5929\left|{}^4\mathrm{d}_{14}\right|^2\\
&- 4.7296\left|{}^4\mathrm{d}_{14}\right|\left|{}^6\mathrm{d}_{14}\right| - 2.0723\left|{}^6\mathrm{d}_{14}\right|^2.
\end{aligned}
\tag{C.26}
$$

C.1.5 T_{22}

Equation 5.9 gives

$$
\begin{aligned}
\frac{\mathrm{T}_{22}(\theta)\;\sigma(\theta)}{\mathrm{A}_0} = \; &\mathrm{Q}_2\mathrm{e}_2\mathrm{P}_2^2(\cos\theta) + \mathrm{Q}_3\mathrm{e}_3\mathrm{P}_3^1(\cos\theta) + \mathrm{Q}_4\mathrm{e}_4\mathrm{P}_4^2(\cos\theta)\\
&+ \mathrm{Q}_5\mathrm{e}_5\mathrm{P}_5^2(\cos\theta) + \mathrm{Q}_6\mathrm{e}_6\mathrm{P}_6^2(\cos\theta)
\end{aligned}
\tag{C.27}
$$

for $\mathrm{T}_{22}(\theta)$, where

$$
\begin{aligned}
e_2 = {} & 0.7303\left|{}^2s_2\right|\left|{}^4s_4\right| + 2.6833\left|{}^2s_2\right|\left|{}^6s_6\right|\cos\left(\delta^s\right) \\
& + 0.7303\left|{}^2s_2\right|\left|{}^4d_6\right|\cos\left(\phi_{d-p}+\phi_{p-s}\right) + 1.1711\left|{}^2s_2\right|\left|{}^6d_6\right|\cos\left(\phi_{d-p}+\phi_{p-s}\right) \\
& - 0.5856\left|{}^2s_2\right|\left|{}^4d_{14}\right|\cos\left(\phi_{d-p}+\phi_{p-s}\right) + 2.8685\left|{}^2s_2\right|\left|{}^6d_{14}\right|\cos\left(\phi_{d-p}+\phi_{p-s}\right) \\
& + 0.9238\left|{}^4s_4\right|^2 - 1.697\left|{}^4s_4\right|\left|{}^6s_6\right|\cos\left(\delta^s\right) - 0.7303\left|{}^4s_4\right|\left|{}^2d_4\right|\cos\left(\phi_{d-p}+\phi_{p-s}\right) \\
& + 1.3064\left|{}^4s_4\right|\left|{}^4d_6\right|\cos\left(\phi_{d-p}+\phi_{p-s}\right) + 2.8314\left|{}^4s_4\right|\left|{}^6d_6\right|\cos\left(\phi_{d-p}+\phi_{p-s}\right) \\
& - 0.313\left|{}^4s_4\right|\left|{}^2d_6\right|\cos\left(\phi_{d-p}+\phi_{p-s}\right) - 0.139\left|{}^4s_4\right|\left|{}^4d_{14}\right|\cos\left(\phi_{d-p}+\phi_{p-s}\right) \\
& + 2.6508\left|{}^4s_4\right|\left|{}^6d_{14}\right|\cos\left(\phi_{d-p}+\phi_{p-s}\right) - 1.3857\left|{}^6s_6\right|^2 \\
& - 0.7667\left|{}^6s_6\right|\left|{}^2d_4\right|\cos\left(\phi_{d-p}+\phi_{p-s}\right) + 0.0122\left|{}^6s_6\right|\left|{}^4d_6\right|\cos\left(\phi_{d-p}+\phi_{p-s}\right) \\
& + 1.168\left|{}^6s_6\right|\left|{}^6d_6\right|\cos\left(\phi_{d-p}+\phi_{p-s}\right) - 3.0666\left|{}^6s_6\right|\left|{}^2d_6\right|\cos\left(\phi_{d-p}+\phi_{p-s}\right) \\
& + 2.3954\left|{}^6s_6\right|\left|{}^4d_{14}\right|\cos\left(\phi_{d-p}+\phi_{p-s}\right) + 0.2101\left|{}^6s_6\right|\left|{}^6d_{14}\right|\cos\left(\phi_{d-p}+\phi_{p-s}\right) \\
& - 0.5798\left|{}^2p_2\right|\left|{}^4p_{10}\right|\cos\left(\delta^p\right) + 2.0805\left|{}^2p_2\right|\left|{}^6p_{10}\right|\cos\left(\delta^p\right) \\
& - 1.0372\left|{}^4p_2\right|\left|{}^4p_{10}\right|\cos\left(\delta^p\right) - 5.0614\left|{}^4p_2\right|\left|{}^6p_{10}\right|\cos\left(\delta^p\right) + 1.4369\left|{}^2p_4\right|\left|{}^4p_{10}\right| \\
& - 1.5193\left|{}^2p_4\right|\left|{}^6p_{10}\right| + 0.0305\left|{}^4p_{10}\right|^2 - 5.2272\left|{}^4p_{10}\right|\left|{}^6p_{10}\right| + 0.3778\left|{}^6p_{10}\right|^2 \\
& - 0.7303\left|{}^2d_4\right|\left|{}^4d_6\right| - 1.1711\left|{}^2d_4\right|\left|{}^6d_6\right| - 0.0777\left|{}^2d_4\right|\left|{}^4d_{14}\right|\cos\left(\delta^d\right) \\
& + 1.0536 abs^2 d_4\left|{}^6d_{14}\right|\cos\left(\delta^d\right) + 0.3827\left|{}^4d_6\right|^2 + 1.9637\left|{}^4d_6\right|\left|{}^6d_6\right| \\
& - 0.313\left|{}^4d_6\right|\left|{}^2d_6\right|\cos\left(\delta^d\right) - 1.383\left|{}^4d_6\right|\left|{}^4d_{14}\right|\cos\left(\delta^d\right) \\
& - 4.8356\left|{}^4d_6\right|\left|{}^6d_{14}\right|\cos\left(\delta^d\right) + 2.165\left|{}^6d_6\right|^2 - 1.0198\left|{}^6d_6\right|\left|{}^4d_{14}\right|\cos\left(\delta^d\right) \\
& + 1.8515\left|{}^6d_6\right|\left|{}^6d_{14}\right|\cos\left(\delta^d\right) + 1.9\left|{}^2d_6\right|\left|{}^4d_{14}\right| - 4.3466\left|{}^2d_6\right|\left|{}^6d_{14}\right| \\
& - 0.0393\left|{}^4d_{14}\right|^2 - 7.9874\left|{}^4d_{14}\right|\left|{}^6d_{14}\right| + 1.4575\left|{}^6d_{14}\right|^2,
\end{aligned}
\tag{C.28}
$$

$$
\begin{aligned}
\mathrm{e}_3 = {} & 0.4\left|{}^2\mathrm{s}_2\right|\left|{}^4\mathrm{p}_{10}\right|\cos\left(\phi_{p-s}\right) + 0.2618\left|{}^2\mathrm{s}_2\right|\left|{}^6\mathrm{p}_{10}\right|\cos\left(\phi_{p-s}\right) \\
& + 0.4382\left|{}^4\mathrm{s}_4\right|\left|{}^2\mathrm{p}_4\right|\cos\left(\phi_{p-s}\right) + 1.3053\left|{}^4\mathrm{s}_4\right|\left|{}^4\mathrm{p}_{10}\right|\cos\left(\phi_{p-s}\right) \\
& + 0.6817\left|{}^4\mathrm{s}_4\right|\left|{}^6\mathrm{p}_{10}\right|\cos\left(\phi_{p-s}\right) + 0.8944\left|{}^6\mathrm{s}_6\right|\left|{}^2\mathrm{p}_2\right|\cos\left(\phi_{p-s}\right) \\
& + 0.4\left|{}^6\mathrm{s}_6\right|\left|{}^4\mathrm{p}_2\right|\cos\left(\phi_{p-s}\right) + 0.7155\left|{}^6\mathrm{s}_6\right|\left|{}^2\mathrm{p}_4\right|\cos\left(\phi_{p-s}\right) \\
& + 0.0659\left|{}^6\mathrm{s}_6\right|\left|{}^4\mathrm{p}_{10}\right|\cos\left(\phi_{p-s}\right) - 0.2389\left|{}^6\mathrm{s}_6\right|\left|{}^6\mathrm{p}_{10}\right|\cos\left(\phi_{p-s}\right) \\
& - 0.3095\left|{}^2\mathrm{p}_2\right|\left|{}^4\mathrm{d}_{14}\right|\cos\left(\phi_{d-p}\right) + 1.8303\left|{}^2\mathrm{p}_2\right|\left|{}^6\mathrm{d}_{14}\right|\cos\left(\phi_{d-p}\right) \\
& - 0.5537\left|{}^4\mathrm{p}_2\right|\left|{}^4\mathrm{d}_{14}\right|\cos\left(\phi_{d-p}\right) - 2.8649\left|{}^4\mathrm{p}_2\right|\left|{}^6\mathrm{d}_{14}\right|\cos\left(\phi_{d-p}\right) \\
& + 0.4382\left|{}^2\mathrm{p}_4\right|\left|{}^4\mathrm{d}_4\right|\cos\left(\phi_{d-p}\right) + 0.4382\left|{}^2\mathrm{p}_4\right|\left|{}^4\mathrm{d}_6\right|\cos\left(\phi_{d-p}\right) \\
& + 0.7027\left|{}^2\mathrm{p}_4\right|\left|{}^6\mathrm{d}_6\right|\cos\left(\phi_{d-p}\right) + 0.51029\left|{}^2\mathrm{p}_4\right|\left|{}^4\mathrm{d}_{14}\right|\cos\left(\phi_{d-p}\right) \\
& + 0.3416\left|{}^2\mathrm{p}_4\right|\left|{}^6\mathrm{d}_{14}\right|\cos\left(\phi_{d-p}\right) - 0.7478\left|{}^4\mathrm{p}_{10}\right|\left|{}^2\mathrm{d}_4\right|\cos\left(\phi_{d-p}\right) \\
& + 0.1288\left|{}^4\mathrm{p}_{10}\right|\left|{}^4\mathrm{d}_6\right|\cos\left(\phi_{d-p}\right) + 1.492\left|{}^4\mathrm{p}_{10}\right|\left|{}^6\mathrm{d}_6\right|\cos\left(\phi_{d-p}\right) \\
& + 0.7478\left|{}^4\mathrm{p}_{10}\right|\left|{}^2\mathrm{d}_6\right|\cos\left(\phi_{d-p}\right) + 0.2092\left|{}^4\mathrm{p}_{10}\right|\left|{}^4\mathrm{d}_{14}\right|\cos\left(\phi_{d-p}\right) \\
& - 1.1769\left|{}^4\mathrm{p}_{10}\right|\left|{}^6\mathrm{d}_{14}\right|\cos\left(\phi_{d-p}\right) + 0.9864\left|{}^6\mathrm{p}_{10}\right|\left|{}^2\mathrm{d}_4\right|\cos\left(\phi_{d-p}\right) \\
& - 3.0794\left|{}^6\mathrm{p}_{10}\right|\left|{}^4\mathrm{d}_6\right|\cos\left(\phi_{d-p}\right) - 1.1814\left|{}^6\mathrm{p}_{10}\right|\left|{}^6\mathrm{d}_6\right|\cos\left(\phi_{d-p}\right) \\
& - 0.9864\left|{}^6\mathrm{p}_{10}\right|\left|{}^2\mathrm{d}_6\right|\cos\left(\phi_{d-p}\right) - 3.6924\left|{}^6\mathrm{p}_{10}\right|\left|{}^4\mathrm{d}_{14}\right|\cos\left(\phi_{d-p}\right) \\
& + 0.25594\left|{}^6\mathrm{p}_{10}\right|\left|{}^6\mathrm{d}_{14}\right|\cos\left(\phi_{d-p}\right),
\end{aligned}
\tag{C.29}
$$

$$
\begin{aligned}
\mathrm{e}_4 = {} & 0.276\left|{}^2\mathrm{s}_2\right|\left|{}^4\mathrm{d}_{14}\right|\cos\left(\phi_{d-p}+\phi_{p-s}\right)+0.2254\left|{}^2\mathrm{s}_2\right|\left|{}^6\mathrm{d}_{14}\right|\cos\left(\phi_{d-p}+\phi_{p-s}\right)\\
& +0.313\left|{}^4\mathrm{s}_4\right|\left|{}^2\mathrm{d}_6\right|\cos\left(\phi_{d-p}+\phi_{p-s}\right)+0.922\left|{}^4\mathrm{s}_4\right|\left|{}^4\mathrm{d}_{14}\right|\cos\left(\phi_{d-p}+\phi_{p-s}\right)\\
& +0.6016\left|{}^4\mathrm{s}_4\right|\left|{}^6\mathrm{d}_{14}\right|\cos\left(\phi_{d-p}+\phi_{p-s}\right)+0.7667\left|{}^6\mathrm{s}_6\right|\left|{}^2\mathrm{d}_4\right|\cos\left(\phi_{d-p}+\phi_{p-s}\right)\\
& +0.4849\left|{}^6\mathrm{s}_6\right|\left|{}^4\mathrm{d}_6\right|\cos\left(\phi_{d-p}+\phi_{p-s}\right)+0.1296\left|{}^6\mathrm{s}_6\right|\left|{}^6\mathrm{d}_6\right|\cos\left(\phi_{d-p}+\phi_{p-s}\right)\\
& +0.3833\left|{}^6\mathrm{s}_6\right|\left|{}^2\mathrm{d}_6\right|\cos\left(\phi_{d-p}+\phi_{p-s}\right)+0.0602\left|{}^6\mathrm{s}_6\right|\left|{}^4\mathrm{d}_{14}\right|\cos\left(\phi_{d-p}+\phi_{p-s}\right)\\
& -0.136\left|{}^6\mathrm{s}_6\right|\left|{}^6\mathrm{d}_{14}\right|\cos\left(\phi_{d-p}+\phi_{p-s}\right)+0.3429\left|{}^2\mathrm{p}_4\right|\left|{}^4\mathrm{p}_{10}\right|+0.2244\left|{}^2\mathrm{p}_4\right|\left|{}^6\mathrm{p}_{10}\right|\\
& +0.6254\left|{}^4\mathrm{p}_{10}\right|^2+0.5649\left|{}^4\mathrm{p}_{10}\right|\left|{}^6\mathrm{p}_{10}\right|+0.1797\left|{}^6\mathrm{p}_{10}\right|^2\\
& -0.5413\left|{}^2\mathrm{d}_4\right|\left|{}^4\mathrm{d}_{14}\right|\cos\left(\delta^d\right)+1.3435\left|{}^2\mathrm{d}_4\right|\left|{}^6\mathrm{d}_{14}\right|\cos\left(\delta^d\right)\\
& +0.313\left|{}^4\mathrm{d}_6\right|\left|{}^2\mathrm{d}_6\right|\cos\left(\delta^d\right)+0.0463\left|{}^4\mathrm{d}_6\right|\left|{}^4\mathrm{d}_{14}\right|\cos\left(\delta^d\right)\\
& -2.412\left|{}^4\mathrm{d}_6\right|\left|{}^6\mathrm{d}_{14}\right|\cos\left(\delta^d\right)+1.1101\left|{}^6\mathrm{d}_6\right|\left|{}^4\mathrm{d}_{14}\right|\cos\left(\delta^d\right)\\
& -0.9729\left|{}^6\mathrm{d}_6\right|\left|{}^6\mathrm{d}_{14}\right|\cos\left(\delta^d\right)+0.4338\left|{}^2\mathrm{d}_6\right|\left|{}^4\mathrm{d}_{14}\right|+0.003\left|{}^2\mathrm{d}_6\right|\left|{}^6\mathrm{d}_{14}\right|\\
& -0.2077\left|{}^4\mathrm{d}_{14}\right|^2-0.4929\left|{}^4\mathrm{d}_{14}\right|\left|{}^6\mathrm{d}_{14}\right|+0.1036\left|{}^6\mathrm{d}_{14}\right|^2,
\end{aligned}
\tag{C.30}
$$

$$
\begin{aligned}
\mathrm{e}_5 = {} & +0.276\left|{}^2\mathrm{p}_4\right|\left|{}^4\mathrm{d}_{14}\right|\cos\left(\phi_{d-p}\right)+0.2254\left|{}^2\mathrm{p}_4\right|\left|{}^6\mathrm{d}_{14}\right|\cos\left(\phi_{d-p}\right)\\
& +0.2857\left|{}^4\mathrm{p}_{10}\right|\left|{}^2\mathrm{d}_6\right|\cos\left(\phi_{d-p}\right)+1.0265\left|{}^4\mathrm{p}_{10}\right|\left|{}^4\mathrm{d}_{14}\right|\cos\left(\phi_{d-p}\right)\\
& +0.7001\left|{}^4\mathrm{p}_{10}\right|\left|{}^6\mathrm{d}_{14}\right|\cos\left(\phi_{d-p}\right)+0.1871\left|{}^6\mathrm{p}_{10}\right|\left|{}^2\mathrm{d}_6\right|\cos\left(\phi_{d-p}\right)\\
& +0.5631\left|{}^6\mathrm{p}_{10}\right|\left|{}^4\mathrm{d}_{14}\right|\cos\left(\phi_{d-p}\right)+0.3694\left|{}^6\mathrm{p}_{10}\right|\left|{}^6\mathrm{d}_{14}\right|\cos\left(\phi_{d-p}\right),
\end{aligned}
\tag{C.31}
$$

and

$$
\begin{aligned}
\mathrm{e}_6 = {} & 0.2509\left|{}^2\mathrm{d}_6\right|\left|{}^4\mathrm{d}_{14}\right|+0.2049\left|{}^2\mathrm{d}_6\right|\left|{}^6\mathrm{d}_{14}\right|+0.4593\left|{}^4\mathrm{d}_{14}\right|^2\\
& +0.4729\left|{}^4\mathrm{d}_{14}\right|\left|{}^6\mathrm{d}_{14}\right|+0.2072\left|{}^6\mathrm{d}_{14}\right|^2.
\end{aligned}
\tag{C.32}
$$

C.2 Equations for the $^{7}\mathrm{Li}(\vec{\mathrm{d}},\mathrm{n}_1)^{8}\mathrm{Be}$ Reaction

Using Equation 5.1 through Equation 5.9 in the same way as the previous section, the equations for the observables of the $^{7}\mathrm{Li}(\vec{\mathrm{d}},\mathrm{n}_1)^{8}\mathrm{Be}$ reaction are listed below.

C.2.1 Cross Section

The cross section becomes

$$\sigma(\theta) = \mathrm{A}_0\left(\mathrm{a}_0 + \mathrm{Q}_1\mathrm{a}_1\mathrm{P}_1(\cos\theta) + \mathrm{Q}_2\mathrm{a}_2\mathrm{P}_2(\cos\theta)\right), \tag{C.33}$$

where

$$\begin{aligned}\mathrm{a}_0 = \; & 2\left|{}^{2}\mathrm{s}_2\right|^2 + 8\left|{}^{4}\mathrm{s}_8\right|^2 + 12\left|{}^{6}\mathrm{s}_{12}\right|^2 + 4\left|{}^{2}\mathrm{p}_4\right|^2 + 10\left|{}^{4}\mathrm{p}_{10}\right|^2 \\ & + 10\left|{}^{6}\mathrm{p}_{10}\right|^2 + 12\left|{}^{2}\mathrm{p}_{12}\right|^2 + 24\left|{}^{4}\mathrm{p}_{24}\right|^2 + 20\left|{}^{6}\mathrm{p}_{20}\right|^2,\end{aligned} \tag{C.34}$$

$$\begin{aligned}\mathrm{a}_1 = \; & -5.6568\left|{}^{2}\mathrm{s}_2\right|\left|{}^{2}\mathrm{p}_4\right|\cos(\phi_{p-s}) + 9.6568\left|{}^{2}\mathrm{s}_2\right|\left|{}^{2}\mathrm{p}_{12}\right|\cos(\phi_{p-s}) \\ & - 1.7979\left|{}^{4}\mathrm{s}_8\right|\left|{}^{4}\mathrm{p}_{10}\right|\cos(\phi_{p-s}) + 38.2331\left|{}^{4}\mathrm{s}_8\right|\left|{}^{4}\mathrm{p}_{24}\right|\cos(\phi_{p-s}) \\ & + 2.202\left|{}^{6}\mathrm{s}_{12}\right|\left|{}^{6}\mathrm{p}_{10}\right|\cos(\phi_{p-s}) + 24.2224\left|{}^{6}\mathrm{s}_{12}\right|\left|{}^{6}\mathrm{p}_{20}\right|\cos(\phi_{p-s}),\end{aligned} \tag{C.35}$$

and

$$\begin{aligned}\mathrm{a}_2 = \; & -13.6569\left|{}^{2}\mathrm{p}_4\right|\left|{}^{2}\mathrm{p}_{12}\right|\cos(\delta^p) - 4.1395\left|{}^{4}\mathrm{p}_{10}\right|\left|{}^{4}\mathrm{p}_{24}\right|\cos(\delta^p) \\ & + 7.584\left|{}^{6}\mathrm{p}_{12}\right|\left|{}^{6}\mathrm{p}_{20}\right|\cos(\delta^p) + 2.4091\left|{}^{2}\mathrm{p}_{12}\right|^2 \\ & + 41.6898\left|{}^{4}\mathrm{p}_{24}\right|^2 - 12.635\left|{}^{6}\mathrm{p}_{20}\right|^2.\end{aligned} \tag{C.36}$$

C.2.2 $i\mathrm{T}_{11}$

The vector analyzing power $i\mathrm{T}_{11}(\theta)$ is given to be

$$\frac{i\mathrm{T}_{11}(\theta)\;\sigma(\theta)}{\mathrm{A}_0} = \mathrm{Q}_1\mathrm{b}_1\mathrm{P}_1^1(\cos\theta) + \mathrm{Q}_2\mathrm{b}_2\mathrm{P}_2^1(\cos\theta), \tag{C.37}$$

where the coefficients are

$$\begin{aligned}
\mathrm{b}_1 = & -1.633\left|{}^2\mathrm{s}_2\right|\left|{}^2\mathrm{p}_4\right|\sin\left(\phi_{p-s}\right)+5.7735\left|{}^2\mathrm{s}_2\right|\left|{}^4\mathrm{p}_{10}\right|\sin\left(\phi_{p-s}\right)\\
& -0.6764\left|{}^2\mathrm{s}_2\right|\left|{}^2\mathrm{p}_{12}\right|\sin\left(\phi_{p-s}\right)-8.3555\left|{}^2\mathrm{s}_2\right|\left|{}^4\mathrm{p}_{24}\right|\sin\left(\phi_{p-s}\right)\\
& -8.1649\left|{}^4\mathrm{s}_8\right|\left|{}^2\mathrm{p}_4\right|\sin\left(\phi_{p-s}\right)+5.2416\left|{}^4\mathrm{s}_8\right|\left|{}^4\mathrm{p}_{10}\right|\sin\left(\phi_{p-s}\right)\\
& +2.6857\left|{}^4\mathrm{s}_8\right|\left|{}^6\mathrm{p}_{10}\right|\sin\left(\phi_{p-s}\right)-17.9984\left|{}^4\mathrm{s}_8\right|\left|{}^2\mathrm{p}_{12}\right|\sin\left(\phi_{p-s}\right)\\
& +0.3841\left|{}^4\mathrm{s}_8\right|\left|{}^4\mathrm{p}_{24}\right|\sin\left(\phi_{p-s}\right)-23.2883\left|{}^4\mathrm{s}_8\right|\left|{}^6\mathrm{p}_{20}\right|\sin\left(\phi_{p-s}\right)\\
& -3.2893\left|{}^6\mathrm{s}_{12}\right|\left|{}^4\mathrm{p}_{10}\right|\sin\left(\phi_{p-s}\right)-7.7224\left|{}^6\mathrm{s}_{12}\right|\left|{}^6\mathrm{p}_{10}\right|\sin\left(\phi_{p-s}\right)\\
& -18.1625\left|{}^6\mathrm{s}_{12}\right|\left|{}^4\mathrm{p}_{24}\right|\sin\left(\phi_{p-s}\right)+14.2449\left|{}^6\mathrm{s}_{12}\right|\left|{}^6\mathrm{p}_{20}\right|\sin\left(\phi_{p-s}\right)
\end{aligned} \tag{C.38}$$

and

$$\begin{aligned}
\mathrm{b}_2 = & 1.633\left|{}^2\mathrm{p}_4\right|\left|{}^2\mathrm{p}_{12}\right|\sin\left(\delta^p\right)+10.4664\left|{}^2\mathrm{p}_4\right|\left|{}^4\mathrm{p}_{24}\right|\sin\left(\delta^p\right)\\
& -2.9987\left|{}^4\mathrm{p}_{10}\right|\left|{}^2\mathrm{p}_{12}\right|\sin\left(\delta^p\right)-5.2908\left|{}^4\mathrm{p}_{10}\right|\left|{}^4\mathrm{p}_{24}\right|\sin\left(\delta^p\right)\\
& +2.4121\left|{}^4\mathrm{p}_{10}\right|\left|{}^6\mathrm{p}_{20}\right|\sin\left(\delta^p\right)-3.9402\left|{}^6\mathrm{p}_{10}\right|\left|{}^4\mathrm{p}_{24}\right|\sin\left(\delta^p\right)\\
& +3.0827\left|{}^6\mathrm{p}_{10}\right|\left|{}^6\mathrm{p}_{20}\right|\sin\left(\delta^p\right).
\end{aligned} \tag{C.39}$$

C.2.3 T_{20}

The tensor analyzing power $\mathrm{T}_{20}(\theta)$ is

$$\begin{aligned}
\frac{\mathrm{T}_{20}(\theta)\ \sigma(\theta)}{\mathrm{A}_0} = & \ \mathrm{c}_0+\mathrm{Q}_1\mathrm{c}_1\mathrm{P}_1(\cos\theta)+\mathrm{Q}_2\mathrm{c}_2\mathrm{P}_2(\cos\theta)\\
& +\mathrm{Q}_3\mathrm{c}_3\mathrm{P}_3(\cos\theta)+\mathrm{Q}_4\mathrm{c}_4\mathrm{P}_4(\cos\theta).
\end{aligned} \tag{C.40}$$

The coefficients are

$$\begin{aligned}
\mathrm{c}_0 = & 0.8\left|{}^2\mathrm{p}_4\right|\left|{}^4\mathrm{p}_{10}\right|-5.8788\left|{}^2\mathrm{p}_4\right|\left|{}^6\mathrm{p}_{10}\right|-1.1314\left|{}^4\mathrm{p}_{10}\right|^2\\
& +1.1536\left|{}^4\mathrm{p}_{10}\right|\left|{}^6\mathrm{p}_{10}\right|+1.1314\left|{}^6\mathrm{p}_{10}\right|^2-0.9298\left|{}^2\mathrm{p}_{12}\right|\left|{}^4\mathrm{p}_{24}\right|\\
& -11.7575\left|{}^2\mathrm{p}_{12}\right|\left|{}^6\mathrm{p}_{20}\right|+2.3072\left|{}^4\mathrm{p}_{24}\right|\left|{}^6\mathrm{p}_{20}\right|+2.2628\left|{}^6\mathrm{p}_{20}\right|^2,
\end{aligned} \tag{C.41}$$

$$
\begin{aligned}
c_1 = & -0.5657\left|{}^2s_2\right|\left|{}^4p_{10}\right|\cos\left(\phi_{p-s}\right)+4.1569\left|{}^2s_2\right|\left|{}^6p_{10}\right|\cos\left(\phi_{p-s}\right)\\
& -0.6992\left|{}^2s_2\right|\left|{}^4p_{24}\right|\cos\left(\phi_{p-s}\right)-4.1569\left|{}^2s_2\right|\left|{}^6p_{20}\right|\cos\left(\phi_{p-s}\right)\\
& +0.8\left|{}^4s_8\right|\left|{}^2p_4\right|\cos\left(\phi_{p-s}\right)-4.7289\left|{}^4s_8\right|\left|{}^4p_{10}\right|\cos\left(\phi_{p-s}\right)\\
& +9.6296\left|{}^4s_8\right|\left|{}^6p_{10}\right|\cos\left(\phi_{p-s}\right)-0.5782\left|{}^4s_8\right|\left|{}^2p_{12}\right|\cos\left(\phi_{p-s}\right)\\
& -0.65\left|{}^4s_8\right|\left|{}^4p_{24}\right|\cos\left(\phi_{p-s}\right)+2.862\left|{}^4s_8\right|\left|{}^6p_{20}\right|\cos\left(\phi_{p-s}\right)\\
& +7.2\left|{}^6s_{12}\right|\left|{}^2p_4\right|\cos\left(\phi_{p-s}\right)-11.7937\left|{}^6s_{12}\right|\left|{}^4p_{10}\right|\cos\left(\phi_{p-s}\right)\\
& +9.3104\left|{}^6s_{12}\right|\left|{}^6p_{10}\right|\cos\left(\phi_{p-s}\right)-4.9673\left|{}^6s_{12}\right|\left|{}^2p_{12}\right|\cos\left(\phi_{p-s}\right)\\
& -1.873\left|{}^6s_{12}\right|\left|{}^4p_{24}\right|\cos\left(\phi_{p-s}\right)+5.2261\left|{}^6s_{12}\right|\left|{}^6p_{20}\right|\cos\left(\phi_{p-s}\right),
\end{aligned}
\tag{C.42}
$$

$$
\begin{aligned}
c_2 = & -0.5657\left|{}^2s_2\right|\left|{}^4s_8\right|-5.0912\left|{}^2s_2\right|\left|{}^6s_{12}\right|-1.3576\left|{}^4s_8\right|^2\\
& -3.3177\left|{}^4s_8\right|\left|{}^6s_{12}\right|+0.3395\left|{}^6s_{12}\right|^2+2.56\left|{}^2p_4\right|\left|{}^4p_{24}\right|\cos\left(\delta^p\right)\\
& +6.9073\left|{}^2p_4\right|\left|{}^6p_{20}\right|\cos\left(\delta^p\right)-0.9515\left|{}^4p_{10}\right|\left|{}^2p_{12}\right|\cos\left(\delta^p\right)\\
& -10.9933\left|{}^4p_{10}\right|\left|{}^4p_{24}\right|\cos\left(\delta^p\right)-8.7278\left|{}^4p_{10}\right|\left|{}^6p_{20}\right|\cos\left(\delta^p\right)\\
& +10.3068\left|{}^6p_{10}\right|\left|{}^2p_{12}\right|\cos\left(\delta^p\right)+22.9907\left|{}^6p_{10}\right|\left|{}^4p_{24}\right|\cos\left(\delta^p\right)\\
& +10.9039\left|{}^6p_{10}\right|\left|{}^6p_{20}\right|\cos\left(\delta^p\right)-2.454\left|{}^2p_{12}\right|\left|{}^4p_{24}\right|+1.4045\left|{}^2p_{12}\right|\left|{}^6p_{20}\right|\\
& -1.212\left|{}^4p_{24}\right|^2+1.4154\left|{}^4p_{24}\right|\left|{}^6p_{20}\right|+3.2454\left|{}^6p_{20}\right|^2,
\end{aligned}
\tag{C.43}
$$

$$
\begin{aligned}
c_3 = & -1.111\left|{}^2s_2\right|\left|{}^4p_{24}\right|\cos\left(\phi_{p-s}\right)-0.7273\left|{}^2s_2\right|\left|{}^6p_{20}\right|\cos\left(\phi_{p-s}\right)\\
& -1.1257\left|{}^4s_8\right|\left|{}^2p_{12}\right|\cos\left(\phi_{p-s}\right)-4.8288\left|{}^4s_8\right|\left|{}^4p_{24}\right|\cos\left(\phi_{p-s}\right)\\
& -2.7174\left|{}^4s_8\right|\left|{}^6p_{20}\right|\cos\left(\phi_{p-s}\right)-7.0527\left|{}^6s_{12}\right|\left|{}^2p_{12}\right|\cos\left(\phi_{p-s}\right)\\
& -6.6832\left|{}^6s_{12}\right|\left|{}^4p_{24}\right|\cos\left(\phi_{p-s}\right)-1.9985\left|{}^6s_{12}\right|\left|{}^6p_{20}\right|\cos\left(\phi_{p-s}\right),
\end{aligned}
\tag{C.44}
$$

and

$$\begin{aligned} c_4 = & -1.8118\left|{}^2p_{12}\right|\left|{}^4p_{24}\right| - 1.1861\left|{}^2p_{12}\right|\left|{}^6p_{20}\right| \\ & - 5.8452\left|{}^4p_{24}\right|^2 - 4.255\left|{}^4p_{24}\right|\left|{}^6p_{20}\right| - 1.5698\left|{}^6p_{20}\right|^2 . \end{aligned} \tag{C.45}$$

C.2.4 T_{21}

The tensor analyzing power $T_{21}(\theta)$ can be written as

$$\begin{aligned} \frac{T_{21}(\theta)\ \sigma(\theta)}{A_0} = & Q_1 d_1 P_1^1(\cos\theta) + Q_2 d_2 P_2^1(\cos\theta) + Q_3 d_3 P_3^1(\cos\theta) \\ & + Q_4 d_4 P_4^1(\cos\theta), \end{aligned} \tag{C.46}$$

where

$$\begin{aligned} d_1 = & 0.6928\left|{}^2s_2\right|\left|{}^4p_{10}\right|\cos(\phi_{p-s}) - 5.0912\left|{}^2s_2\right|\left|{}^6p_{10}\right|\cos(\phi_{p-s}) \\ & + 0.8564\left|{}^2s_2\right|\left|{}^4p_{24}\right|\cos(\phi_{p-s}) + 5.0912\left|{}^2s_2\right|\left|{}^6p_{20}\right|\cos(\phi_{p-s}) \\ & - 0.9798\left|{}^4s_8\right|\left|{}^2p_4\right|\cos(\phi_{p-s}) + 5.7917\left|{}^4s_8\right|\left|{}^4p_{10}\right|\cos(\phi_{p-s}) \\ & - 11.7937\left|{}^4s_8\right|\left|{}^6p_{10}\right|\cos(\phi_{p-s}) + 0.708\left|{}^4s_8\right|\left|{}^2p_{12}\right|\cos(\phi_{p-s}) \\ & + 0.796\left|{}^4s_8\right|\left|{}^4p_{24}\right|\cos(\phi_{p-s}) - 3.5052\left|{}^4s_8\right|\left|{}^6p_{20}\right|\cos(\phi_{p-s}) \\ & - 8.8182\left|{}^6s_{12}\right|\left|{}^2p_4\right|\cos(\phi_{p-s}) + 14.4444\left|{}^6s_{12}\right|\left|{}^4p_{10}\right|\cos(\phi_{p-s}) \\ & - 11.4028\left|{}^6s_{12}\right|\left|{}^6p_{10}\right|\cos(\phi_{p-s}) + 6.0836\left|{}^6s_{12}\right|\left|{}^2p_{12}\right|\cos(\phi_{p-s}) \\ & + 2.2939\left|{}^6s_{12}\right|\left|{}^4p_{24}\right|\cos(\phi_{p-s}) - 6.4007\left|{}^6s_{12}\right|\left|{}^6p_{20}\right|\cos(\phi_{p-s}) , \end{aligned} \tag{C.47}$$

$$
\begin{aligned}
\mathrm{d}_2 = {} & 0.4619\left|{}^2\mathrm{s}_2\right|\left|{}^4\mathrm{s}_8\right| + 4.1569\left|{}^2\mathrm{s}_2\right|\left|{}^6\mathrm{s}_{12}\right| + 1.1085\left|{}^4\mathrm{s}_8\right|^2 \\
& + 2.709\left|{}^4\mathrm{s}_8\right|\left|{}^6\mathrm{s}_{12}\right| - 0.2771\left|{}^6\mathrm{s}_{12}\right|^2 - 1.5054\left|{}^2\mathrm{p}_4\right|\left|{}^4\mathrm{p}_{24}\right|\cos\left(\delta^p\right) \\
& - 1.6603\left|{}^2\mathrm{p}_4\right|\left|{}^6\mathrm{p}_{20}\right|\cos\left(\delta^p\right) + 0.9598\left|{}^4\mathrm{p}_{10}\right|\left|{}^2\mathrm{p}_{12}\right|\cos\left(\delta^p\right) \\
& + 6.829\left|{}^4\mathrm{p}_{10}\right|\left|{}^4\mathrm{p}_{24}\right|\cos\left(\delta^p\right) + 2.379\left|{}^4\mathrm{p}_{10}\right|\left|{}^6\mathrm{p}_{20}\right|\cos\left(\delta^p\right) \\
& - 8.7974\left|{}^6\mathrm{p}_{10}\right|\left|{}^2\mathrm{p}_{12}\right|\cos\left(\delta^p\right) - 15.1937\left|{}^6\mathrm{p}_{10}\right|\left|{}^4\mathrm{p}_{24}\right|\cos\left(\delta^p\right) \\
& - 7.6974\left|{}^6\mathrm{p}_{10}\right|\left|{}^6\mathrm{p}_{20}\right|\cos\left(\delta^p\right) + 1.7742\left|{}^2\mathrm{p}_{12}\right|\left|{}^4\mathrm{p}_{24}\right| + 3.2167\left|{}^2\mathrm{p}_{12}\right|\left|{}^6\mathrm{p}_{20}\right| \\
& + 3.4465\left|{}^4\mathrm{p}_{24}\right|^2 - 1.8784\left|{}^4\mathrm{p}_{24}\right|\left|{}^6\mathrm{p}_{20}\right| - 4.5727\left|{}^6\mathrm{p}_{20}\right|^2,
\end{aligned}
\tag{C.48}
$$

$$
\begin{aligned}
\mathrm{d}_3 = {} & 0.6048\left|{}^2\mathrm{s}_2\right|\left|{}^4\mathrm{p}_{24}\right|\cos\left(\phi_{p-s}\right) + 0.3959\left|{}^2\mathrm{s}_2\right|\left|{}^6\mathrm{p}_{20}\right|\cos\left(\phi_{p-s}\right) \\
& + 0.6128\left|{}^4\mathrm{s}_8\right|\left|{}^2\mathrm{p}_{12}\right|\cos\left(\phi_{p-s}\right) + 2.6284\left|{}^4\mathrm{s}_8\right|\left|{}^4\mathrm{p}_{24}\right|\cos\left(\phi_{p-s}\right) \\
& + 1.4792\left|{}^4\mathrm{s}_8\right|\left|{}^6\mathrm{p}_{20}\right|\cos\left(\phi_{p-s}\right) + 3.839\left|{}^6\mathrm{s}_{12}\right|\left|{}^2\mathrm{p}_{12}\right|\cos\left(\phi_{p-s}\right) \\
& + 3.6379\left|{}^6\mathrm{s}_{12}\right|\left|{}^4\mathrm{p}_{24}\right|\cos\left(\phi_{p-s}\right) + 1.0879\left|{}^6\mathrm{s}_{12}\right|\left|{}^6\mathrm{p}_{20}\right|\cos\left(\phi_{p-s}\right),
\end{aligned}
\tag{C.49}
$$

and

$$
\begin{aligned}
\mathrm{d}_4 = {} & 0.7397\left|{}^2\mathrm{p}_{12}\right|\left|{}^4\mathrm{p}_{24}\right| + 0.4842\left|{}^2\mathrm{p}_{12}\right|\left|{}^6\mathrm{p}_{20}\right| + 2.3863\left|{}^4\mathrm{p}_{24}\right|^2 \\
& + 1.7371\left|{}^4\mathrm{p}_{24}\right|\left|{}^6\mathrm{p}_{20}\right| + 0.6409\left|{}^6\mathrm{p}_{20}\right|^2.
\end{aligned}
\tag{C.50}
$$

C.2.5 T_{22}

The tensor analyzing power $\mathrm{T}_{22}(\theta)$ is

$$
\frac{\mathrm{T}_{22}(\theta)\ \sigma(\theta)}{\mathrm{A}_0} = \mathrm{Q}_2\mathrm{e}_2\mathrm{P}_2^2(\cos\theta) + \mathrm{Q}_3\mathrm{e}_3\mathrm{P}_3^1(\cos\theta) + \mathrm{Q}_4\mathrm{e}_4\mathrm{P}_4^2(\cos\theta). \tag{C.51}
$$

The coefficients can be expanded as

$$\begin{aligned}
\mathrm{e}_2 = & -0.2309\left|{}^2\mathrm{s}_2\right|\left|{}^4\mathrm{s}_8\right| - 2.0784\left|{}^2\mathrm{s}_2\right|\left|{}^6\mathrm{s}_{12}\right| - 0.5543\left|{}^4\mathrm{s}_8\right|^2 \\
& - 1.3545\left|{}^4\mathrm{s}_8\right|\left|{}^6\mathrm{s}_{12}\right| + 0.1386\left|{}^6\mathrm{s}_{12}\right|^2 - 0.1246\left|{}^2\mathrm{p}_4\right|\left|{}^4\mathrm{p}_{24}\right|\cos\left(\delta^p\right) \\
& - 5.1391\left|{}^2\mathrm{p}_4\right|\left|{}^6\mathrm{p}_{20}\right|\cos\left(\delta^p\right) - 0.7543\left|{}^4\mathrm{p}_{10}\right|\left|{}^2\mathrm{p}_{12}\right|\cos\left(\delta^p\right) \\
& - 0.1939\left|{}^4\mathrm{p}_{10}\right|\left|{}^4\mathrm{p}_{24}\right|\cos\left(\delta^p\right) + 5.9313\left|{}^4\mathrm{p}_{10}\right|\left|{}^6\mathrm{p}_{20}\right|\cos\left(\delta^p\right) \\
& + 4.9716\left|{}^6\mathrm{p}_{10}\right|\left|{}^2\mathrm{p}_{12}\right|\cos\left(\delta^p\right) + 2.2296\left|{}^6\mathrm{p}_{10}\right|\left|{}^4\mathrm{p}_{24}\right|\cos\left(\delta^p\right) \\
& + 2.0403\left|{}^6\mathrm{p}_{10}\right|\left|{}^6\mathrm{p}_{20}\right|\cos\left(\delta^p\right) - 0.5429\left|{}^2\mathrm{p}_{12}\right|\left|{}^4\mathrm{p}_{24}\right| - 8.1534\left|{}^2\mathrm{p}_{12}\right|\left|{}^6\mathrm{p}_{20}\right| \\
& - 5.4086\left|{}^4\mathrm{p}_{24}\right|^2 + 2.0232\left|{}^4\mathrm{p}_{24}\right|\left|{}^6\mathrm{p}_{20}\right| + 5.1709\left|{}^6\mathrm{p}_{20}\right|^2,
\end{aligned} \tag{C.52}$$

$$\begin{aligned}
\mathrm{e}_3 = & -0.1512\left|{}^2\mathrm{s}_2\right|\left|{}^4\mathrm{p}_{24}\right|\cos\left(\phi_{p-s}\right) - 0.099\left|{}^2\mathrm{s}_2\right|\left|{}^6\mathrm{p}_{20}\right|\cos\left(\phi_{p-s}\right) \\
& - 0.1532\left|{}^4\mathrm{s}_8\right|\left|{}^2\mathrm{p}_{12}\right|\cos\left(\phi_{p-s}\right) - 0.6571\left|{}^4\mathrm{s}_8\right|\left|{}^4\mathrm{p}_{24}\right|\cos\left(\phi_{p-s}\right) \\
& - 0.3697\left|{}^4\mathrm{s}_8\right|\left|{}^6\mathrm{p}_{20}\right|\cos\left(\phi_{p-s}\right) - 0.9598\left|{}^6\mathrm{s}_{12}\right|\left|{}^2\mathrm{p}_{12}\right|\cos\left(\phi_{p-s}\right) \\
& - 0.9095\left|{}^6\mathrm{s}_{12}\right|\left|{}^4\mathrm{p}_{24}\right|\cos\left(\phi_{p-s}\right) - 0.272\left|{}^6\mathrm{s}_{12}\right|\left|{}^6\mathrm{p}_{20}\right|\cos\left(\phi_{p-s}\right),
\end{aligned} \tag{C.53}$$

and

$$\begin{aligned}
\mathrm{e}_4 = & -0.1233\left|{}^2\mathrm{p}_{12}\right|\left|{}^4\mathrm{p}_{24}\right| - 0.0807\left|{}^2\mathrm{p}_{12}\right|\left|{}^6\mathrm{p}_{20}\right| - 0.3978\left|{}^4\mathrm{p}_{24}\right|^2 \\
& - 0.2895\left|{}^4\mathrm{p}_{24}\right|\left|{}^6\mathrm{p}_{20}\right| - 0.1069\left|{}^6\mathrm{p}_{20}\right|^2.
\end{aligned} \tag{C.54}$$

Appendix D

Astrophysical S Factor for the ^{7}Li(d,n$_0$)^{8}Be and ^{7}Li(d,n$_1$)^{8}Be Reactions

Included here is the paper published in Physical Review C (**73**, 015801, January 2006) concerning the astrophysical S-factor results presented in Chapter 6.

D.1 Abstract

The absolute astrophysical S factor and cross section for the ^{7}Li(d,n$_0$)^{8}Be and ^{7}Li(d,n$_1$)^{8}Be reactions have been determined using deuteron beams with energies between 45 keV and 80 keV. The slope of the S factor is consistent with zero in the n$_0$ case but is slightly negative in the n$_1$ case. The S factor for the sum of both neutron groups for center-of-mass (c.m.) energies below 70 keV is $S(E)$ =

$5400(\pm 1500) - 37(\pm 21)E$ keV b where E is the c.m. energy in keV.

D.2 Introduction

The primordial abundance of ^{7}Li is one of the more important diagnostics of the degree of baryon inhomogeneity in early universe models [Boy93]. The ^{7}Li yield is determined from a balance between production and destruction reactions. An accurate knowledge of both types of reactions is necessary for cosmological model calculations to be reliable.

For one set of destruction reactions, the ^{7}Li+d reactions, recent primordial nucleosynthesis codes have incorporated resonant terms in addition to the direct term [Boy93]. These reaction rates were calculated using measured astrophysical S factors. However, the direct term for energies below the 280-keV resonance was assumed to have zero slope on the basis of (d,n) and (d,p) data taken between 1.6 to 2.0 MeV [Boy93, Sla57].

The cross section for the (d,n) channel, which is dominant over the (d,p) channel, has been studied below a center-of-mass (c.m.) energy of 280 keV [Hof01, Bag52] and has been measured at c.m. energies down to 50 keV [Hof01]. The S factor was experimentally determined at effective c.m. energies of 50 keV, 83.5 keV, and 100 keV [Hof01] which indicated that the slope of the S factor is non-zero and negative.

The present measurements were undertaken to determine the slope and absolute value of the S factor and the absolute cross section for ^{7}Li(d,n)^{8}Be at c.m. energies below 70 keV for the n_0 transition to the 0^+ground state of ^{8}Be and for the n_1 transition to the 2^+ first excited state. An investigation into the n_2 transition to the 4^+ second excited state was also undertaken, but the spectrum in this region was too

complicated to extract reliable results. The present results indicate that the S factor for the n_0 transition has a slope consistent with zero, whereas the S factor for the n_1 transition has a small negative slope at c.m. energies below 70 keV. These results are in reasonable agreement with the zero-slope S-factor assumption of Ref. [Boy93].

D.3 Experimental Method

The Triangle Universities Nuclear Laboratory (TUNL) atomic beam polarized ion source produced unpolarized deuteron beams for measurements at three separate energies: E_d = 45 keV, 60 keV, and 80 keV. Beam currents averaged about 40 μA. Data sets at 80 keV and 60 keV were taken at the beginning and end of the week-long run with the 45-keV set taken in the middle.

The target was made *in situ* in the vacuum chamber. Enriched 99% ^{7}Li was evaporated directly onto the 3-mm-thick aluminum target chamber face and was replenished every 4 hours. The deposited lithium layer was thick enough to stop the deuteron beam and was previously determined to be Li_2O. The measurements which established this are described in detail in Prior *et al.* [Pri04]. Target conditions were monitored by observing the counting rate as well as visual inspection of the target.

The emitted neutrons were detected using six 12.7-cm diameter and three 11.4-cm diameter organic liquid scintillators containing BC-501 fluid. Detectors were placed approximately 43 cm from the target face at angles of 0°, 23°, 45°, 68°, 90°, 113°, 135°, and 150°. The detector efficiency is vital to the determination of the total cross section and S factor; this efficiency is well modeled for given fractions of the ^{137}Cs edge using the Physikalisch-Technische Bundesanstalt (PTB) group's Monte Carlo programs NRESP7 and NEFF7 [Die82] and has been experimentally measured

previously at TUNL [GT97, SM98]. Therefore, the thresholds were carefully set at 1.0 times the ^{137}Cs edge (defined to be the point at which the yield falls to one-half its peak value) for these measurements. Data acquisition was configured to utilize pulse-shape discrimination (PSD) to enable separation of the neutrons from the gamma-ray background.

Prior to these measurements, the response function for each type of detector was measured using a monoenergetic neutron beam in TUNL's Shielded Source Area (SSA). Fast neutrons were produced via the ^{2}H(d,n)^{3}He reaction. The detector response function was then measured for a neutron energy corresponding to the n_0 group of the ^{7}Li(d,n)^{8}Be reaction (E_{lab} = 14 MeV) and for a neutron energy corresponding to the peak energy of the n_1 group (E_{lab} = 11 MeV). Time-of-flight techniques were used to separate the monoenergetic ^{2}H(d,n)^{3}He neutrons from the lower energy continuum neutrons generated by breakup reactions. The response functions for the 11 MeV and 14 MeV neutrons had identical shapes, differing only in where the endpoint energy was located. Because the n_1 group has a width of 1.5 MeV, the monoenergetic 11-MeV spectrum was then convoluted with a Breit-Wigner function of the same width to represent the actual response function for that neutron group. To obtain the response function for the n_2 group (E_{lab}=3.4 MeV), a blank titanium target was implanted with deuterium, and the E_{lab} = 2.8 MeV neutrons from the ^{2}H(d,n)^{3}He reaction were measured at E_d = 80 keV. This signal was then convoluted with a Breit-Wigner function of width 3.5 MeV to represent the actual response function for the n_2 group.

In addition to the neutron groups from the ^{7}Li(d,n)^{8}Be reaction, a neutron group from the ^{2}H(d,n)^{3}He reaction was also evident in the spectrum in nearly the same location as the n_2 peak. This state at E_{lab} = 2.8 MeV was fitted with the response

function mentioned in the previous paragraph and subtracted from the ^{7}Li(d,n)^{8}Be spectrum. This background peak was identified by studying the rise its yield in conjunction with the integrated beam current, especially with respect to the time at which a new ^{7}Li target layer was evaporated. Any other room background, gamma or neutron, was of sufficiently low energy that it was either eliminated by our threshold setting or low enough in energy to not impact our fitting region.

D.4 Data Analysis

The raw neutron spectrum for each angle was fitted with a combination of the measured n_0, n_1, n_2, and ^{2}H(d,n)^{3}He response functions as shown in Fig. D.1. To obtain raw n_0 yields, the n_1, n_2, and ^{2}H(d,n)^{3}He functions were subtracted from the spectrum; a similar procedure was performed to obtain the n_1 and n_2 yields. For n_0, the remaining spectrum was summed from approximately 2 MeV to 14 MeV. Because the entire spectral region was not summed, a correction factor was obtained to determine the absolute cross section by dividing the number of counts in the corresponding summation region of the response spectrum by the entire number of counts in the response spectrum. For the n_0 and n_1 states this ratio was generally on the order of 60%. However, for the n_2 state this ratio was 10% on average. More of the spectrum could not be used due to the efficiency of the detectors changing rapidly below 3 MeV. The small percentage of the spectrum that was usable and disentanglement issues with the neutrons from the ^{2}H(d,n)^{3}He reaction made the n_2 data extraction difficult and unreliable.

Each raw neutron spectrum was also fitted at each angle with just a combination of the measured n_0 and n_1 response functions in the region between approximately 6

MeV and 14 MeV, where the n_2 and ^{2}H(d,n)^{3}He states should have little effect on the data. These yield results agreed with the yield results computed as described above. For these cases, the ratio of the number of counts in the summed region to those of the entire spectrum was generally 30-50%.

Because the target stops the deuteron beam, the observed yield is the total yield from the beam energy to zero and can be written as:

$$Y(E_d) = C \int_{E_d}^{0} \frac{\sigma(E) f}{STP(E)} dE \tag{D.1}$$

where E_d is the deuteron beam energy, $\sigma(E)$ is the energy-dependent cross section, f is the atomic fraction of the target, and $STP(E)$ is the stopping power of the target for deuterons. The constant C is the total number of incident deuterons times the detector solid angle and efficiency. The raw yield for each angle was normalized by this constant. The cross section can be written in terms of the astrophysical S(E) factor:

$$\sigma(E_{c.m.}) = \frac{S(E_{c.m.})}{E_{c.m.}} e^{-2\pi\eta} \tag{D.2}$$

where η is the Sommerfeld parameter and $2\pi\eta = 31.29 Z_1 Z_2 (\mu / E_{c.m.})^{1/2}$. The projectile and target charges are Z_1 and Z_2, respectively, μ is the reduced mass in amu, and $E_{c.m.}$ is the center-of-mass energy in keV.

At the low energies of this experiment, the S factor was assumed to be linear with energy:

$$S(E_{c.m.}) = S_0 + S_1 E_{c.m.} \tag{D.3}$$

The yield in Eq. (D.1) can then be calculated for a given beam energy from the values of S_0 and S_1.

As a preliminary evaluation of our data, the ratios of the experimental yields at each energy were compared to the ratios predicted given a constant S factor, i.e.

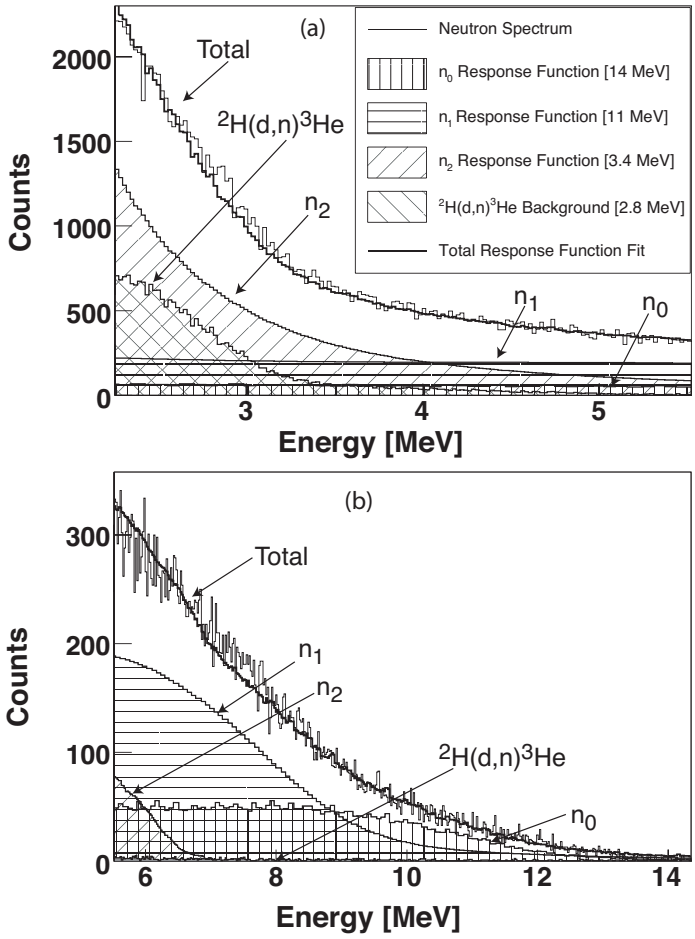

Figure D.1: The measured total neutron spectrum for the ^{7}Li(d,n)^{8}Be reaction at an incident deuteron energy of 80 keV in the fitting region between 2 MeV and 14 MeV. (a) shows the low energy end of the fitting region, and (b) shows the high energy end. The legend in (b) is the same as that in (a). The energy calibration used for the x-axis is uncertain to $\pm$ 0.5 MeV and was determined by pinpointing the channel corresponding to the 14 MeV endpoint energy of the n_0 state, dividing that channel number by the energy to obtain a calibration factor, and applying that calibration factor to all channels in the spectrum.

$S_1 = 0$ in Eq. (D.3). This comparison is shown in Table D.1 and indicates that the slope of the S factor is zero for the n_0 case but not for the n_1 case.

	Theoretical	Experimental	
	constant S(E)	n_0	n_1
$Y(80)/Y(60)$	10	11 ± 1.5	8.4 ± 0.91
$Y(60)/Y(45)$	15	14 ± 3.9	15 ± 2.6

Table D.1: Comparison of the yield ratios for a theoretical calculation assuming S(E) is constant and the experimental ratios for the n_0 and n_1 neutron yields. $Y(80)$, $Y(60)$, and $Y(45)$ are the yields at a beam energy of 80 keV, 60 keV, and 45 keV, respectively.

To determine the slope, the integral in Eq. (D.1) was evaluated numerically, and the slope was determined by fitting the three yields simultaneously. The target was divided into 1-μg/cm^2 layers corresponding to less than 1-keV energy loss in the target material. The stopping power of the target was calculated using Anderson and Ziegler's energy loss equations [And77]. Using Eq. (D.3) as the form of S(E) and starting with arbitrary values for S_0 and S_1, the yield and energy loss for the first layer was calculated. The yield calculation was then repeated for the next layer at the decreased energy. This process was repeated until the yield of a subsequent layer was less than 0.1% of the yield in the first layer. The sum of the yields from all layers of the target equaled the total yield at the beam energy. This process was performed at all three beam energies and repeated iteratively, continuously adjusting the values of S_0 and S_1 until the best fit to the measured yields was obtained. The errors in S_0 and S_1 arise from both the statistical uncertainties associated with the experimental yields and the systematic errors from the response function fits to the spectra, from the S-factor fits to the three yields, and from the parameters necessary to determine the absolute scale. The statistical errors were at most 15%; the components of the systematic error, which were added in quadrature, were an average error of 20% for

the response function fits to the spectra and a 4% error for the parameters which comprised the absolute scale. The errors in the S-factor fits to the three yields, which were also included in the systematic error, were 5% for the S_0 parameter for the n_0 data, 20% for the S_0 parameter for the n_1 data, and 50% for the S_1 parameter for the n_1 data.

The constant C in Eq. (D.1) allows an absolute scale to be included in the yield calculation, and thus in the S-factor and cross-section determination. This scale factor was folded into the S-factor result, giving it units of keV b. Using the results of the S factor derived from the yields, the absolute cross section for each energy was then determined.

D.5 Experimental Results and Discussion

The measured yields as a function of beam energy for the ground-state and first-excited-state transitions are shown in Fig. D.2. The error bars represent the statistical errors from the raw yields and the systematic errors from fitting the response functions to the spectra. The two curves shown in each plot are the best fits to the experimental results assuming the S factor is constant with energy (dotted line) or varies linearly (non-zero slope, solid line). The numerical results and the corresponding χ^2 values are given in Table D.2. As seen in Fig. D.2 and the χ^2 values in Table D.2, the linear fit with a negative slope is much better than the constant fit for the n_1 transition, but the addition of a non-zero slope in the n_0 case changes little. Therefore, for the n_0 case, a zero slope is the best fit for the data.

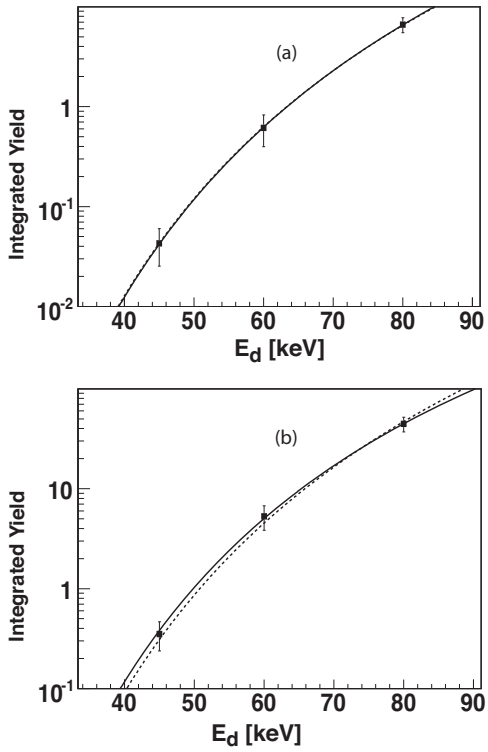

Figure D.2: Measured energy-integrated yields for (a) ^{7}Li(d,n$_0$)^{8}Be and (b) ^{7}Li(d,n$_1$)^{8}Be plotted at the incident beam energy. The error bars include statistical and systematic uncertainties. The solid lines were obtained by assuming an S factor that varies linearly with deuteron energy; the dashed lines were obtained by assuming a constant S factor (zero slope).

For the n$_1$ transitions, this negative slope makes a significant difference in the S(0) value, as is shown in Fig. D.3. The S(0) value for the linear S(E) is a factor of 1.6 greater than that for a constant S(E) for the n$_1$ neutron group.

Electron screening effects, which are discussed in detail in [Lat01], are expected to give the S factor a negative slope at very low energies. For ^{7}Li+d, this is anticipated to only significantly influence the results for incoming deuteron beam energies of $E_d < 50$ keV. In the present experiment, the incident deuterons slow from the beam energy to zero within the target , but because the cross section decreases exponentially with decreasing deuteron energy, most of the yield will occur for the initial higher

state	$S(E) = S_0 + S_1 E$ [keV b]	χ^2
n_0	$S(E) = 430(\pm 120)$	0.032
	$S(E) = 400(\pm 200) + 0.62(\pm 3.3)E$	0.030
n_1	$S(E) = 3100(\pm 750)$	2.2
	$S(E) = 5000(\pm 1500) - 37(\pm 21)E$	0.62

Table D.2: Numerical values for the constant and linear S(E) fits to the experimental yields.

energies in the target. For a deuteron beam with E_d=45 keV, the energy at which 50% of the yield is produced is E_{50} = 43 keV, and that at which 90% of the yield is produced is E_{90} = 37 keV. Using the formalism of [Lat01], electron screening would be expected to attribute an average relative slope $S_1/S_0 = -0.006$ keV^{-1} for 45 keV incident deuterons on ^{7}Li. We conclude that the negative relative slope of the (d, n_1) channel ($S_1/S_0 = -0.007 \pm 0.005$ keV^{-1}) could be attributed to electron screening effects. Although the relative slope for the (d, n_0) channel is consistent with zero ($S_1/S_0 = 0.002 \pm 0.008$ keV^{-1}), the uncertainty also allows for a slope compatible with screening effects.

Fig. D.4 shows the S-factor results of the present measurement along with previous results for ^{7}Li(d,n)^{8}Be. The solid line is the linear S(E) result obtained from the analysis discussed above. The S factor for n_0+n_1 is $S(E) = 5400(\pm 1500) - 37(\pm 21)E$ keV b. The data points of Ref. [Hof01, Bag52] and the line representing the assumptions of Ref. [Boy93] are for all three neutron groups. Therefore, the present measurement can only act as a lower limit on these measurements. However, the small slope of the present result is in reasonable agreement with the zero-slope assumption of Ref. [Boy93]. Boyd *et al.* examined cross-section data measured by Ref. [Sla57] and found that values obtained for $S(E)$ from those data were fairly constant from 1.6 to 2.0 MeV. They then assumed this constant value for the S factor and extrapolated it

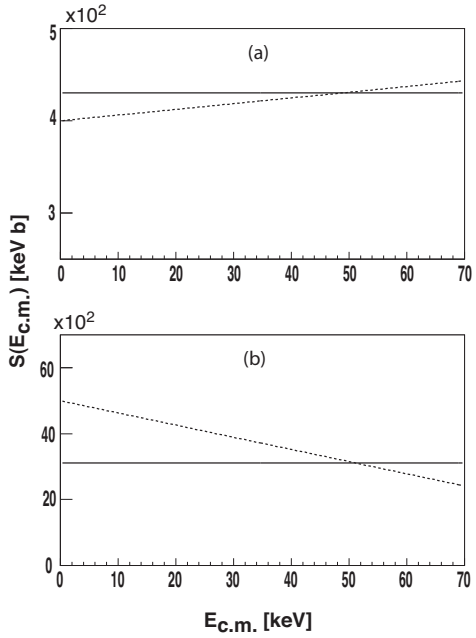

Figure D.3: Comparison of the constant S(E) result (solid line) and the linear, non-zero-slope S(E) result (dotted line) for the (a) n_0 and (b) n_1 groups. In the n_1 case, the slope of the S factor makes a significant difference in the value of S(0).

down to zero energy [Boy93]. In order to compare the slope of the present data with that of Ref. [Hof01], their data points at $E_{c.m.} = 50$ and 83.5 keV were fitted to a line with slope equal to our slope of -37 b. The best fit resulted in a line equal to our line plus 75000 keV b, or $80000 - 37E$ keV b. This line is shown in Fig. D.4 as the dot-dashed line and indicates that the slope of the S factor at higher energies, as seen in the Hofstee *et al*. data, appears to be more negative than the slope of the present result. Note, however, that the present result does not include the n_2 neutron group.

Fig. D.5 shows the corresponding comparison of the total cross sections. The points representing these present measurements are plotted at the effective center of mass energy, i.e. the energy at which half the yield is deposited in the target, and are the results for n_0+ n_1; these results are given in Table D.3. The present work lies below the (d,n) cross section calculated from the S factor given by Ref. [Boy93], which

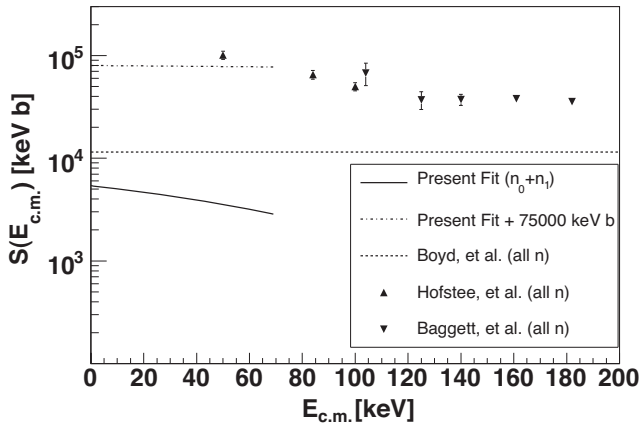

Figure D.4: Results of the present measurement (solid line) along with the previous data of Ref. [Boy93], [Hof01], and [Bag52]. The line assumed by Ref. [Boy93] is based on data from Ref. [Sla57]. The points for Ref. [Bag52] were computed by assuming their differential cross section data at 90^o was isotropic, multiplying it by 4π to get the total cross section, and finally using the total cross section to deduce the S factor. It should be noted that the data for Ref. [Boy93], [Hof01], and [Bag52] include all neutron groups whereas the present result is for the n_0 and n_1 groups only. The dot-dashed line is the present result + 75000 keV b, resulting from the best fit of a line with slope equal to the present slope of -37 b to the two lower energy points of Ref. [Hof01].

	$\sigma_{Total}(E_{c.m.,eff})[\mu$b]	
$E_{c.m.,eff}$ [keV]	n_0	n_1
33	0.017 ± 0.0047	0.15 ± 0.066
43	0.17 ± 0.047	1.3 ± 0.67
57	1.3 ± 0.39	9.1 ± 6.0

Table D.3: Numerical values for the absolute cross section for n_0 and n_1 as computed from the S factors $S(E) = 430(\pm 120)$ keV b and $S(E) = 5000(\pm 1500) - 37(\pm 21)E$ keV b, respectively.

is to be expected due to the absence of the n_2 group in the present results. Hofstee *et al.* (Ref. [Hof01]) measured the branching ratio of the ^{7}Li(d,n)^{8}Be$\rightarrow 2\alpha$ yields with respect to the yield of the ^{6}Li(d,p_0+p_1) reaction and noted that contributions from ^{6}Li reactions complicated the spectra [Hof01].

D.6 Conclusion

These measurements have determined the absolute astrophysical S factor and cross section for the ^{7}Li(d,n_0)^{8}Be and ^{7}Li(d,n_1)^{8}Be reactions at center-of-mass energies below 70 keV. The slope of the S factor is consistent with zero in the n_0 case but slightly negative in the n_1 case. The S(E) for the ^{7}Li(d,n_0)^{8}Be reaction was found to be $S(E) = 430(\pm 120)$ keV b, and that for the ^{7}Li(d,n_1)^{8}Be reaction was found to be $S(E) = 5000(\pm 1500) - 37(\pm 21)E$ keV b. The total S factor for the ^{7}Li(d,n_0+n_1)^{8}Be reaction is $S(E) = 5400(\pm 1500) - 37(\pm 21)E$ keV b where E is the c.m. energy in keV for all three results. The negative value of the slope is consistent with the value expected from an estimate of the effects due to electron screening. We therefore recommend that this slope should not be included in determining the S factor at zero energy.

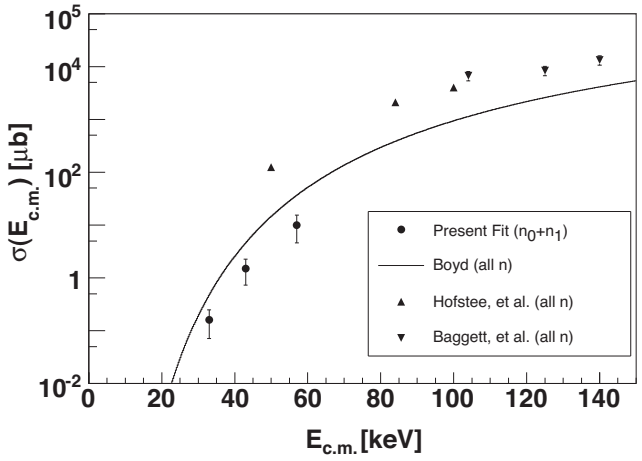

Figure D.5: Results of the present measurement (circular points) along with the previous data of Ref. [Boy93], [Hof01], and [Bag52]. The points for Ref. [Bag52] were computed by assuming their differential cross section data at 90^o was isotropic and then multiplying it by 4π to get the total cross section. The line representing Ref. [Boy93] was obtained by using the S-factor result they presented to compute the cross section. It should be noted that the data for Ref. [Boy93], [Hof01], and [Bag52] include all neutron groups whereas the present result is for the n_0 and n_1 groups only.

D.7 Acknowledgments

This work was partially supported by grants from the U. S. Department of Energy under grant numbers DE-FG02-97ER41046, DE-FG02-97ER41033, and DE-FG02-97ER41042.

Bibliography

[Ali00] M. Aliotta, C. Spitaleri, M. Lattuada, A. Musumarra, R. G. Pizzone, A. Tumino, C. Rolfs, and F. Strieder. Eur. Phys. J., **9**(2000) 435.

[And77] D. A. Andrews and G. Newton. J. Phys. D, **10**(1977) 845.

[Arn96] D. Arnett. *Supernovae and Nucleosynthesis*. Princeton University Press, Princeton, N. J., 1996.

[AS60] F. Ajzenberg-Selove, editor. *The Compound Nucleus*, page 625. Academic Press, New York, 1960.

[Ass87] H. J. Assenbaum, K. Langanke, and C. Rolfs. Z. Physik A, **327**(1987) 461.

[Bag52] L. M. Baggett and S. J. Bame. Phys. Rev., **85**(1952) 434.

[Bar71] H. H. Barschall, editor. *Polarization Phenomena in Nuclear Reactions*, page xxv. University of Wisconson Press, Madison, Wisconsin, 1971.

[Bel05] T. Belgya, O. Bersillon, R. Capote, T. Fukahori, G. Zhigang, S. Goriely, M. Herman, A. V. Ignatyuk, S. Kailas, A. Konig, P. Oblozhinsky, V. Plujko, and P. Young. *Handbook for calculations of nuclear reaction data: Reference Input Parameter Library*. IAEA, Vienna, http://www-nds.iaea.org/RIPL-2/, 2005.

[Bev03] P. R. Bevington and D. K. Robinson. *Data Reduction and Error Analysis for the Physical Sciences*. McGraw-Hill, Inc., New York, 2003.

[Boy93] R. N. Boyd, C.A. Mitchell, and B. S. Meyer. Phys. Rev. C, **47**(1993) 2369.

[Boy01] R. N. Boyd. Nucl. Phys., **A693**(2001) 249.

[Bra05a] B. Braizinha. Private communications, (2005).

[Bra05b] B. Braizinha, H. R. Weller, A. Sabourov, and I. J. Thompson. TUNL Progress Report, **XLIV**(2005).

[Bre31] G. Breit and I. I. Rabi. Phys. Rev., **38**(1931) 2082–2083.

[Cle90] T. B. Clegg. Rev. Sci. Instr., **61**(1990) 385.

[Cro01] A. S. Crowell. Ph.D. thesis, Duke University, 2001.

[Die82] G. Dietz and H. Klein. *NRESP4 and NEFF4 Monte Carlo Codes for the Calculation of Neutron Response Functions and Detection Efficiencies for NE 213 Scintillation Detectors*. Physikalisch-Technische Bundesanstalt, Bundesallee 100, W-3300 Braunschweig, 1982.

[Dol02] A. D. Dolgov. Nucl. Phys., **B110**(2002) 137.

[Edm74] A. R. Edmonds. *Angular Momentrum In Quantum Mechanics*. Princeton University Press, Princeton, New Jersey, 1974.

[Fer65] A. J. Ferguseon. *Angular Correlation Methods in Gamma-Ray Spectroscopy*. John Wiley & Sons, New York, 1965.

[Gal84] R. B. Galloway and A. M. Ghazarian. Phys. Rev. C, **29**(1984) 2349.

[GT97] D. E. Gonzalez Trotter. Ph.D. thesis, Duke University, 1997.

[Hof01] M. A. Hofstee, A. K. Pallone, F. E. Cecil, J. A. McNeil, and C. S. Galovich. Nucl. Phys., **A688**(2001) 527c.

[Jam71] F. James and M. Roos. *MINUIT*. CERN Computer Centre Program Library, 1971.

[Kno00] G. F. Knoll. *Radiation Detection and Measurement*. John Wiley and Sons, Inc., 2000.

[Kun] P. D. Kunz. *Zero Range Distorted Wave Born Approximation*. http://spot.colorado.edu/∼kunz/DWBA.html.

[Kun03] P. D. Kunz. Private communications, (2003).

[Lat01] M. Lattuada, R. G. Pizzone, S. Typel, P. Figuera, D. Miljanic, A. Musumarra, M. G. Pellegriti, C. Rolfs, C. Spitaleri, and H. H. Wolter. The Astrophysical Journal, **562**(2001) 1076.

[Leo94] W. R. Leo. *Techniques for Nuclear and Particle Physics Experiments*. Springer-Verlag, 1994.

[McC75] C. R. McClenahan and R. E. Segel. Phys. Rev. C, **11**(1975) 370.

[Nis82] H. Nishioka, R. C. Johnson, J. A. Tostevin, and K. I. Kubo. Phys. Rev. Lett., **48**(1982) 1795.

[Phi87] R. J. Philpott. NIM, **A259**(1987) 317–323.

[Pri04] R. M. Prior, M. C. Spraker, A. M. Amthor, K. J. Keeter, S. O. Nelson, A. Sabourov, K. Sabourov, A. Tonchev, M. Ahmed, J. H. Kelley, D. R. Tilley, H. R. Weller, and H. M. Hofmann. Phys. Rev. C, **70**(2004) 055801.

[Pri05] R. M. Prior. Private communications, (2005).

[Rol88] C. E. Rolfs and W. S. Rodney. *Cauldrons in the Cosmos*. University of Chicago Press, Chicago, 1988.

[Ros53] M. E. Rose. Phys. Rev., **91**(1953) 610.

[Sab03] K. Sabourov. Ph.D. thesis, Duke University, 2003.

[Sat83] G. R. Satchler. *Direct Nuclear Reactions*. Oxford University Press, 1983.

[Sch76] A. E. Schilling, N. F. Mangleson, K. K. Nielson, D. R. Dixon, M. W. Hill, G. L. Jensen, and V. C. Rogers. Nucl. Phys., **A263**(1976) 389.

[Sei74] F. Seiler. Computer Physics Communication, **6**(1974) 229.

[Ser04] P. D. Serpico, S. Esposito, F. Iocco, G. Mangano, G. Miele, and O. Pisanti. J. Cosmol. Astropart. Phys., **12**(2004) 010.

[Sey79] R. G. Seyler and H. R. Weller. Phys. Rev. C, **20**(1979) 453.

[Sho93] T. D. Shoppa, S. E. Koonin, K. Langanke, and R. Seki. Phys. Rev. C, **48**(1993) 837.

[Sla57] J. C. Slattery, R. A. Chapman, and T. W. Bonner. Phys. Rev., **108**(1957) 809.

[SM98] F. Salinas Meneses. Ph.D. thesis, Duke University, 1998.

[Spr00] M. Spraker, R. M. Prior, M. A. Godwin, B. J. Rice, E. A. Wulf, J. H. Kelley, D. R. Tilley, and H. R. Weller. Phys. Rev. C, **61**(2000) 015802.

[Tho88] I. J. Thompson. Computer Physics Reports, **7**(1988) 167.

[Tho04] I. J. Thompson. *FRESCO Manual*. http://www.fresco.org.uk, 2004.

[vM73] U. von Möllendorff, A. Janett, F. Seiler, and H. R. Striebel. Nucl. Phys., **A209**(1973) 323.

[Wag72] R. V. Wagoner. The Astrophysical Journal, **179**(1972) 343.

[Wul99] Eric A. Wulf. Ph.D. thesis, Duke University, 1999.

Biography

Amanda Leigh Sabourov

Personal

- Born in Charleston, SC on April 21, 1978

Education

- B.S. Physics, North Carolina State University, Raleigh, NC, 2001
- M.A. Physics, Duke University, Durham, NC, 2003

Positions

- Research Assistant, Idaho National Engineering Laboratory, Summer 1999
- Research Assistant, Idaho State University, 1998-1999
- Research Assistant, Duke University, TUNL, Summer 1999 and 2000-2001
- Teaching Assistant, Duke University, 2001-2003
- Research Assistant, Duke University, TUNL, 2001-2006

Publications

"Astrophysical S factor for the ^{7}Li(d, n_0)^{8}Be and ^{7}Li(d, n_1)^{8}Be reactions," (A. Sabourov, M. W. Ahmed, M. A. Blackston, A. S. Crowell, C. R. Howell, B. A. Perdue,R. Prior, K. Sabourov, M. C. Spraker, A. P. Tonchev, and H. R. Weller), Phys. Rev. C, **73**, 015801 (2006).

"Experimental and theoretical study of the ^{2}H($\vec{d}, \gamma$)^{4}He reaction below $E_{c.m.}$= 60 keV," (K. Sabourov, M. W. Ahmed, S. R. Canon, B. Crowley, H. M. Hofmann,K. Joshi, J. H. Kelley, S. O. Nelson, B. A. Perdue, E. C. Schreiber, R. Prior, A. Sabourov, M. C. Spraker, A. Tonchev, M. Trini, and H. R. Weller), Phys. Rev. C **70**, 064601 (2004).

"Energy dependence of the astrophysical S factor for the ^{6}Li(p,γ)^{7}Be reaction," (R. M. Prior, M. Ahmed, A. M. Amthor, H. M. Hofmann, K. J. Keeter, J. H. Kelley, S. O. Nelson, A. Sabourov, K. Sabourov, M. C. Spraker, D. R. Tilley, A. Tonchev, and H. R. Weller), Phys. Rev. C **70** , 055801 (2004).

"Analyzing power measurement for ^{14}N(p,γ)^{1}5O reaction at astrophysically relevant energies," (S. O. Nelson, M. W. Ahmed, B. A. Perdue, R. M. Prior, A. L. Sabourov, K. Sabourov, M. Spraker, A. P. Tonchev, and H. R. Weller), Phys. Rev. C **68** , 065804 (2003).